Journal of Healthcare Engineering

Human-Centered Systems in Rehabilitation Engineering

Lead Guest Editor: Duk Shin
Guest Editors: Ludovico Minati, Chao Chen, Jaehyo Kim, and Yousun Kang

Human-Centered Systems in Rehabilitation Engineering

Journal of Healthcare Engineering

Human-Centered Systems in Rehabilitation Engineering

Lead Guest Editor: Duk Shin
Guest Editors: Ludovico Minati, Chao Chen, Jaehyo Kim, and Yousun Kang

Contents

Hindawi
Journal of Healthcare Engineering
Volume 2020, Article ID 1823268, 11 pages
https://doi.org/10.1155/2020/1823268

Research Article

Design of a Machine Learning-Assisted Wearable Accelerometer-Based Automated System for Studying the Effect of Dopaminergic Medicine on Gait Characteristics of Parkinson's Patients

Satyabrata Aich,[1] **Pyari Mohan Pradhan**,[2] **Sabyasachi Chakraborty**,[3] **Hee-Cheol Kim**,[1] **Hee-Tae Kim**,[4] **Hae-Gu Lee**,[5] **Il Hwan Kim**,[6] **Moon-il Joo**,[1] **Sim Jong Seong**,[1] **and Jinse Park**[7]

[1]*Institute of Digital Anti-Aging Healthcare, Inje University, Gimhae, Republic of Korea*
[2]*Department of Electronics and Communication Engineering, IIT, Roorkee, India*
[3]*Department of Computer Engineering, Inje University, Gimhae, Republic of Korea*
[4]*Department of Neurology, Hanyang University Hospital, College of Medicine, Seoul, Republic of Korea*
[5]*Department of Industrial Design, Kyoung Sung University, Busan, Republic of Korea*
[6]*Department of Oncology, Haeundae Paik Hospital, Inje University, Busan, Republic of Korea*
[7]*Department of Neurology, Haeundae Paik Hospital, Inje University, Busan, Republic of Korea*

Correspondence should be addressed to Jinse Park; jinsepark@gmail.com

Received 24 September 2019; Revised 15 December 2019; Accepted 8 January 2020; Published 18 February 2020

Guest Editor: Chao Chen

In the last few years, the importance of measuring gait characteristics has increased tenfold due to their direct relationship with various neurological diseases. As patients suffering from Parkinson's disease (PD) are more prone to a movement disorder, the quantification of gait characteristics helps in personalizing the treatment. The wearable sensors make the measurement process more convenient as well as feasible in a practical environment. However, the question remains to be answered about the validation of the wearable sensor-based measurement system in a real-world scenario. This paper proposes a study that includes an algorithmic approach based on collected data from the wearable accelerometers for the estimation of the gait characteristics and its validation using the Tinetti mobility test and 3D motion capture system. It also proposes a machine learning-based approach to classify the PD patients from the healthy older group (HOG) based on the estimated gait characteristics. The results show a good correlation between the proposed approach, the Tinetti mobility test, and the 3D motion capture system. It was found that decision tree classifiers outperformed other classifiers with a classification accuracy of 88.46%. The obtained results showed enough evidence about the proposed approach that could be suitable for assessing PD in a home-based free-living real-time environment.

1. Introduction

The most important symptom of Parkinson's disease (PD) is the disturbances in gait that directly affects the daily activities as well as the quality of life [1]. The disturbances in gait characteristics in PD patients are categorized into continuous gait and episodic gait disturbances [2]. Typical features of gait in PD are short-step, hypokinetic, slow gait with decreased arm swing, and episodic gait, which includes freezing of gait (FOG) and festinating gait [3]. Despite the clinical importance, most clinicians usually depend on neurological examination or self-questionnaire-based examination for a short period of time. Therefore, it is very difficult to assess the PD patient's gait status outside the

clinic and in a real-world environment. Objective quantification of gait is crucial for the measurement of overall condition as well as disease monitoring in PD. Several clinical scales such as Tinetti mobility test (TMT), Timed Up and Go (TUG), and Unified Parkinson's Disease Rating Scales (UPDRS) are widely used to assess the PD and its severity. In the last decade, numerous studies have investigated the usefulness of gait analysis. Quantitative gait analysis includes infrared-based motion capture (three-dimensional (3D) motion capture), pressure-based gait analysis (GAITRite), and treadmill gait analysis [4–6]. Despite their strength of accurate quantification of gait, clinical implication is still controversial due to high cost and large space or laboratory required for system set up.

To overcome the previous limitations, an attempt has been made in this study to quantify the gait characteristics using the algorithmic-based approach with a wearable accelerometer and its validation using a 3D motion capture system as well as TMT. TMT is widely used for predicting the fall risk of elderly people based on the balance and gait test score. TMT test consists of two components such as the Tinetti balance scale and the Tinetti gait scale. The balance scale consists of 9 parameters, and each parameter has subparameters with a score of 0/1 or 0/1/2. The total possible score of the balance section is 16. The gait scale consists of 8 parameters, and each parameter has subparameters with a score of 0/1 or 0/1/2. The total possible score of the gait section is 12. Each patient has to be assessed based on these two scores. The combined score determines the risk of falls in elderly people. According to Tinetti, a total score of ≤ 18 is treated as high risk, 19–23 is treated as moderate risk, and ≥ 24 is treated as low risk [7]. Since the Korean version of TMT has already been validated with the PD patients in the laboratory [8], this version has been used in this study.

The contributions of the proposed study are as follows:

(1) This study includes enrolment of a large number of participants with PD, higher than that recommended by the movement disorder society [9]. While the recommended minimum number of patients is 30, this study involves 48 PD patients to provide proper validity and reliability of the result. In addition, 40 healthy older patients' group has been included in the study for the classification of PD subjects from healthy older group based on estimated gait characteristics. Due to a large number of subjects, the proposed study could be recommended for a real-life scenario.

(2) The proposed study focuses on the PD patients when they are clinically in "on" state, i.e., after taking dopaminergic medicine. "On" state is the state where the effect of the medicine is present, and the improvement in the gait characteristics is closer to the healthy older group.

(3) The good accuracy found by using only accelerometer data for estimating spatiotemporal gait characteristics indicates that the gyroscope data could be excluded for these kinds of studies. This will lead to low power consumption in wearable devices and hence a longer battery life for gait monitoring.

(4) The validation study provides a low-cost alternative for assessing gait characteristics in the "on" state of PD patients for both indoor and outdoor environments.

(5) The proposed study demonstrates that spatiotemporal gait characteristics estimated by using only accelerometer data are highly correlated with those obtained from a 3D motion capture system. Furthermore, a high correlation was also found between results obtained from the proposed approach and those obtained from the clinical TMT test.

(6) The proposed study proposed an automatic system that can classify PD patients and HOG with machine learning techniques based on gait characteristics.

The structure of the paper is outlined in the following way: Section 2 describes the past work related to this study. Section 3 describes the data collection methods as well as the proposed methodology. Section 4 presents the results and outcomes of the proposed approach. Section 5 provides the discussion. Section 6 describes the conclusion.

2. Related Work

The gait analysis performed using a conventional way using a qualitative analysis technique is usually performed in the clinics, and it required a complete medical history of the patients to determine the gait characteristics. The conventional method is relatively simple; however, it depends on the expertise of the physicians, and it is relatively difficult to measure the parameters in a quantitative manner with high accuracy that could be useful for clinical applications. To address this aforementioned problem, a new method has been introduced in this paper to quantify the gait characteristics in an objective way by using quantitative measurement techniques [10, 11]. Wearable devices are now used for a wide range of healthcare observations as well as the measurement of gait. The triaxial wearable accelerometer is known to be a useful tool for assessing gait as well as various motor symptoms in PD. It is not expensive as well as can be used in a comfortable way by the user [12]. Beck et al. proposed a new approach to quantify the gait smoothness using accelerometer and gyroscope signals. They have implemented this method in PD patients as well as healthy controls, and they found clear differentiation in terms of smoothness between two groups. For validation, they have used the correlation technique by comparing their algorithm spectral arc length measure (SPARC) with traditional gait measures and the UPDRS scale. This is one of the potential use cases for using wearable sensors; however, their method did not use 3D motion capture and TMT gait scale for correlation [13]. Hausdorff et al. mentioned that quantification of gait characteristics was possible using a wearable device. They have collected the accelerometer data during the tandem walking and also validated the method. This method also mentioned the potential of using wearable devices for gait analysis. They have not implemented this

method to the PD patients, and at the same time, they have not used any other methods such as 3D motion capture or clinical scale for correlation of their method [14]. Gazit et al. proposed a method for quantifying gait initiations using wearable sensors. They have used only one IMU sensor for evaluating the gait initiations and found good results. They have validated the method with the ground truth and found that the interclass correlation coefficient with one wearable sensor ranges from 0.75 to 0.96. They have tested this method on the data collected from younger and older adults. They have not used the 3D motion capture system for validation of their results and also not implemented for PD patients [15]. Anwary et al. proposed a method to find the best location in the foot to place wearable sensors. They have used accelerometer data and gyroscopic data for determining the gait features. For validation of this method, they have used a quality motion capture system. They have done this analysis for healthy groups and mentioned that wearable sensors have the potential to quantify the gait characteristics with high accuracy [16]. Qiu et al. proposed a method that used body-worn sensors to collect the gait data for the assessment of stroke patients. They have found that the gait analysis has a huge contribution towards the diagnosis and treatment of the stroke patients and mentioned that a wearable sensor-based gait analysis system has the potential for supporting rehabilitation in the clinics and hospitals [17]. Byun et al. have proposed a method that uses the wearable accelerometer to measure the gait characteristics of older people having normal cognition. The gait characteristics are quantified using the signal-processing algorithm. Validation of the measurement method was carried out using the GAITRite system. The two methods show a good level of correlation with a correlation coefficient that ranges from 0.91 to 0.96. They have not used the 3D motion capture system, and this method was not tested for PD patients [18]. Pham et al. have proposed a technique that used an inertial measurement system which consists of a gyroscope and an accelerometer to detect the gait patterns such as toe-off and heel strike in the patients with PD as well as older adults when they were encountered with turning as well as straight walking. An algorithm based on continuous wavelet transform is used to detect the gait patterns, and the validation study was carried out using the optoelectronic system. They have not used any clinical scale for comparing the result. 3D motion capture has not been used in this research [19]. Del Din et al. have used the wearable accelerometer for measuring the gait characteristics of older adults as well as PD patients. Signal processing of the collected accelerometer data provides gait characteristics, and the validation was carried out using the instrumented walkway. Fourteen gait characteristics were compared; it was found that four characteristics show a good amount of correlation, another four gait characteristics show an agreement of moderate level, and the rest six characteristics show an agreement of a poor level. This paper does not have any correlation analysis of gait characteristics with the clinical scale, and they did not use the 3D motion capture system [20]. Aich et al. proposed a method that used a wearable accelerometer that can detect FoG, and the validation study was performed that shows a good level of correlation with a correlation coefficient that ranges from 0.961 to 0.984. The study also proposed a machine learning-based approach to distinguish PD with FoG from PD with no FoG, and an accuracy of 88% has been found using SVM classifier. In this research, the effect of dopaminergic medicine has not been considered, and the correlation analysis has not been performed with clinical scale [21]. Mikos et al. proposed a method for FoG detection using a single sensor node. They have developed a system using machine learning based on the extracted features from the signals. They have found a classification accuracy of 92.9% in average of sensitivity and specificity when exploiting its patient adaptive learning capability. This research has given enough evidence that a single sensor can be used for the detection of FoG and machine learning systems for the classification of FoG [22]. Jeon et al. proposed a study that used the wearable device to detect the severity of tremor in PD. The wearable device used in this study consists of an accelerometer and gyroscope. This study also used machine learning techniques to classify the severity of tremor based on the score of UPDRS. It was found that the decision tree outweighs other classifiers with an accuracy of 85.5%. This research has provided enough evidence that the wearable sensors can be used for the diagnosis of PD, and machine learning techniques can be used to automate the system [23]. Samà et al. proposed a study using wearable accelerometer that can detect freezing of gait at real-time environment using a set of features which are related to the previous approaches mentioned by the previous researchers. These features were trained using machine learning classifiers and used to detect the FoG with an improvement over the previous methods. This research suggested that the wearable sensor has the potential to be used for measuring the gait characteristics, and machine learning techniques could be used for the detection of the PD group [24].

The past works mentioned above provide a strong recommendation about the use of the wearable device in the field of PD as well as the effective use of machine learning techniques for autodetection of gait patterns in PD and HOG. The proposed approach has got a lot of inspiration from the previous pieces of literature cited by different researchers. In this study, an algorithmic-based approach has been developed, and it was validated using clinical test and well-known measuring instruments, and a machine learning-based approach has been proposed to detect the PD from the healthy older group using estimated gait characteristics. This system is developed by keeping in mind that it can be used in the home environment as well as in clinical environments.

3. Proposed Methodology

3.1. Data Collection. This study was performed clinically in the "on" state, i.e., after taking dopaminergic medicine for the PD group of patients. "On" state is the state where there is an effect of the medicine. In this state, there is an improvement in gait characteristics. The resulting gait characteristics are very similar to those of the healthy older group. The accelerometer data for PD patients have been

collected in the "on" state so as to study the difference between two groups, i.e., PD patients and healthy older group when they are in a similar state. This study was performed at Haeundae Paik Hospital located at Busan, South Korea. The approval was taken from the review board of the institute (IRB No. 2017-01-028). Prior approval has been taken from all participants before joining this study. The details about the PD group are shown in Table 1.

The healthy older group comprises normal persons with no signs of PD. No medication has been given to them prior to this study. The healthy group consists of 22 males and 18 females. All the subjects in the healthy group were age-matched. The details regarding the patients belonging to the healthy group are shown in Table 2.

UPDRS and H&Y represent Unified Parkinson's Disease Rating Scale and Hoehn and Yahr scale, respectively. UPDRS is widely used for checking the severity of the disease [25]. H&Y scale is a clinical rating scale, which is used to define different categories of motor functions in the PD [26]. Tinetti gait scale is widely used for predicting the fall risk of elderly people.

The participants were asked to wear the accelerometer on the left knee as well as the right knee. Two wearable triaxial accelerometers with a sampling frequency of 32 Hz (Fit Meter, Fit. Life, Suwon, Korea) were used. The triaxial accelerometer measures body movements in all directions: anterior-posterior, mediolateral, and vertical. It is small and lightweight (35 mm × 35 mm × 13 mm and 13.7 gm). It is sensitive to acceleration from −8 g to 8 g, allowing for monitoring of almost all human physical activities. All the participants wore the accelerometers at a distance of 34 cm from the ground, as shown in Figure 1. All the participants were asked to walk along a six-meter track. For validation of the proposed approach, the gait characteristics were also measured by using the 3D motion analysis system (VICON, Oxford, UK). The motion was captured during the walking process. Five important gait characteristics were measured that include step time, stride time, step length, stride length, and walking speed. For estimating gait status more objectively, the Korean version of the Tinetti gait scale [7] was used. The gait characteristics obtained from the 3D motion system and the Tinetti gait scale were used for validation of the proposed approach.

3.2. Estimation of Gait Characteristics. A variant of the method proposed by Del Din et al. [12] was used to detect the gait cycle. The measured acceleration values along *X*-, *Y*-, and *Z*-axes represent linear accelerations along the medial-lateral (ML), anterior-posterior (AP), and vertical (V) directions, respectively. The corrections are needed to overcome the effect of gravitational component, error due to imprecise position of wearable accelerometer, etc. [27]. The dynamic tilt correction approach proposed in [27] was used to transform the acceleration from ML and AP directions to a global horizontal-vertical coordinate system. The resulting vertical acceleration signal was used hereafter for gait event identification. A low-pass fourth-order Butterworth filter with a cutoff frequency of 15 Hz was used to filter the vertical acceleration signal. The filtered signal was integrated for gait event detection. The objective was to detect the initial contacts (ICs) of the leg, which are also termed as the heel-strike event in a gait cycle. The locations of ICs were detected from the points of minima in the smoothed signal by determining the first-order derivative using the Gaussian continuous wavelet transform. The flowchart of the proposed algorithmic approach based on the accelerometer data is shown in Figure 2.

In this study, five gait characteristics such as step time, stride time, step length, stride length, and walking speed were estimated for the feasibility study of objective assessment of PD using wearable accelerometer data. These five characteristics have received great attention from the researchers in gait-related study and its effectiveness for the assessment of PD. Five major domains of gait study have been proposed by Hollman et al. using the factor analysis: (1) step time and stride time represented by the rhythm domain; (2) temporophasic domain of gait cycle represented by the phase domain; (3) step variability represented by the variability domain; (4) step length, stride length, and gait speed represented by the pace domain; (5) step width represented by the base of the support domain [28]. The aforementioned five characteristics have also been used recently to detect the FoG [20]. Walking speed, stride length, and stride time have been given high importance by Schlachetzki et al. [29] for the discrimination of healthy subjects from the PD subjects.

Table 1: Details of the PD group.

M/F ($n = 48$)	25/23
Age	70.61 ± 9.51
UPDRS part III	20.9 ± 12.31
H&Y stage	2.10 ± 0.74
Disease duration (months)	35.49 ± 27.07
Timed-up and go	20.87 ± 15.78
Tinetti gait scale	9.86 ± 2.56

Table 2: Details of the healthy group.

M/F ($n = 40$)	22/18
Age	69.36 ± 7.42
UPDRS part III	0
Disease duration (months)	0

Figure 1: Location of the accelerometers specified for the proposed study.

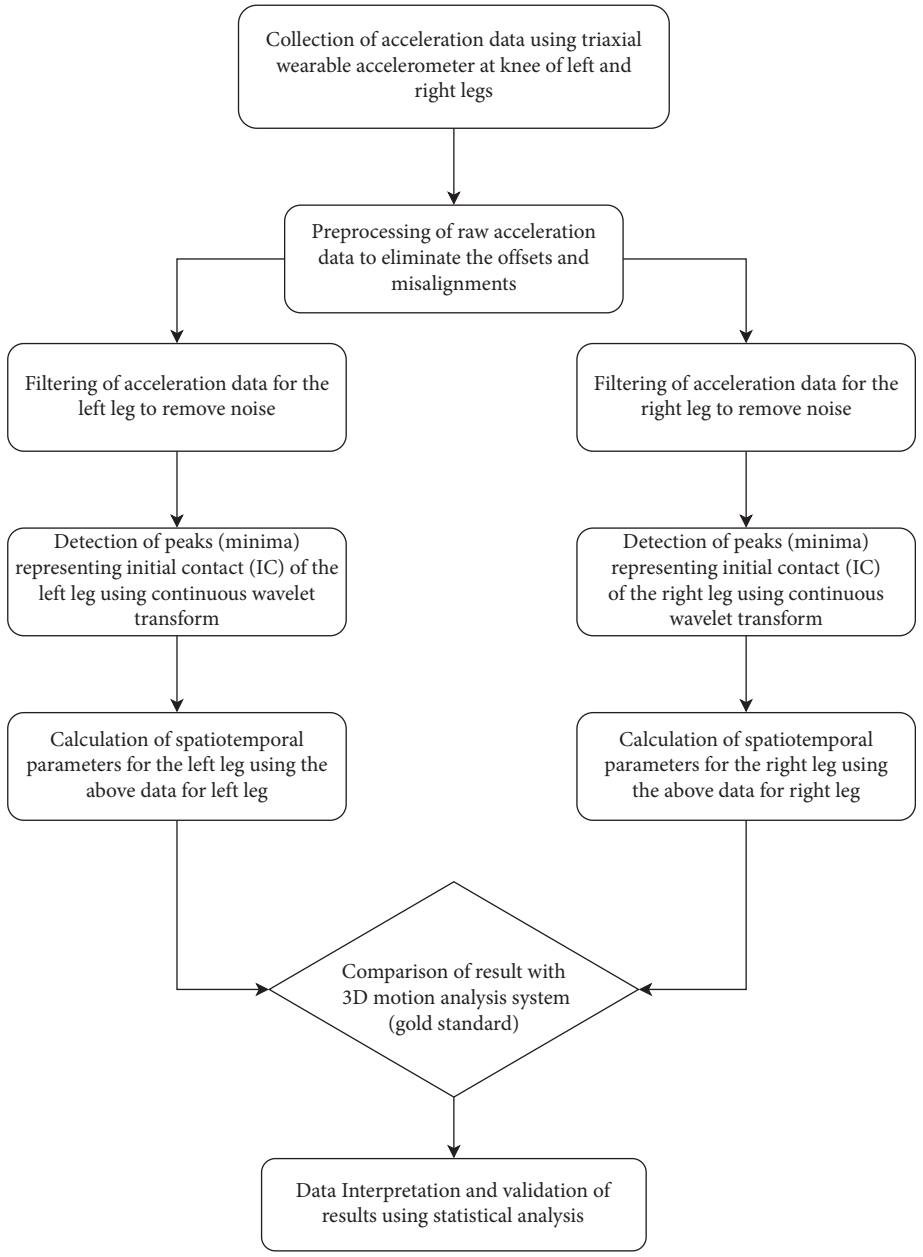

Figure 2: Flowchart of the algorithmic approach for the estimation of gait characteristics.

Bertoli et al. estimated the spatiotemporal parameters such as stride time, step time, swing time, stance time, stride length, and gait velocity for the quantitative assessment of PD, mild cognitive impairment patients, and healthy older adults [30].

The step time can be calculated based on the IC events [9] as follows:

$$\text{step time}\,(i) = \text{IC}\,(i+1) - \text{IC}\,(i). \tag{1}$$

Similarly, the stride time can also be computed based on the IC events [9] as follows:

$$\text{stride time}\,(i) = \text{IC}\,(i+2) - \text{IC}\,(i), \tag{2}$$

where i denotes the index of the IC event in the signal. In the proposed approach, the step length has been estimated using the inverted pendulum model [21, 31], as shown in Figure 3. The step length and stride length can be computed as follows:

$$\begin{aligned} \text{step length} &= K_I * 2\sqrt{\left(2W_h H - H^2\right)}, \\ \text{stride length} &= 2 * \text{step length}, \end{aligned} \tag{3}$$

where W_h represents the distance from the ground to the wearable accelerometer and H represents the change in height of the wearable sensor between two consecutive IC events. This is computed by finding the difference between the maximum and minimum values of the double integrated vertical acceleration signal between two IC events. The generic multiplying factor K_I is used for mapping the center of mass in an inverted pendulum model with that of the

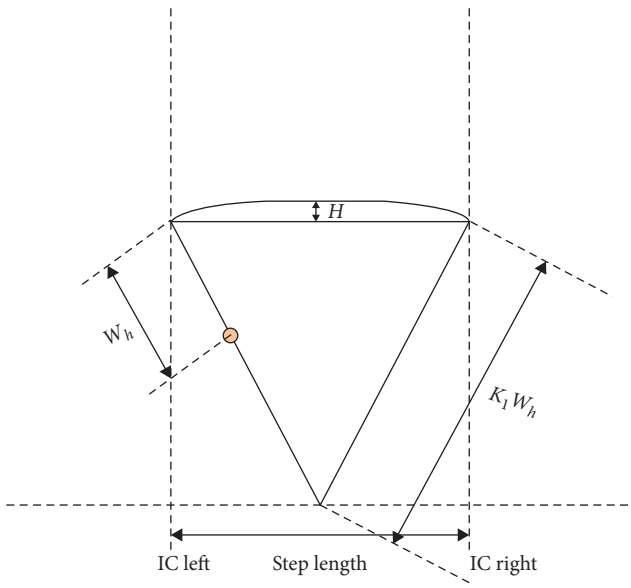

Figure 3: Extended inverted pendulum model [20] for estimation of step length.

wearable sensor. The value of K_I will change based on the value of W_h. Therefore, to avoid the time-consuming task of mapping for each participant that requires determining K_I for each participant, W_h has been fixed at 34 cm, and correspondingly, $K_I = 4$ has been chosen for this study. Walking speed is calculated as follows [21]:

$$\text{walking speed} = \frac{\text{mean step length}}{\text{mean step time}}. \quad (4)$$

These aforementioned five estimated gait characteristics were used as features for the classification of PD groups and healthy older group.

3.3. Machine Learning Classifiers and Its Effectiveness for This Study. In this study, comparative performance analysis has been carried out between four machine learning classifiers that have been employed to perform the classification task between the PD patients and the healthy control adults.

3.3.1. The k-Nearest Neighbour Classifier (k-NN). The k-NN classifier performs the classification process based on the proximity of a data point to the nearest training data points. It generally measures the Euclidean distance to measure the closeness between them. The local data structure has a strong influence on the k-NN algorithm. There is no standardized rule to define the value of k. The classes are selected based on the majority rule from among the selected number of k-nearest neighbors, where k is always greater than zero and an integer. The instability in the result, as well as an increase in the variance, can be seen with the smaller values of k. The reduction in sensitivity, as well as increasing bias, can be seen with the higher values of k. In general, the k values are chosen depending on the dataset. In this study, a value of $k = 5$ is chosen as it provides good accuracy [32, 33].

3.3.2. Support Vector Machine (SVM) Classifier. SVM is one of the classifiers suitable to deal with binary classification problems. The classifier tries to maximize the margin arithmetically between two input datasets by defining a surface in an input space, which is multidimensional in nature [34]. In another way, SVM selects the hyperplane with the highest possible margin between two classes while separating them. It is impossible for a hyperplane to separate the data between two classes, but it tries to separate as much data as possible to provide good accuracy [35]. In this study, the radial basis kernel function is used, which provides good accuracy compared to other available kernel functions.

3.3.3. Naïve Bayes (NB) Classifier. NB classifier is one of the simple probabilistic classifiers based on the Bayes' theorem. This classifier selects mutually independent variables. This kind of classifier can be employed in the complex real-life scenario as it can be trained efficiently using the supervised learning technique. The advantage of this algorithm is that it needs less amount of data for training purposes to perform the classification task. In this study, the classification task has been performed by using the Bayes' rule to calculate the probability of class label PD or a healthy group [36].

3.3.4. Decision Tree Classifier. The decision tree classifier works on the basis of conditional statements and its possible consequences. It is a tree-like model. Nodes and branches are the primary components to build a decision tree model. Three steps are followed for building a well-designed decision tree model. The first step is splitting, followed by stopping, and then finally pruning. The continuation of the splitting process stops when the model reaches the desired stopping criteria. The stopping rule is used to avoid the problem of overfitting and underfitting. If the stopping rule does not work well, the pruning method is used to improve the overall classification accuracy [37].

A planned-designed PD detection framework should be efficient and quick enough to perform the binary classification for the classification of PD patients from the healthy older group. Accuracy, sensitivity, and specificity are widely used to measure the effectiveness of the system. The amount of correctness required for the distinction of PD patients from the healthy older group could be measured using the term accuracy. The potential to identify PD is measured by sensitivity, and it is usually expressed as the ratio of true positives to the total number of PD patients [21]. The potential to identify PD when the system identifies the PD can be measured by the term specificity. The subjects belong to the PD group, correctly identified as PD subject, and are represented as true positives. The subjects belong to a healthy older group, correctly identified as healthy older groups, and are represented as true negatives. The subjects belong to the healthy older group but wrongly identified as PD subjects are represented as false positives. The subjects belong to the PD group but wrongly identified as the healthy older group are represented as false negatives. In this study, the objective is to reduce the false negatives as it affects the effectiveness of the system.

Table 3: Mean value of gait characteristics and average error rate for the left and right legs.

Sl. no.	Parameters	Mean value (3D motion capture)	Mean value (algorithm)	Mean error rate (%)
Left leg				
1	Step time (s)	0.57	0.54	6.94 ± 2.82
2	Stride time (s)	1.17	1.13	4.76 ± 3.55
3	Step length (m)	0.37	0.34	6.35 ± 2.85
4	Stride length (m)	0.74	0.71	6.51 ± 2.92
5	Walking speed (m/s)	0.64	0.61	7.12 ± 2.74
Right leg				
1	Step time (s)	0.54	0.56	7.14 ± 2.52
2	Stride time (s)	1.18	1.14	5.25 ± 3.62
3	Step length (m)	0.37	0.34	6.15 ± 2.81
4	Stride length (m)	0.74	0.70	6.35 ± 2.71
5	Walking speed (m/s)	0.69	0.66	6.72 ± 3.14

4. Results

The mean value of five estimated gait characteristics based on the accelerometer data as well as the mean error rate between the algorithmic approach and the 3D motion capture system are highlighted in Table 3. The correlation plots between the algorithmic approach as well as a 3D motion capture system are shown in Figures 4–8. The mean error rate was calculated based on the formula [21] as follows:

$$\text{average error rate}\,(\%) = \frac{(\text{value estimated from acc}) - (\text{value estimated from 3D capture})}{(\text{value estimated from 3D capture})} * 100. \quad (5)$$

In this paper, Tinetti mobility test (TMT) gait scale is used to assess the spatiotemporal gait characteristics such as step time, stride time, step length, stride length, and walking speed and its importance in terms of clinical practices by comparing the score with the result obtained using other methods, in this case, computerized gait analysis using accelerometer data and 3D motion capture system. The true changes in the gait characteristics can be easily understand based on the accuracy of the clinical observation measures, and it is an important step in clinical practices. So, in this paper, we have used Pearson's correlation coefficient to analyze the relationship between the TMT gait scale score, and spatiotemporal gait characteristics derived objectively used computerized gait analysis using accelerometer data and 3D motion capture system. The correlation plots between TMT gait scale and gait characteristics measured from the 3D motion capture system are shown in Figures 4–8. We have found strong correlations between them, and the results were mentioned as follows: step time (0.96, $p < 0.01$), stride time (0.97, $p < 0.01$), step length (0.98, $p < 0.01$), stride length (0.99, $p < 0.01$), and walking speed (0.99, $p < 0.01$). Similarly, the correlation plots between TMT gait scale and gait characteristics obtained from the wearable accelerometer data are shown in Figures 9–13. We have found moderate to strong correlations between them, and the results were mentioned as follows: step time (0.57, $p < 0.01$), stride time (0.54, $p < 0.01$), step length (0.84, $p < 0.01$), stride length (0.84, $p < 0.01$), and walking speed (0.75, $p < 0.01$).

This study used the split named as stratified train-validation [21] with a ratio of 70 : 30 for training and validation. The total number of subjects including both the groups is 88. Out of 88 subjects, 62 subjects belong to the training group, and the rest 26 belong to the validation group. Out of 26 subjects, which belong to the validation group, 14 subjects belong to the PD group (PDG) and 12 subjects belong to the healthy older group (HOG). Moreover, a 5 split cross-validation was also performed based on the subject's data to check the generalizability of the model. The cross-validation was performed in such a way where the data of 62 random subjects were used to train a classifier and the rest data of 26 subjects were used for checking the testing accuracy. Test set 1, test set 2, test set 3, and test set 4 consist of 26 subjects each. The cross-validation was performed using 4 different classifiers, namely, KNN, SVM, Naive Bayes, and decision tree. The implementation of four different algorithms was done to perform a comparative analysis between the classifiers. After successful cross-validation, it was found that the decision tree plotted the best set of results by prompting a maximum accuracy of 88.46%, sensitivity of 92.86%, and specificity of 90.91%, respectively. Table 4 shows the results for the cross-validation.

The classifiers' performance has been evaluated using three parameters such as accuracy, sensitivity, and specificity. The classification results are shown in Table 5. The decision tree classifier could able to provide the highest accuracy of 88.46% with a sensitivity of 0.9286 and specificity of 0.9091. From 14 subjects belonging to PDG, the proposed model correctly identified 13 as PDG. Similarly, from the 12 subjects belonging to HOG, the proposed model correctly identified 10 as HOG. The confusion matrix is shown in Figure 14.

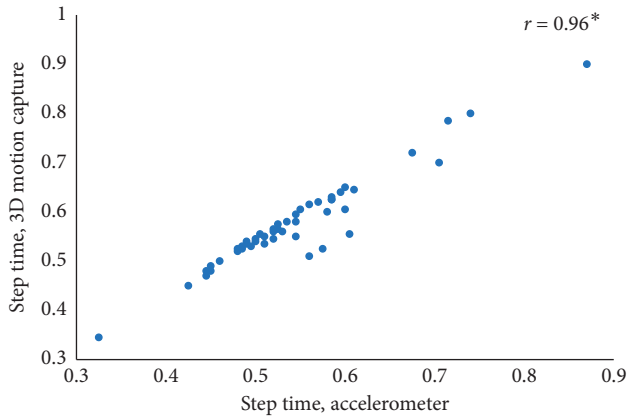

Figure 4: Step time correlation plot between the accelerometer-based approach and 3D motion system ($^{*}p < 0.01$).

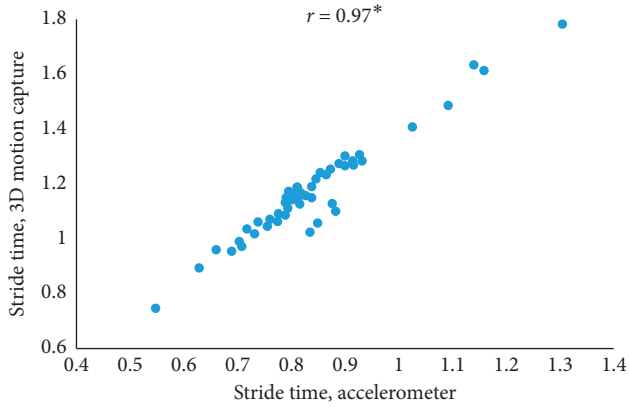

Figure 5: Stride time correlation plot between the accelerometer-based approach and 3D motion system ($^{*}p < 0.01$).

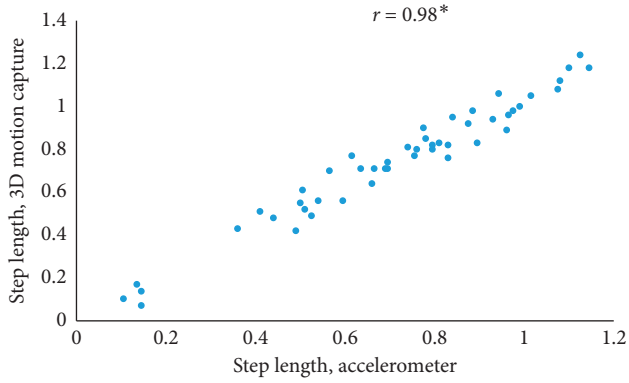

Figure 6: Step length correlation plot between the accelerometer-based approach and 3D motion system ($^{*}p < 0.01$).

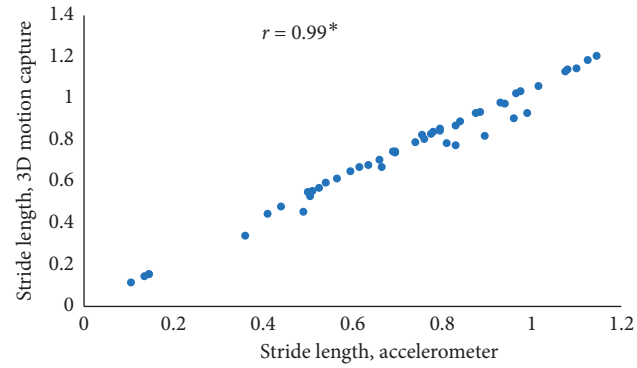

Figure 7: Stride length correlation plot between the accelerometer-based approach and 3D motion system ($^{*}p < 0.01$).

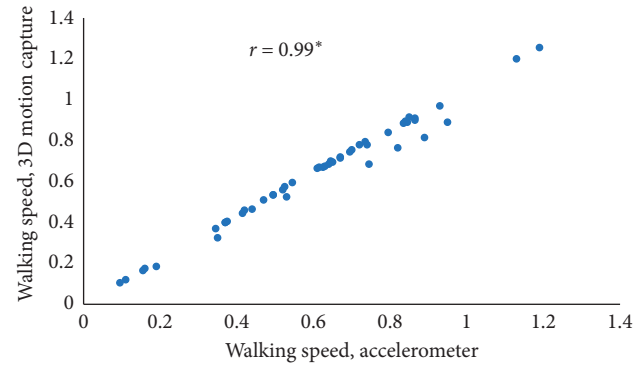

Figure 8: Walking speed correlation plot between the accelerometer-based approach and 3D motion system ($^{*}p < 0.01$).

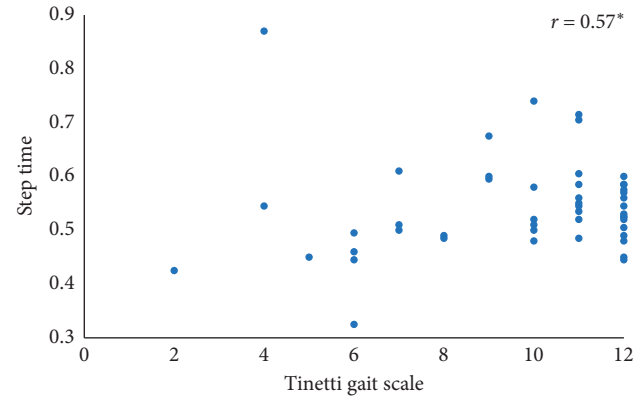

Figure 9: Step time correlation plot between the accelerometer-based approach and Tinetti gait scale ($^{*}p < 0.01$).

5. Discussion

This study proposes an algorithmic approach to estimate the gait characteristics of PD subjects as well as the healthy older groups. The approach is validated using measuring instruments and clinical scale. It is also proposed that the machine learning approach can be used for automatic detection and differentiation of PD patients from the healthy older group.

Although wearable sensors have been widely used in many fields, these have not been given enough importance in PD-related assessment due to distorted gait pattern. Sijobert et al. [38] have proposed a technique that provides a mean error rate of 10.3% for the PD group and 6% for the healthy group. The comparison has been made based on the estimated stride length calculated using wearable sensor data

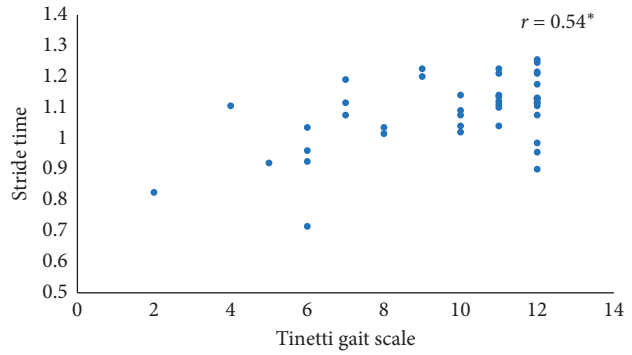

Figure 10: Stride time correlation plot between the accelerometer-based approach and Tinetti gait scale (* $p < 0.01$).

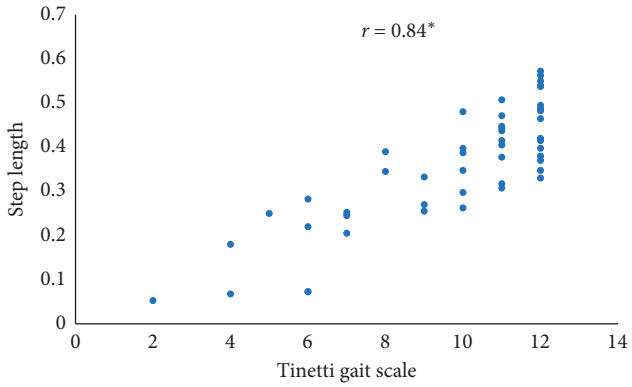

Figure 11: Step length correlation plot between the accelerometer-based approach and Tinetti gait scale (* $p < 0.01$).

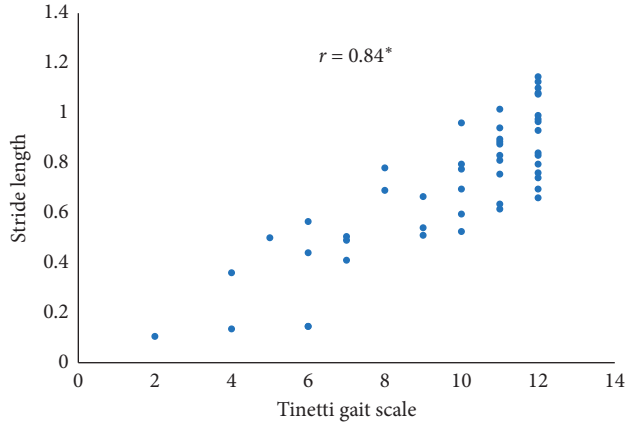

Figure 12: Stride length correlation plot between the accelerometer-based approach and Tinetti gait scale (* $p < 0.01$).

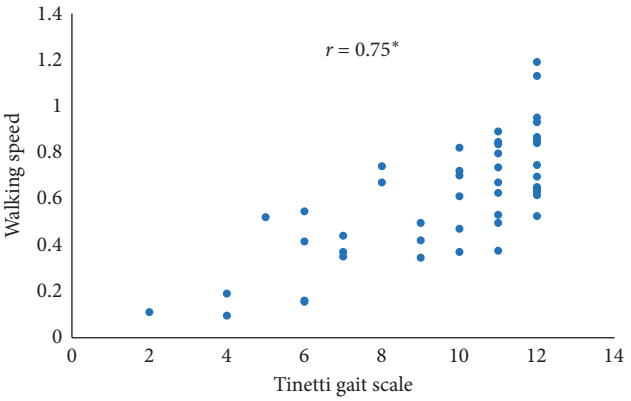

Figure 13: Walking speed correlation plot between the accelerometer-based approach and Tinetti gait scale (* $p < 0.01$).

Table 4: 5 split cross-validation.

Performance (%)	KNN	SVM	NB	Decision tree
Accuracy test set 1	82.11	81.36	84.52	86.28
Sensitivity test set 1	0.8746	0.7801	0.8225	0.9152
Specificity test set 1	0.8452	0.725	0.8654	0.8833
Accuracy test set 2	83.64	84.25	81.20	84.31
Sensitivity test set 2	0.8055	0.8139	0.8558	0.8631
Specificity test set 2	0.8519	0.8687	0.8411	0.8551
Accuracy test set 3	86.32	84.93	85.31	82.28
Sensitivity test set 3	0.9025	0.8755	0.9032	0.8111
Specificity test set 3	0.8947	0.9054	0.8748	0.8364
Accuracy test set 4	85.57	87.23	84.41	88.46
Sensitivity test set 4	0.9125	0.9189	0.8956	0.9286
Specificity test set 4	0.8836	0.8997	0.8735	0.9091
Accuracy test set 5	87.26	84.39	79.32	87.32
Sensitivity test set 5	0.8568	0.8793	0.8178	0.9025
Specificity test set 5	0.9034	0.8998	0.8227	0.9131

Table 5: Classification results.

Performance	k-NN	SVM	NB	Decision tree
Accuracy (%)	85.57	87.23	84.41	88.46
Sensitivity (%)	0.9125	0.9189	0.8956	0.9286
Specificity (%)	0.8836	0.8997	0.8735	0.9091

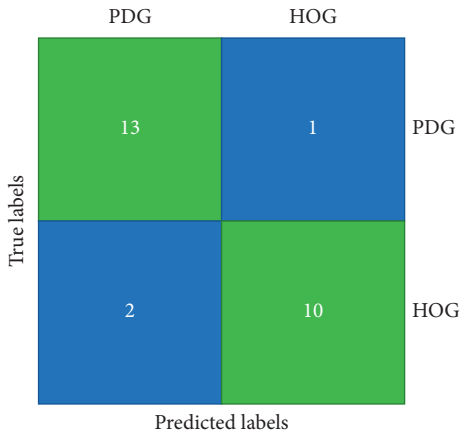

Figure 14: Confusion matrix.

and further validated using the GAITRite-based walkway system. The estimated mean error rate for the five gait characteristics is found to be less than 8% with our proposed approach, which used the wearable accelerometer to collect the data. The results of our proposed approach provide the feasibility of our approach when compared with the previous study. The proposed study provides some new ideas that are as follows:

(i) The results obtained in this study include various phenotypes and severity of PD due to the large sample size.

(ii) This study uses the Tinetti gait scale [7] and the 3D motion capture system [39] for validation of gait status. The previous report [38] has demonstrated the validation using GAITRite that can assess spatiotemporal data by using pressure parameters.

(iii) The gait characteristics estimated using our proposed approach have been compared with the clinical scale, and the result shows a good level of agreement, which makes the method feasible to be implemented in the real-life environment.

(iii) It is observed from the study that only accelerometer data can provide enough information for performing the gait analysis, which leads to redundancy of gyroscopic data, which indirectly saves battery power, time, and cost.

The strength and possibility of the wearable sensor-based PD assessment are aimed at long-term monitoring of gait. Gait disturbance usually gets aggravated in specific cases such as starting time, meeting narrow space, or obstacle [40]. The hospital has limited space, and therefore, it is difficult to replicate gait disturbance observed in a real-world scenario. The battery mounted in our device lasts up to 72 hours. The limitation of this study is that the patients in the relatively early stage of PD were not enrolled, and therefore, this study is not intended at assessing various balance status in PD such as a freeze of gait (FOG) or hypokinetic and short-step gait. The classifiers used in this study have shown good accuracy. All the classifiers showed the acceptable results in terms of performance parameters such as accuracy, sensitivity, and specificity.

6. Conclusion

The proposed study highlights the feasibility of wearable accelerometers for gait analysis of PD patients. The algorithmic approach used in this study is able to estimate the gait characteristics with an acceptable mean error rate. The validation study was performed to compare the estimated values from the algorithmic approach with those obtained from the 3D motion capture system and TMT. The proposed approach is a low-cost approach for the detection of PD as well as able to distinguish PD subjects from the healthy older group. It is also observed that the proposed classification model could able to achieve an accuracy of 88.46% with a sensitivity of 0.9286 and a specificity of 0.9091. The objective of reducing the false negatives as much as possible could be achieved. The proposed approach showed enough potential to get recommended for the clinicians to use in the laboratory as well as in the home environment.

In the future, we will collect gait data from a large number of PD patients to summarize the gait characteristics in a better way so that it could be promoted for clinical applications. We would also like to combine brain EEG signals with the gait data to understand more about the relation and detect the symptoms like freezing of gait before it happens. We would like to combine the MRI image with the gait data for more accurate diagnosis and early detection of PD.

Data Availability

The data used to support the experiments and the finding of the study have been duly included in Section 3 of the paper. Section 3.1 clearly describes about the data.

Conflicts of Interest

The authors declare that they have no conflicts of interest.

Acknowledgments

This research was supported by the National Research Foundation (NRF) of Korea grant funded by the Korea government (MSIT) (Grant number 2019R1C1C1011197) and also funded by Ministry of Trade, Industry and Energy (MOTIE), Korea, through the Education program for Creative and Industrial Convergence (Grant number N0000717).

References

[1] C. C. Walton, J. M. Shine, J. M. Hall et al., "The major impact of freezing of gait on quality of life in Parkinson's disease," *Journal of Neurology*, vol. 262, no. 1, pp. 108–115, 2014.

[2] J. M. Hausdorff, "Gait dynamics in Parkinson's disease: common and distinct behavior among stride length, gait variability, and fractal-like scaling," *Chaos: An Interdisciplinary Journal of Nonlinear Science*, vol. 19, no. 2, Article ID 026113, 2009.

[3] N. Giladi and Y. Balash, "The clinical approach to gait disturbances in Parkinson's disease; maintaining independent mobility," *Journal of Neural Transmission*, vol. 70, pp. 327–332, 2006.

[4] M. Morris, R. Iansek, J. Mcginley, T. Matyas, and F. Huxham, "Three-dimensional gait biomechanics in Parkinson's disease: evidence for a centrally mediated amplitude regulation disorder," *Movement Disorders*, vol. 20, no. 1, pp. 40–50, 2004.

[5] T. R. Beijer, S. R. Lord, and M. A. D. Brodie, "Comparison of handheld video camera and GAITRite measurement of gait impairment in people with early stage Parkinson's disease: a pilot study," *Journal of Parkinson's Disease*, vol. 3, no. 2, pp. 199–203, 2013.

[6] T. G. Hampton and I. Amende, "Treadmill gait analysis characterizes gait alterations in Parkinson's disease and amyotrophic lateral sclerosis mouse models," *Journal of Motor Behavior*, vol. 42, no. 1, pp. 1–4, 2009.

[7] M. E. Tinetti, T. Franklin Williams, and R. Mayewski, "Fall risk index for elderly patients based on number of chronic disabilities," *The American Journal of Medicine*, vol. 80, no. 3, pp. 429–434, 1986.

[8] J. Park, S.-B. Koh, H. J. Kim et al., "Validity and reliability study of the Korean Tinetti mobility test for Parkinson's disease," *Journal of Movement Disorders*, vol. 11, no. 1, pp. 24–29, 2018.

[9] W. Maetzler, J. Klucken, and M. Horne, "A clinical view on the development of technology-based tools in managing Parkinson's disease," *Movement Disorders*, vol. 31, no. 9, pp. 1263–1271, 2016.

[10] J. Taborri, E. Palermo, S. Rossi, and P. Cappa, "Gait partitioning methods: a systematic review," *Sensors*, vol. 16, no. 1, p. 66, 2016.

[11] W. Zhao, M. A. Reinthal, D. D. Espy, and X. Luo, "Rule-based human motion tracking for rehabilitation exercises: realtime assessment, feedback, and guidance," *IEEE Access*, vol. 5, pp. 21382–21394, 2017.

[12] W. Tao, T. Liu, R. Zheng, and H. Feng, "Gait analysis using wearable sensors," *Sensors*, vol. 12, no. 2, pp. 2255–2283, 2012.

[13] Y. Beck, T. Herman, M. Brozgol, N. Giladi, A. Mirelman, and J. M. Hausdorff, "SPARC: a new approach to quantifying gait smoothness in patients with Parkinson's disease," *Journal of Neuroengineering and Rehabilitation*, vol. 15, no. 1, p. 49, 2018.

[14] J. M. Hausdorff, N. Ganz, E. Gazit, A. Hadad, A. S. Buchman, and A. Mirelman, "Automatic quantification of tandem walking using a wearable device: validity of the instrumented tandem walk," *Innovation in Aging*, vol. 3, no. Supplement_1, p. S335, 2019.

[15] E. Gazit, A. S. Buchman, R. Dawe et al., "What happens before the first step? A new approach to quantifying gait initiation using a wearable sensor," *Gait & Posture*, vol. 76, pp. 128–135, 2019.

[16] A. R. Anwary, H. Yu, and M. Vassallo, "Optimal foot location for placing wearable IMU sensors and automatic feature extraction for gait analysis," *IEEE Sensors Journal*, vol. 18, no. 6, pp. 2555–2567, 2018.

[17] S. Qiu, Z. Wang, H. Zhao, L. Liu, and Y. Jiang, "Using body-worn sensors for preliminary rehabilitation assessment in stroke victims with gait impairment," *IEEE Access*, vol. 6, pp. 31249–31258, 2018.

[18] S. Byun, J. W. Han, T. H. Kim, and K. W. Kim, "Test-Retest reliability and concurrent validity of a single tri-axial accelerometer-based gait analysis in older adults with normal cognition," *PLoS One*, vol. 11, no. 7, Article ID e0158956, 2016.

[19] M. H. Pham, M. Elshehabi, L. Haertner et al., "Validation of a step detection algorithm during straight walking and turning in patients with Parkinson's disease and older adults using an inertial measurement unit at the lower back," *Frontiers in Neurology*, vol. 8, 2017.

[20] S. D. Din, A. Godfrey, and L. Rochester, "Validation of an accelerometer to quantify a comprehensive battery of gait characteristics in healthy older adults and Parkinson's disease: toward clinical and at home use," *IEEE Journal of Biomedical and Health Informatics*, vol. 20, no. 3, pp. 838–847, 2016.

[21] S. Aich, P. Pradhan, J. Park, N. Sethi, V. Vathsa, and H.-C. Kim, "A validation study of freezing of gait (FoG) detection and machine-learning-based FoG prediction using estimated gait characteristics with a wearable accelerometer," *Sensors*, vol. 18, no. 10, p. 3287, 2018.

[22] V. Mikos, C.-H. Heng, A. Tay et al., "A wearable, patient-adaptive freezing of gait detection system for biofeedback cueing in Parkinson's disease," *IEEE Transactions on Biomedical Circuits and Systems*, vol. 13, no. 3, pp. 503–515, 2019.

[23] H. Jeon, W. Lee, H. Park et al., "Automatic classification of tremor severity in Parkinson's disease using a wearable device," *Sensors*, vol. 17, no. 9, p. 2067, 2017.

[24] A. Samà, C. Pérez-López, D. Rodríguez-Martín et al., "A double closed loop to enhance the quality of life of Parkinson's Disease patients: REMPARK system," *Studies in Health Technology and Informatics*, vol. 207, pp. 115–124, 2015.

[25] S. Fahn, "Members of the UPDRS development committee. Unified Parkinson's disease rating scale," *Recent Developments in Parkinson's Disease*, vol. 2, pp. 293–304, 1987.

[26] R. Bhidayasiri and D. Tarsy, "Parkinson's disease: Hoehn and Yahr scale," in *Movement Disorders: A Video Atlas*, pp. 4-5, Humana Press, Totowa, NJ, USA, 2012.

[27] A. Millecamps, K. A. Lowry, J. S. Brach, S. Perera, M. S. Redfern, and E. Sejdić, "Understanding the effects of pre-processing on extracted signal features from gait accelerometry signals," *Computers in Biology and Medicine*, vol. 62, pp. 164–174, 2015.

[28] J. H. Hollman, E. M. Mcdade, and R. C. Petersen, "Normative spatiotemporal gait parameters in older adults," *Gait & Posture*, vol. 34, no. 1, pp. 111–118, 2011.

[29] J. C. M. Schlachetzki, J. Barth, F. Marxreiter et al., "Wearable sensors objectively measure gait parameters in Parkinson's disease," *PLoS One*, vol. 12, no. 10, Article ID e0183989, 2017.

[30] M. Bertoli, A. Cereatti, D. Trojaniello et al., "Estimation of spatio-temporal parameters of gait from magneto-inertial measurement units: multicenter validation among Parkinson, mildly cognitively impaired and healthy older adults," *Biomedical Engineering Online*, vol. 17, no. 1, p. 58, 2018.

[31] W. Zijlstra and A. L. Hof, "Displacement of the pelvis during human walking: experimental data and model predictions," *Gait & Posture*, vol. 6, no. 3, pp. 249–262, 1997.

[32] L.-Y. Hu, M.-W. Huang, S.-W. Ke, and C.-F. Tsai, "The distance function effect on k-nearest neighbour classification for medical datasets," *Springer Plus*, vol. 5, no. 1, 2016.

[33] A. Özdemir and B. Barshan, "Detecting falls with wearable sensors using machine learning techniques," *Sensors*, vol. 14, no. 6, pp. 10691–10708, 2014.

[34] X.-Y. Wang, Q.-Y. Wang, H.-Y. Yang, and J. Bu, "Color image segmentation using automatic pixel classification with support vector machine," *Neurocomputing*, vol. 74, no. 18, pp. 3898–3911, 2011.

[35] S. Akbarzadeh, A. Paap, S. Ahderom, B. Apopei, and K. Alameh, "Plant discrimination by Support Vector Machine classifier based on spectral reflectance," *Computers and Electronics in Agriculture*, vol. 148, pp. 250–258, 2018.

[36] B. M. Gayathri and C. P. Sumathi, "An automated technique using Gaussian naïve Bayes classifier to classify breast cancer," *International Journal of Computer Applications*, vol. 148, no. 6, pp. 16–21, 2016.

[37] Y. Y. Song and L. U. Ying, "Decision tree methods: applications for classification and prediction," *Shanghai Archives of Psychiatry*, vol. 27, pp. 130–135, 2015.

[38] B. Sijobert, M. Benoussaad, J. Denys, R. Pissard-Gibollet, C. Geny, and C. A. Coste, "Implementation and validation of a stride length estimation algorithm, using a single basic inertial sensor on healthy subjects and patients suffering from Parkinson's disease," *Health*, vol. 7, no. 6, pp. 704–714, 2015.

[39] D. Meldrum, C. Shouldice, R. Conroy, K. Jones, and M. Forward, "Test-retest reliability of three dimensional gait analysis: including a novel approach to visualising agreement of gait cycle waveforms with Bland and Altman plots," *Gait & Posture*, vol. 39, no. 1, pp. 265–271, 2014.

[40] Y. Okuma, "Freezing of gait in Parkinson's disease," *Journal of Neurology*, vol. 253, pp. 27–32, 2006.

Hindawi
Journal of Healthcare Engineering
Volume 2020, Article ID 1078251, 12 pages
https://doi.org/10.1155/2020/1078251

Research Article

An Optimization Study of Estimating Blood Pressure Models Based on Pulse Arrival Time for Continuous Monitoring

Jiang Shao,[1] **Ping Shi**,[1] **Sijung Hu**,[2] **Yang Liu**,[3] **and Hongliu Yu**[1]

[1]*Institute of Rehabilitation Engineering and Technology, University of Shanghai for Science and Technology, Shanghai 200093, China*
[2]*Wolfson School of Mechanical, Electrical and Manufacturing Engineering, Loughborough University, Ashby Road, Loughborough, Leicestershire LE11 3TU, UK*
[3]*Department of Cardiovascular Surgery, Changhai Hospital, Second Military Medical University, Shanghai 200433, China*

Correspondence should be addressed to Ping Shi; garendon@163.com

Received 6 July 2019; Revised 18 September 2019; Accepted 19 October 2019; Published 10 February 2020

Guest Editor: Ludovico Minati

Continuous blood pressure (BP) monitoring has a significant meaning for the prevention and early diagnosis of cardiovascular disease. However, under different calibration methods, it is difficult to determine which model is better for estimating BP. This study was firstly designed to reveal a better BP estimation model by evaluating and optimizing different BP models under a justified and uniform criterion, i.e., the advanced point-to-point pairing method (PTP). Here, the physical trial in this study caused the BP increase largely. In addition, the PPG and ECG signals were collected while the cuff bps were measured for each subject. The validation was conducted on four popular vascular elasticity (VE) models (MK-EE, L-MK, MK-BH, and dMK-BH) and one representative elastic tube (ET) model, i.e., M-M. The results revealed that the VE models except for L-MK outperformed the ET model. The linear L-MK as a VE model had the largest estimated error, and the nonlinear M-M model had a weaker correlation between the estimated BP and the cuff BP than MK-EE, MK-BH, and dMK-BH models. Further, in contrast to L-MK, the dMK-BH model had the strongest correlation and the smallest difference between the estimated BP and the cuff BP including systolic blood pressure (SBP) and diastolic blood pressure (DBP) than others. In this study, the simple MK-EE model showed the best similarity to the dMK-BH model. There were no significant changes between MK-EE and dMK-BH models. These findings indicated that the nonlinear MK-EE model with low estimated error and simple mathematical expression was a good choice for application in wearable sensor devices for cuff-less BP monitoring compared to others.

1. Introduction

Increased aortic stiffness in hypertensive individuals is a fundamental manifestation of longstanding hypertension-related damage that stiffens the large arteries [1]. Uncontrolled hypertension or high blood pressure (BP) is a major risk factor that links to the potential development of serious diseases such as stroke, hypertensive heart disease, and coronary artery disease [2]. BP is influenced by many factors such as food, exercise, mental situations, and stress, among others; thus, it varies considerably from time to time [3]. Instantaneous information about BP status can be obtained from conventional standard cuff-based BP measurements, such as oscillometry [4] and auscultation. However, the above methods are not applicable to ambulatory BP monitoring (ABPM) or home BP monitoring (HBPM) due to the population-averaged nature of the BP estimation algorithm [5] and the limited frequency of measurement [6]. For cuff-based approaches, recurrent inflating and deflating of the cuff stress the patient, which causes periodic interruptions to blood flow, affecting the physiological state of the patient and disturbing the quality of sleep [7]. Moreover, cuff measurements are occlusive, cumbersome, provide only intermittent BP readings, and do not readily extend to low-resource settings [1, 3]. Hence, cuff-less continuous BP monitoring has received much attention due to its comfort and convenience compared to cuff-based approaches. Moreover, the cuff-less solution has a

promising application prospect for continuous noninvasive BP monitoring by virtue of overcoming disturbance issues existing in the traditional cuff-based method [8, 9]. Photoplethysmography (PPG), a noninvasive optical measurement technique by means of photoelectric measurement, obtains physiological signals and characteristics of the human body by detecting changes in blood volume in microvessels. PPG is also a feasible technology for cuff-less continuous BP monitoring, especially in surgery, and can provide valuable information on physiological heart monitoring and cardiovascular system assessment of vascular parameters [10, 11].

Pulse arrival time (PAT) is defined as a time interval between *R*-peak and the point with maximum gradient on the rising edge of the PPG [8] which is a noninvasive optic-electrical signal. The PAT in PAT-based BP measurement can be simply measured from electrocardiography (ECG) and from PPG by wearable devices [12, 13] or a contactless video camera [14]. More importantly, PAT is dependent on both ventricular contraction and vascular function [15]. Thus, it has been commonly used as an indicator to cufflessly and continuously estimate BP under various BP changing conditions.

In the past few years, several studies reported that PAT has shown a high correlation with BP, especially systolic blood pressure (SBP) [8, 11, 16]. Some studies also investigated the potential of PAT-based measurement as a surrogate for cuff BP under different protocols [17, 18]. Advances in dynamic monitoring technologies have reinforced these impressions, especially for wearable technologies [4, 9, 19, 20]. For example, Bilo et al. designed a wearable device (Somnotouch NIBP) to evaluate its accuracy for noninvasive continuous BP monitoring using PAT according to the European Society of Hypertension International Protocol [19]. Pandian et al. developed a smart vest, which used an array of sensors connected to a central processing unit with firmware for continuously monitoring physiological signals including ECG, PPG, and BP [20]. Similarly, Zheng et al. proposed an armband wearable system, which was evaluated against a standard cuff-based device on both healthy and hypertensive subjects over a 24 h period for potential use in hypertensive management [9]. Tang et al. also developed a chair-based unobtrusive monitoring system that estimates BP using PAT calculated from ECG and PPG signals for facilitating long-term HBPM [4]. Furthermore, the methods of neural network or machine learning were paid more attention during investigating these PAT-based approaches for BP modeling [20]. Although the BP monitoring solutions described above were helpful, their accuracy of estimated BP methods, such as linear estimation [21], nonlinear estimation [4, 9, 22, 23], and regression approaches [24, 25], is still needed to improve to meet the association for the Advancement of Medical Instrumentation (AAMI) standard [26].

Most importantly, the PAT-based BP estimation method needed an individualized calibration procedure to obtain unknown coefficients or parameters in the BP estimation model for each subject before BP monitoring. The model's parameters determined after initial calibration will not change in the process of BP estimation. It was well known that different calibration methods made the model showing different performance [27]. In order to show which model had better performance, it was necessary to employ a comparison study under the same calibration mode. The least-square method (L-S) and point-to-point pairing method (PTP) were usually employed to determine the calibration parameters for BP estimation. For the L-S method, sample numbers were directly related to the accuracy of the BP estimation model. It was difficult to explain how large sample numbers were needed to meet long-term ABPM and HBPM [28]. For example, Nabeel et al. recruited 32 subjects for the calibration of the BP estimation model [22] and Esmaili et al. collected 35 subjects for the calibration of their model [29]. They largely limited BP estimation's practical application. Comparing with the L-S method, PTP required only a small initial sample number for the calibration of the estimation model. At present, there were many reports that only one sample (point) was required to calibrate the specific model [4, 9], and the model's parameters determined after initial calibration will not change in the process of BP estimation. Therefore, this paper used PTP as the BP estimation model's calibration method and further optimized this method.

There was no doubt that it was essential to study and improve the accuracy of cuff-less BP estimation models and the simplicity of calibration methods for providing a more practical solution to achieve long-term ABPM and HBPM. To date, under a justified criterion, no investigations have conducted comparative and optimal studies on the PAT-based BP estimation to reveal a better BP estimation method with both simplicity and accuracy. In the present study, five representative BP-PAT models, under a uniform criterion, were analyzed and optimized to work out which model was accurate and fitted well in continuous cuff-less BP monitoring based on a cardiovascular mechanism. This study also offered insights into future research in ambulatory cuff-less BP estimation.

2. Mathematical Models

Electromechanical coupling in the heart causes blood to eject into the whole arterial tree. This physiological process affects the velocity of blood flow and generates systemic pressure waves from the central to the peripheral artery. The velocity of this pressure pulse is determined by the elastic and geometric properties of the arterial wall and the blood density. The central arteries push blood to narrow distal arteries under the pressure of circulating blood on the walls of blood vessels, causing the phenomenon that the heart expands during systole and contracts during diastole. Here, the circulatory pressure is BP. Arterial BP, as a hemodynamic parameter, fluctuates on a beat-to-beat basis due to the dynamic interplay from vasomotion, neural regulation, and arterial mechanisms [30]. Physiologically, it is affected by four factors: arterial compliance, cardiac output, peripheral resistance, and blood volume [31].

Given the fluid is contained in an elastic conduits system, energy is transmitted predominantly in the arterial wall

rather than through the in-compressible blood. The material characteristics, thickness, and lumen diameter of the arterial wall thus become the major determinants of the pressure wave velocity (PWV). Considering that the Moens–Korteweg (M-K) equation [8] models a relationship between the wave speed or pulse wave velocity (PWV) and the incremental elastic modulus (a coefficient of elasticity) of the arterial wall or its distensibility [32], VE models are built on this basis. Combining it with an exponential arterial elasticity model [21, 33], a new BP-PAT model, called the MK-EE model, will be obtained. It gives a logarithmic relationship between BP and the PAT. For the MK-EE model, assuming there is a negligible change in the arterial thickness and diameter with pressure variations, BP and the PAT can be linearly related by differentiating the M-K equation, called the L-MK model [21]. To overcome the bad linear correlation of DBP in the L-MK model, the Bramwell–Hill (B-H) equation [9] is introduced in estimating BP to make it have a high correlation, which is called the MK-BH model [4]. Recently, Poon et al. established a mathematical relationship between MBP and a factor that the change in elasticity is caused by pressure wave variations. It could be regarded as the development model of MK-BH, called the dMK-BH model [9].

In recent years, models used for estimating BP based on PAT and capturing BP variations indirectly mainly fell into two categories: vascular elasticity (VE) models and elastic tube (ET) model. ET models were built on the theory of elastic tubes. It was noted that the blood flow in the arteries could be modeled as the propagation of pressure waves inside elastic tubes. A novel BP estimation nonlinear model was derived from the conservation of mass and momentum principle equation, called the M-M model [29]. Understanding the internal relationship between VE models and ET models was necessary. The principles of their modeling were shown in Figure 1.

The mathematical relationships between BP and the PAT reported in the literature were summarized in Table 1.

3. Methods

3.1. Hardware and Parameter Identification. In the experiments, the PowerLab/16sp system (Castle Hill, AD Instruments, Australia, 2002) was used to synchronously record and amplify the ECG and PPG signals. The ECG signal was filtered by a 1 Hz high-pass filter and a 40 Hz low-pass filter. Meanwhile, the PPG signal was filtered by a 0.5 Hz high-pass filter and a 20 Hz low-pass filter, and the sampling frequency was 1 kHz [24]. To obtain the PAT parameter, the ECG signal was employed as the proximal timing reference, and the PPG signal was used as the distal timing reference. The PAT was calculated as the time elapsed from the *R*-peak of the ECG signal to the maximum of the first derivative of the PPG wave within the same cardiac cycle in Figure 2.

3.2. Data Acquisition Procedure. Twelve subjects without a history of cardiovascular or neurological disorders participated in this study (see Table 2). All participants gave written informed consent. The study was approved by the health center authorities at the University of Shanghai for Science and Technology.

Each subject was required to climb 12 floors at a constant rate lasting for five minutes, which guaranteed a greater change in BP to obtain more accurate model estimation [15]. When the physical exercise was finished, each subject was asked to sit upright and measure the cuff BP, the ECG signal, and the PPG signal. Each subject was asked to sit on a chair 25 cm away from the table, with the cuff wrapped around his/her right arm at the same level between its center and the subject's heart. The PPG sensor was placed on their left hand to avoid the effect of cuff inflation on the PPG signals [4] (see Figure 3).

During the data collection, carrying mobile phones and wearing devices were not allowed. Moreover, subjects were also required to remain stable and breathe naturally to avoid motion causing interference from the collected signals. The data collection took approximately 15 minutes for each subject. The measured BPs generally decreased. Hence, the continuous ECG and PPG signals were collected to calculate a series of continuous PATs ($\overline{\text{PATs}}$).

3.3. Data Analysis

3.3.1. The Advanced PTP Method: A Justified and Uniform Criterion. An automatic digital BP monitor device (MB-300C, Jasun, China) was used to measure cuff BP values. Based on its manufacturer's introduction manual, the accuracy was approximately 3 mm·Hg, which was in compliance with the conventional health standards [26]. For instance, the mean absolute error (MAE) of less than 5 mm·Hg was considered to be the acceptable maximum error according to the AAMI guidelines [26]. In addition, prior to the data collection process, we randomly measured the BP for six subjects using both an MB-300C Jasun device and a conventional mercury sphygmomanometer operated by a professional nurse with the rigorous experimental process to carry out contrast verification. During BP measurement using both monitors, the measured BPs for each subject at the rest condition were approximately the same as expected. Specifically, the mean absolute errors (MAEs) of SBP and DBP measurements using these two devices were 2.7 and 3.2 mm·Hg for six subjects, respectively.

Considering that it took 30 seconds to measure one cuff BP with MB-300C, an average value of PATs in these 30 seconds [22] from corresponding PPG and ECG signals was calculated to estimate BP based on its estimation model. The mapping relationship between the dependent variable and the independent variable was established through the available initial values. This technique was called the PTP method, i.e., cuff BP vs. $\overline{\text{PATs}}$. Recently, the PTP method [4, 9, 30] only used one point (sample) to calibrate the parameters of the corresponding BP estimation model. In fact, such a single point (sample) played a vital role in the BP estimation models. Consider the truth that the subject's BP was not a constant even in a quiet or peace state; therefore, it was necessary to average and balance this quiet and peace process. In this study, a new calibration method was proposed, which was shown in Figure 4.

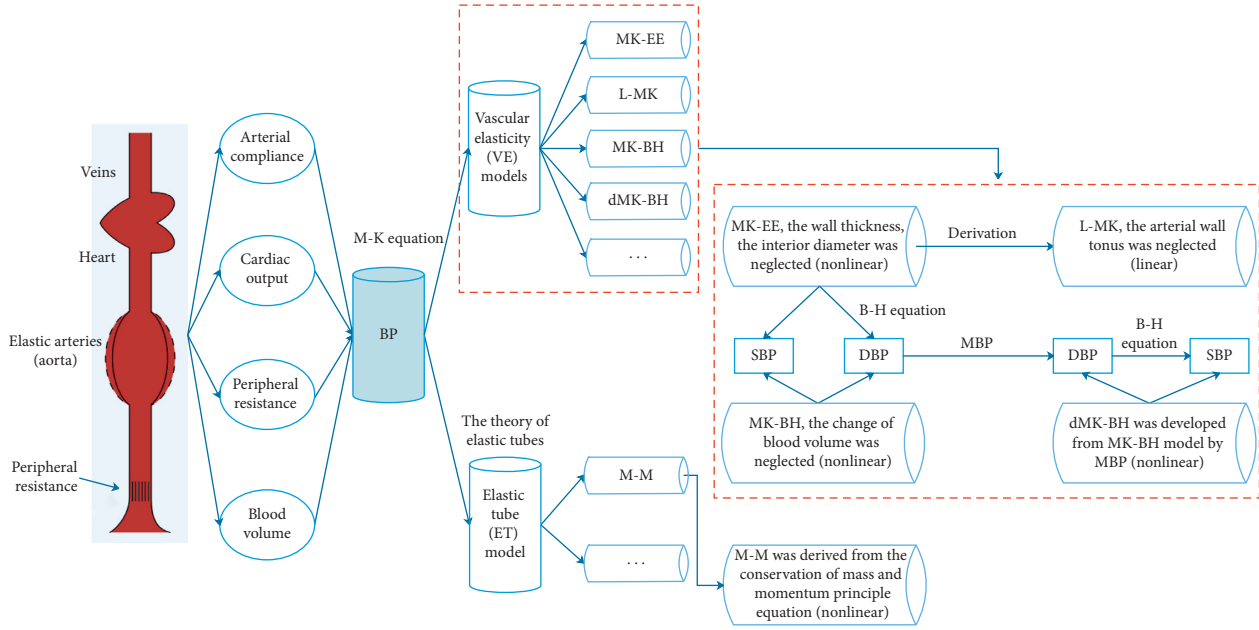

Figure 1: The relationships between the BP estimation models.

Table 1: Summary of mathematical models to calculate BP from PAT.

Models	SBP	DBP	Category and mechanism (linear or nonlinear)	
MK-EE [22, 23]	$a_1 * \ln \mathrm{PAT} + b_1$	$a_1' * \ln \mathrm{PAT} + b_1'$	Nonlinear	Vascular elasticity (VE) models
L-MK [21]	$a_2 + b_2 * \mathrm{PAT}$	$a_2' + b_2' * \mathrm{PAT}$	Linear	
MK-BH [4]	$\mathrm{SBP}_0 - (2/(\gamma * \mathrm{PAT}_0)) * (\mathrm{PAT} - \mathrm{PAT}_0)$	$\mathrm{SBP} - \mathrm{PP}_0 * (\mathrm{PAT}_0/\mathrm{PAT})^2$	Nonlinear	
dMK-BH [9]	$\mathrm{DBP} + \mathrm{PP}_0 * (\mathrm{PAT}_0/\mathrm{PAT})^2$	$\mathrm{MBP}_0 + (2/\gamma)\ln(\mathrm{PAT}_0/\mathrm{PAT}) - (\mathrm{PP}_0/3) * (\mathrm{PAT}_0/\mathrm{PAT})^2$	Nonlinear	
M-M [29]	$a_3 + \sqrt{b_3 + c_3 * (1/\mathrm{PAT}^2)}$	$a_3' + \sqrt{b_3' + c_3' * (1/\mathrm{PAT}^2)}$	Nonlinear	Elastic tube (ET) model

Note. γ denoted a vascular information parameter which might be altered with age and the development of cardiovascular diseases. For the healthy subjects, it was set as 0.031 mm·Hg^{-1} [9]. $\mathrm{PP}_0 = \mathrm{SBP}_0 - \mathrm{DBP}_0$, $\mathrm{MBP}_0 = (1/3)\mathrm{SBP}_0 + (2/3)\mathrm{DBP}_0$. SBP_0, DBP_0, PP_0 could be determined at the beginning of monitoring by calibration using an additional cuff-type BP monitor device (see Subsection 3.2). a_i, b_i, a_i', b_i' (i = 1, 2, 3); c_i, c_i' were the corresponding function coefficients. i was the subscript, and for their calibration method, see Subsection 3.2.

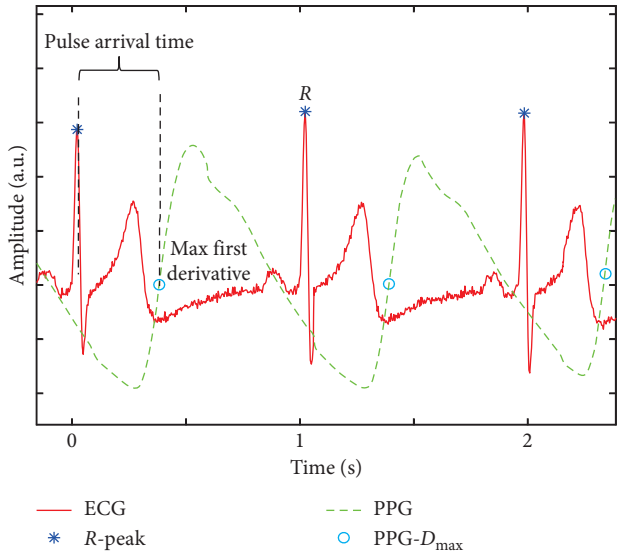

Figure 2: Example of PAT delineation.

Once the parameters of the BP estimation model were determined, they would not be changed in the estimating BP process. In the advanced PTP method, four pairs of cuff BP vs. $\overline{\mathrm{PATs}}$ were collected to obtain four sets of parameters of

Table 2: Characteristics of the subjects.

Selection factor	Number
Total number (M, F)	12 (9, 3)
Age (years)	25.3 ± 4.1
Height (cm)	168.5 ± 7.4
Body mass (kg)	60.4 ± 9.4
BMI (kg/m^2)	21.2 ± 2.1
SBP (mm·Hg)	118.37 ± 12.95
DBP (mm·Hg)	69.40 ± 8.79

BP estimation models. For example, the M-M model only needed to select three in the four pairs of cuff BP vs. $\overline{\mathrm{PATs}}$ to complete one round calibration and got four (C_4^3) group model parameters. Given the possibility that cuff BP values of subjects in quiet state were the same, four rounds of calibration procedure were repeated to guarantee the validity of calibration in the present study. Finally, the average values of these parameters were taken as the final BP monitoring parameters, i.e., SBP_0, DBP_0, PAT_0, a_i, b_i. The whole calibration process took about eight minutes, and the subjects were required peace and quiet state.

For the ET model, three cuff BPs were used with one round calibration. For the VE models, the MK-BH and dMK-BH required one cuff BP, and the L-MK and MK-EE

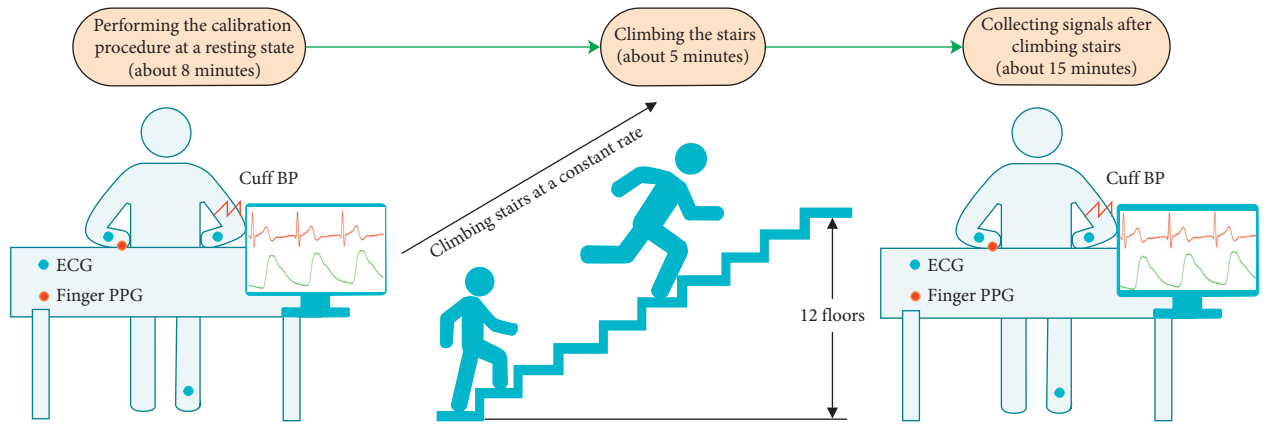

Figure 3: Illustration of the experimental design and the data collection procedure.

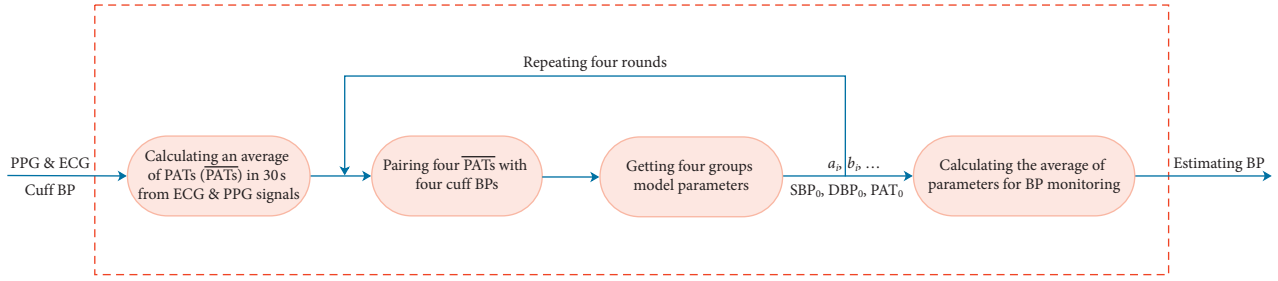

Figure 4: The advanced PTP method for the BP monitoring system.

needed two cuff BPs with one round calibration. The calibration was done only one time for each subject, and after deriving parameters in the BP estimator model, the BP could be estimated continuously.

3.3.2. Data Test. In the present experiment, over 30,000 heartbeats were analyzed. Moreover, about 3,000 heartbeats were studied for each subject. The estimated BP from a 30 s period of ECG and PPG signals was calculated. To avoid the effect of breathing, at least eight cardiac cycles [34] were used for calculating the average value of $\overline{\text{PATs}}$. A total of 365 pairs of valid $\overline{\text{PATs}}$ vs. BPs were found, and 30 $\overline{\text{PATs}}$ during the 15-minute experiment were applied in the BP estimation for each subject.

The estimated errors between the cuff BP and the estimated BP were evaluated as the mean error (ME) ± standard deviations (SD) as well as the mean absolute difference (MAD), which were defined below:

$$\text{ME} = \frac{1}{n}\sum_{i=1}^{n}\left(\text{BP}_{\text{est}_i} - \text{BP}_{\text{cuf}_i}\right),$$

$$\text{MAD} = \frac{1}{n}\sum_{i=1}^{n}\left|\left(\text{BP}_{\text{est}_i} - \text{BP}_{\text{cuf}_i}\right)\right|,$$

$$\text{SSE} = \sum_{i=1}^{n}\left(\text{BP}_{\text{est}_i} - \text{BP}_{\text{cuf}_i}\right)^2,$$

$$\sigma = \sqrt{\frac{\text{SSE}}{n-1}},$$

$$\begin{aligned}\text{c.v.} &= \frac{|\sigma|}{\text{ME}},\\ \text{SD} &= \sqrt{\frac{1}{n}\sum_{i=1}^{n}(x-\overline{x})^2},\end{aligned} \tag{1}$$

where BP_{est_i} and BP_{cuf_i} denoted the ith BP measured through BP estimation models and by the reference cuff method, respectively, and n was the number of measured BP used for evaluation. Further, the x_i denoted the ith error sample.

4. Results

The merits of the BP model based on PAT were evaluated from three different analytical methods, i.e., correlation analysis, performance analysis, and statistical analysis.

4.1. Correlation Analysis. The correlations between estimated BPs (BP_{est}) and cuff BPs (BP_{cuf}) for five models were shown in Table 3.

As shown in Table 3, the correlation between estimated SBP and cuff SBP was stronger than that between estimated DBP and cuff DBP during each nonlinear PAT-based BP monitoring model. The L-Mk model, as a linear VE model, had the weakest correlation between both SBP ($R = 0.5537$) and DBP ($R = 0.6837$) than other nonlinear BP estimation models. For MK-BH and M-M, the correlation between the cuff BP and the estimated BP was weak with a correlation coefficient of $R_{\#3} = 0.8131$ for SBP and $R_{\#5} = 0.7651$ for DBP. In our experiments, MK-EE and dMK-BH had a higher

Table 3: The correlations between BP_{est} and BP_{cuf}.

Models	SBP_{est} vs. SBP_{cuf}	DBP_{est} vs. DBP_{cuf}
MK-EE	**0.8851**	**0.8571**
L-MK	0.5537	0.6831
MK-BH	0.8131	0.7653
dMK-BH	**0.8873**	**0.8611**
M-M	0.8329	0.7350

correlation between both SBP and DBP than other models. dMK-BH had the highest correlation between both SBP ($R = 0.8873$) and DBP ($R = 0.8611$) among all subjects.

4.2. Performance Analysis. To optimize and analyze the performance of the five popular models, the dispersion degree, overall comparison, and sensitivity analysis were analyzed in this study.

4.2.1. Dispersion Degree. A good BP estimation model should be widely applicable, not only for a few individuals to show better performance. Based on this, the estimation errors of all subjects were analyzed and compared under the same BP-PAT model. The box plot of the dispersion degree comparison was shown in Figure 5 to indicate different levels of estimated BP quality for five popular BP-PAT models.

In Figure 5, the L-MK model showed the largest MAD and ME for BP and SBP, respectively. The dMK-BH model showed the minimum median MAD of SBP with 4.38 mm·Hg and a MAD of DBP with 3.36 mm·Hg, while the ME of BP was more scattered than others in the M-M model.

As mentioned above, the great changing range of BP benefited the BP estimation for each subject. Therefore, the subject with the largest range for cuff BP (SBP: 137.19 ± 12.02 mm·Hg and DBP: 84.14 ± 5.56 mm·Hg) was further investigated to estimated BP on five models quantitatively during this research. The summed square of residuals (SSE) and the root mean square error (RMSE) were computed to report how much difference between estimated BPs and cuff BPs in this subject. The results were reported in Table 4.

In Table 4, it could be observed that SSE and RMSE were largest in L-MK. Moreover, this model had the smallest CV for BP estimation, while the dMK-BH model had the opposite performance as the L-MK. The M-M model, as a ET model, had larger SSE and RMSE and smaller CV than others for SBP and DBP estimation. It also could be found that the CV values were immensely different on SBP and DBP estimation for five models in this subject. Further, their function curves were shown in Figure 6.

As shown in Figure 6, the five models showed to be quite different. The MK-BH was not a bound function and not always maintains positive, which made no sense that BP varies in a negative and infinite range in Figure 6(a). Additionally, the L-MK was inconsistent with the downward trend of others in SBP and DBP estimation based on the experiment data. The MK-EE model and dMK-BH model showed the closest estimated BP performance between SBP and DBP estimation. It was worthy of note that the M-M model converged prematurely although it was a bound function. In other words, it was not insistent with the real condition due to little changed BP estimation with the increase of PAT.

4.2.2. Overall Comparison. Another criterion for performance evaluation included ME, MAD of estimation, and SD of estimation during five BP estimation models was shown in Table 5.

It could be found that the L-MK model had a mean ± SD (MAD) of -5.89 ± 12.74 (9.34) mm·Hg for SBP and -3.72 ± 6.79 (5.91) mm·Hg for DBP, respectively. The dMK-BH model had a mean ± SD (MAD) of -0.01 ± 5.90 (4.55) mm·Hg for SBP and 0.04 ± 4.40 (3.38) mm·Hg for DBP, respectively. The M-M model had a mean ± SD (MAD) of 1.11 ± 7.51 (5.57) mm·Hg for SBP and -0.23 ± 6.47 (5.13) mm·Hg for DBP estimated error, respectively. For the dMK-BH model, the precision of estimation was approximately 0.06 mm·Hg higher than that of MK-EE and approximately 0.1–6 mm·Hg higher than all the other comparison methods. Among the optimized methods, both MK-EE and dMK-BH worked best for the estimated BP_{cuf} value due to the SD of the error bias being less than 5.90 mm·Hg and MAD being less than 4.55 mm·Hg. It was noteworthy to mention that the SD of the errors for MK-EE, MK-BH, dMK-BH, and M-M was within 8 mm·Hg for SBP and DBP. It was consistent with the AAMI requirements of 5 ± 8 mm·Hg (mean ± SD) for BP estimated error [26].

4.3. Statistical Analysis. Differences were tested with the Kruskal–Wallis tests and with Dunn's multiple comparison tests to determine whether statistically significant differences were observed between the mean errors of the ET model and the VE models, i.e., L-MK, MK-BH, MK-EE, and dMK-BH, as shown in Figure 7.

In Figure 7, there was a significant difference between the linear model and the nonlinear model in terms of estimating SBP. Similarly, a significant difference between the MK-BH model and the other nonlinear estimation models was also found during estimating DBP. It was noteworthy that MK-BH and M-M showed weaker significant changes. Additionally, there were no significant changes in MK-EE and dMK-BH models.

4.4. Sensitivity Analysis. As mentioned above, the dMK-BH model with the smallest estimated BP error merited a more in-depth analysis. From its mathematical representation, the determination of γ, a vascular information parameter which might be altered with age and the development of cardiovascular diseases, was critical to better estimate BP in long-term ABPM and HBPM. Next, the relationship between MAD and the parameter γ (across all 12 subjects over 30,000 heartbeats in Subsection 3.2) was plotted for the dMK-BH model in Figure 8.

In Figure 8, some comparisons could be made. For instance, the minimums of cardiovascular parameter γ with

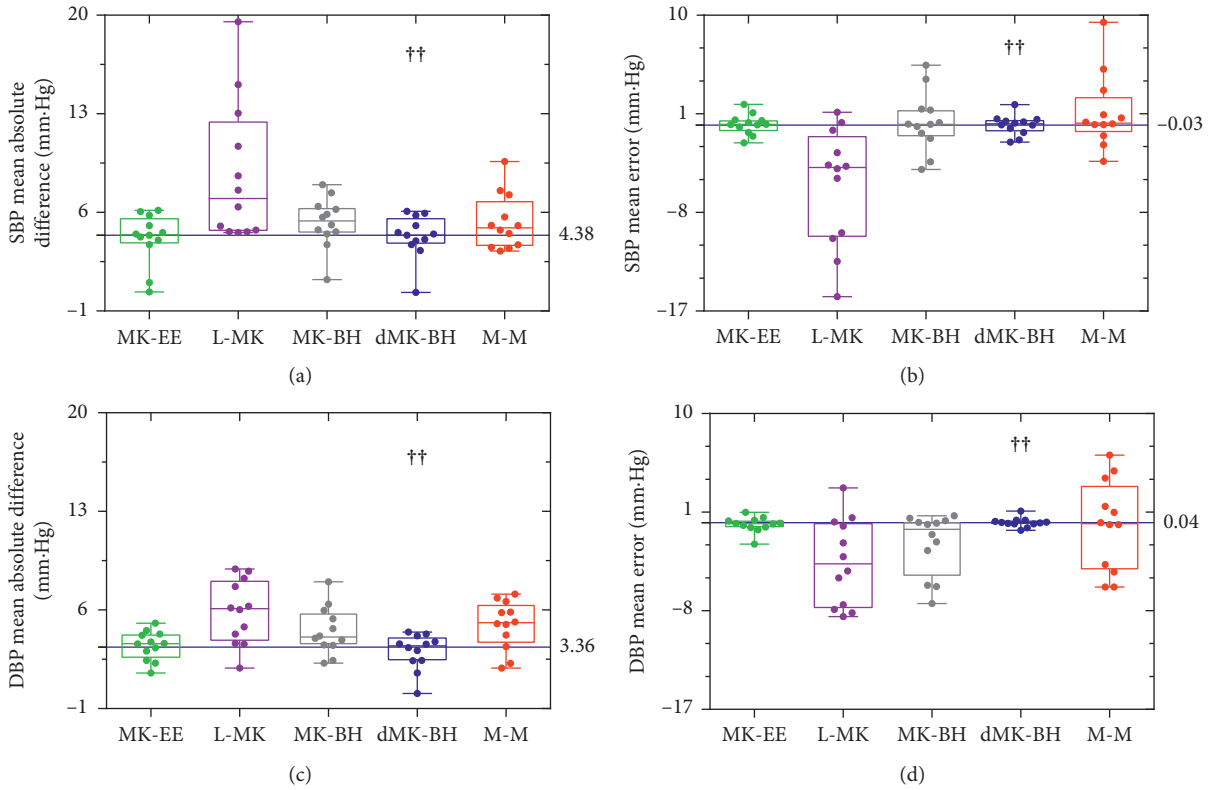

Figure 5: Box plots of dispersion degree comparison during different estimation methods in (a), (b) and (c) (d). Box and whisker plots: box, first and third quartiles; horizontal line, median; whiskers, the furthest point that lies no more than 1.5 times the interquartile range from the median. Note: each point represented an independent subject (estimated error). The dotted blue line represented the median value for dMK-BH (the strongest correlation, see Table 3). "††" indicated the BP estimation model with the strongest correlation.

Table 4: Quantitative comparison of the SSE and RMSE for the subject with the largest BP range.

Indexes	SBP					DBP				
	MK-EE	L-MK	MK-BH	dMK-BH	M-M	MK-EE	L-MK	MK-BH	dMK-BH	M-M
SSE	306.51	**11226**	890.08	283.65	798.00	262.50	**2500.1**	256.71	264.53	428.14
RMSE	3.5737	21.628	6.0899	3.4379	5.7663	3.3072	10.206	3.2705	3.3200	4.2236
*CV	22.593	**1.2544**	9.2495	951.70	16.500	27.954	**1.2763**	513.98	35.204	9.4641

Note. *CV, a standardized measure of dispersion of a probability distribution or frequency distribution, denoted the coefficient of variation.

SBP and DBP estimation were different for each subject. Moreover, these minimums mainly concentrated in a small range about 0.001–0.03 mm·Hg^{-1} in most subjects. Specifically, the two curves reached the minimums when γ were nearby 0.0021 and 0.0239, respectively. Besides, an upward trend approximately with the increase of γ between SBP and DBP estimation could be observed after one minimum value ($\gamma = 0.0239$) in this model based on the experiment. Hence, γ was a sensitive cardiovascular parameter for different subjects. In this paper, γ was set as 0.031 mm·Hg^{-1} according to Zheng et al.'s report for the healthy subjects (24–35 years old) [9].

5. Discussion

In this study, five representative BP-PAT models were studied and optimized based on the same justified and uniform criterion to work out which accurate and practical mode compared with others was well fitted in continuous cuff-less BP monitoring through an implementation of the designated protocol, i.e., the same advanced PTP method. To better evaluate the performance of the five BP-PAT models, the correlation analysis, performance analysis, and statistical analysis were applied.

As for the L-MK, similar to the linear description in the VE models, the BP estimation error was larger than other models. Indeed, this model neglected the complex regulation of the cardiovascular system. There was no explanation for phenomena such as subject's BP fluctuations alternately throughout the day. Besides, it was also not a bound function and not always positive. These performances (see Subsection 4.2) further proved that L-MK was not a good BP estimation method. Usually, linear regression was usually applied for BP estimation, in which the indicators included PAT or extra parameters, such as HR [36], PPG intensity ratio [11, 29], TDB, a kind of arterial stiffness index [36], and other features

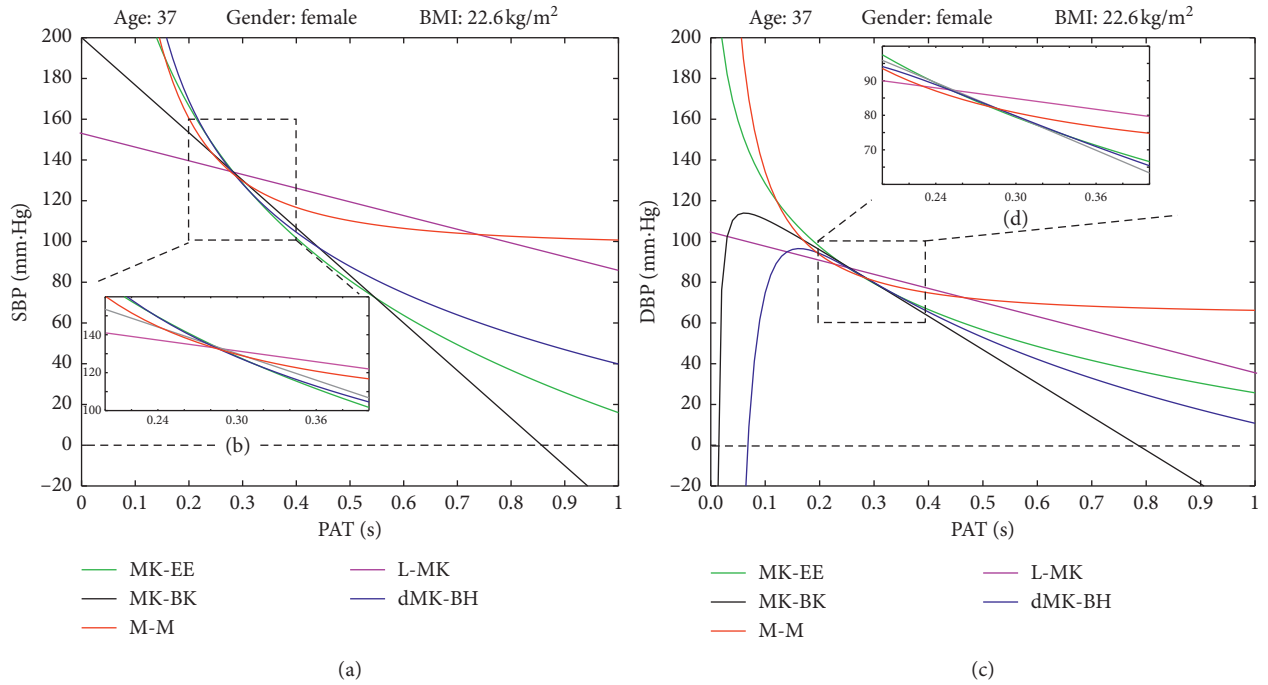

Figure 6: The five BP-PAT function curves of the subject with the largest BP range: (a) SBP trend in general. (b) SBP trend in the experiment. (c) DBP trend in general. (d) DBP trend in experiment.

Table 5: The estimated BP errors in different BP models.

Models	Systolic blood pressure (SBP)		Diastolic blood pressure (DBP)	
	Mean ± SD (mm·Hg)	MAD (mm·Hg)	Mean ± SD (mm·Hg)	MAD (mm·Hg)
MK-EE	**0.07 ± 5.87**	**4.46**	**−0.13 ± 4.54**	**3.58**
L-MK	**−5.89 ± 12.74**	**9.34**	**−3.72 ± 6.79**	**5.91**
MK-BH	0.11 ± 7.53	5.48	−2.10 ± 5.69	4.69
dMK-BH	**−0.01 ± 5.90**	**4.55**	**0.04 ± 4.40**	**3.38**
M-M	1.11 ± 7.51	5.57	−0.23 ± 6.47	5.13
ANSI/AAMI SP10 standard	|mean| ≤ 5 mm·Hg |SD| ≤ 8 mm·Hg	≤7 mm·Hg	|mean| ≤ 5 mm·Hg |SD| ≤ 8 mm·Hg	≤7 mm·Hg

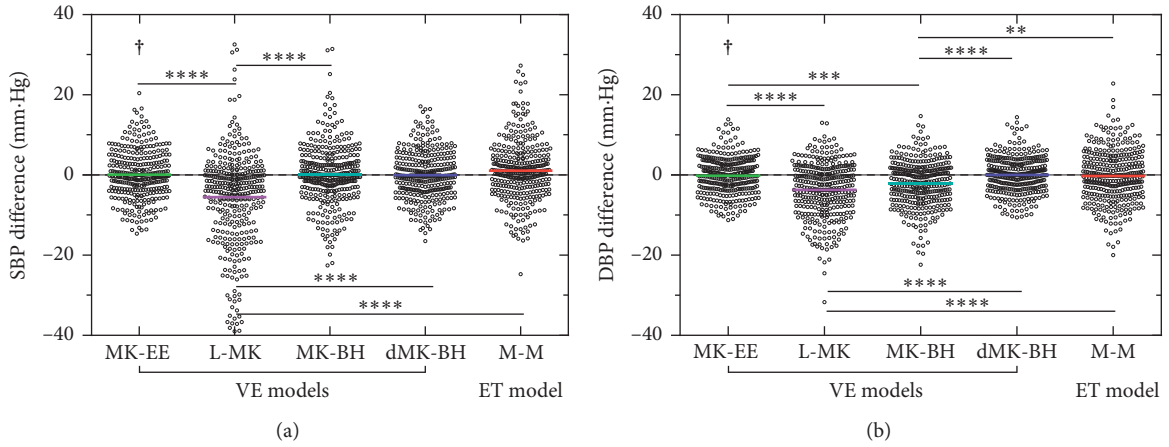

Figure 7: Scatter plot of differences among the five models. Note: significant differences between different PAT models were identified as follows: $^{*}p < 0.05$, $^{**}p < 0.01$, $^{***}p < 0.001$, and $^{****}p < 0.0001$. "†"indicates the recommended BP estimation model.

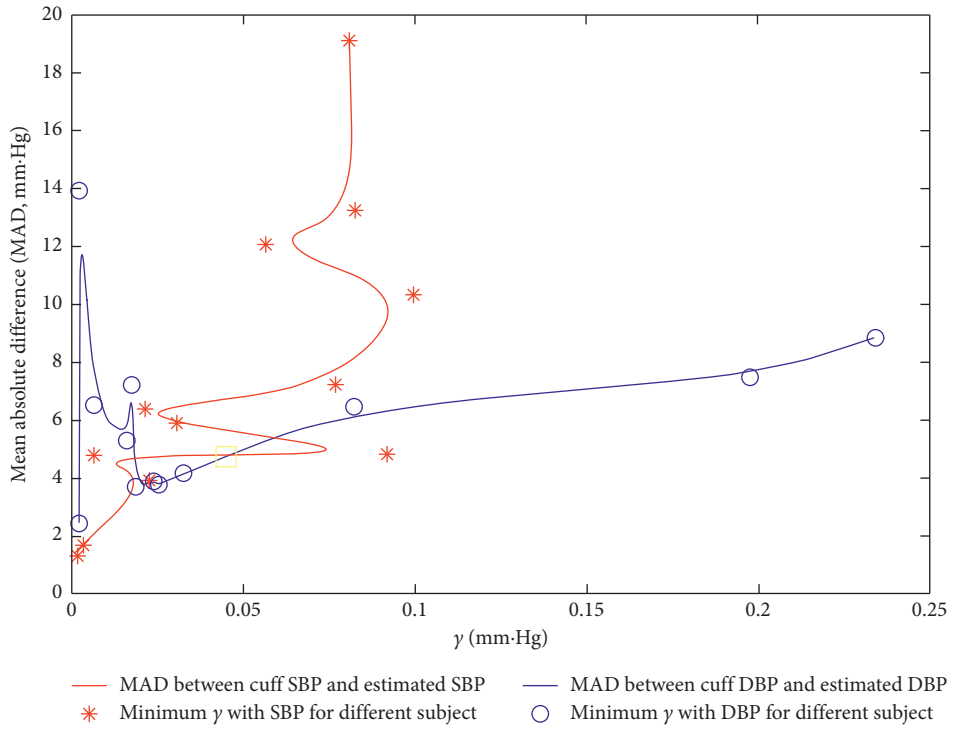

Figure 8: Sensitivity analysis with regard to γ for the dMK-BH model. Note: the curves with MAD and γ were based on De Boor algorithm [35] to the real-time interpolation for SBP and DBP in all subjects.

[19, 37] that could be obtained from ECG and PPG signals. The accuracy of the L-MK model for BP estimation was expected to improve through the combination of PAT and the above indicators by means of multiple regression analysis; however, the computation burden increased sharply.

The MK-BH model, as a VE model, had the lower correlation and the greater estimated error between estimated SBP and cuff SBP (see Tables 3 and 5 and Figure 5) in nonlinear models. For MK-BH, the stroke volume was considered as a constant; however, this parameter varied with the body's demand to oxygen-filled blood, e.g., during exercise [4]. When estimating DBP, the MK-BH model consisted of two parts: a linear function with SBP and a power function without SBP. This suggested that DBP might decrease with an increase in SBP, which was inconsistent with the situation where the SBP varied with the same trend as DBP during the experiment. This study also confirmed that MK-BH was not the better BP estimation model (see Tables 3–5 and Figures 5 and 6) for long-term ABPM and HBPM.

Referring to Esmaili et al.'s report [29], M-M (i.e., the ET model) was good for BP estimation. In contrast to their expectations, this model had the lowest correlation and the greatest estimated error for DBP and SBP, respectively (see Section 4, especially Tables 3–5 and Figures 5 and 6). One reason was that the denominator of the M-M model contained a square root leading to no real solution, which might cause inconvenience in calibration. Another important reason was that the actual arterial system was obviously not a simple tube but rather contained branches, which elastically and geometrically tapered and terminated with the microcirculation [8]. Hence, the M-M model was left for further study to take better account of the influence of the vascular branches in this model.

The dMK-BH model, as a nonlinear VE model and bound function, was based on the Moens–Korteweg equation and the Bramwell–Hill equation (here, MBP as BP). This model, with the strongest correlation between cuff BP and estimated BP and the lowest BP estimated error (see Section 4), was the best BP estimation model because of its rigorous interpretation of physiological parameters (see Table 1). Compared to MK-BH, dMK-BH in BP estimation had a significantly higher accuracy, for which the MBP applied in dMK-BH was a decisive factor. However, it was unsuitable for long-term monitoring due to its complex mathematical relationship about BP vs. PAT including a compound function of power and logarithmic function with γ (see Figure 8). Some investigations reported γ would change with aging [9, 21, 38] and the development of cardiovascular diseases [33]. It was not easy to obtain an optimal value in different ages and pathophysiologic conditions. Hence, its practicality was limited to an extent.

The nonlinear MK-EE model was conducive to practice due to its rational explanation of physiological information compared to others (see Section 2). In addition, MK-EE, as well as dMK-BH, showed a stronger correlation and lower estimated BP error with both cuff BP and estimated BP than others (see Subsection 4). Furthermore, it could be easily built into wearable sensor devices [23] due to its simple mathematical relationship about BP vs. PAT including a traditional logarithmic function. Recently, the variate of PTT

or PWV was suggested for introduction into the MK-EE model for further comprehensive modeling [8, 22].

As mentioned above, the nonlinear dMK-BH model had the strongest correlation and the smallest BP estimation error. Further, there were no significant changes between MK-EE and dMK-BH. Besides, the performance of the MK-EE model showed the best similarity to the dMK-BH model. The MK-BH and M-M, as nonlinear models, could not estimate BP well based on the experiment data, while the MK-EE model and dMK-BH model could estimate BP well (see Section 4). Although the dMK-BH model had the lowest estimated BP error between estimated BP and cuff BP, it needed a further investigation in the practical application since a sensitive cardiovascular parameter (γ) was introduced in it. These findings indicated that MK-EE could be a good substitute for dMK-BH in continuous cuff-less BP monitoring. Based on this study, we were confident that the calibration method could be used for ABPM and HBPM to some extent in the future. It was mentioned that periodic calibration should be considered to improve the reliability of BP measurement since the period between calibrations was short and might possibly affect the accuracy of parameters. Recently, Mukkamala and Hahn proposed predictions on the maximum calibration period and acceptable error limits during different ages and genders [28]. Additionally, some research had proposed several methods to improve calibration accuracy. For instance, the covariates were also introduced into calibration methods to better predict BPs, e.g., HR [39], PWV [13], and PIR [11, 29].

The Moens–Korteweg equation has provided a mathematical foundation for advancing research towards the direction of noninvasive BP monitoring. It should be noted that the practical use of the equation implies several assumptions (see Figure 1), which might be invalid for complex behavior and for regulation of the involved arterial tree, such as the thickness-to-radius ratio [24] seen as a constant. Additionally, arterial segments involved in BP estimation were formed for both elastic and muscular arteries, with different biomechanical properties. The influence of these factors on BP estimation needed further study.

6. Conclusion and Future Work

In this study, five most popular BP estimation models were investigated and optimized based on PAT under the same advanced PTP method for the first time. The investigation revealed that the MK-EE and dMK-BH, as two VE models based on the Moens–Korteweg equation, were more efficient than the ET model based on the conservation of mass and momentum equation. Considering that the change of human BP was affected by many physiological factors and manifests as a complex nonlinear system, the L-MK with the largest estimated BP error among VE models was not a good choice for ABPM. For family long-term ABPM or HBPM, we suggested selecting MK-EE, a type of VE model, as both cuff BP and estimated BP in this model had stronger correlation and lower estimated BP error than others.

One of the limitations of this investigation was the fact that subjects engaged in the present experiment were generally young and healthy volunteers rather than patients with cardiovascular disease. Thus, further studies with extensive validation that included a larger population of individuals recruited from different age groups and with various pathophysiologies were needed to confirm these outcomes. In addition, the BP-PAT models did not take into account the influence of the pre-ejection period (PEP) and vascular tone changes due to the difficulties in quantitative measuring PEP and vascular tone in ambulatory settings. Hence, a new model including the description of PEP was worth to be established in the future work.

Data Availability

The data used to support the findings of this study are available from the corresponding author upon request.

Conflicts of Interest

The authors declare that they have no conflicts of interest.

Acknowledgments

The authors would like to thank all the participants in this study.

References

[1] R. T. Raymond, B. W. Ian, L. S. Ernesto et al., "Recommendations for improving and standardizing vascular research on arterial stiffness," *Hypertension*, vol. 66, no. 3, pp. 698–722, 2015.

[2] S. Lewington, R. Clarke, N. Qizilbash, R. Peto, R. Collins, and P. S. Collaboration, "Age-specific relevance of usual blood pressure to vascular mortality: a meta-analysis of individual data for one million adults in 61 prospective studies," *The Lancet*, vol. 361, no. 9366, pp. 1389-1390, 2002.

[3] M. Kachuee, M. M. Kiani, H. Mohammadzade, and M. Shabany, "Cuffless blood pressure estimation algorithms for continuous health-care monitoring," *IEEE Transactions on Biomedical Engineering*, vol. 64, no. 4, pp. 859–869, 2017.

[4] Z. Tang, T. Tamura, M. Sekine, A. Huang, W. Chen, and M. Yoshida, "A chair-based unobtrusive cuffless blood pressure monitoring system based on pulse arrival time," *IEEE Journal of Biomedical and Health Informatics*, vol. 21, no. 5, pp. 1194–1205, 2016.

[5] J. Liu, J.-O. Hahn, and R. Mukkamala, "Error mechanisms of the oscillometric fixed-ratio blood pressure measurement method," *Annals of Biomedical Engineering*, vol. 41, no. 3, pp. 587–597, 2013.

[6] S. Josep, C. Olivier, C. Sartori, Y. Allemann, and S. F. Rimoldi, "Chest pulse-wave velocity: a novel approach to assess arterial stiffness," *IEEE Transactions on Biomedical Engineering*, vol. 58, no. 1, pp. 215–223, 2011.

[7] E. Kaniusas, H. Pfutzner, L. Mehnen et al., "Method for continuous nondisturbing monitoring of blood pressure by magnetoelastic skin curvature sensor and ECG," *IEEE Sensors Journal*, vol. 6, no. 3, pp. 819–828, 2006.

[8] R. Mukkamala, J.-O. Hahn, O. T. Inan et al., "Toward ubiquitous blood pressure monitoring via pulse transit time: theory and practice," *IEEE Transactions on Biomedical Engineering*, vol. 62, no. 8, pp. 1879–1901, 2015.

[9] Y. Zheng, C. C. Y. Poon, B. P. Yan, and J. Y. W. Lau, "Pulse arrival time based cuff-less and 24-h wearable blood pressure monitoring and its diagnostic value in hypertension," *Journal of Medical Systems*, vol. 40, no. 9, pp. 1–11, 2016.

[10] Q. Liu, B. P. Yan, C. M. Yu, Y. T. Zhang, and C. C. Y. Poon, "Attenuation of systolic blood pressure and pulse transit time hysteresis during exercise and recovery in cardiovascular patients," *IEEE Transactions on Biomedical Engineering*, vol. 61, no. 2, pp. 346–352, 2014.

[11] X. Ding, B. P. Yan, Y. T. Zhang, J. Liu, N. Zhao, and H. K. Tsang, "Pulse transit time based continuous cuffless blood pressure estimation: a new extension and a comprehensive evaluation," *Scientific Reports*, vol. 7, no. 1, Article ID 11554, 2017.

[12] H. Lin, W. Xu, N. Guan, D. Ji, Y. Wei, and W. Yi, "Non-invasive and continuous blood pressure monitoring using wearable body sensor networks," *IEEE Intelligent Systems*, vol. 30, no. 6, pp. 38–48, 2015.

[13] D. Buxi, J.-M. Redouté, and M. R. Yuce, "A survey on signals and systems in ambulatory blood pressure monitoring using pulse transit time," *Physiological Measurement*, vol. 36, no. 3, pp. R1–R26, 2015.

[14] I. C. Jeong and J. Finkelstein, "Introducing contactless blood pressure assessment using a high speed video camera," *Journal of Medical Systems*, vol. 40, no. 4, p. 77, 2016.

[15] A. Noordergraaf, *Circulatory System Dynamics*, Vol. 1, Elsevier, Amsterdam, Netherlands, 2012.

[16] M. Y.-M. Wong, C. C.-Y. Poon, and Y.-T. Zhang, "An evaluation of the cuffless blood pressure estimation based on pulse transit time technique: a half year study on normotensive subjects," *Cardiovascular Engineering*, vol. 9, no. 1, pp. 32–38, 2009.

[17] S.-H. Kim, J.-G. Song, J.-H. Park, J.-W. Kim, Y.-S. Park, and G.-S. Hwang, "Beat-to-beat tracking of systolic blood pressure using noninvasive pulse transit time during anesthesia induction in hypertensive patients," *Anesthesia & Analgesia*, vol. 116, no. 1, pp. 94–100, 2013.

[18] B. M. Mccarthy, C. J. Vaughan, B. O'Flynn, A. Mathewson, and C. Ó. Mathd s, "An examination of calibration intervals required for accurately tracking blood pressure using pulse transit time algorithms," *Journal of Human Hypertension*, vol. 27, no. 12, pp. 744–750, 2013.

[19] G. Bilo, C. Zorzi, J. E. Ochoa Munera, C. Torlasco, V. Giuli, and G. Parati, "Validation of the somnotouch-NIBP non-invasive continuous blood pressure monitor according to the European society of hypertension international protocol revision 2010," *Blood Pressure Monitoring*, vol. 20, no. 5, pp. 291–294, 2015.

[20] P. S. Pandian, K. Mohanavelu, K. P. Safeer et al., "Smart vest: wearable multi-parameter remote physiological monitoring system," *Medical Engineering & Physics*, vol. 30, no. 4, pp. 466–477, 2008.

[21] W. Chen, T. Kobayashi, S. Ichikawa, Y. Takeuchi, and T. Togawa, "Continuous estimation of systolic blood pressure using the pulse arrival time and intermittent calibration," *Medical & Biological Engineering & Computing*, vol. 38, no. 5, pp. 569–574, 2000.

[22] P. M. Nabeel, J. Jayaraj, and S. Mohanasankar, "Single-source PPG-based local pulse wave velocity measurement: a potential cuffless blood pressure estimation technique," *Physiological Measurement*, vol. 38, no. 12, pp. 2122–2140, 2017.

[23] Q. Zhang, X. Chen, Z. Fang et al., "Cuff-less blood pressure measurement using pulse arrival time and a Kalman filter," *Journal of Micromechanics and Microengineering*, vol. 27, no. 2, Article ID 024002, 2017.

[24] B. Escobar and R. Torres, "Feasibility of non-invasive blood pressure estimation based on pulse arrival time: a MIMIC database study," in *Proceedings of the 41st Computing in Cardiology Conference (CinC)*, vol. 41, pp. 1113–1116, Cambridge, MA, USA, September 2014.

[25] J. Kim, J. Park, K. Kim, Y. Chee, Y. Lim, and K. Park, "Development of a nonintrusive blood pressure estimation system for computer users," *Telemedicine and e-Health*, vol. 13, no. 1, pp. 57–64, 2007.

[26] AAMI, *American National Standard for Electronic or Automated Sphygmomanometers-ANSI/AAMI SP 10*, AAMI, Arlington, VA, USA, 2002.

[27] E. Bresch, L. Schmitt, D. De Matteis, and J. Muehlsteff, "Cuff-pressure induced PAT changes—modelling and experimental verification towards calibration of blood pressure surrogates," in *Proceedings of the 38th Annual International Conference of the IEEE Engineering in Medicine & Biology Society (EMBC)*, vol. 1, pp. 4252–4255, Orlando, FL, USA, August 2016.

[28] R. Mukkamala and J.-O. Hahn, "Toward ubiquitous blood pressure monitoring via pulse transit time: predictions on maximum calibration period and acceptable error limits," *IEEE Transactions on Biomedical Engineering*, vol. 65, no. 6, pp. 1410–1420, 2018.

[29] A. Esmaili, M. Kachuee, and M. Shabany, "Nonlinear cuffless blood pressure estimation of healthy subjects using pulse transit time and arrival time," *IEEE Transactions on Instrumentation and Measurement*, vol. 66, no. 12, pp. 3299–3308, 2017.

[30] X.-R. Ding, Y.-T. Zhang, J. Liu, W.-X. Dai, and H. K. Tsang, "Continuous cuffless blood pressure estimation using pulse transit time and photoplethysmogram intensity ratio," *IEEE Transactions on Biomedical Engineering*, vol. 63, no. 5, pp. 964–972, 2016.

[31] Factors That Affect Blood Pressure, http://www.edises.it/file/minicd/germ002/misc/assignmentfiles/cardiovascular/Fact_Aff_Blood_Pressure.pdf.

[32] D. J. Korteweg, "Ueber die fortpflanzungsgeschwindigkeit des schalles in elastischen Röhren," *Annalen der Physik und Chemie*, vol. 241, no. 12, pp. 525–542, 1878.

[33] D. Hughes, C. F. Babbs, L. A. Geddes, and J. D. Bourland, "Measurements of Young's modulus of elasticity of the canine aorta with ultrasound," *Ultrasonic Imaging*, vol. 1, no. 4, pp. 356–367, 1979.

[34] Y. Chen, C. Wen, G. Tao, M. Bi, and G. Li, "Continuous and noninvasive blood pressure measurement: a novel modeling methodology of the relationship between blood pressure and pulse wave velocity," *Annals of Biomedical Engineering*, vol. 37, no. 11, pp. 2222–2233, 2009.

[35] S. Chen, X. Hong, Y. Gong, and C. J. Harris, "Digital predistorter design using b-spline neural network and inverse of De Boor algorithm," *IEEE Transactions on Circuits and Systems I: Regular Papers*, vol. 60, no. 6, pp. 1584–1594, 2013.

[36] H. J. Baek, K. K. Kim, J. S. Kim, B. Lee, and K. S. Park, "Enhancing the estimation of blood pressure using pulse arrival time and two confounding factors," *Physiological Measurement*, vol. 31, no. 2, pp. 145–157, 2010.

[37] T. H. Huynh, R. Jafari, and W.-Y. Chung, "Noninvasive cuffless blood pressure estimation using pulse transit time and impedance plethysmography," *IEEE Transactions on Biomedical Engineering*, vol. 66, no. 4, pp. 967–976, 2019.

[38] Y. Chen, C. Wen, G. Tao, and M. Bi, "Continuous and noninvasive measurement of systolic and diastolic blood

pressure by one mathematical model with the same model parameters and two separate pulse wave velocities," *Annals of Biomedical Engineering*, vol. 40, no. 4, pp. 871–882, 2012.

[39] F. S. Cattivelli and H. Garudadri, "Noninvasive cuffless estimation of blood pressure from pulse arrival time and heart rate with adaptive calibration," in *Proceedings of the 6th International Workshop on Wearable and Implantable Body Sensor Networks*, pp. 114–119, Berkeley, CA, USA, June 2009.

Hindawi
Journal of Healthcare Engineering
Volume 2020, Article ID 1418437, 9 pages
https://doi.org/10.1155/2020/1418437

Research Article

Investigation of Delayed Response during Real-Time Cursor Control Using Electroencephalography

Hyeonseok Kim,[1] Natsue Yoshimura,[2,3] and Yasuharu Koike[2]

[1]*Department of Information and Communications Engineering, Tokyo Institute of Technology, Yokohama, Japan*
[2]*Institute of Innovative Research, Tokyo Institute of Technology, Yokohama, Japan*
[3]*Precursory Research for Embryonic Science and Technology (PRESTO), Japan Science and Technology Agency (JST), Saitama, Japan*

Correspondence should be addressed to Yasuharu Koike; koike@pi.titech.ac.jp

Received 27 September 2019; Accepted 7 January 2020; Published 8 February 2020

Guest Editor: Yousun Kang

Error-related brain activation has been investigated for advanced brain-machine interfaces (BMI). However, how a delayed response of cursor control in BMI systems should be handled is not clear. Therefore, the purpose of this study was to investigate how participants responded to delayed cursor control. Six subjects participated in the experiment and performed a wrist-bending task. For three distinct delay intervals (an interval where participants could not perceive the delay, an interval where participants could not be sure whether there was a delay or not, and an interval where participants could perceive the delay), we assessed two types of binary classifications ("Yes + No" vs. "I don't know" and "Yes" vs. "No") based on participants' responses and applied delay times (thus, four types of classification, overall). For most participants, the "Yes vs. No" classification had higher accuracy than "Yes + No" vs. "I don't know" classification. For the "Yes + No" vs. "I don't know" classification, most participants displayed higher accuracy based on response classification than delay classification. Our results demonstrate that a class only for "I don't know" largely contributed to these differences. Many independent components (ICs) that exhibited high accuracy in "Yes + No" vs. "I don't know" response classification were associated with activation of areas from the frontal to parietal lobes, while many ICs that showed high accuracy in the "Yes vs. No" classification were associated with activation of an area ranging from the parietal to the occipital lobes and were more broadly localized in cortical regions than was seen for the "Yes + No" vs. "I don't know" classification. Our results suggest that small and large delays in real-time cursor control differ not only in the magnitude of the delay but should be handled as distinct information in different ways and might involve differential processing in the brain.

1. Introduction

In the realm of brain-machine interfaces (BMIs), attempts have been made to decode brain activity to allow the input of commands into BMI systems. Due to its practical advantages, electroencephalography (EEG) has been widely used in BMI systems to infer information about intention to move the upper limb [1], targets and distractors [2], finger movement [3], resting states or motor attempts to move the paretic hand [4], intention to stand or sit [5], and intended direction of movement [6, 7]. Information that is not directly used could still be useful for improving BMI systems.

Passive BMIs exploit implicit information from involuntary brain activity [8]. Likewise, such information can be used to make unsupervised adaptive decoders for BMI systems to improve their performance [9]. Error-related potentials, which occur when an error is made [10], can be used to inhibit the previous command upon detection or to update BMI classifiers through reinforcement learning [11]. As the case may be, the magnitude of error-related potentials reflects the degree of error [12], and several studies have investigated error-related potential in various situations. During a video game task, for example, outcome error and execution error have been classified [13]. Moreover, it has been reported that errors resulting from failures in motor

control and sustained attention could be classified and that these errors might involve differential processing mechanisms [14]. A BMI system capable of ignoring command inputs and making corrections when error-related potentials are generated by moving in the opposite direction has also been developed [15]. Even in driving tasks, brain activity associated with discrepancies between cued direction and human intention has been classified [16].

Controlling a cursor in real-time is a common performance task in BMI systems used to execute practical functions such as reaching, which is a common and fundamental action required to perform tasks in daily life. Since errors can take many different forms depending on the BMI system being used and the fact that error-related potentials are task-dependent [17], various kinds of errors can occur when attempting to control a cursor, such as movement in an unintended direction, differences in end points and movement speed, and misclicking; however, response lag to user inputs in BMI systems used in real-time cursor control should be particularly considered. While it is difficult to call the delay an "error," in this context, the term is related to the performance of the system. Many kinds of errors may result from discrepancies between brain activities associated with the input of a command and the command configuration already programmed into the BMI system; however, lagged responses can occur even if a user supplies the system with suitably relevant inputs. If the user recognizes that the delay is an error and the BMI system learns from this dummy training data, the performance of the system will get worse over time. Moreover, since the user also tries to learn to control the BMI system [18], communication with the system may be prone to failure.

Even though delayed responses can result in communication failure between the user and the BMI system, few studies have investigated these relationships. Errors themselves and error-related potentials that may be similar to response delays have been investigated. Such delayed system responses not only occur in BMI systems but are seen in other systems as well, such as haptic interfaces [19]. It has been reported that in haptic interfacing, task performance can decrease due to delayed responses of the system [20, 21], though the degree to which the delayed response affects performance differs depending on the task [22]. In addition, auditory delays can also affect normal speech [23], which can negatively impact the user's ability to communicate. Thus, delayed responses must also be investigated in BMI systems.

Therefore, the purpose of the study was to investigate how participants respond to delayed cursor control, which is a typical application of BMI systems. Wrist bending was performed to control a cursor, and we investigated brain activity during delayed responses. We divided the delay interval into three groups depending on its length: an interval where participants were unable to perceive the delay, an interval where participants could not be sure whether there was a delay or not, and an interval where participants were able to perceive the delay. Then, we performed two kinds ("Yes + No" vs. "I don't know" and "Yes vs. No") of binary classifications based on participant's responses and an applied delay (overall, four types of classification). In addition, we identified independent components (ICs) that were associated with high accuracy rates.

2. Materials and Methods

2.1. Experimental Procedure. Six individuals (five males and one female) with a mean age of 27.0 years (standard deviation: 3.22) participated in the experiment. The lone female participant was left-handed; the other participants were all right-handed. All participants provided written informed consent prior to participating in the experiment. This study was approved by the ethics committee of the Tokyo Institute of Technology (ethics approval number: 2019001), and the experimental protocol was conducted in accordance with the ethical standards outlined in the Declaration of Helsinki.

Before the experiment, a participant sat in a chair in front of a monitor and was allowed to adjust the chair to feel comfortable. The participant was affixed with an electroencephalogram (EEG) cap to which electrodes were attached. Two markers for a motion sensor were attached on the participant's wrist and on a plastic stick that the participant was instructed to hold during the experiment. Figure 1 shows the flow of a single trial. At the start of the experiment, a red circle, used as an initial position indicator, was aligned in the center of the screen to fix the initial position of movement. The participant controlled the cyan pole (tracer) by bending his/her wrist on the dominant side while holding the stick with the marker. The tracer was moved along the gray arc as shown in Figure 1. When the tracer reached the red circle, another red circle appeared on the screen as a target. The target was positioned to allow participants to access it by bending their wrists by 35 degrees; this angle was selected to allow participants to bend their wrists easily for an extended duration and to allow for the greatest possible range of motion. The target appeared on the left side of the screen for the right-handed participants and on the right side for the left-handed participants. The participants were instructed to wait at least 1.5 s before reaching the target because the delay was applied to the tracer after 1 s. The timing of the delay was selected to make it more difficult for the participant to know whether the delay was applied or not as the tracer reached the initial position indicator. The duration of the delay was between 0 ms and 200 ms; the delay changed between runs by 20 ms intervals. When the participant reached the target, the tracer and the target disappeared, and a question appeared on the screen asking whether the participant perceived the delay or not. When the participant was sure there was a delay, the participant was instructed to press the key to indicate "Yes." When the participant was sure there was no delay, the participant was instructed to press the key to indicate "No." When the participant was not sure whether there was a delay or not, the participant was instructed to press the key to indicate "I don't know." When the participant pressed the corresponding key to respond, the initial position indicator appeared for the next trial. This procedure was repeated so that all participants performed five runs, each consisting of 140 trials; therefore, each participant repeated trials ten times for each delay between 20 ms and 200 ms; they then

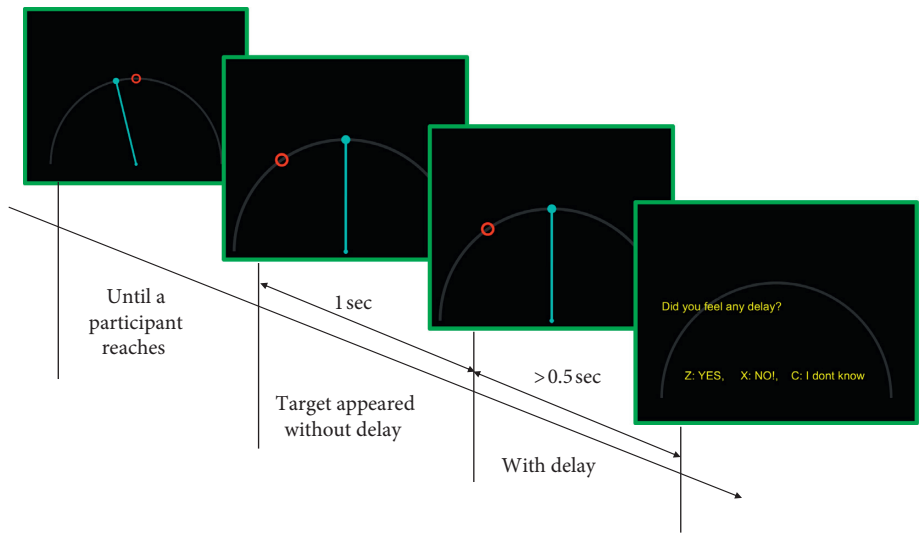

Figure 1: Flow of a single trial. At the beginning of the trial, an initial position indicator (identified by the red circle on the first screen) appeared on the screen to allow the participant to fix the initial position of the movement. When the tracer (cyan pole) reached the initial position indicator, a new target (larger red circle on the second screen) appeared. After 1 s, a delay was applied to the tracer, but nothing changed on the screen. During this stage, the participant performed self-paced reaching. If the participant initialized in the stage without the delay, a "Wait more" message appeared on the screen and data for that trial were discarded. When the tracer reached the target, the target and the tracer disappeared and the participant was asked whether he or she perceived the delay, to which they needed to respond by pressing a corresponding key. This procedure was repeated for each trial.

repeated trials 40 times per run without the delay. The trials were presented in pseudo-random order, with a rest between runs.

2.2. Data Acquisition and Preprocessing. The angle data of the wrists were calculated from the positions of the two markers on the wrist and the stick. Each position was measured using the Optotrak Certus motion capture system (NDI, Inc., Waterloo, Canada) and sampled at 100 Hz. Based on the international 10–20 system, EEG signals were measured from 64 channels (Fp1, Fp2, Fpz, AF3, AF4, AF7, AF8, AFz, F1, F2, F3, F4, F5, F6, F7, F8, Fz, FT7, FT8, FC1, FC2, FC3, FC4, FC5, FC6, FCz, C1, C2, C3, C4, C5, C6, Cz, T7, T8, TP7, TP8, CP1, CP2, CP3, CP4, CP5, CP6, CPz, P1, P2, P3, P4, P5, P6, P7, P8, P9, P10, Pz, PO3, PO4, PO7, PO8, POz, O1, O2, Oz, and Iz) using the ActiveTwo system (BioSemi, Amsterdam, The Netherlands), sampled at 2,048 Hz.

EEGLAB [24] was used for preprocessing of the EEG signals, which were re-referenced based on an average reference value and filtered using a band-pass filter (1–40 Hz). Epochs were then extracted from 1 s before the onset of the movement to 1 s after the onset. Epochs in noisy trials and trials where the participant did not wait at least 1.5 s after the target appeared were rejected. We performed independent component analysis to obtain independent electrical sources using the extended Infomax algorithm in EEGLAB [25]. ICs related to noise were rejected.

2.3. Classifications. Four types of binary classification were employed. Two classifications were based on the participants' responses ("Yes + No vs. I don't know" and "Yes vs. No"); the other classifications were based on the actual delays. Since the threshold to detect delays varies among individuals, we classified participants into three classes: a class where the participant detected a delay in most of the trials ("Yes"), a class where the participant did not detect a delay in most of the trials ("No"), and an unsure class ("I don't know"). Classifications based on actual delay times were also employed for "Yes + No" vs. "I don't know" and for "Yes vs. No." Table 1 shows the duration of the delay for each class. The interval was determined by the selection rate for each answer for each participant (see the Results section).

Linear discriminant analysis (LDA) classifiers were used to generate four types of binary classifications. Classifiers were implemented using the Statistics and Machine Learning Toolbox in MATLAB (MathWorks, Inc., Natick, MA, USA). During a period from the onset of the movement to 1 s after the onset, the time series of the remaining ICs were used for analysis. Since a high sampling frequency for EEG signals generates too many factors, the data were downsampled to 100 Hz to reduce computation loads. We used one IC for each classification to determine the relative contribution of each for detecting delays; thus, the ICs could be compared by performance within a classification. Since each IC was used for each classification, as was the last 1 s of each epoch, 100 features were fed into each classifier. The performance of each classifier was assessed using five-fold cross validation. For each fold, the dataset for each participant was partitioned into five smaller datasets with the same number of datapoints using the Statistics and Machine Learning Toolbox in MATLAB. The last remaining dataset had a different number of datapoints when the dataset was not divided by five, without a remainder.

Table 1: Delay for each response class based on the delay (unit: ms).

Was a delay felt?	P1	P2	P3	P4	P5	P6
No (not felt)	0–70	0–30	0–70	0–50	0–30	0–30
I don't know (not sure)	70–170	30–90	70–110	50–110	30–110	30–110
Yes (felt)	170–200	90–200	110–200	110–200	110–200	110–200

3. Results

Figure 2 displays individual selection rates based on the duration of the delay. For most of the participants, a delay threshold had to be reached before they became confident that they perceived the delay. However, participant 1 showed a consistent selection rate for "I don't know" at all delay intervals, resulting in a lower selection rate in trials with a long delay compared to other participants. All participants, except for participant 1, were more unsure of the existence of a delay in trials with short delays of 40–100 ms compared to other delay durations. The selection rate for the "I don't know" response was the highest for participant 4 for most delay intervals, while participant 3 exhibited the lowest selection rate for this response for most delay intervals.

Figure 3 shows mean accuracy rates based on response and delay classifications. For most of the participants, the "Yes + No" vs. "I don't know" response classification was associated with the highest accuracy compared to other types of classifications ($p < 0.01$ for participants 2, 3, 5, and 6 based on a t-test comparing the "Yes + No" vs. "I don't know" response classification and the "Yes + No" vs. "I don't know" delay classification). For participant 4, the accuracy of the "Yes + No" vs. "I don't know" response classification and the "Yes + No" vs. "I don't know" delay classification was similar ($p > 0.05$ for participant 4, based on a t-test comparing the "Yes + No" vs. "I don't know" response classification and the "Yes + No" vs. "I don't know"delay classification). Participant 1 showed the higher accuracy for the "Yes vs. No" delay classification, while the other participants showed lower accuracy for the "Yes vs. No" delay classification than the other kinds of classifications. Moreover, accuracy for the "Yes + No" vs. "I don't know" response classification and the "Yes vs. No" delay classification was similar for participant 1 ($p > 0.1$).

We investigated which ICs contributed to the highest accuracy rates for each type of classification. Figure 4 shows the top five ICs that achieved the highest accuracy for the "Yes + No" vs. "I don't know" classification. Figure 5 shows the top five ICs that achieved the highest accuracy for the "Yes vs. No" classification.

4. Discussion

In this study, we performed two types of binary classifications ("Yes + No" vs. "I don't know" and "Yes vs. No") based on the participants' responses and the duration of the delays. For most participants, the "Yes vs. No" classification was associated with higher accuracy than the "Yes + No" vs. "I don't know" classification. That is, classifying participants' confidence in their response, regardless of a delay, was easier than classifying based on whether there was a delay or not. From a BMI system's viewpoint, our results imply that in cases where brain activity can be affected by a delay in the BMI system, short delays do not allow a user to be sure whether there is a delay or not; these short delays may be more problematic, as longer delays provide enough time to perceive the lag. For the "Yes + No" vs. "I don't know" classification, most participants displayed higher accuracy in the response classification than in the delay classification. For all participants, selection rates were below 100% for intervals where they responded with "I don't know," which means that participants' responses were different even between trials with the same delay. The performance for the "Yes + No" vs. "I don't know" classification based on actual delay times was lower than for the "Yes + No" vs. "I don't know" response classification. In addition, our results show that a class solely for "I don't know" largely contributed to these differences, indicating that some information associated with uncertain responses, rather than delay times, might be represented by information processing in certain areas of the brain. Since participants might think they cannot control the cursor when there is a significantly large delay, "Yes vs. No" might be classified by a sense of agency [26], as ICs are associated with brain areas related to a sense of agency, such as the presupplementary motor area [27], the parietal-premotor network [28], and the inferior parietal areas [29]. For "No" and "I don't know" responses, participants might think they have a sense of agency, but in cases where they respond with "I don't know," they might experience poor control performance even though they can control the cursor by themselves.

Many ICs that showed high accuracy in the "Yes + No" vs. "I don't know" response classification were related to areas of the brain ranging from the frontal to the parietal lobes, and some of these signals were narrowly localized in the brain, as shown in Figure 4. At the same time, many ICs that showed high accuracy in the "Yes vs. No" classification were related to areas of the brain ranging from the parietal to the occipital lobes, with broader cortical localization compared to the areas associated with the "Yes + No" vs. "I don't know" classification, as shown in Figure 5. The medial frontal cortex plays an important role in monitoring performance outcomes [30]. It has been reported that the frontal midline in the theta band is strongly associated with error-related negativity [31], and the medial prefrontal cortex, which modulates error-related processing, communicates with the lateral prefrontal cortex to comprise a network for action monitoring [32]. In addition, it has been reported that brain activity in the anterior cingulate cortex is related to processing of error-related information [33]; this area is activated not only by the error itself but also by correct outcomes in situations where repetitive errors can be anticipated [34]. These previous studies may support our

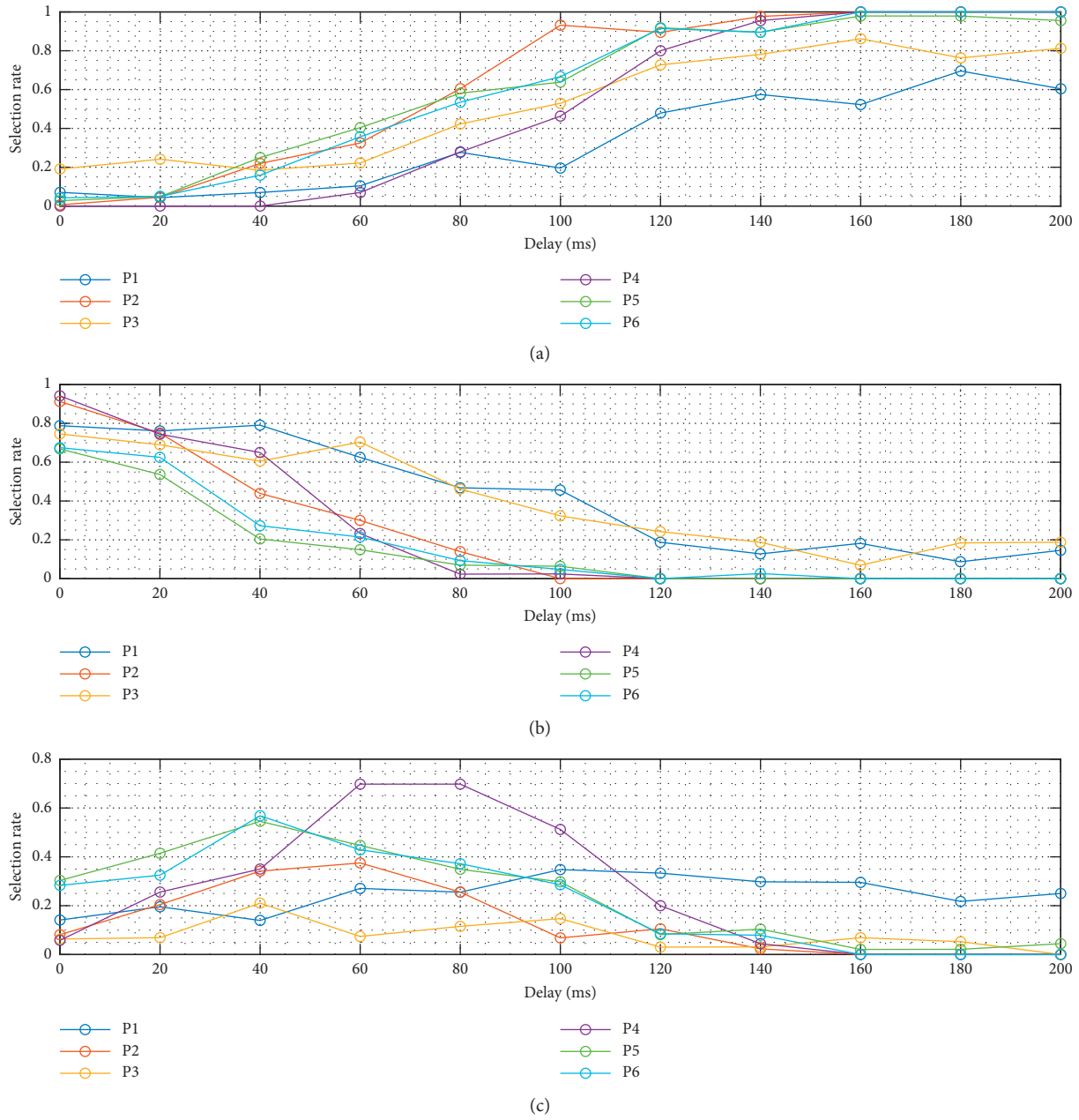

Figure 2: Individual selection rates based on the duration of the delay. Each plot represents a "yes" response (a), a "no" response (b), and an "I don't know" response (c). The selection rate for each response is plotted against the duration of the delay (ms).

results, which showed ICs related to the areas associated with the "Yes + No" vs. "I don't know" response classification, reflecting how uncertain delay is perceived for a user of a BMI system. For the "Yes vs. No" classification, few ICs that achieved high accuracy were related to the frontal or central areas; most of the ICs were observed from the parietal and occipital lobes. These areas are related to the dorsal pathway, which is important for information processing from the primary visual cortex to the posterior parietal lobe [35, 36] that is associated with visual sensory perception [37]. It is difficult to know precisely which functional areas in the brain are related to small delays, since the frontal lobe performs many, varied tasks; for example, the anterior cingulate cortex plays a role in conflict detection, error monitoring [38], and response adaptation [39]. Our results suggest that larger delays may not have any relationship with these functions. Moreover, our results suggest that small and large delays in real-time cursor control differ not only in the magnitude of the delay but may be processed in different ways.

We selected some ICs that achieved high accuracy to investigate how the brain recognizes large delays within trials. We observed event-related spectral perturbations (ERSP) [40] of each IC that achieved high accuracy in the "Yes vs. No" delay classification. Figure 6 shows ERSPs of certain ICs related to the processing of visual information for

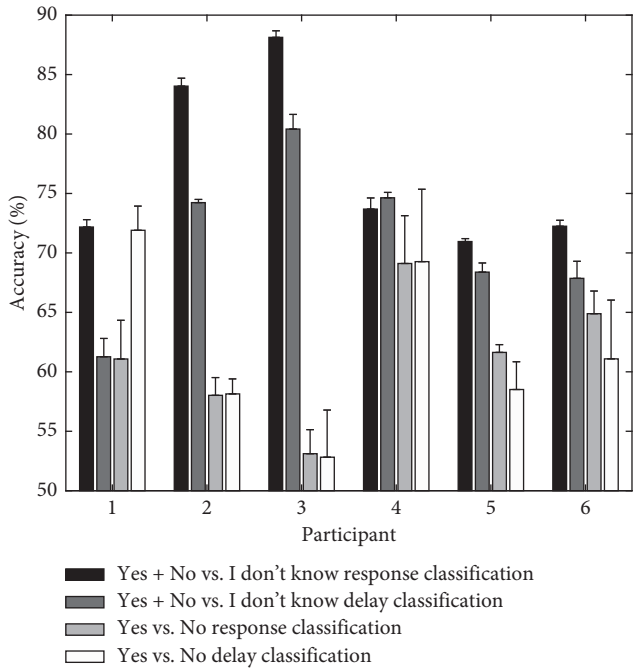

Figure 3: Mean accuracy (%) based on response and delay classifications. The accuracy was averaged across the top five ICs that achieved the highest accuracy rates. Response classification was based solely on each participant's response, regardless of the actual delay duration. Delay classification was based on the delay duration, regardless of participant's response. Each class for the delay classification was determined based on the selection rate for each participant (refer to Table 1).

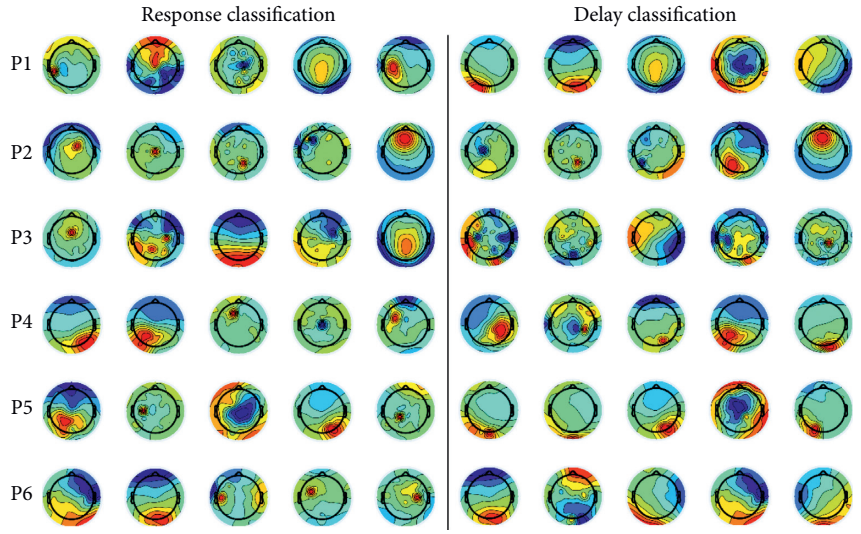

Figure 4: The top five independent components (ICs) that achieved the five highest accuracy rates for the "Yes + No" vs. "I don't know" classification. Each row represents the ICs for each participant (P1–P6). The five ICs in the left grouping are for the response classification, and the five ICs in the right grouping are for the delay classification. The accuracy rates of the five ICs are ranked in the order of decreasing accuracy, moving from left to right.

participants 1, 4, and 6. The ICs in the trials with a delay exhibited delayed activation compared to the trials without a delay, suggesting that delayed recognition of the onset of the motion is a key factor contributing to the classification. Likewise, since this recognition of the onset of motion had no relation to participants' responses, more ICs that contributed to high accuracy rates were found in the "Yes + No" vs. "I do not know" delay classification than in the "Yes + No" vs. "I don't know" response classification.

In our experiment, most of the participants were unsure of the existence of a delay in trials where the duration of the delay ranged from 40 to 100 ms. However, when we tried to categorize the delays as uncertain and certain, it was difficult to define uncertain delays because participants could

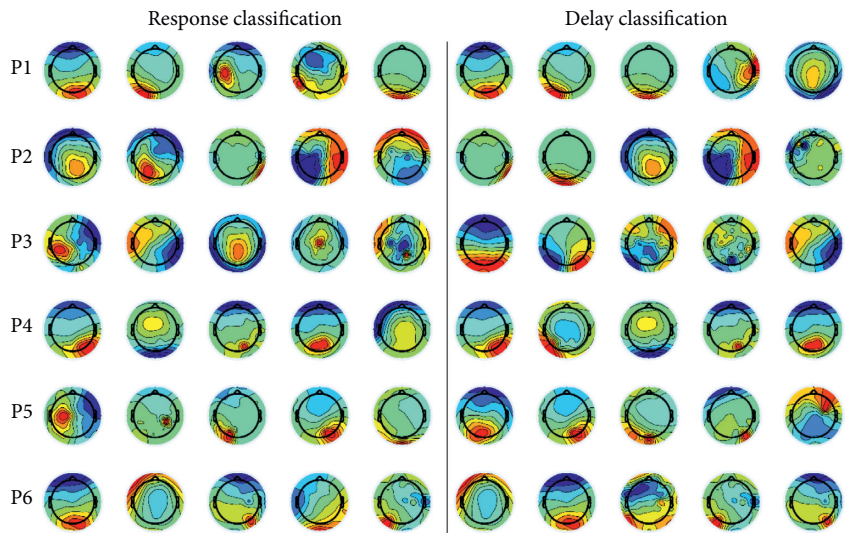

Figure 5: The top five independent components (ICs) that achieved the five highest accuracy rates for the "Yes vs. No" classification. Each row represents the ICs for each of the six participants (P1–P6). The five ICs in the left grouping are for the response classification, and the five ICs in the right grouping are for the delay classification. The accuracy rates of the five ICs are ranked in the order of decreasing accuracy, moving from left to right.

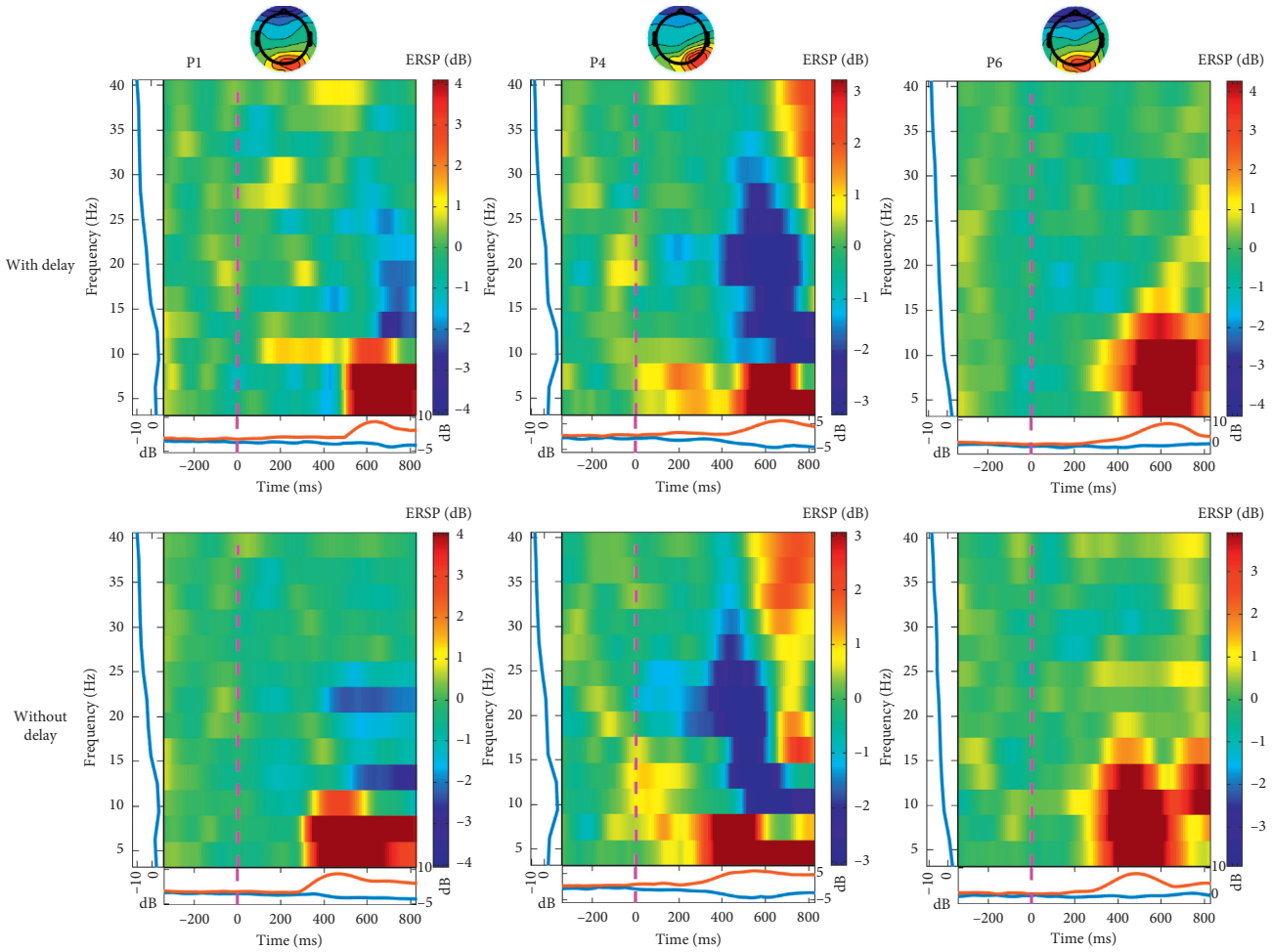

Figure 6: Event-related spectral perturbations of independent components (ICs) related to the processing of visual information from participants 1, 4, and 6. The ICs that achieved the highest accuracy for participants 1 and 4, and the top two highest accuracies for participant 6 based on the "Yes vs. No" delay classification are shown, respectively. The dotted line at 0 s represents the initiation of the movement. The ICs show delayed responses in trials with a delay compared to trials without a delay.

respond differently even in trials where the duration of the delay was the same. Instead, the duration of the delay was related to task performance. Point-to-point movement is normally modeled and assessed by Fitts' law [41, 42], which, when fitted with a linearly combined delay term, explained 93.5% of the variance, indicating that task performance may be linearly related to the duration of the delay [43].

We investigated brain activity during delayed cursor control, which can often occur in BMI systems. This can be used to construct intelligent BMI systems to update a decoder online when a BMI system experiences an error. So far, feedforward control has been employed in a BMI system that decodes neural signals to use them as an input command and obtain movement parameters [44]. When a BMI system works well and a user wants to move, feedforward control is sufficient; however, when the system experiences an error because it does not perceive correct user intention, a feedback controller is needed to perform calculations and correct for the delay. This feedback controller is different with a decoder. For real-time control, both the feedforward controller and the feedback controller are components of the system. Input commands generated by the brain are corrected by summing the output of the feedback controller and then transferred as corrected signals, rather than the individual components working in isolation. In this study, we investigated brain activity involved in controlling responses based on the duration of delays. Our results showed that, unlike in general situations when a system is working optimally, when there is a delay between intention to move and the actual movement itself, signals can be generated that are not optimal for feedforward control. Thus, additional systems such as a feedback controller are needed in BMIs; based on our results, commands generated by feedforward and feedback controllers should be separated for the system to work optimally.

5. Conclusion

In this study, we confirmed that small and large delays in real-time cursor control might result in differential processing in the brain. However, since the delay may not always be an error, how the delay is related to other kinds of errors should be investigated based on the magnitude of the delay. Understanding these mechanisms may allow for the advanced construction of BMI systems for real-time cursor control in which learning can occur from these errors.

Data Availability

The data used to support the findings of this study are included within the article.

Conflicts of Interest

The authors declare that there are no conflicts of interest regarding the publication of this article.

Acknowledgments

This work was supported by the JSPS KAKENHI (grant no. 17H05903); Tateishi Science and Technology Foundation (grant no. 2188001); JST PRESTO (Precursory Research for Embryonic Science and Technology) (grant no. JPMJPR17JA); and JST MIRAI (grant no. JPMJM18C8).

References

[1] E. López-Larraz, L. Montesano, Á. Gil-Agudo, and J. Minguez, "Continuous decoding of movement intention of upper limb self-initiated analytic movements from pre-movement EEG correlates," *Journal of NeuroEngineering and Rehabilitation*, vol. 11, no. 1, p. 153, 2014.

[2] D. Joshi, Sweetii, B. K. Panigrahi, S. Anand, and J. Santhosh, "Classification of targets and distractors present in visual hemifields using time-frequency domain EEG features," *Journal of Healthcare Engineering*, vol. 2018, Article ID 9213707, 10 pages, 2018.

[3] N. Yoshimura, H. Tsuda, T. Kawase, H. Kambara, and Y. Koike, "Decoding finger movement in humans using synergy of EEG cortical current signals," *Scientific Reports*, vol. 7, no. 1, p. 11382, 2017.

[4] C. Li, T. Jia, Q. Xu, L. Ji, and Y. Pan, "Brain-computer interface channel-selection strategy based on analysis of event-related desynchronization topography in stroke patients," *Journal of Healthcare Engineering*, vol. 2019, Article ID 3817124, 12 pages, 2019.

[5] T. C. Bulea, S. Prasad, A. Kilicarslan, and J. L. Contreras-Vidal, "Sitting and standing intention can be decoded from scalp EEG recorded prior to movement execution," *Frontiers in Neuroscience*, vol. 8, p. 376, 2014.

[6] P. Hammon, S. Makeig, H. Poizner, E. Todorov, and V. De Sa, "Predicting reaching targets from human EEG," *IEEE Signal Processing Magazine*, vol. 25, no. 1, pp. 69–77, 2008.

[7] H. Kim, N. Yoshimura, and Y. Koike, "Classification of movement intention using independent components of premovement EEG," *Frontiers in Human Neuroscience*, vol. 13, p. 63, 2019.

[8] T. O. Zander and C. Kothe, "Towards passive brain–computer interfaces: applying brain–computer interface technology to human–machine systems in general," *Journal of Neural Engineering*, vol. 8, no. 2, Article ID 025005, 2011.

[9] T. Gürel and C. Mehring, "Unsupervised adaptation of brain-machine interface decoders," *Frontiers in Neuroscience*, vol. 6, no. 6, p. 164, 2012.

[10] G. Schalk, J. R. Wolpaw, D. J. McFarland, and G. Pfurtscheller, "EEG-based communication: presence of an error potential," *Clinical Neurophysiology*, vol. 111, no. 12, pp. 2138–2144, 2000.

[11] R. Chavarriaga, S. Aleksander, and J. D. R. Millán, "Errare machinale est: the use of error-related potentials in brain-machine interfaces," *Frontiers in Neuroscience*, vol. 8, p. 208, 2014.

[12] G. Hajcak, J. S. Moser, N. Yeung, and R. F. Simons, "On th'e ERN and the significance of errors," *Psychophysiology*, vol. 42, no. 2, pp. 151–160, 2005.

[13] M. Spüler and C. Niethammer, "Error-related potentials during continuous feedback: using EEG to detect errors of different type and severity," *Frontiers in Human Neuroscience*, vol. 9, no. 9, p. 155, 2015.

[14] J. van Driel, K. R. Ridderinkhof, and M. X. Cohen, "Not all errors are alike: theta and alpha EEG dynamics relate to differences in error-processing dynamics," *Journal of Neuroscience*, vol. 32, no. 47, pp. 16795–16806, 2012.

[15] P. W. Ferrez and J. D. R. Millan, "Error-related EEG potentials generated during simulated brain-computer interaction,"

IEEE Transactions on Biomedical Engineering, vol. 55, no. 3, pp. 923–929, 2008.

[16] H. Zhang, R. Chavarriaga, Z. Khaliliardali, L. Gheorghe, I. Iturrate, and J. d. R. Millán, "EEG-based decoding of error-related brain activity in a real-world driving task," *Journal of Neural Engineering*, vol. 12, no. 6, Article ID 066028, 2015.

[17] I. Iturrate, L. Montesano, and J. Minguez, "Task-dependent signal variations in EEG error-related potentials for brain–computer interfaces," *Journal of Neural Engineering*, vol. 10, no. 2, Article ID 026024, 2013.

[18] M. Ahn, H. Cho, S. Ahn, and S. C. Jun, "User's self-prediction of performance in motor imagery brain–computer interface," *Frontiers in Human Neuroscience*, vol. 12, p. 59, 2018.

[19] M. Rank, Z. Shi, and S. Hirche, "Perception of delay in haptic telepresence systems," *Presence: Teleoperators and Virtual Environments*, vol. 19, no. 5, pp. 389–399, 2010.

[20] C. Jay, M. Glencross, and R. Hubbold, "Modeling the effects of delayed haptic and visual feedback in a collaborative virtual environment," *ACM Transactions on Computer-Human Interaction*, vol. 14, no. 2, pp. 8–es, 2007.

[21] J. R. Kim, R. H. Osgouei, and S. Choi, "Effects of visual and haptic latency on touchscreen interaction: a case study using painting task," in *Proceedings of the 2017 IEEE World Haptics Conference*, pp. 159–164, Munich, Germany, June 2017.

[22] J. Dabrowski and E. V. Munson, "40 years of searching for the best computer system response time," *Interacting with Computers*, vol. 23, no. 5, pp. 555–564, 2011.

[23] A. Stuart, J. Kalinowski, M. P. Rastatter, and K. Lynch, "Effect of delayed auditory feedback on normal speakers at two speech rates," *The Journal of the Acoustical Society of America*, vol. 111, no. 5, pp. 2237–2241, 2002.

[24] A. Delorme and S. Makeig, "EEGLAB: an open source toolbox for analysis of single-trial EEG dynamics including independent component analysis," *Journal of Neuroscience Methods*, vol. 134, no. 1, pp. 9–21, 2004.

[25] A. J. Bell and T. J. Sejnowski, "An information-maximization approach to blind separation and blind deconvolution," *Neural Computation*, vol. 7, no. 6, pp. 1129–1159, 1995.

[26] N. David, A. Newen, and K. Vogeley, "The "sense of agency" and its underlying cognitive and neural mechanisms," *Consciousness and Cognition*, vol. 17, no. 2, pp. 523–534, 2008.

[27] J. W. Moore, D. Ruge, D. Wenke, J. Rothwell, and P. Haggard, "Disrupting the experience of control in the human brain: pre-supplementary motor area contributes to the sense of agency," *Proceedings of the Royal Society B: Biological Sciences*, vol. 277, no. 1693, pp. 2503–2509, 2010.

[28] M. Desmurget and A. Sirigu, "A parietal-premotor network for movement intention and motor awareness," *Trends in Cognitive Sciences*, vol. 13, no. 10, pp. 411–419, 2009.

[29] S. Shimada, K. Hiraki, and I. Oda, "The parietal role in the sense of self-ownership with temporal discrepancy between visual and proprioceptive feedbacks," *NeuroImage*, vol. 24, no. 4, pp. 1225–1232, 2005.

[30] K. R. Ridderinkhof, M. Ullsperger, E. A. Crone, and S. Nieuwenhuis, "The role of the medial frontal cortex in cognitive control," *Science*, vol. 306, no. 5695, pp. 443–447, 2004.

[31] P. Luu, D. M. Tucker, and S. Makeig, "Frontal midline theta and the error-related negativity: neurophysiological mechanisms of action regulation," *Clinical Neurophysiology*, vol. 115, no. 8, pp. 1821–1835, 2004.

[32] J. F. Cavanagh, M. X. Cohen, and J. J. B. Allen, "Prelude to and resolution of an error: EEG phase synchrony reveals cognitive control dynamics during action monitoring," *Journal of Neuroscience*, vol. 29, no. 1, pp. 98–105, 2009.

[33] C. B. Holroyd, S. Nieuwenhuis, N. Yeung et al., "Dorsal anterior cingulate cortex shows fMRI response to internal and external error signals," *Nature Neuroscience*, vol. 7, no. 5, pp. 497-498, 2004.

[34] C. S. Carter, T. S. Braver, D. M. Barch, M. M. Botvinick, D. Noll, and J. D. Cohen, "Anterior cingulate cortex, error detection, and the online monitoring of performance," *Science*, vol. 280, no. 5364, pp. 747–749, 1998.

[35] C. S. Konen and S. Kastner, "Two hierarchically organized neural systems for object information in human visual cortex," *Nature Neuroscience*, vol. 11, no. 2, pp. 224–231, 2008.

[36] E. Freud, D. C. Plaut, and M. Behrmann, ""What" is happening in the dorsal visual pathway," *Trends in Cognitive Sciences*, vol. 20, no. 10, pp. 773–784, 2016.

[37] J. Hyvärinen, "Posterior parietal lobe of the primate brain," *Physiological Reviews*, vol. 62, no. 3, pp. 1060–1129, 1982.

[38] D. Swick and A. U. Turken, "Dissociation between conflict detection and error monitoring in the human anterior cingulate cortex," *Proceedings of the National Academy of Sciences of the United States of America*, vol. 99, no. 25, pp. 16354–16359, 2002.

[39] H. D. Critchley, J. Tang, D. Glaser, B. Butterworth, and R. J. Dolan, "Anterior cingulate activity during error and autonomic response," *Neuroimage*, vol. 27, no. 4, pp. 885–895, 2005.

[40] S. Makeig, "Auditory event-related dynamics of the EEG spectrum and effects of exposure to tones," *Electroencephalography and Clinical Neurophysiology*, vol. 86, no. 4, pp. 283–293, 1993.

[41] P. M. Fitts, "The information capacity of the human motor system in controlling the amplitude of movement," *Journal of Experimental Psychology*, vol. 47, no. 6, pp. 381–391, 1954.

[42] I. S. MacKenzie, "Fitts' law as a research and design tool in human-computer interaction," *Human-Computer Interaction*, vol. 7, no. 1, pp. 91–139, 1992.

[43] I. S. MacKenzie and C. Ware, "Lag as a determinant of human performance in interactive systems," in *Proceedings of the INTERACT'93 and CHI'93 Conference on Human Factors in Computing Systems*, pp. 488–493, Amsterdam, The Netherlands, April 1993.

[44] H. Kim, N. Yoshimura, and Y. Koike, "Characteristics of kinematic parameters in decoding intended reaching movements using electroencephalography (EEG)," *Frontiers in Neuroscience*, vol. 13, p. 1148, 2019.

Hindawi
Journal of Healthcare Engineering
Volume 2020, Article ID 1506250, 9 pages
https://doi.org/10.1155/2020/1506250

Research Article

Tip-Over Stability Analysis of a Pelvic Support Walking Robot

Yawei Han,[1] Shuai Guo ,[1] Leigang Zhang,[1] Fengfeng (Jeff) Xi,[2] and Weiwei Lu[3]

[1]*Department of Mechatronic Engineering and Automation, Shanghai University, Shanghai, China*
[2]*Department of Aerospace Engineering, Ryerson University, Toronto, Canada*
[3]*Shanghai Testing & Inspection Institute for Medical Devices, Shanghai, China*

Correspondence should be addressed to Shuai Guo; guoshuai@shu.edu.cn

Received 12 August 2019; Revised 21 November 2019; Accepted 23 December 2019; Published 7 February 2020

Guest Editor: Ludovico Minati

Discussed in this paper is the tip-over stability analysis of a pelvic support walking robot. To improve the activities of daily living (ADL) in hemiplegic patients, a pelvic support walking robot is proposed to help patients facilitating their rehabilitation. During the gait training with the robot, the abnormal man-machine interaction forces may lead to the tip-over of the robot, which is not beneficial to the rehabilitation process. A new method is proposed to predict the possibility of tipping over and evaluate the stability of the robot based on statics model, dynamics model, and zero-moment point (ZMP) theory. Through the interaction forces and moments analysis with static case, the safe point (ZMP) is studied, and the influence factors of force/moment are analyzed by dynamics case. An optimization algorithm based on the genetic algorithm (GA) is proposed to reduce the risk of tipping over. The simulation results show that the optimization algorithm can keep the robot from tipping over when the interaction forces exceed the safety threshold.

1. Introduction

As a result of the acceleration of population aging, the World Health Organization reported over 17 million confirmed cases of stroke in 2016 [1]. Most stroke patients suffer from lower-extremity motor dysfunction after surgery, which severely affects the ADL of the patient. However, ~70–80% of patients can benefit from the timely and effective rehabilitation process and can restore the motor function and balance function. During the gait training, the fall prevention and safe training environment are important. It is necessary to analyze the safety of the robot by the tip-over stability analysis.

In recent years, many universities, research institutes, and hospitals have developed mechanical equipment that can help the patients with the gait training. The Lokomat [2] is a highly automated suspension lower-limb rehabilitation robot that connects the lower-extremity exoskeleton system to the suspension weight reduction device through a four-bar mechanism. The robot is stationary and has little possibility of tipping over. The Andago [3] assisted rehabilitation robot developed by HOCOMA in Switzerland reduces the load on the lower limbs during the gait training by suspending weight loss on the pelvis. This suspension weight loss has a great influence on the coordinated movement of the upper and lower limbs. The designers avoid the tip-over by adding counterweight to the moving platform. The KineAssist [4] robot uses a pelvic support device with a moving platform to realize the movement of the patient, but the rotation center of the chassis is not on the same vertical line with the rotation center of the human body, directly affecting the patient's steering comfort. Carleton University developed a mobile limb training robot called GaitEnable [5]. This robot is smaller and lighter than KineAssist. It is a combination of a mobile lower-limb training robot and a walking robot. GaitEnable step trainer is omnidirectional. The device controls the support polygon of the robot, the position of the pelvis, and the posture of the robot. The GaitEnable and KineAssist are equipped with universal wheels to maintain stability via the change of the center of mass.

During the gait training, the man-machine interaction forces may exceed the normal values. There is a risk that the robot will tip over because the forces acting on the robot are beyond the safety threshold, causing potential harm to the patients. Based on this concerning, the tip-over stability of the robot should be analyzed to study the threshold of the interaction forces and the effective ways to stabilize the robot.

In this paper, the tip-over stability of a pelvic support walking robot, as shown in Figure 1, is analyzed: (1) the analysis of the safe range of interaction forces; (2) the analysis of the influence factors of tipping over; (3) the study of the optimization algorithm based on ZMP and GA.

2. System Description

The mechanical structure diagram of the robot is shown in Figure 2. Combining the revolute pair and the prismatic pair, the robot can realize the six degrees of freedom of motion in space: flexion and extension in the sagittal plane; adduction and abduction in the coronal plane; internal rotation and external rotation on the horizontal plane; and movement of the front, back, left, and right, and up and down. According the range of motion of healthy people [6, 7], the workspace of the robot is designed to be larger than the healthy people's need. Also, the rotation center of the robot should coincide with the people's rotation center to make the people more comfortable during the gait training.

The function of the robot is to provide the patients with pelvic support and help them during the gait training. This function is realized through the mobile platform (MP), the body weight support (BWS), and the pelvic-assisted mechanism (PAM). The PAM can support the patient and help them to realize the movement in cross section and the rotation around the sagittal axis, the vertical axis, and the coronal axis. The BWS can lift the pelvic support mechanism and patient to realize the movement in the vertical direction: the pelvis moves periodically along the vertical axis. With the help of the MP, the motion range of the patient can be extended throughout the environment.

As shown in Figure 2, the MP has two driving wheels installed on the rear to drive the mobile platform, and two universal wheels are installed at the front. With the differential motion of the two driving wheels, the robot can realize turning motion on the ground. And the robot can rotate around the center of two drive wheels' connection (around the Z-axis).

The BWS consists of a ball screw and a slider. The PAM is fixed at the slider, and the slider can move along the ball screw with low friction. The PAM can move along the Z-axis to adapt the motion of the pelvis.

The PAM provides support to the pelvis and can realize the motion of the pelvis. And the signals that needed to control the robot or evaluate the patient's movement are detected in this part.

The movement along the X-axis and Y-axis on the horizontal plane is realized by a four-bar mechanism as shown in Figure 2(b). The four-bar mechanism consists of four links. The rotation of J_2 will produce the movement of J_3 on the horizontal plane. A potentiometer is installed on J_2 to detect θ_2. The movement of J_3 can be calculated: $X = l_2 \cos\theta_2$, $Y = l_2 \sin\theta_2$. In order to provide elasticity in the direction of X-axis and Y-axis, a spring damping mechanism is installed between the four links. The forces will overcome the movement along the X-axis and Y-axis and make the patient know whether their pelvis center deviates from the normal position. The elasticity also can be adjusted according to different patients' needs. The rotation of J_4 realizes the rotation around the X-axis (the sagittal axis (α)). Springs are placed between J_4 and the fixed base of the pelvic support mechanism to provide elasticity around the X-axis. θ_4 can be detected by the potentiometer installed on J_4. P_5 and P_6 are prismatic pairs. When P_5 moves forward and P_6 moves backward, the patient will realize the rotation around the Z-axis (the vertical axis (γ)). The sliders of P_5 and P_6 are located between springs to provide elasticity along the Z-axis. The pressure sensors detect the force from patient's rotation acting on the spring. By analyzing the forces, the direction of the rotation along the Z-axis can be studied. Also, the movement of P_5 and P_6 can be calculated through the force F and spring stiffness k: $s = F/k$. And θ_5 can be calculated as: $\theta_5 \approx (S_5 - S_6)/D$ when θ_5 is small enough. Two universal joints are fixed at P_5 and P_6 to realize the rotation around the Y-axis (coronal axis (β)).

3. System Modeling and ZMP Theory

3.1. Statics Modeling. As shown in Figure 2, the robot coordinate system ($O_0X_0Y_0Z_0$) is fixed at the center of the connection of two driving wheels. The end-effector of the robot is the pelvis of patient, the $O_6X_6Y_6Z_6$ is attached. $O_iX_iY_iZ_i$ ($i = 1, 2, \ldots, 5$) is the joint coordinate system. The rotation center of the pelvis has to be consistent with the rotation center of the mechanism: $l_0 = l_1 + l_2 + l_3 + l_4$; During the gait training, the parameter Z_1 will change accordingly to realize the displacement in the Z-axis direction. The parallel four-bar mechanism composed of joints J_2 and J_3 realizes the X-axis and the displacement in the Y-axis direction: $X = l_2 \cos\theta_2$, $Y = l_2 \sin\theta_2$ (relative to the coordinate system $\sum 2$). The establishment of the positive solution matrix equation is based on the recursive formula proposed by Xi et al., which is as follows [8]:

$$\begin{aligned} \mathbf{p}_i &= \mathbf{p}_0 + \sum_{i=1}^{n} \mathbf{R}_i \mathbf{p}_i', \\ \mathbf{R}_i &= \prod_{j=1}^{i} \mathbf{R}_{sj} \mathbf{R}_{mj}, \end{aligned} \tag{1}$$

where

(i) $\mathbf{p}_i$ is the position of each joint relative to the world coordinate system;

(ii) $\mathbf{p}_i'$ is the position vector;

(iii) $\mathbf{R}_i$ is the rotation transformation matrix;

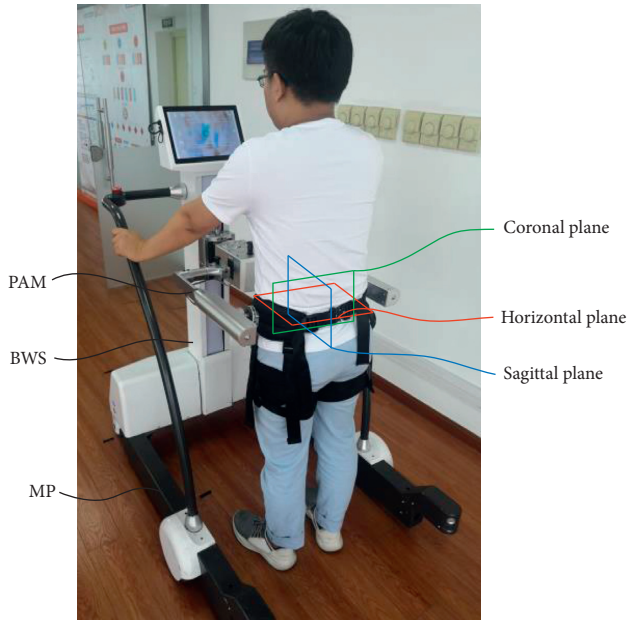

Figure 1: The components of the pelvic support walking robot. (a) The coordinate system. (b) The setting of the springs and sensors.

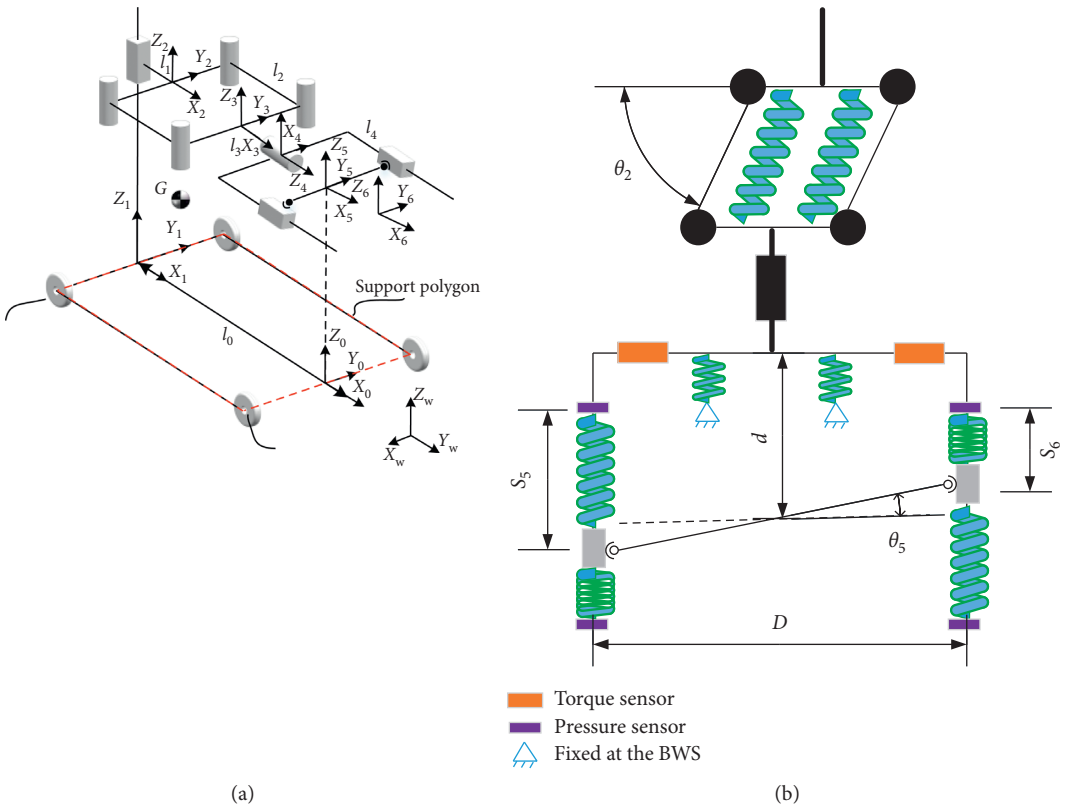

Figure 2: The schematic diagram of the mechanism.

(iv) $\mathbf{R}_{sj}$ is the coordinate transformation of the adjacent coordinate system;

(v) $\mathbf{R}_{mj}$ is the rotation around the current coordinate system, according to the mechanism diagram:

$$\begin{bmatrix} \mathbf{R} & \mathbf{P} \\ 0 & 1 \end{bmatrix} = \begin{bmatrix} C_5C_6 & -S_5 & C_5S_6 & T_1 \\ T_2 & C_4C_5 & T_3 & l_2S_2 \\ T_4 & C_5S_4 & T_5 & Z_0 \\ 0 & 0 & 0 & 1 \end{bmatrix}, \quad (2)$$

where

$C_2 = \cos\theta_2$, $S_2 = \sin\theta_2$, and so on; $T_1 = l_0 - l_1 - l_3 - l_2C_2 - l_4$; $T_2 = S_4S_6 + C_4S_5C_6$; $T_3 = C_4S_5S_6 - S_4C_6$; $T_4 = C_6S_4S_5 + C_4S_6$; $T_5 = C_4C_6 + S_4S_5S_6$.

$$\begin{bmatrix} v_x \\ v_y \\ v_z \\ \omega_x \\ \omega_y \\ \omega_z \end{bmatrix} = \begin{bmatrix} 0 & -l_2S_2 & 0 & 0 & 0 & 0 \\ 0 & l_2C_2 & 0 & 0 & 0 & 0 \\ 1 & 0 & 0 & 0 & 0 & 0 \\ 0 & 0 & 1 & 0 & 0 & 0 \\ 0 & 0 & 0 & 0 & 0 & 1 \\ 0 & 0 & 0 & \frac{1}{D} & -\frac{1}{D} & 0 \end{bmatrix} \begin{bmatrix} \dot{Z}_1 \\ \dot{\theta}_2 \\ \dot{\theta}_4 \\ \dot{S}_5 \\ \dot{S}_6 \\ \dot{\theta}_6 \end{bmatrix}, \quad (3)$$

where $D = 0.32$ m, as shown in Figure 2, is the width of the mechanism, which hugs the pelvis.

The center of mass of the link can be viewed as at the center of figure of the link. The vector of the ith link centroid position in the $\sum 0$:

$$\mathbf{p}_{ci} = \mathbf{p}_{i-1} + \frac{1}{2}\mathbf{p}_i = \mathbf{R}_i\mathbf{p}'_{ci}. \quad (4)$$

The centroid velocity of the ith link $\dot{p}_{ci}$ can be got by derivation on both sides of the equation:

$$\dot{p}_{ci} = \dot{R}_i\mathbf{p}'_{ci} + \mathbf{R}_i\dot{p}'_{ci} = \boldsymbol{\omega}_i \times \mathbf{p}_{ci} + \mathbf{R}_i\dot{p}'_{ci}. \quad (5)$$

The centroid acceleration of the ith link $\ddot{p}_{ci}$ can be got by derivation on both sides of equation (5):

$$\begin{aligned} \ddot{p}_{ci} &= \dot{\omega}_i \times \mathbf{p}_{ci} + \boldsymbol{\omega}_i \times \dot{p}_{ci} + \dot{R}_i\dot{p}'_{ci} + \mathbf{R}_i\ddot{p}'_{ci} \\ &= \dot{\omega}_i \times \mathbf{p}_{ci} + \boldsymbol{\omega}_i \times (\boldsymbol{\omega}_i \times \mathbf{p}_{ci} + \mathbf{R}_i\mathbf{p}'_{ci}) + \dot{R}_i\mathbf{R}_i^T\mathbf{R}_i\dot{p}'_{ci} + \mathbf{R}_i\ddot{p}'_{ci} \\ &= \dot{\omega}_i \times \mathbf{p}_{ci} + \boldsymbol{\omega}_i \times (\boldsymbol{\omega}_i \times \mathbf{p}_{ci}) + 2(\boldsymbol{\omega}_i \times \mathbf{R}_i\mathbf{p}'_{ci}) + \mathbf{R}_i\ddot{p}'_{ci}, \end{aligned} \quad (6)$$

where

(i) $\boldsymbol{\omega}_i$ is the joint angular velocity of ith link;

(ii) $\mathbf{p}_{ci}$ is the vector of the ith link centroid position in the $\sum 0$; $-\dot{p}'_{ci}$ is the velocity of ith link;

(iii) R_i is the transformation from $\sum 0$ to $\sum i$.

3.2. Dynamics Modeling. As the movement of the pelvis has great influence on the robot's tip-over stability, it is necessary to establish a dynamics model to research the motion parameters' effect on the robot's risk of tipping over.

According to Xi et al., the force and moment acting on the ith joint:

$$\mathbf{w}_i = \mathbf{M}_i\dot{t}_{iJ} + \mathbf{B}_i + \mathbf{H}_{ii+1}\mathbf{w}_{i+1}, \quad (7)$$

where

(i) $\mathbf{w}_i = \begin{bmatrix} \mathbf{f}_{iJ} & \mathbf{m}_{iJ} \end{bmatrix}$ consists of the force and moment of the ith joint;

(ii) $\mathbf{M}_i = \begin{bmatrix} \mathbf{m}_i 1 & \mathbf{m}_i\tilde{p}_{ic}^T \\ \mathbf{m}_i\tilde{p}_{ic} & \mathbf{I}_i \end{bmatrix}$ is the generalized mass matrix of the ith link;

(iii) $\tilde{p}_{ic}$ is the skew symmetric matrix of centroid vector of the ith joint;

(iv) $\mathbf{I}_i$ is the inertia tensor of each link;

(v) $\dot{t}_{iJ} = \begin{bmatrix} \ddot{p}_{ci} - \mathbf{g} \\ \boldsymbol{\alpha}_i \end{bmatrix}$ is the acceleration of the ith link;

(vi) $\mathbf{B}_i = \begin{bmatrix} m_i\boldsymbol{\omega}_i \times (\boldsymbol{\omega}_i \times \mathbf{p}_{ic}) \\ \boldsymbol{\omega}_i \times (\mathbf{I}_i\boldsymbol{\omega}_i) \end{bmatrix}$ consists of the centrifugal force and gyro moment;

(vii) ω_i is the angular velocity of the ith joint;

(viii) $\mathbf{p}_{ic}$ is the vector pointing from the center of the ith link to the ith joint;

(ix) $\mathbf{H}_{ii+1} = \begin{bmatrix} 1 & 0 \\ \tilde{p}_i & 1 \end{bmatrix}$ is the transformation matrix from $i+1$th joint to ith joint;

(x) $\mathbf{p}_i$ is the vector pointing from joint i to the tip;

(xi) $\tilde{p}_i$ is the antisymmetric matrix of $\mathbf{p}_i$.

All the forces and moments acting on the machine converted to joint i can be written as:

$$\begin{aligned} \mathbf{w}_i = \mathbf{M}_i\dot{t}_{iJ} + \sum_{k=i+1}^{5}\left(\prod_{j=k+1}^{k} H_{j-1,j}\right)\mathbf{M}_k\dot{t}_{kJ} + \mathbf{B}_i \\ + \sum_{k=i+1}^{5}\left(\prod_{j=k+1}^{k}\mathbf{H}_{j-1,j}\right)B_k + \left(\prod_{j=i+1}^{5}\mathbf{H}_{j-1,j}\right)\mathbf{w}_p, \end{aligned} \quad (8)$$

where w_p is the forces and moments between patient and robot.

3.3. ZMP Theory. The zero-moment point theory [9] is used to evaluate the tip-over stability by comparing the relative positional relationship between the ZMP and the support polygon. The component of the man-machine interaction forces and moments in the horizontal plane needs to be balanced by the friction and the friction torque:

$$(\overrightarrow{OP} \times \overrightarrow{R})^H + \overrightarrow{OG} \times m_s g + \mathbf{M}_A^H + \left(\overrightarrow{OA} \times \mathbf{F}_A\right)^H = 0, \quad (9)$$

$$\mathbf{R} + \mathbf{F}_A + m_s\mathbf{g} = 0, \quad (10)$$

where

(i) $\overrightarrow{OP}$ is the vector from the $\sum 0$ to the acting point of the friction force;

(ii) $\overrightarrow{R}$ is the friction force from the ground and can be calculated from equation (9);

(iii) G is the center of gravity of the robot.

The force $\mathbf{F}_A$ and moment $\mathbf{M}_A$ equals to the forces and moments above the $\sum 0$.

$$\begin{aligned}\mathbf{R}_x &= -(\mathbf{F}_{Ax} + m_s\mathbf{g}_x),\\ \mathbf{R}_y &= -\left(\mathbf{F}_{Ay} + m_s\mathbf{g}_y\right),\\ \mathbf{R}_z &= -(\mathbf{F}_{Az} + m_s\mathbf{g}_z).\end{aligned} \tag{11}$$

The position of the point P (P_x, P_y) (zero-moment point) can be calculated as:

$$\begin{aligned}P_x &= \frac{\left(\overrightarrow{OG} \times m_s\mathbf{g} + \mathbf{M}_A^H + \left(\overrightarrow{OA} \times \mathbf{F}_A\right)^H\right)_y}{\mathbf{R}_z},\\ P_y &= \frac{\left(\overrightarrow{OG} \times m_s\mathbf{g} + \mathbf{M}_A^H + \left(\overrightarrow{OA} \times \mathbf{F}_A\right)^H\right)_x}{\mathbf{R}_z},\\ P_z &= 0.\end{aligned} \tag{12}$$

The support polygon is made up of a rectangle. Once the P is out of the rectangle, the robot will lose dynamic equilibrium and tip over.

4. System Simulation and Optimization

The simulations are carried out to analyze the possibility of tipping over of the robot. The input is man-machine interaction forces. These forces can be measured and calculated:

$\mathbf{F}_x$ is the force generated by the movement of the patient along the X-axis. $\mathbf{F}_x$ can be measured by the pressure sensors as shown in Figure 2(b).

$\mathbf{F}_y$ is the force generated by the movement of the patient along the Y-axis. $\mathbf{F}_y$ can be calculated as follows:

$$\mathbf{F}_y = \Delta y K_{23}, \tag{13}$$

where Δy is the movement along the Y-axis, K_{23} is the spring damping stiffness between joint2 and joint3. K_{23} can be calculated through experiment. In this robot, $K_{23} = 3.9\,\text{N/mm}$.

$\mathbf{F}_z$ is the force generated by the movement of the patient along the Z-axis. $\mathbf{F}_z$ can be measured and calculated by the torque sensors as shown in Figure 2(b).

$$\mathbf{F}_z = \frac{T}{d}, \tag{14}$$

where T is the torque measured by the torque sensors. d is the distance between the torque sensors and the center of the pelvis.

The support polygon is a rectangle: $L * W$ $(1.03 * 0.7\,\text{m})$. The coinciding of the round reaction force acting point (P) with the center of the rectangle can be seen as the safest condition of the robot. Evaluation function Q can describe the relation between the two points. If P coincides with the center of the support polygon, the function Q is 1. When Q is closer to 1, the robot is safer and less likely to tip over. When Q is closer to 0, the robot is more likely to tip over. If P exceeds the support polygon boundary, the function Q will be negative.

$$Q = \begin{cases} \dfrac{\min\left(\left|P_x\right|, \left|P_x + (L/2)\right|\right)}{L} + \dfrac{\min\left(\left|P_y - (W/2)\right|, \left|P_y + (W/2)\right|\right)}{W}, & \text{when the ZMP}\left(P_x, P_y\right) \text{ is inside the support polygon,}\\ -1, & \text{when the ZMP}\left(P_x, P_y\right) \text{ is outside the support polygon.}\end{cases} \tag{15}$$

4.1. Static Simulation. An experiment is designed to study the range of $\mathbf{F}_x$, $\mathbf{F}_y$, and $\mathbf{F}_z$, when the subject falls over and leans on the machine. As shown in Figure 3, there are four cases when the subject leans on the robot and the 8 subjects involved with different height and weight. The result is shown in Table 1. The static calculation model can be got by making $\boldsymbol{\omega}_i = 0$, $\ddot{p}_{ci} = 0$, and $\boldsymbol{\alpha}_i = 0$ in the dynamic model. And so on, $\mathbf{B}_i = 0$ and $\dot{t}_{iJ} = \begin{bmatrix} -\mathbf{g} \\ 0 \end{bmatrix}$. The force and moment acting on the ith joint in the static model can be written as:

$$\mathbf{w}_i = \mathbf{M}_i \dot{t}_{iJ} + \sum_{k=i+1}^{5} \left(\prod_{j=k+1}^{k} \mathbf{H}_{j-1,j} \right) \mathbf{M}_k \dot{t}_{kJ} + \left(\prod_{j=i+1}^{5} \mathbf{H}_{j-1,j} \right) \mathbf{w}_p. \tag{16}$$

In the statics model, the parameter Z_0 is the height of the pelvis, and the range of Z_1 is from 0.55 m to 1.1 m. The simulations with different Z_1 are carried out. The results in Figure 4 show that the higher the Z_1 is, the more risk the robot with the same interaction force.

In order to analyze the safe range of the input forces, make $\mathbf{F}_x$: −450 N~300 N, $\mathbf{F}_y$: −200 N~300 N, $\mathbf{F}_z$: −350 N~350 N. Within the range of forces set, calculate Q with each force synthesized by $\mathbf{F}_x$, $\mathbf{F}_y$, and $\mathbf{F}_z$, and $Z_1 = 1.1\,\text{m}$. The calculation result is shown in Figure 5, and the force safety range: $\mathbf{F}_{XYZ} = [\mathbf{F}_X, \mathbf{F}_Y, \mathbf{F}_Z]^T$ is as follows:

$$\mathbf{F}_{XYZ} = \begin{cases} \mathbf{F}_Z \le 3.1\mathbf{F}_Y + 320, \mathbf{F}_Z \le 1.2\mathbf{F}_X + 180\\ \text{s.t. } 0 \le \mathbf{F}_Y \le 200, 0 \le \mathbf{F}_X \le 140,\\ \mathbf{F}_Z \le -3.1\mathbf{F}_Y + 320, \mathbf{F}_Z \le 1.2\mathbf{F}_X + 180\\ \text{s.t. } -200 \le \mathbf{F}_Y < 0, -400 \le \mathbf{F}_X \le 0. \end{cases} \tag{17}$$

The points with light color means that with the effect of the forces the point represents, the ZMP: P is within the

(a) (b) (c) (d)

Figure 3: The four cases that the subject leans on the robot. (a) The subject leans on the machine to the left; (b) the subject leans on the machine to the right; (c) the subject leans on the machine to the forward; (d) the subject leans on the machine to the backward.

Table 1: The force along the X-axis and Y-axis when the patient falls over.

Subject	Height (cm)	Weight (kg)	$+F_x$ (N)	$-F_x$ (N)	$+F_y$ (N)	$-F_y$ (N)
S1	178	73	130	140	130	130
S2	170	78	160	165	155	130
S3	178	65	130	130	120	125
S4	173	55	90	90	85	75
S5	173	60	140	130	110	90
S6	173	62	100	110	100	110
S7	173	68	120	120	120	120
S8	169	63	130	140	100	110
Average	173	66	125	128	115	111

support polygon. If the color is blue, the robot will tip over and the patient is in danger.

The analysis of the tip-over stability in the static condition provides reference for the analysis with dynamics model. The impact factors such as $\boldsymbol{\omega}_i$, $\boldsymbol{\alpha}_i$, $\ddot{p}_{ci}$, and so on will be considered, and a control system based on genetic algorithm (GA) [10, 11] is used to optimize the tip-over stability of the robot.

4.2. Dynamic Simulation. The simulation with dynamic model considers the effect from the ω_i(joint angular velocity) on the analysis of robot. The consideration of $\boldsymbol{\omega}_i$ makes $\mathbf{I}_i$ (the inertia tensor of ith link) become an important influencing factor:

$$\mathbf{B}_i = \begin{bmatrix} m_i\boldsymbol{\omega}_i \times (\boldsymbol{\omega}_i \times \mathbf{p}_{ic}) \\ \boldsymbol{\omega}_i \times (\mathbf{I}_i\boldsymbol{\omega}_i) \end{bmatrix}, \tag{18}$$

$$\mathbf{M}_i\dot{t}_{ij} = \begin{bmatrix} m_i 1 & m_i\tilde{p}_{ic}^T \\ m_i\tilde{p}_{ic} & \mathbf{I}_i \end{bmatrix} \begin{bmatrix} \ddot{p}_{ci} - \mathbf{g} \\ \boldsymbol{\alpha}_i \end{bmatrix}. \tag{19}$$

As can be seen from equations (18) and (19), the larger the $\boldsymbol{\omega}_i$ and $\mathbf{I}_i$ are, the larger the $\boldsymbol{\omega}_i$ is. According to the quality of each link and the motion pattern of each joint, $\boldsymbol{\omega}_2$ and $\boldsymbol{\omega}_4$ may have great influence on the tip-over stability of the robot. The results of the simulation about $\boldsymbol{\omega}_2$ and $\boldsymbol{\omega}_4$ are shown in Figures 6 and 7. Although the variation range of ω_2 and ω_4 is four times than the normal value, the results show that ω_2 and ω_4 have little influence on the forces and moments of last joint.

4.3. Optimization. According to the analysis above, the height of the pelvis: Z_1 has great influence on the tip-over stability of the robot. And other parameters such as ω_2 and ω_4 have little influence on the robot. Based on this, in the progress of the optimization, Z_1 and the movement along X-axis: ΔX will be adjusted to look for the best combination of Z_1 and ΔX to make Q nearest to 1.

The range of interaction force: $\mathbf{F}_{nxyz} = [\mathbf{F}_{nx}, \mathbf{F}_{ny}, \mathbf{F}_{nz}]$ when healthy people walks with the robot normally can be obtained from the study by Ji et al. [12].

According to the analysis in the static simulation, the safe range of the interaction force: $\mathbf{F}_X$ $\mathbf{F}_Y$ and $\mathbf{F}_Z$ is studied. Also, when the patient loses support and falls over, the interaction force: $\mathbf{F}_{xyz} = [\mathbf{F}_x, \mathbf{F}_y, \mathbf{F}_z]$ is beyond the safe range. In order to make sure the robot is safer during using, safety factor H is proposed to calculate the safety threshold of the interaction force:

$$\mathbf{F}_{XYZ} > \mathbf{F}_{sxyz} = \frac{\mathbf{F}_{XYZ}}{H} > \mathbf{F}_{nxyz}. \tag{20}$$

An optimization algorithm based on genetic algorithm (GA) is proposed to prevent the robot from tipping over and make the evaluation function Q nearest to 1. The control flow chart is shown in Figure 8. When the interaction force is beyond $\mathbf{F}_{sxyz}$, GA will calculate the optimal ΔZ_1 and ΔX. GA calculates the Q with different combinations of Z_1 and ΔX, and chooses Z_{Q1} and ΔX_Q as the best combination when Q is the maximum. And the signals will be sent to the motors to adjust the height of the pelvic and the position of the support polygon.

$$\begin{aligned} \underset{Z_{Q1},\Delta X_Q,Q}{\text{Maximize}} \quad & \text{GA}(Z_1, \Delta X, Q) \\ \text{s.t.} \quad & 0.55 \le Z_1 \le 1.1, \\ & -0.3 \le \Delta X \le 0.3. \end{aligned} \tag{21}$$

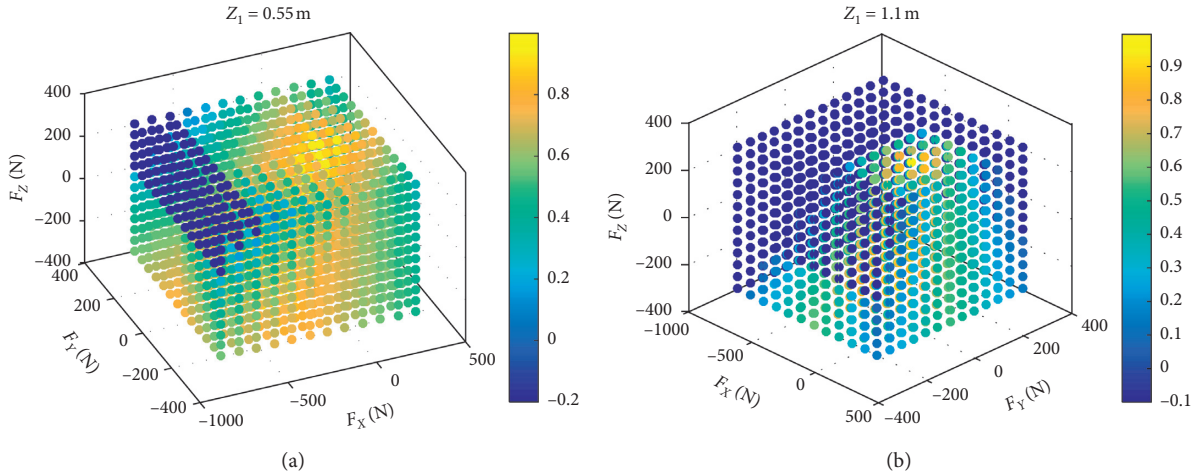

Figure 4: The relationship between the tip-over stability of the robot and the height of the pelvis: Z_1. Each point represents an interaction force: $\mathbf{F}_{xyz}$. The points with light color mean the robot will not tip over, and the points with blue color mean the robot will tip over. (a) The number of the safe points is 1898 with the $Z_1 = 0.55$ m. (b) The number of the safe points is 1225 with the $Z_1 = 1.1$ m.

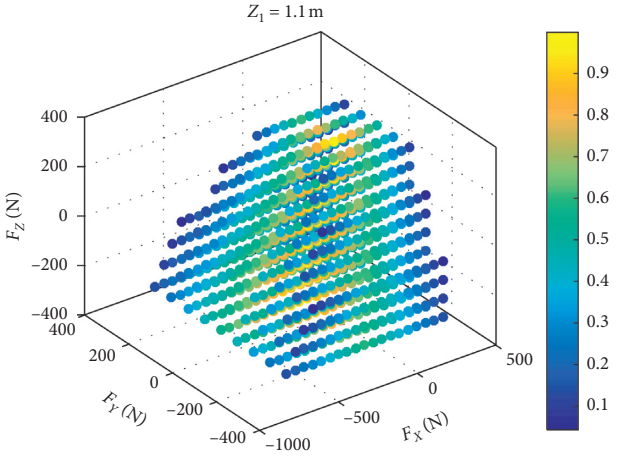

Figure 5: The safe range of F_{XYZ} with $Z_1 = 1.1$ m.

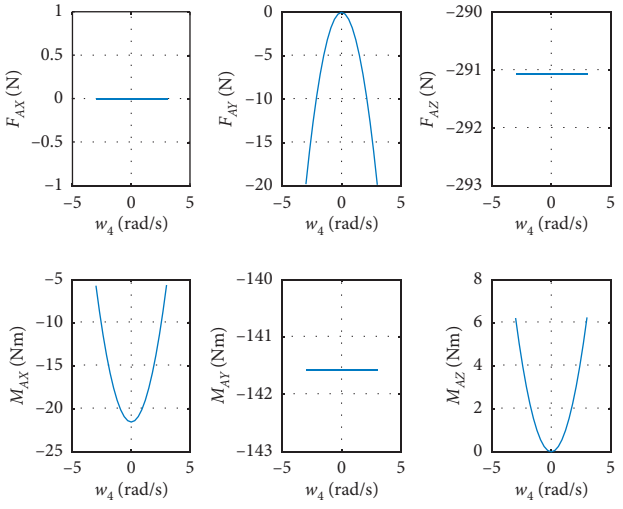

Figure 6: The influence of ω_2 on the forces: F_{Ax}, F_{Ay} and F_{Az} and the moments: M_{Ax}, M_{Ay} and M_{Az}.

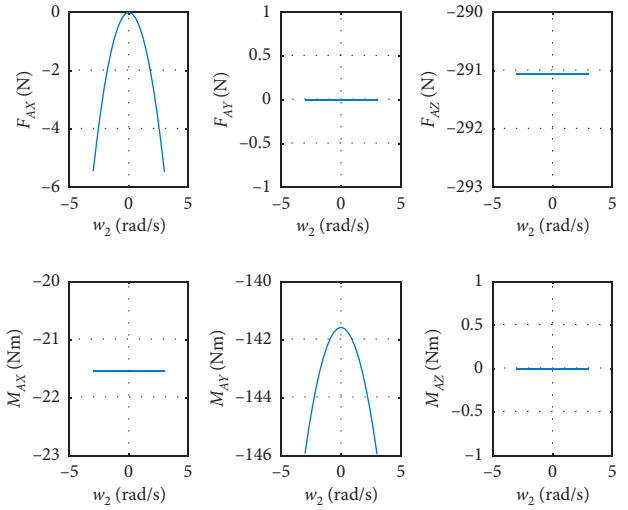

Figure 7: The influence of ω_4 on the forces: F_{Ax}, F_{Ay} and F_{Az} and the moments: M_{Ax}, M_{Ay} and M_{Az}.

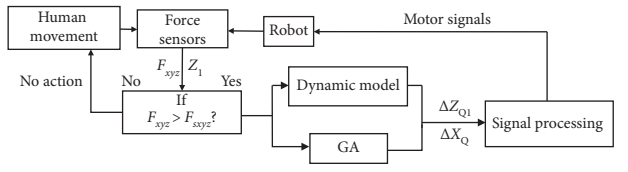

Figure 8: The control flow of the optimization algorithm.

4.4. Simulation. In order to ensure the safety of the subject, a simulation is carried to instead of an experiment. The results are shown in Figures 9 and 10. In Figure 9, without the optimization algorithm, the distribution of the zero-moment points: P is throughout the support polygon. And in Figure 10, with the optimization, all the points are distributed around the center of the center of the support polygon.

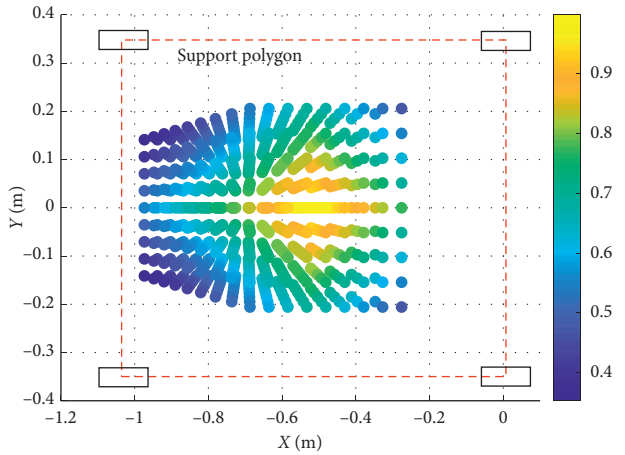

Figure 9: The distribution of P(ZMP) without the optimization algorithm.

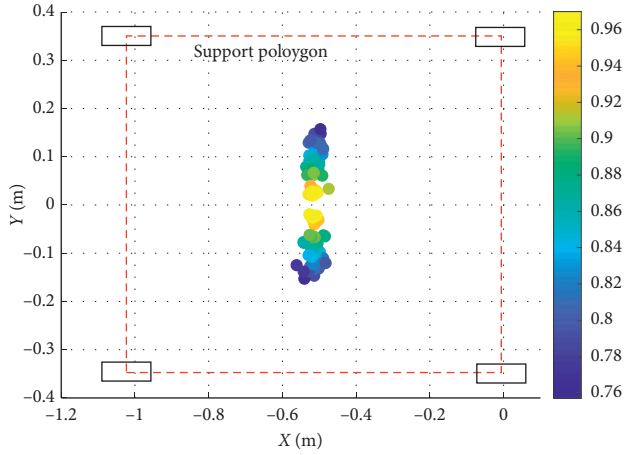

Figure 10: The distribution of P(ZMP) with the optimization algorithm.

4.5. Data Analysis and Discussion. The tip-over stability of the pelvic support walking robot is analyzed based on the statics model, the dynamics model, and the ZMP theory. Figure 3 shows the results of two simulations carried out with $\mathbf{F}_x$: −800 N~300 N, $\mathbf{F}_y$: −300 N~300 N, $\mathbf{F}_z$: −350 N~350 N. In Figure 4(a), with $Z_1 = 0.55$ m, the most points' Q is positive with light color. The number of safe points is 1898. In Figure 4(b), with $Z_1 = 1.1$ m, half of the points' Q is negative. The number of safe points is 1225. The results show that the height of the pelvis: Z_1 has great influence on the tip-over stability of the robot. The safe range of the interaction forces is studied in Figure 5 with $Z_1 = 1.1$ m. The safe range of $\mathbf{F}_y$ is symmetric around the Y-axis from −200 N to 200 N for that the robot is symmetry about the *xoz* plane. The safe range of $\mathbf{F}_x$ is from −400 N~140 N for that the center of mass position is at the front of the robot. The safe range of $\mathbf{F}_z$ is a function of $\mathbf{F}_x$ and $\mathbf{F}_y$ as shown in (17). The influence of $\boldsymbol{\omega}_2$ and $\boldsymbol{\omega}_4$ is analyzed, and the results are shown in Figures 6 and 7. It shows that the influence of ω_2 and ω_4 is not so obvious, for that the max variation of $\mathbf{F}_A$ and $\mathbf{M}_A$ is 15 N and 20 N·m, respectively. The optimization based on the GA and the influence factors: Z_1 and ΔX is proven to be effective in Figures 9 and 10. In Figure 9, without the optimization algorithm, the P(ZMP) is distributed throughout the support polygon. Some points' Q is close to 0.3, and the position is close to the boundary of the support polygon. With the interaction forces, these dangerous points represent the robot is likely to tip over. In Figure 10, the Q of these points is from 0.76 to 1, and the distribution of these points is limited to a rectangle: X: −0.58~−0.48; Y: −0.16~0.16. It means that with the optimization algorithm, the points whose interaction forces are beyond the safe range: $\mathbf{F}_{sxyz}$ are focused around the center of the support polygon with the adjustments of Z_1 and ΔX.

5. Conclusions

The tip-over stability analysis of a pelvic support walking robot was introduced in this paper, and an optimization algorithm was proposed to optimize the tip-over stability of the robot. The influence of the height of the pelvis and the safe range of the interaction forces were studied through the simulation with statics model. With the dynamics model, it was proven that the joint angular velocity such as ω_2 and ω_4 have little influence on the forces and moments of the last joint. An optimization algorithm based on the dynamics model and the GA was proposed to optimize the tip-over stability when the interaction forces are beyond the safe range. Simulations were carried to verify the effectiveness of the optimization system. The follow-up work will be concentrated on the improvement of the optimization algorithm to reduce the running time of the algorithm. Also, the counterweight of the robot can be optimized to improve the tip-over stability.

Appendix

Rotation Matrix

The rotation matrix referred in 3.1 kinematics modeling is shown as:

$$\mathbf{R}_{s0} = \begin{bmatrix} 1 & 0 & 0 \\ 0 & 1 & 0 \\ 0 & 0 & 1 \end{bmatrix}; \mathbf{P}_0' = \begin{bmatrix} -l_0 \\ 0 \\ 0 \end{bmatrix}; \mathbf{R}_{s1} = \begin{bmatrix} 1 & 0 & 0 \\ 0 & 1 & 0 \\ 0 & 0 & 1 \end{bmatrix};$$

$$\mathbf{P}_1' = \begin{bmatrix} Z_1 \\ 0 \\ Z_0 \end{bmatrix}; \mathbf{R}_{s2} = \begin{bmatrix} 1 & 0 & 0 \\ 0 & 1 & 0 \\ 0 & 0 & 1 \end{bmatrix}; \mathbf{P}_2' = \begin{bmatrix} l_2 C_2 \\ l_2 S_2 \\ 0 \end{bmatrix};$$

$$\mathbf{R}_{s3} = \begin{bmatrix} 1 & 0 & 0 \\ 0 & 1 & 0 \\ 0 & 0 & 1 \end{bmatrix}; \mathbf{P}_3' = \begin{bmatrix} l_3 \\ 0 \\ 0 \end{bmatrix}; \mathbf{R}_{s4} = \begin{bmatrix} 0 & 0 & 1 \\ 1 & 0 & 0 \\ 0 & 1 & 0 \end{bmatrix}; \quad \text{(A.1)}$$

$$\mathbf{R}_{m4} = \begin{bmatrix} C4 & -S4 & 0 \\ S4 & C4 & 0 \\ 0 & 0 & 1 \end{bmatrix}; \mathbf{P}_4' = \begin{bmatrix} 0 \\ 0 \\ l_4 \end{bmatrix}; \mathbf{R}_{s5} = \begin{bmatrix} 1 & 0 & 0 \\ 0 & 0 & 1 \\ 0 & -1 & 0 \end{bmatrix};$$

$$\mathbf{R}_{m5} = \begin{bmatrix} C5 & -S5 & 0 \\ S5 & C5 & 0 \\ 0 & 0 & 1 \end{bmatrix}; \mathbf{P}_5' = \begin{bmatrix} 0 \\ 0 \\ 0 \end{bmatrix}; \mathbf{R}_{s6} = \begin{bmatrix} 0 & 1 & 0 \\ -1 & 0 & 0 \\ 0 & 0 & 1 \end{bmatrix}.$$

Data Availability

The data used to support the findings of this study are available from the corresponding author upon request.

Conflicts of Interest

The authors indicated no potential conflicts of interest.

Acknowledgments

This work was supported by the National Key R&D Program of China (Grant No: 2018YFC2001600) and National Natural Science Foundation of China (Grant No: 61973205).

References

[1] World Health Organization, *WHO: Avoiding Heart Attacks and Strokes*, Vol. 23, WHO, Geneva, Switzerland, 2005.

[2] S. Jezernik, G. Colombo, T. Keller, H. Frueh, and M. Morari, "Robotic orthosis lokomat: a rehabilitation and research tool," *Neuromodulation: Technology at the Neural Interface*, vol. 6, no. 2, pp. 108–115, 2003.

[3] Andago: https://www.hocoma.com/solutions/andago/.

[4] J. Patton, D. A. Brown, M. Peshkin et al., "KineAssist: design and development of a robotic overground gait and balance therapy device," *Topics in Stroke Rehabilitation*, vol. 15, no. 2, pp. 131–139, 2008.

[5] A. Morbi, M. Ahmadi, and A. Nativ, "GaitEnable: an omnidirectional robotic system for gait rehabilitation," in *Proceedings of the International Conference on Mechatronics and Automation*, August 2012.

[6] F. Firmani and E. J. Park, "A framework for the analysis and synthesis of 3D dynamic human gait," *Robotica*, vol. 30, no. 1, pp. 145–157, 2012.

[7] J. Ji, S. Guo, F. Xi, and L. Zhang, "Design and analysis of a smart rehabilitation walker with passive pelvic mechanism," *Journal of Mechanisms and Robotics*, vol. 12, no. 3, 2020.

[8] F. Xi, "Inverse kinematics of free-floating space robots with minimum dynamic disturbance," *Robotica*, vol. 14, no. 6, pp. 667–675, 1996.

[9] M. Vukobratovi and B. Borovac, "Zero-moment point -thirty -five years of its life," *International Journal of Humanoid Robotics*, vol. 1, no. 1, pp. 157–173, 2004.

[10] M. D. Vose, *The Simple Genetic Algorithm*, MIT Press, no. 1, pp. 31–57, Cambridge, MA, USA, 1999.

[11] C.-L. Huang and C.-J. Wang, "A GA-based feature selection and parameters optimizationfor support vector machines," *Expert Systems with Applications*, vol. 31, no. 2, pp. 231–240, 2006.

[12] J. Ji, S. Guo, and F. Xi, "Force analysis and evaluation of a pelvic support walking robot with joint compliance," *Journal of Healthcare Engineering*, vol. 2018, Article ID 9235023, 12 pages, 2018.

Hindawi
Journal of Healthcare Engineering
Volume 2020, Article ID 5451219, 13 pages
https://doi.org/10.1155/2020/5451219

Research Article

Muscle Synergy and Musculoskeletal Model-Based Continuous Multi-Dimensional Estimation of Wrist and Hand Motions

Yeongdae Kim,[1] **Sorawit Stapornchaisit**,[1] **Hiroyuki Kambara**,[2] **Natsue Yoshimura**,[2,3] **and Yasuharu Koike**[2]

[1]*Department of Information and Communications Engineering, Tokyo Institute of Technology, Yokohama, Japan*
[2]*Institute of Innovative Research, Tokyo Institute of Technology, Yokohama, Japan*
[3]*PRESTO, JST, Saitama, Japan*

Correspondence should be addressed to Yasuharu Koike; koike@pi.titech.ac.jp

Received 27 September 2019; Revised 11 December 2019; Accepted 6 January 2020; Published 28 January 2020

Guest Editor: Yousun Kang

In this study, seven-channel electromyography signal-based two-dimensional wrist joint movement estimation with and without handgrip motions was carried out. Electromyography signals were analyzed using the synergy-based linear regression model and musculoskeletal model; they were subsequently compared with respect to single and combined wrist joint movements and handgrip. Using each one of wrist motion and grip trial as a training set, the synergy-based linear regression model exhibited a statistically significant performance with 0.7891 ± 0.0844 Pearson correlation coefficient (r) value in two-dimensional wrist motion estimation compared with 0.7608 ± 0.1037 r value of the musculoskeletal model. Estimates on the grip force produced 0.8463 ± 0.0503 r value with 0.2559 ± 0.1397 normalized root-mean-square error of the wrist motion range. This continuous wrist and handgrip estimation can be considered when electromyography-based multi-dimensional input signals in the prosthesis, virtual interface, and rehabilitation are needed.

1. Introduction

Owing to advances in surface electromyography (EMG) signal-based models and algorithms, numerous techniques have been proposed for prosthesis controls and clinical controllers. Though in a discreet fashion, several studies had attempted to convert hand motion into input signals to control prosthetic machines [1], virtual hands [2], and exoskeletons [3], with the aim of estimating both the wrist motion and hand gesture. Nishikawa et al. [1], Sebelius et al. [2], and Kita et al. [4] classified several gestures, such as hand gestures and wrist motions, using algorithms like machine learning, Gaussian mixture models (GMMs), and other linear classifiers (e.g., k-NN and Bayes).

Continuous estimations are applied in response to feedback from real users who require various movements suitable for daily life [5]. Vogel et al. [6] used standard supervised machine learning algorithms to create a mapping between arm/forearm muscle activities and 6-dimensional (6D) position/orientation; this has extended the four rotational degree-of-freedom (DOF) models for the joints of the shoulder and elbow [7]. An algorithm for simultaneous estimation of the three DOFs of the wrist was also proposed [8]; it showed promise of applicability to unilateral amputees by employing a bilateral mirror-training strategy [9]. However, these continuous estimations did not consider the combined motions of the wrist and fingers.

Under the flexor muscles are the multiple finger muscles that lie deep inside the forearm [10]. Many researchers use their expertise to minimize the interference of surface EMG (sEMG), without fully solving crosstalk. For this reason, the sEMG electrode is not free from the inclusion of both external and internal muscle signals. These mixed signals can influence the estimates obtained via the other.

Muscle synergy is defined as a set of muscles recruited by a neural command [11]. A muscle synergy generates a primitive motion, and complex motions are produced by the combination of several synergies [12, 13]. Real-time

classification for upper limb motion was conducted using a machine learning technique [14]. However, synergies were differentially weighted according to task constraints [15]; therefore, in this study, two different synergy calculations were attempts: deriving wrist and grip synergies simultaneously and deriving each synergy separately. Besides, synergy model performance with the change of synergy was analyzed, and the choice of number of wrist synergy was checked.

The musculoskeletal model (MSM) is a second-order computational motor control model with nonlinear dynamics. It estimates a one-degree-of-freedom joint angle for flexion and extension considering muscle elasticity and viscosity [16]. Kawase et al. [17] developed a simplified computational model that investigated the estimation of three different joint angles (i.e., elbow, wrist, and finger) with a little influence between finger joint and wrist position estimation.

To realize the prosthetic hand for daily use, wrist motion and grip motion have to be controlled simultaneously; however, few papers treat this problem [17] because of the crosstalk of muscle activation measurement.

This study aims to estimate wrist motion with and without grip motion and compared the estimation performance between optimized MSM and synergy models.

2. Materials and Methods

2.1. Subjects. Ten healthy subjects (males, aged 28.0 ± 5.7, 9 right-handed, 1 left-handed, none ambidextrous) participated in the experiment. They did not have a history of any form of neurological disorder. They used their dominant hand (either left or right hand) during the conduct of this experiment.

2.2. Experimental Protocol. The study protocol was approved by the ethics committee of the Tokyo Institute of Technology (2014042) and was carried out in accordance with the Declaration of Helsinki. Written consent was obtained from each subject before the experiment.

Table 1 indicates the muscle groups chosen to estimate the wrist and grip movements. Five muscles are associated with wrist motion (i.e., ECR, ECU, FCU, FCR, and APL) and two with grip action (i.e., FDS and FDP). Previous wrist-based experiments analyzed ECR, ECU, FCU, and FCR [17, 18], which are the flexor and extensor muscles of the wrist with different deviations (radial and ulnar). In addition to these muscles, in particular APL, an extensor of the thumb was included to trace the radial movement of the wrist. The FDS and FDP—the flexor muscles of the finger—were included to estimate the grip force with a synergy-based model.

Figure 1 shows the placement of the EMG sensor on the forearm. The EMG signals were measured using Trigno™ EMG system.

In the experiment, two tasks were conducted. The first task was a wrist motion, which measured motion in different movement conditions. For the second task, isometric grip force was measured in different grip force levels. Thus, the trials were divided into two tasks to check the wrist movement at a certain grip condition and grip force at a certain posture.

Table 1: Forearm muscle with channel number.

Muscle position	
Ch. 1	Extensor carpi radialis (ECR)
Ch. 2	Extensor carpi ulnaris (ECU)
Ch. 3	Flexor carpi ulnaris (FCU)
Ch. 4	Flexor carpi radialis (FCR)
Ch. 5	Abductor pollicis longus (APL)
Ch. 6	Flexor digitorum superficialis (FDS)
Ch. 7	Flexor digitorum profundus (FDP)

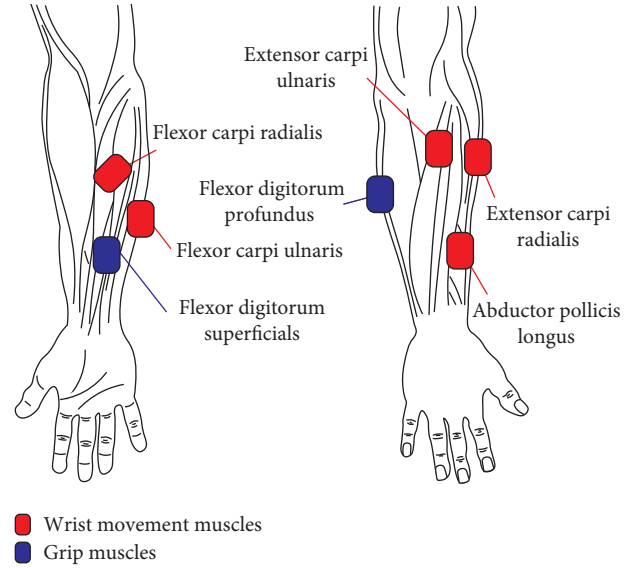

Figure 1: Seven EMG channel placement on five wrist joint-related muscles (red) and two grip muscles (blue).

In the first task, EMG was measured using wireless Trigno™ EMG system sensors, and wrist joint angles were measured using the IM sensors of the system. Figure 2 shows the placement of the IM sensors, which were attached to the back of the hand and the back of the forearm; they were attached to detect the relative wrist joint angle from the forearm.

Subjects placed their forearms on the table fastened by a wrist binder. Thereafter, they performed four wrist motions: flexion, extension, radial deviation, and ulnar deviation. These motions were conducted while the hand was free (no gripping action) and in gripping mode (normal strength). Wrist motions were conducted under three conditions based on the subject's comfort: comfortable maximum limit (with and without grip), half of comfortable maximum limit (without grip only), and stiffened movement with force exertion (without grip only). The subjects performed each motion three times per trial. Three trials were conducted for each condition. Thereafter, the gripping action (without wrist motion) was conducted in the center position (Figure 2) for which the subjects performed strong grips and weak grips. Three trials were conducted for the gripping experiment.

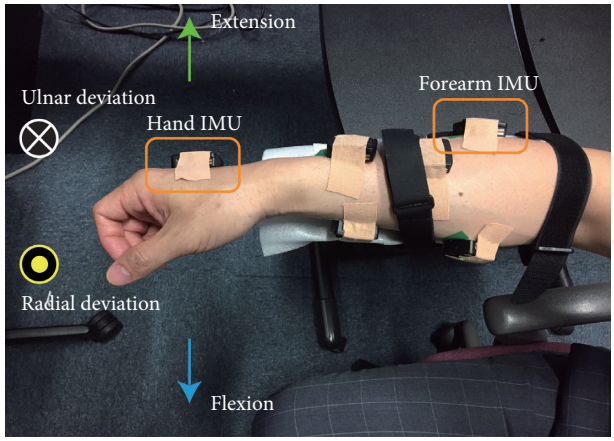

Figure 2: First task: experimental posture in the center-position and movement direction with the placement of the IMU sensors. Yellow-colored rectangles emphasize the positions of the IMU sensors placed at the back of the hand and forearm.

In the second task, EMG and grip force were measured, with the latter done using ReachMAN robot [19]. The subjects adjusted the angle of the grip to their best fit while maintaining a center position posture, as demonstrated in Figure 2, after which the grip force was measured. Three levels of grip strength were performed: strongest, half, and a quarter of gripping power. The strongest grip force (in newton N) varied for every subject with an average of 16.2 ± 3.2 N.

2.3. Data Acquisition. The data were sampled separately per signal category using lab streaming layer (LSL) in MATLAB 2018b program base [20]. The EMG signals were sampled at 2000 Hz, IMU sensors at 74 Hz, and ReachMAN force sensor at 100 Hz.

The seven EMG signal channels were filtered and normalized before computing the synergy set. The EMG signals were rectified and filtered using a second-order Butterworth low-pass filtering with 5 Hz cutoff frequency [21]. Figure 3 shows the conversion of an EMG signal. The filtered EMG signals are called "quasi-tension" because it showed a high correlation between the joint torques of its muscle [21].

A recurring issue during experiments and analyses was the fact that the magnitude of EMG signals for each channel had to be changed every time the sensor was detached then attached again. To resolve this, all signals were normalized by the peak activation level of the whole task, including a range of joint angles and maximum effort of trials [22]. Normalization was performed after quasi-tension signal filtering. In this experiment, the combined hand motion tasks, co-activating both grip and wrist motions, were chosen; hence, the normalized quasi-tension signals, which were obtained by filtering and normalizing the EMG signals, were resampled into the other sampling rates and measured together.

2.4. Wrist Angle Derivation. The Madgwick IMU algorithm was implemented to estimate the two-dimensional wrist joint angle [23]. IMU sensors were placed on the back of the hand and forearm to track the orientational difference between the hand and forearm.

Subjects performed self-paced movements without visual feedback; consequently, most of them performed diagonal movements even if only vertical and horizontal movements had been requested. To compensate for this, the two angles obtained by the IMU algorithm were normalized by each angle's absolute maximum value; the sum and difference obtained can be seen in Figure 4. In each model, these calculations were estimated and the summation was recalculated to estimate the angle; furthermore, considering the EMG crosstalk error and wide range of wrist angle movements, a comfortable maximum limit trial was mainly used as the train data.

2.5. Synergy-Based Linear Regression Model. A synergy-based linear regression model was used to estimate wrist and grip values. To reduce computational costs in a model calculation, a simplified version of the nonnegative matrix method, i.e., the hierarchical alternating least square (HALS) method, was used [24]. Apart from the computational cost, HALS also has a wide capability: it can work with a large number of components [24], in contrast to the canonical NMF method [25], which is only applicable if the number of the sources is greater than the number of components; it can work in conditions where the number of components is large [24]. This feature of HALS is appropriate when multiple hand gestures need to be applied. Hence, this computation method is valid even when the number of combined synergy set exceeds the number of measured EMG signals. The HALS decomposes the normalized quasi-tension as follows:

$$[E] = [M][S]^{\mathrm{T}}, \tag{1}$$

where E is the normalized quasi-tension signals in an m by n matrix with m being the number of time series and n the number of EMG channel inputs; $S = [s_1, \ldots, s_j]$ is the synergy set, where j is the number of synergies and $s_j = [c_1, \ldots c_n]^{\mathrm{T}}$ representing a single set of synergy, where c_n is the coactivation coefficient of EMG n; and furthermore, M is the coactivation coefficients of the synergy in m by j matrix:

$$[S_k] \leftarrow [S_k] + \frac{\left([E][M]^{\mathrm{T}} - [S][M][M]^{\mathrm{T}}\right)_k}{[M_k][M_k]^{\mathrm{T}}}, \tag{2}$$

$$[M_k] \leftarrow [M_k]^{\mathrm{T}} + \frac{\left([E]^{\mathrm{T}}[S] - [M]^{\mathrm{T}}[S]^{\mathrm{T}}[S]\right)_k}{[S_k]^{\mathrm{T}}[S_k]}. \tag{3}$$

When the synergy model is derived, learning algorithm procedures are used to iterate (2) and (3) several times, where k (1, 2, …, j) denotes the label of synergies. The matrices S and M were computed using one set of single wrist motion data and single grip motion data.

In the analysis, wrist synergies with varying numbers from one to six were calculated from a wrist movement trial to confirm the validity number of synergies; thereafter, a single grip synergy was taken from a grip trial. More often

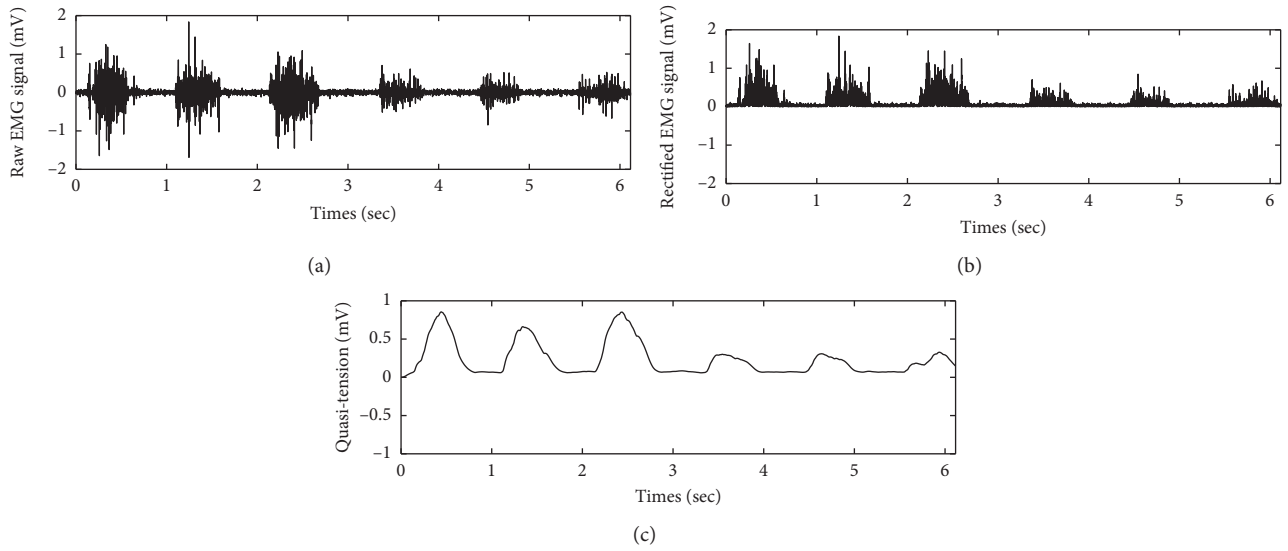

Figure 3: Quasi-tension data filtering process. The low-pass filter was the second-order Butterworth filter with 5 Hz cutoff frequency. (a) Raw EMG signal. (b) Rectified EMG signal. (c) Low-pass filtered EMG signal.

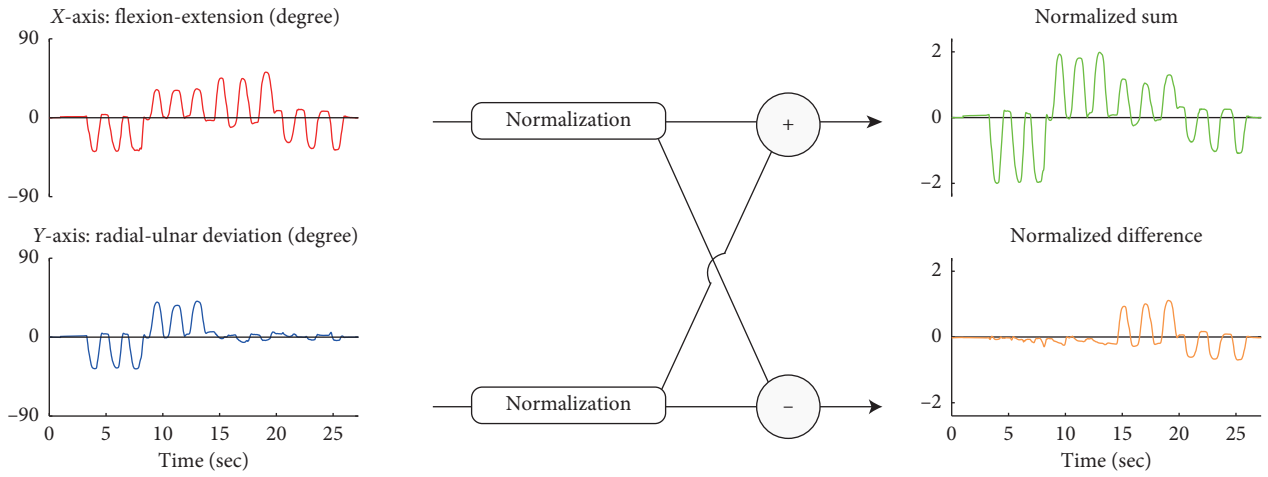

Figure 4: (EPS cross needed) X-axis stands for flexion-extension dimension, while Y-axis stands for radial-ulnar deviation. To compensate for the inclined diagonal movement of subjects in self-paced movement, two angles were normalized and their sum and difference were subsequently computed.

than note, the variance account for (VAF) became the standard means of choosing the muscle synergy number [26–28]. In the same context, this study applies the number of synergies that matches over 0.9 VAF to all the subjects to ensure the synergy model consistency. The gains of the wrist motion synergy for the angles were derived using linear regression to compute the normalized sum and difference of the wrist angle (flexion-extension, radial-ulnar deviation) θ_i from the following equation:

$$\theta_i = a_{0,i} + a_{j,i} m_j + \cdots + \varepsilon, \tag{4}$$

where $a_{0,i}$ denotes the angle bias, $a_{j,i}$ s are the regression coefficients for each synergy coefficient m_j, and ε denotes the random noise error. A combined synergy set with regression coefficients were used to estimate both grip motion and wrist motion task; hence, the synergies and gains from a combination of two trials were applied to all other tasks.

The computation of the wrist and grip synergies was conducted in two different ways. A facial image study showed that NMF learns the object in part-based representation [29]. In the case of grip motion, the muscles of all channels work together; therefore, multitrial-based muscle synergy was calculated in two ways: simultaneously from jointed wrist and grip trials (SLRM1) and separately per trial (SLRM2). The synergy sets were derived from comfortable maximum limit trials and grip trials.

2.6. Musculoskeletal Model (MSM). The musculoskeletal model was used to compare the angle estimates of the synergy-based model. The MSM succeeded in estimating the

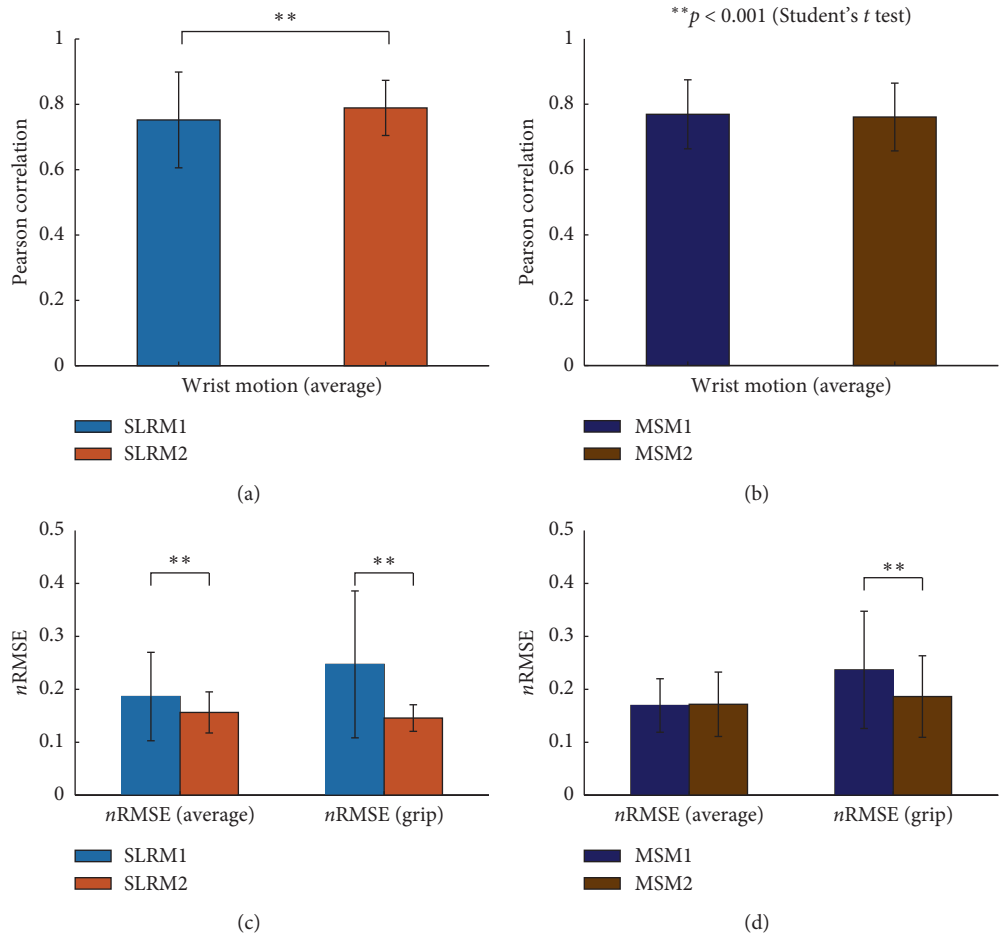

Figure 5: Model condition-related wrist joint movement estimation performance changes in the synergy-based linear regression model (SLRM) and musculoskeletal model (MSM) in terms of the Pearson correlation coefficient (r) and normalized root-mean-square error (nRMSE). (a) r of SLRM2 had statistically significant differences with SLRM1 ($p < 0.001$, Student's t-test). (b) There was no statistically significant change in r between MSM1 and MSM2. (c) nRMSE of SLRM1 and SLRM2 had statistically significant differences both in wrist average and grip motion with higher error in SLRM1. (d) There was no statistically significant change in the nRMSE for wrist motion trials between MSM1 and MSM2 while having a significant difference in grip. ($p < 0.001$, Student's t-test).

joint angles of the elbow, wrist, and index finger with little influence from a change in wrist position [17]. The performances of SLRM and MSM were compared with each other to ascertain how good that of SLRM is; furthermore, the train set of MSM was taken from a comfortable maximum limit, which are the same trials used in SLRM. To optimize the MSM performance, MSM was derived from two different muscle numbers, namely, MSMS1 and MSMS2; the former used all measured muscles, while the latter used five wrist muscles. Kawase et al. constructed a one-degree-of-freedom model per joint [17]; to fit the model into this experiment, two wrist joint angles were converted as depicted in Figure 4.

2.6.1. Statistical Analysis. An exhaustive cross-validation was used to test the performance of each model per subject, with indices used to estimate performance. The Pearson correlation coefficient (r) and normalized root-mean-square error (nRMSE) are defined as follows:

$$r = \frac{\Sigma_{i=1}^{n}(x_i - \overline{x})(y_i - \overline{y})}{\sqrt{\Sigma_{i=1}^{n}(x_i - \overline{x})^2}\sqrt{\Sigma_{i=1}^{n}(y_i - \overline{y})^2}},$$
$$\text{nRMSE} = \frac{1}{a}\sqrt{\frac{\Sigma_{i=1}^{n}(x_i - y_i)^2}{n}}, \tag{5}$$

where n is the number of samples, y is a reference, x is an estimate, and a is defined as the normalization coefficient. nRMSE chooses a to be 90, the limit of the wrist angle range. All statistical analyses were conducted using t test2 function of MATLAB 2018b.

3. Results

3.1. Synergy Number Optimization. The reproducibility check of SLRM1 and SLRM2 in the different number of synergies was tested in VAF. The number of grip synergies was fixed to one, both in SLRM1 and SLRM2 to ensure that SLRM1 computed the synergy one more from the joint trials.

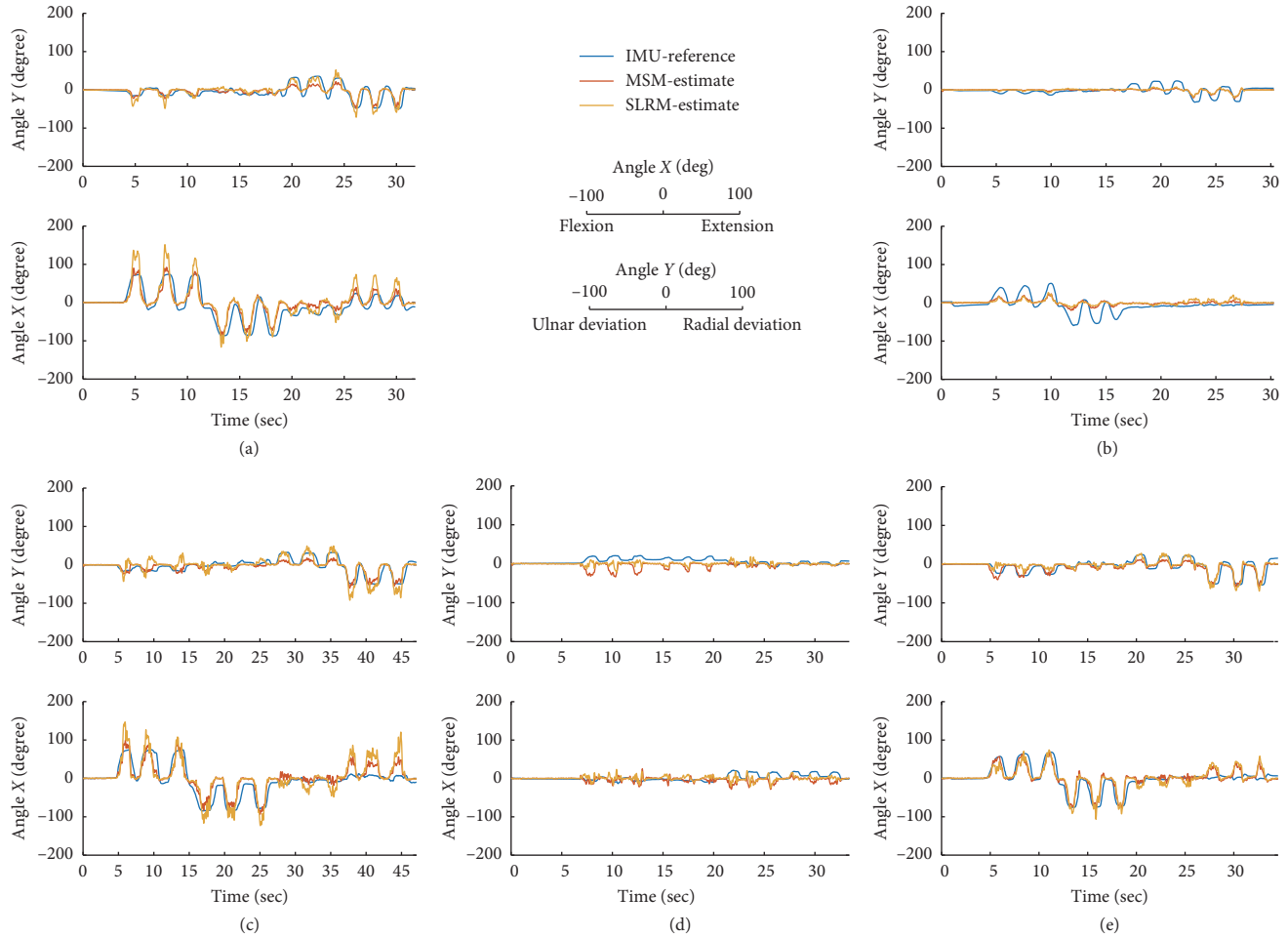

Figure 6: 2D wrist joint angle estimation in 5 different trials. Angle X corresponds to flexion-extension dimension taking extension as positive. Angle Y corresponds to radial-ulnar deviation having radial deviation as positive. The blue-colored line represents the IMU-reference angle derived from two IMU sensors by differentiating relative orientation in the Euler angle. The red-colored estimate is a musculoskeletal model- (MSM-) based estimation having 5 input signals. Yellow-colored estimate stands for synergy-based linear regression model- (SLRM-) based estimation deriving synergy derived separately per trial. An example of (a) a comfortable maximum limit trial, (b) half of a comfortable maximum trial, (c) a stiffened movement trial, (d) a grip-trial having twelve times gripping, and (e) combined movement of a comfortable maximum limit with grip.

SLRM1 with two wrist synergies had over 0.9 VAF on average (0.9342 ± 0.0245), and the minimum VAF of three wrist synergies was 0.9529. For SLRM2, three wrist synergies had over 0.9 VAF on average (0.9442 ± 0.0340), and the minimum VAF of four wrist synergies was 0.9647. To include all subjects, four wrist motion synergy numbers were chosen and used throughout the study.

3.2. Task 1: Wrist Motion Test. Figures 5(a) and 5(c) show the r and nRMSE values of SLRMs in wrist motion task. The r values of SLRM1 and SLRM2 were 0.7523 ± 0.1466 and 0.7891 ± 0.0844, respectively. For nRMSE, SLRM1 had 0.1864 ± 0.0835 in wrist motion and 0.2471 ± 0.1387 in grip motion, while SLRM2 had 0.1564 ± 0.0388 in wrist motion and 0.1458 ± 0.0251 in grip motion. The differences are statistically significant in both cases ($p < 0.001$, Student's t-test). From the results, SLRM2 was chosen as the representative SLRM model.

Similarly, Figures 5(b) and 5(d) show the r values and nRMSE values of the MSMs in wrist motion task. The r values of MSM1 and MSM2 were 0.7691 ± 0.1056 and 0.7608 ± 0.1037, respectively, which exhibits no statistical significance. For nRMSE, MSM1 had 0.1695 ± 0.0505 in wrist motion and 0.2368 ± 0.1107 in grip motion, while MSM2 had 0.1718 ± 0.0608 in wrist motion and 0.1864 ± 0.0770 in grip motion. The nRMSE of the grip motion implies a statistical significance ($p < 0.001$, Student's t-test). From the results, MSM2 was chosen as the representative MSM model.

The time series of the wrist angle in two dimensions is shown in Figure 6. Subjects were asked to rotate their wrists in four directions. They were able to move freely at their own pace, moving in an inclined diagonal direction at different angles. Because of this tendency, both models appear to have the underlying assumption that a subject moved in a diagonal direction even if they performed a gradual movement, as shown in Figure 6(c).

Table 2: MSM performance indicator per subjects and trial.

Sub	Data type	Comfortable max		Comfortable half		Stiffened movement		Grip and motion		Wrist motion (average)		Grip
		r	nRMSE	*r*	nRMSE	*r*	nRMSE	*r*	nRMSE	*r*	nRMSE	nRMSE
Sub1	*Mean*	0.8542	0.1544	0.7297	0.1256	0.8818	0.1882	0.8092	0.1742	0.8155	0.1612	0.1287
	SD	0.0218	0.0167	0.0725	0.0123	0.0156	0.0348	0.0661	0.0315	0.0805	0.0371	0.0214
Sub2	*Mean*	0.8527	0.1024	0.7626	0.0719	0.8362	0.1666	0.7300	0.0971	0.7902	0.1101	0.1468
	SD	0.0286	0.0140	0.0478	0.0103	0.0361	0.0161	0.1813	0.0334	0.1107	0.0429	0.0279
Sub3	*Mean*	0.6816	0.1699	0.5557	0.1291	0.7094	0.2084	0.6722	0.1704	0.6523	0.1694	0.1400
	SD	0.0475	0.0214	0.1039	0.0195	0.0590	0.0322	0.0616	0.0220	0.0968	0.0407	0.0608
Sub4	*Mean*	0.8261	0.2113	0.7196	0.1196	0.8178	0.2593	0.8278	0.1820	0.7952	0.1914	0.0975
	SD	0.0503	0.0371	0.0587	0.0185	0.0603	0.0415	0.0431	0.0235	0.0746	0.0646	0.0594
Sub5	*Mean*	0.8156	0.1451	0.6870	0.1091	0.8174	0.2170	0.7497	0.2104	0.7630	0.1727	0.3005
	SD	0.0835	0.0342	0.1324	0.0163	0.0526	0.0422	0.0604	0.0401	0.1019	0.0581	0.1109
Sub6	*Mean*	0.8364	0.1998	0.6855	0.1940	0.8003	0.2613	0.8055	0.1934	0.7770	0.2132	0.1741
	SD	0.0273	0.0281	0.1028	0.0140	0.0651	0.0351	0.0447	0.0271	0.0928	0.0425	0.0479
Sub7	*Mean*	0.6775	0.2235	0.4702	0.1338	0.6994	0.2258	0.6742	0.1793	0.6261	0.1876	0.5055
	SD	0.0697	0.0205	0.1268	0.0113	0.1093	0.0370	0.0790	0.0243	0.1386	0.0480	0.1803
Sub8	*Mean*	0.8078	0.1333	0.6616	0.1104	0.8478	0.1524	0.7541	0.1578	0.7642	0.1389	0.4311
	SD	0.0613	0.0278	0.0992	0.0150	0.0405	0.0214	0.0474	0.0293	0.1070	0.0330	0.0778
Sub9	*Mean*	0.8688	0.1823	0.8637	0.1260	0.8807	0.1801	0.8537	0.1549	0.8665	0.1588	0.3206
	SD	0.0443	0.0298	0.0420	0.0096	0.0256	0.0227	0.0407	0.0210	0.0425	0.0315	0.1702
Sub10	*Mean*	0.7728	0.1915	0.7087	0.1361	0.8517	0.2392	0.7024	0.2844	0.7576	0.2147	0.1750
	SD	0.0302	0.0501	0.0927	0.0436	0.0363	0.1044	0.1091	0.1058	0.1057	0.1006	0.0817
Mean	*Mean*	0.7994	0.1713	0.6844	0.1256	0.8142	0.2098	0.7579	0.1804	0.7608	0.1718	0.1864
	SD	0.0528	0.0343	0.1022	0.0219	0.0589	0.0558	0.0877	0.0511	0.1037	0.0568	0.0770

Table 3: SLRM performance indicator per subjects and trial.

Sub	Data type	Comfortable max		Comfortable half		Stiffened movement		Grip and motion		Wrist motion (average)		Grip
		r	nRMSE	*r*	nRMSE	*r*	nRMSE	*r*	nRMSE	*r*	nRMSE	nRMSE
Sub1	*MeanSD*	0.8847	0.1368	0.7850	0.1155	0.8618	0.1738	0.8625	0.1313	0.8452	0.1396	0.1121
		0.0173	0.0137	0.0508	0.0120	0.0269	0.0291	0.0207	0.0158	0.0527	0.0299	0.0162
Sub2	*Mean SD*	0.8868	0.0925	0.7801	0.0640	0.8778	0.1425	0.7860	0.0831	0.8277	0.0958	0.1207
		0.0200	0.0148	0.0251	0.0073	0.0391	0.0166	0.1166	0.0184	0.0867	0.0339	0.0098
Sub3	*Mean SD*	0.6643	0.1658	0.5037	0.1205	0.7749	0.1704	0.4568	0.1750	0.5941	0.1572	0.0620
		0.0215	0.0129	0.0865	0.0104	0.0291	0.0098	0.0691	0.0128	0.1457	0.0274	0.0088
Sub4	*Mean SD*	0.8430	0.1858	0.7368	0.1355	0.8460	0.2094	0.7756	0.1769	0.7965	0.1761	0.1157
		0.0178	0.0176	0.0661	0.0166	0.0208	0.0239	0.0305	0.0103	0.0654	0.0341	0.0189
Sub5	*Mean SD*	0.8368	0.1444	0.7698	0.1001	0.8321	0.2390	0.7598	0.2403	0.7963	0.1843	0.0888
		0.0291	0.0166	0.0335	0.0069	0.0380	0.0238	0.0467	0.0425	0.0603	0.0727	0.0191
Sub6	*Mean SD*	0.8233	0.1997	0.7483	0.1935	0.8546	0.2118	0.8364	0.1783	0.8149	0.1955	0.2236
		0.0266	0.0179	0.0848	0.0074	0.0228	0.0155	0.0216	0.0169	0.0665	0.0215	0.0432
Sub7	*Mean SD*	0.8009	0.1622	0.7162	0.1328	0.7955	0.1767	0.6393	0.1762	0.7323	0.1620	0.1653
		0.0256	0.0068	0.1374	0.0076	0.0448	0.0178	0.0997	0.0251	0.1135	0.0272	0.0285
Sub8	*Mean SD*	0.8573	0.1155	0.8210	0.0873	0.8571	0.1523	0.7960	0.1474	0.8306	0.1266	0.2876
		0.0243	0.0115	0.0541	0.0133	0.0320	0.0193	0.0454	0.0316	0.0547	0.0358	0.0503
Sub9	*Mean SD*	0.8417	0.1788	0.8240	0.1380	0.8316	0.1901	0.8196	0.1606	0.8281	0.1658	0.1037
		0.0249	0.0225	0.0324	0.0033	0.0309	0.0205	0.0402	0.0158	0.0369	0.0271	0.0233
Sub10	*Mean SD*	0.8170	0.1576	0.7754	0.1162	0.8745	0.1863	0.8302	0.1848	0.8249	0.1616	0.1969
		0.0329	0.0227	0.0232	0.0049	0.0250	0.0270	0.0265	0.0363	0.0618	0.0417	0.0299
Mean	*Mean SD*	0.8256	0.1539	0.7460	0.1204	0.8406	0.1852	0.7562	0.1654	0.7891	0.1564	0.1458
		0.0270	0.0178	0.0731	0.0106	0.0344	0.0216	0.0631	0.0271	0.0844	0.0382	0.0251

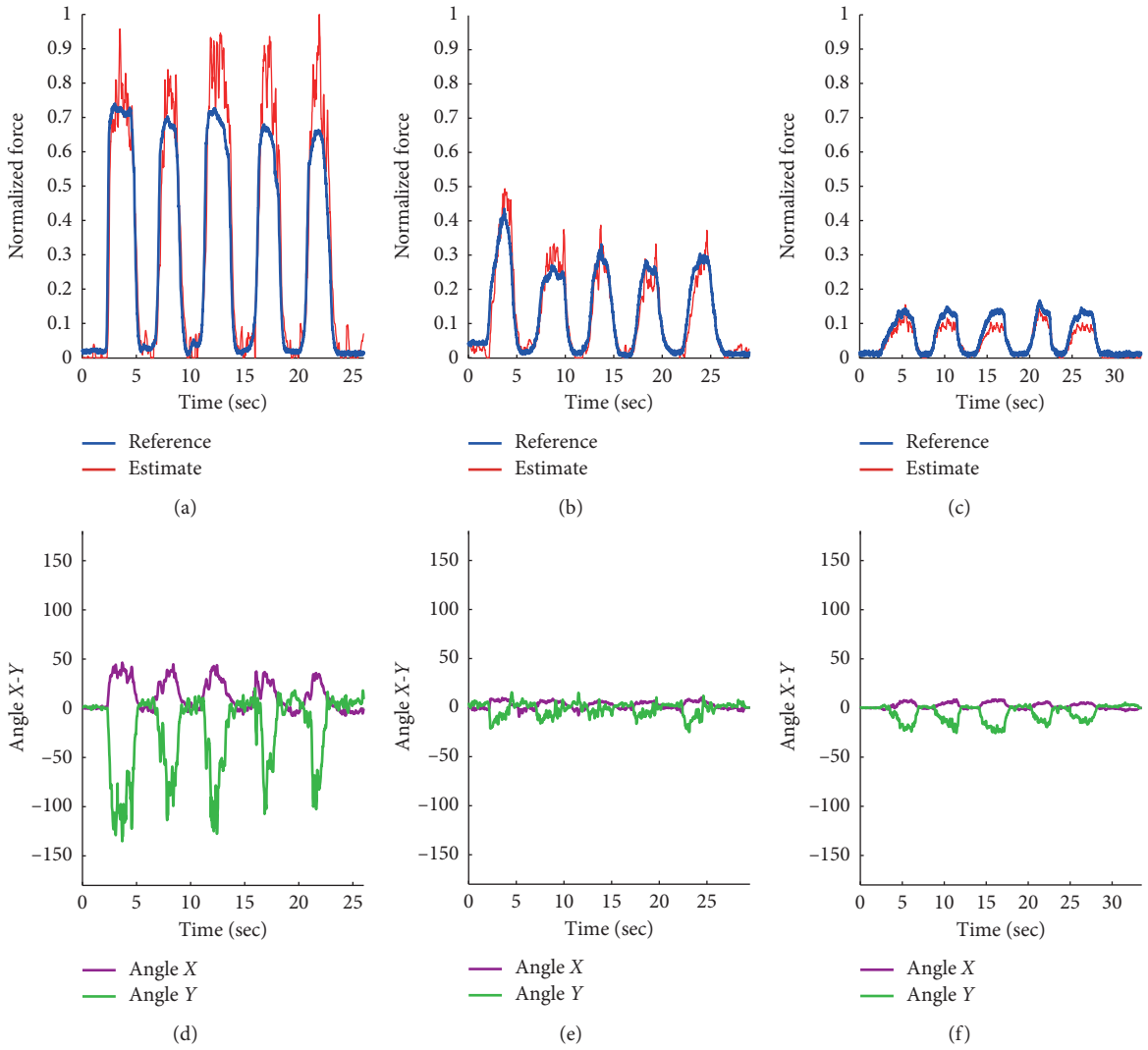

Figure 7: Time series estimation of grip task with ReachMAN robot. Time series for (a) the normalized max grip force reference and synergy-based linear regression (SLRM) grip force estimate, (b) the normalized half grip force reference and synergy-based linear regression (SLRM) grip force estimate, (c) the normalized quarter grip force reference and synergy-based linear regression (SLRM) grip force estimate, (d) wrist joint motion estimate from SLRM in the maximum grip force task, (e) wrist joint motion estimate from SLRM in half grip force task, and (f) wrist joint motion estimate from SLRM in quarter grip force task. Angle X-Y is the same axis in Figure 8.

The exact performances of SLRM and MSM in r and nRMSE are shown in Tables 2 and 3. Wrist motion performances r on average are 0.7891 ± 0.0844 in SLRM and 0.7608 ± 0.1037 in MSM, implying a statistically significant difference ($p < 0.001$, Student's t-test). Similarly, nRMSE also shows a significant difference between SLRM and MSM ($p < 0.01$, Student's t-test). This trend continued during wrist motion trials without a grip (comfortable maximum limit trial, comfortable half limit trial, and stiffened movement trial).

However, when grip motion was added, there was no statistically significant difference in r; however, differences were still apparent in nRMSE. The r of the comfortable maximum with grip trials were 0.7562 ± 0.0631 in SLRM and 0.7579 ± 0.0877 in MSM, and nRMSEs were $0.1654 \pm 0.0.271$ in SLRM and 0.1804 ± 0.0511 in MSM ($p < 0.001$, Student's t-test). Finally, in the grip trial, where r measurement was inappropriate because the wrist motion in the trial is just an indication of a perturbation, here, SLRM had 0.1458 ± 0.0251 and MSM had 0.1864 ± 0.0770 in nRMSE, implying a statistically significant difference ($p < 0.001$, Student's t-test).

In detail, the r values of the comfortable maximum limit trials were 0.8256 ± 0.0270 in SLRM and 0.7994 ± 0.0528 in MSM ($p < 0.001$, Student's t-test); the nRMSEs were 0.1539 ± 0.0178 in SLRM and 0.1713 ± 0.0343 in MSM ($p < 0.001$, Student's t-test). In comfortable half limit trials, the corresponding values were 0.7460 ± 0.0731 in SLRM and 0.6844 ± 0.1022 in MSM when measuring r values ($p < 0.001$, Student's t-test), and the nRMSEs were 0.1204 ± 0.0106 in SLRM and 0.1256 ± 0.0219 in MSM ($p < 0.01$, Student's t-test). The stiffened movement trials also had the same trend in r values, being 0.8406 ± 0.0344 in SLRM and 0.8142 ± 0.0589

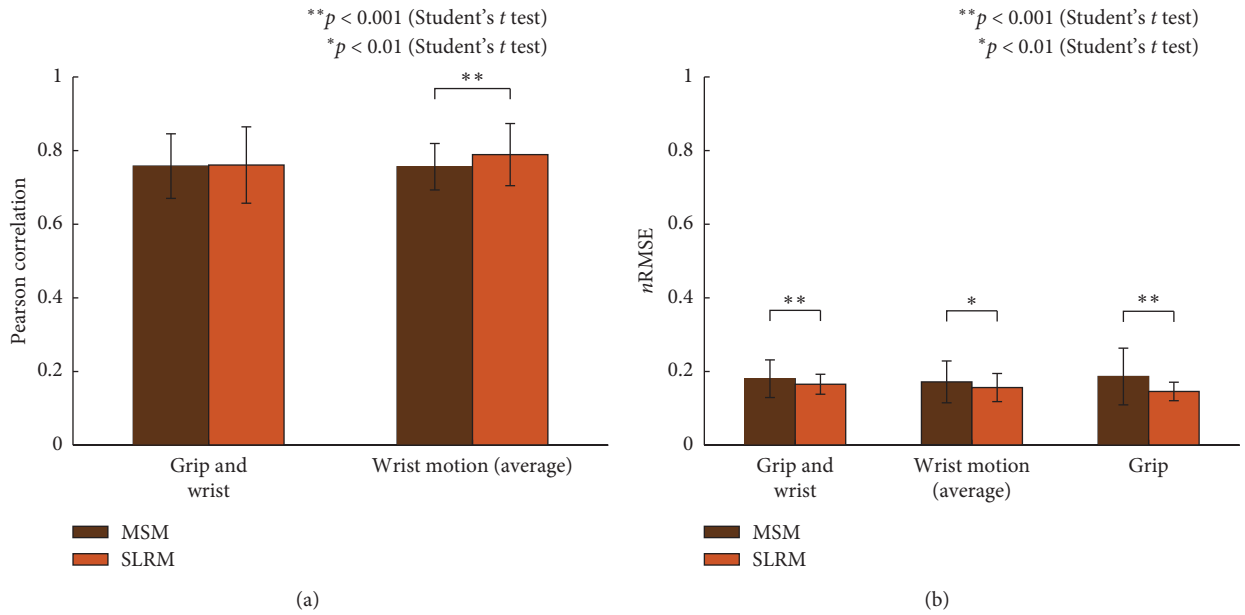

Figure 8: Trial-based wrist joint movement estimation performance changes in the synergy-based linear regression model (SLRM) and musculoskeletal model (MSM) in terms of the Pearson correlation coefficient (r) and normalized root-mean-square error (nRMSE). (a) SLRM and MSM had no statistically significant difference in wrist motion with grip, while wrist motion average had a statistically significant difference between the models ($p < 0.001$, Student's t-test). (b) nRMSE between SLRM and MSM had a statistically significant difference in every trial.

in MSM ($p < 0.001$, Student's t-test); and, for nRMSEs, 0.1852 ± 0.0216 in SLRM and 0.2098 ± 0.0558 in MSM ($p < 0.001$, Student's t-test).

3.3. Task 2: Grip Motion Test. Figure 7 shows the SLRM-based time series grip force estimate and resulting angle estimate perturbation. Subjects were constrained to a grip device during the task to ensure that there was no actual wrist motion during the entirety of task. Hence, wrist motion estimation during grip motion was checked for strong distortion in angle estimate. The results showed that during the gripping task, instability of the wrist angle estimation occurred in the presence of a strong force activation, as may be seen in Figure 7(d). For the half and quarter grip force task, angle estimation was less than 30°, as shown in Figures 7(e) and 7(f). The r value for grip force estimate and nRMSE of the X-Y angle estimate, compared with zero angle (no movement), were computed as indicated in Table 4. Sub8 data were omitted in this task because the EMG signal was saturated during the ADC converting process using NIDAQ (±5 voltage). The SLRM-based grip-force estimate from nine subjects was 0.8463 ± 0.0503 in r with 0.2559 ± 0.1397 nRMSE in wrist movement estimation.

Table 4: SLRM grip force estimate per subjects with corresponding wrist movement estimate perturbation.

Sub	Data type	Grip force estimate R	Angle X-Y (average) nRMSE
Sub1	*Mean*	0.8408	0.3068
	SD	0.0206	0.0748
Sub2	*Mean*	0.7164	0.4527
	SD	0.0579	0.1922
Sub3	*Mean*	0.7909	0.0925
	SD	0.1235	0.0760
Sub4	*Mean*	0.8929	0.1980
	SD	0.0184	0.0370
Sub5	*Mean*	0.8682	0.3162
	SD	0.0416	0.1192
Sub6	*Mean*	0.9526	0.2749
	SD	0.0098	0.1652
Sub7	*Mean*	0.9488	0.2001
	SD	0.0132	0.1733
Sub8	*Mean*	—	—
	SD		
Sub9	*Mean*	0.8588	0.2436
	SD	0.0318	0.0257
Sub10	*Mean*	0.7471	0.2180
	SD	0.0198	0.2319
Mean	*Mean*	0.8463	0.2559
	SD	0.0503	0.1397

4. Discussion

This study tested both MSM and SLRM in two different conditions to optimize each model. Figure 9 shows the VAF from SLRM1 and SLRM2 with the different number of wrist motion synergies. The VAF of SLRM1 converged in three wrist motion synergies and overfitted thereafter. This trend was the same as obtained in other studies whether in patients or healthy subjects [26–28]. For SLRM2, the VAF converged

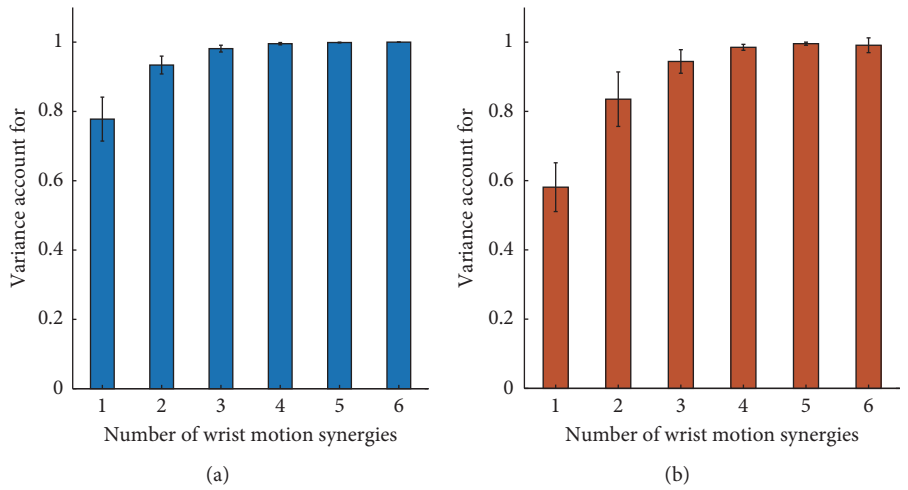

Figure 9: Two conditional SLRM-based R-square. (a) Variance account for with the different number of wrist motion synergies in SLRM1 (joint-trial-based synergy set) (b) Variance account for with the different number of wrist motion synergies in SLRM2 (separately derived synergy set).

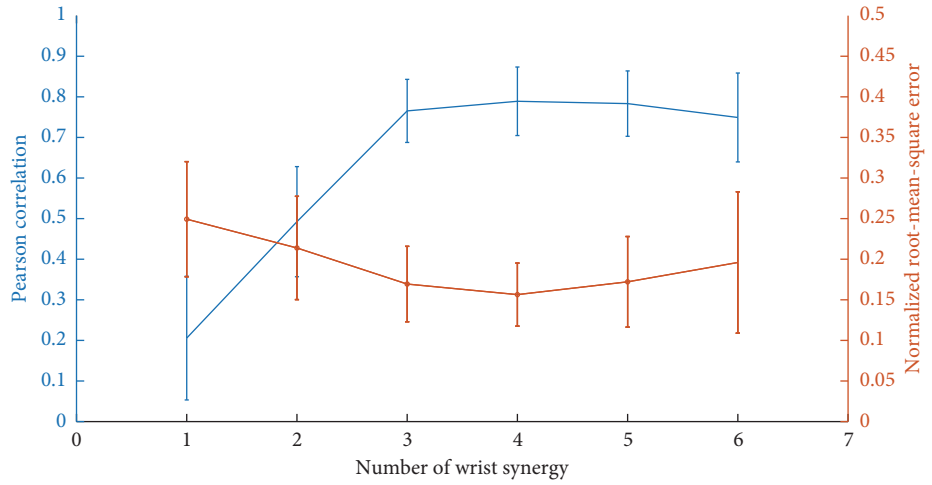

Figure 10: SLRM2-based two-dimensional wrist joint angle estimation performance with regard to the wrist synergy number.

in four wrist motion synergies and overfitted up to five. There was also a decrease in VAF in SLRM2. d' Avella et al. suggested that when the number of extracted synergies is greater than the generator synergies combination, each additional synergy captures an equal amount of noise-generated variation [30]. In that sense, fifth and sixth muscle synergies are noise-derived synergies. This study measured five wrist motion muscles and two finger motion muscles; thus, the sixth muscle synergy in SLRM2 formulated synergy set with finger motion muscles, which made reproducibility impossible. Such noise-derived synergies contaminated the estimation performance. The wrist joint angle estimation performance of SLRM2 with varying numbers of wrist synergies are shown in Figure 10. The highest performance was obtained in four wrist motion synergies; the additional number of synergies deteriorates the estimation performance.

In the SLRM, wrist movement estimation performance showed statistical significance depending on the synergy extraction method both in r and nRMSE. This study aims to use NMF for prosthetic and interface purposes; therefore, synergies were modulated per subject and trial. Separate synergy sets preserve multi-EMG coactivation in the grip synergy, which enables synergy to cluster movement type. In a joint-trial-based synergy set, the NMF divided multi-EMG signals into several part-based groups, resulting in tying the grip synergy to be a combination of EMG signals not used in other synergies. Therefore, the joint-trial-based synergy set could not discriminate movement type. This tendency can be seen in Figure 11. Synergy 5 had the most distinctive shape, representing grip synergy. In a time-domain reaction, SLRM1 responded to grip activation regardless of grip force. In SLRM2, it also increased other synergy coefficients albeit, relatively, by a small amount when a strong grip was assumed. This result could support extracting a unique synergy for each motion [31].

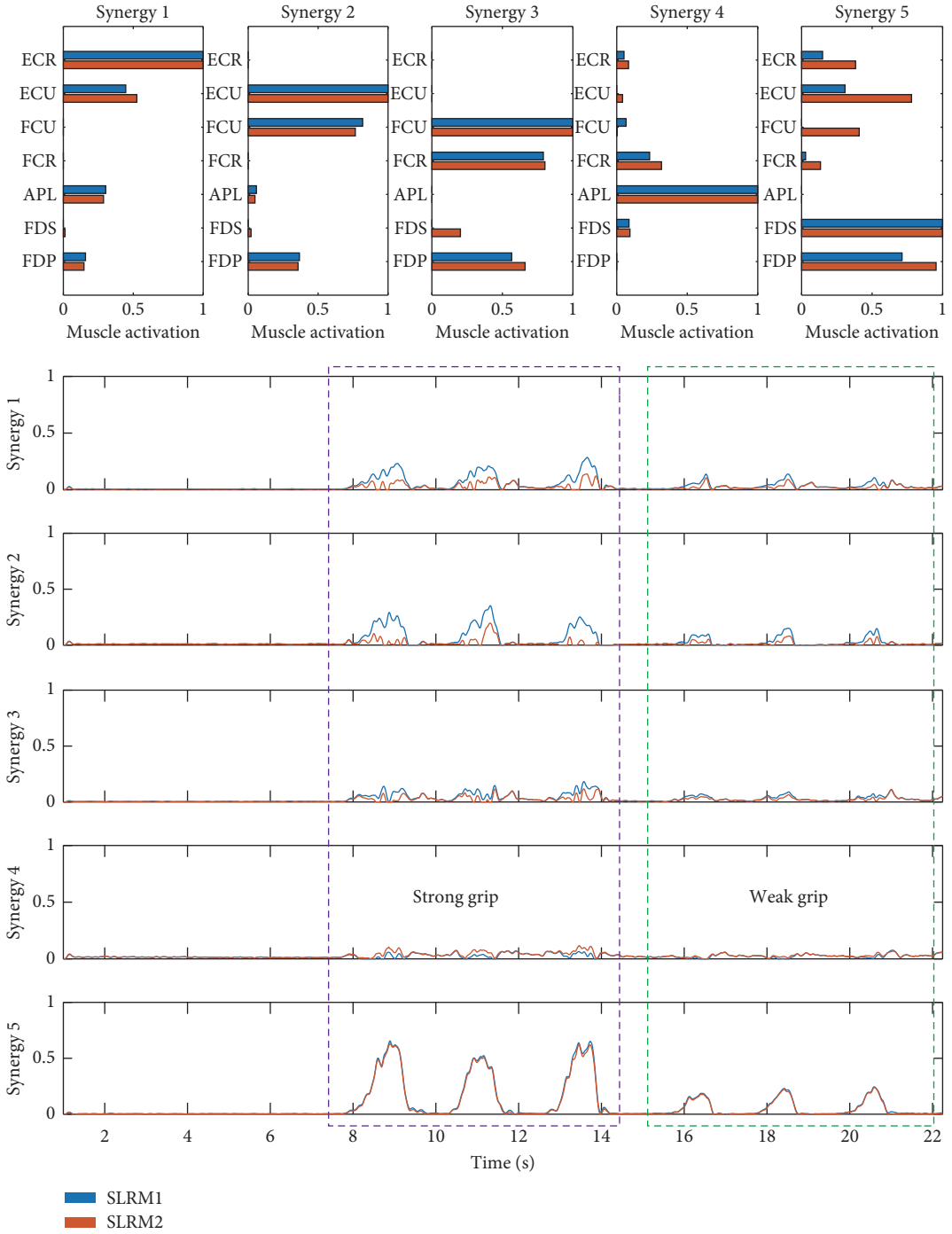

Figure 11: Time series synergy coefficient data with corresponding synergy matrix in the synergy-based linear regression model in the grip task. Synergies one to four represent wrist synergy, and synergy five represents grip synergy. The purple-colored region represents three-time strong grip actions and the green-colored region represents three-time weak grip actions.

The FDS and FDP are flexor muscles of the fingers from an anatomical point of view. Those two muscles are separated by synergy analysis, which can be observed from Synergy 5, as shown in Figure 10. For the wrist motion with and without grip task, the other five muscles are appropriate to estimate joint angles. For the MSM, the minimum number of muscles exhibited good performance.

The estimation performance between SLRM and MSM had a statistically significant difference in the entire wrist-only movement task both in r and nRMSE values; however, there were no other r values in wrist motion with grip. The results show the robustness of the wrist movements with respect to finger movement of the MSM, which is the same as those obtained by Kawase et al.'s experiment [17]. The estimation performance of SLRM also showed comparable

performance with previous results in the literature on trajectory [6] and joint force [9] estimation. The advantage of SLRM is that it estimates not only continuous wrist movements but also complex movements in addition to grip motion. In this experiment, we confirmed that the estimation performance of SLRM for complex motion was equivalent to MSM performance.

Within the wrist-only motion trials, both SLRM and MSM had the lowest performance in comfortable half performance. This is most likely due to the nonlinearity between EMG signals and arm motion or contamination of movement artifact and baseline noise to the EMG (representatively, Sub3). Therefore, the nonlinear regression techniques used in the previous studies [6, 9] could be comparable with the synergy-based model having an alternative to using linear regression.

The linear envelope filtering used in the EMG signal analysis was proven to have highly correlated signals with joint torque induced by the target muscle [21]. Grip synergy, which is a coactivation of these filtered EMG signals, also showed a high grip force estimation performance of 0.8463 ± 0.0503 without resort to further conversion or regression techniques. However, in the strong grip trial, it was confirmed that the wrist angle estimation was distorted by gripping EMG signals. This strong grip distortion indicates the necessity to investigate the limits of the SLRM in grip force estimation. Within the current experiment results, it is difficult to determine whether each subject distorted the wrist angle estimation with a similar absolute force level or with a specific ratio of the maximum force.

5. Conclusions

In this study, we explored a model for estimating wrist joint angle with and without grip action. In the first task, in which we examined wrist angle estimation of SLRM and MSM, the SLRM exhibited a relatively higher performance in wrist motion. In the grip task, SLRM showed robustness in angle estimation when the grip force is half or a quarter of its maximum force level. In addition, SLRM can provide the extent of grip force exerted in the center position with little perturbation. These characteristics of SLRM are useful for combined wrist and grip action; however, obtaining limiting grip force required to crash the wrist angle estimation, and vice versa, was beyond the scope of this study. Further studies are required to obtain the simultaneous estimation of both parameters necessary for daily usage.

Data Availability

The experimental results from the individual participants are provided as a table within the article. Data of the raw EMG, IMU, and force sensors are available upon request to the corresponding author.

Conflicts of Interest

The authors declare that there are no conflicts of interest regarding the publication of this paper.

Acknowledgments

This work was supported by JSPS under KAKENHI grants (grant no. 17H05903), Tateishi Science and Technology Foundation (grant no. 2188001), JST PRESTO (Precursory Research for Embryonic Science and Technology) (grant no. JPMJPR17JA), and JST MIRAI (grant no. JY300171).

References

[1] D. Nishikawa, W. Yu, H. Yokoi, and Y. Kakazu, "EMG prosthetic hand controller using real-time learning method," in *Proceedings of the IEEE International Conference on Systems, Man, and Cybernetics (Cat. No. 99CH37028)*, vol. 1, pp. 153–158, IEEE, Tokyo, Japan, October, 1999.

[2] F. Sebelius, M. Axelsson, N. Danielsen, J. Schouenborg, and T. Laurell, "Real-time control of a virtual hand," *Technology and Disability*, vol. 17, no. 3, pp. 131–141, 2005.

[3] Z. O. Khokhar, Z. G. Xiao, and C. Menon, "Surface EMG pattern recognition for real-time control of a wrist exoskeleton," *Biomedical Engineering Online*, vol. 9, no. 1, p. 41, 2010.

[4] K. Kita, R. Kato, H. Yokoi, and T. Arai, "Development of autonomous assistive devices-analysis of change of human motion patterns-," in *Proceedings of the International Conference on Systems, Man and Cybernetics*, vol. 1, pp. 316–321, IEEE, Taipei, Taiwan, October, 2006.

[5] E. Biddiss, "Need-directed design of prostheses and enabling resources," in *Amputation, Prosthesis Use, and Phantom Limb Pain*, Springer, New York, NY, USA, 2009.

[6] J. Vogel, C. Castellini, and P. van der Smagt, "EMG-based teleoperation and manipulation with the DLR LWR-III," in *Proceedings of the International Conference on Intelligent Robots and Systems*, pp. 672–678, IEEE, September, 2011, San Francisco, CA, USA.

[7] P. K. Artemiadis and K. J. Kyriakopoulos, "A switching regime model for the EMG-based control of a robot arm," *IEEE Transactions on Systems, Man, and Cybernetics, Part B (Cybernetics)*, vol. 41, no. 1, pp. 53–63, 2010.

[8] N. Jiang, J. L. Vest-Nielsen, S. Muceli, and D. Farina, "EMG-based simultaneous and proportional estimation of wrist/hand kinematics in uni-lateral trans-radial amputees," *Journal of Neuroengineering and Rehabilitation*, vol. 9, no. 1, p. 42, 2012.

[9] J. L. G. Nielsen, S. Holmgaard, N. Jiang, K. B. Englehart, D. Farina, and P. A. Parker, "Simultaneous and proportional force estimation for multifunction myoelectric prostheses using mirrored bilateral training," *IEEE Transactions on Biomedical Engineering*, vol. 58, no. 3, pp. 681–688, 2010.

[10] T. B. Möller and E. Reif, *Pocket Atlas of Radiographic Positioning*, Thieme, New york, NY, USA, 2nd edition, 2011.

[11] G. Torres-Oviedo, J. M. Macpherson, and L. H. Ting, "Muscle synergy organization is robust across a variety of postural perturbations," *Journal of Neurophysiology*, vol. 96, no. 3, pp. 1530–1546, 2006.

[12] M. C. Tresch, P. Saltiel, and E. Bizzi, "The construction of movement by the spinal cord," *Nature Neuroscience*, vol. 2, no. 2, pp. 162–167, 1999.

[13] K. Shima and T. Tsuji, "Classification of combined motions in human joints through learning of individual motions based on muscle synergy theory," in *Proceedings of the International Symposium on System Integration*, pp. 323–328, IEEE, Sendai, Japan, December, 2010.

[14] C. W. Antuvan, F. Bisio, F. Marini, S. C. Yen, E. Cambria, and L. Masia, "Role of muscle synergies in real-time classification

of upper limb motions using extreme learning machines," *Journal of Neuroengineering and Rehabilitation*, vol. 13, no. 1, p. 76, 2016.

[15] J. Roh, W. Z. Rymer, and R. F. Beer, "Robustness of muscle synergies underlying three-dimensional force generation at the hand in healthy humans," *Journal of Neurophysiology*, vol. 107, no. 8, pp. 2123–2142, 2012.

[16] H. Kambara, D. Shin, and Y. Koike, "A computational model for optimal muscle activity considering muscle viscoelasticity in wrist movements," *Journal of Neurophysiology*, vol. 109, no. 8, pp. 2145–2160, 2013.

[17] T. Kawase, T. Sakurada, Y. Koike, and K. Kansaku, "Estimating joint angles from biological signals for multi-joint exoskeletons," in *Proceedings of the International Conference on Systems, Man, and Cybernetics (SMC)*, pp. 1470–1474, IEEE, San Diego, CA, USA, October 2014.

[18] J. Lee, Y. Kagamihara, and S. Kakei, "Quantitative evaluation of movement disorders in neurological diseases based on EMG signals," in *Proceedings of the 30th Annual International Conference of the IEEE Engineering in Medicine and Biology Society*, pp. 181–184, IEEE, Vancouver, Canada, August, 2008.

[19] C. F. Yeong, A. Melendez-Calderon, R. Gassert, and E. Burdet, "ReachMAN: a personal robot to train reaching and manipulation," in *Proceedings of the International Conference on Intelligent Robots and Systems*, pp. 4080–4085, IEEE, St. Louis, MO, USA, October 2009.

[20] C. Kothe, "Lab streaming layer (LSL)," 2014, https://code.google.com/p/labstreaminglayer/.

[21] Y. Koike and M. Kawato, "Estimation of dynamic joint torques and trajectory formation from surface electromyography signals using a neural network model," *Biological Cybernetics*, vol. 73, no. 4, pp. 291–300, 1995.

[22] M. Halaki and K. Ginn, "Normalization of EMG signals: to normalize or not to normalize and what to normalize to?" in *Computational Intelligence in Electromyography Analysis-A Perspective on Current Applications and Future Challenges*, IntechOpen, London, UK, 2012.

[23] S. O. H Madgwick, A. J. Harrison, and R. Vaidyanathan, "Estimation of IMU and MARG orientation using a gradient descent algorithm," *2011 IEEE International Conference on Rehabilitation Robotics*, vol. 2011, Article ID 5975346, 7 pages, 2010.

[24] A. Cichocki and A.-H. Phan, "Fast local algorithms for large scale nonnegative matrix and tensor factorizations," *IEICE Transactions on Fundamentals of Electronics, Communications and Computer Sciences*, vol. E92-A, no. 3, pp. 708–721, 2009.

[25] D. D. Lee and H. S. Seung, "Algorithms for non-negative matrix factorization," in *Advances in Neural Information Processing Systems*, T. G. Dietterich, S. Becker, and Z. Ghahramani, Eds., pp. 556–562, MIT Press, London UK, 2001.

[26] L. Tang, F. Li, S. Cao, X. Zhang, D. Wu, and X. Chen, "Muscle synergy analysis in children with cerebral palsy," *Journal of Neural Engineering*, vol. 12, no. 4, Article ID 046017, 2015.

[27] H. Kim, J. Lee, and J. Kim, "Muscle synergy analysis for stroke during two degrees of freedom reaching task on horizontal plane," *International Journal of Precision Engineering and Manufacturing*, pp. 1–10, 2019.

[28] D. J. Clark, L. H. Ting, F. E. Zajac, R. R. Neptune, and S. A. Kautz, "Merging of healthy motor modules predicts reduced locomotor performance and muscle coordination complexity post-stroke," *Journal of Neurophysiology*, vol. 103, no. 2, pp. 844–857, 2009.

[29] D. D. Lee and H. S. Seung, "Learning the parts of objects by non-negative matrix factorization," *Nature*, vol. 401, no. 6755, pp. 788–791, 1999.

[30] A. d'Avella, A. Portone, L. Fernandez, and F. Lacquaniti, "Control of fast-reaching movements by muscle synergy combinations," *Journal of Neuroscience*, vol. 26, no. 30, pp. 7791–7810, 2006.

[31] A. Furui, S. Eto, K. Nakagaki et al., "A myoelectric prosthetic hand with muscle synergy–based motion determination and impedance model–based biomimetic control," *Science Robotics*, vol. 4, no. 31, Article ID eaaw6339, 2019.

Hindawi
Journal of Healthcare Engineering
Volume 2020, Article ID 8714070, 11 pages
https://doi.org/10.1155/2020/8714070

Research Article

A Phlegm Stagnation Monitoring Based on VDS Algorithm

Zhiguo Gao[1] **and Xin Yu**[2]

[1]*School of Artificial Intelligence and Information Technology, Nanjing University of Chinese Medicine, Nanjing 210044, China*
[2]*College of Computer and Software, Nanjing University of Information Science and Technology, Nanjing 210044, China*

Correspondence should be addressed to Xin Yu; 20171211493@nuist.edu.cn

Received 23 September 2019; Revised 4 December 2019; Accepted 19 December 2019; Published 24 January 2020

Guest Editor: Yousun Kang

In the nonmedical sputum monitoring system, a practical solution for phlegm stagnation care of patients was proposed. Through the camera, the video images of patients' laryngeal area were obtained in real time. After processing and analysis on these video frame images, the throat movement area was found out. A three-frame differential method was used to detect the throat moving targets. Anomalies were identified according to the information of moving targets and the proposed algorithm. Warning on the abnormal situation can help nursing personnel to deal with sputum blocking problem more effectively. To monitor the patients' situation in real time, this paper proposed a VDS algorithm, which extracted the speed characteristics of moving objects and combined with the DTW algorithm and SVM algorithm for sequence image classification. Phlegm stagnation symptoms of patients were identified timely for further medical care. In order to evaluate the effectiveness, our method was compared with the DTW, SVM, CTM, and HMM methods. The experimental results showed that this method had a higher recognition rate and was more practical in a nonmedical monitoring system.

1. Introduction

Phlegm stagnation, airway obstruction with phlegm, and other respiratory problems may occur during the care of older or terminal patients, resulting in serious complications such as hypoxia, asphyxia, pulmonary infection, and respiratory failure [1, 2]. To deal with such problems in the use of remote healthcare systems, a monitoring system is necessary to monitor the physiological parameters of patients in real time.

The respiratory monitoring mainly focuses on parameters of the frequency, intensity, duration of coughs, etc., to provide an important clinical reference for disease diagnosis, treatment, and drug-efficacy evaluation. So far, the analysis and recognition of cough mainly refer to the speech recognition system and depend on neural networks, dynamic time warping (DTW), the hidden Markov model (HMM), the classification tree method (CTM), and the k-means algorithm [3–10]. For example, Kou et al. [4] detected cough signals in continuous speech streams by using the keyword recognition method in the HMM. Yin and Mo and Shin [5, 6] made cough recognition by introducing a DTW-based [11, 12] classification model. The Hull Automatic Cough Counter (HACC) achieved automatic cough recognition by establishing a classification model with a probabilistic neural network (PNN). Drugman et al. and Wang et al. [7, 13] distinguished cough sounds from environmental sounds by establishing a hybrid model with both a neural network and a hidden Markov model. Sun and Zhu [14] distinguished the two kinds of sounds by using the classification tree method (CTM). Meng et al. [15] reduced noise and expanded the characteristics of breathing sound by an integrated serial algorithm. Niu et al. [16] detects sputum by using image processing techniques. Heretofore, no research concerns about the physical change of the human body for the diagnosis and prediction in cough relative respiratory monitoring system. However, in a practical monitoring system of older or terminal patients, phlegm stagnation and airway obstruction with phlegm are rarely solved by cough recognition technology [17]. We still need manual work to diagnose these dangerous symptoms. There is a wide gap between the current health monitoring system and the

practical nonmedical monitoring system of older or terminal patients.

Cough recognition and extraction system can recognize cough signals and display the severity of the coughs and the efficacy of the treatment, which is convenient for doctors to diagnose. During the care of older and terminal patients with the phlegm accumulation symptom, a practical method is needed to monitor the patients in real time and give an early warning so that the caregiver can help the patient expel phlegm in a timely manner. However, there is no detailed and effective method currently. Therefore, a new method based on image detection is proposed in this paper. Firstly, the computer collects the video images of the patient's throat by a camera, and then a category learning algorithm proposed in this paper is used to analyze these video images. Finally, the computer sends the analyzed results to the client in real time, which can timely provide the patient with moderate care and decrease the risk of accidental death.

2. Related Work

2.1. The DTW Method. DTW has good performance in template matching. It generally uses an action in the training set as a template and compares actions to be recognized with the template. The action closest to the template is viewed as the action of the template. In our experiment, the nearest neighbor algorithm is used and each action corresponds to multiple templates. A test action can be recognized if we can find a template closest to it.

The main limitation of DTW is that it requires the monotonous change of a sequence over time. In motion recognition, however, actions occur according to time order. Besides, DTW is believed to have nice results in the experiment for the following reasons. (1) It utilizes multiple templates and adopts the nearest neighbor method. (2) It well displays the similarity in shape. Though DTW is replaced by HMM in speech recognition, it still plays an important role in motion recognition.

Since motion features cannot be represented by a single image, it is necessary to recognize actions by a plurality of sequential images. In this paper, actions are recognized through a sequence of images. From the above, we know how to obtain the similarity in shape between two images. But it is still difficult to obtain the similarity between sequential images because other information about the sequence is unknown, for example, the length and starting position of the sequence and the interval between sequences.

An advanced DTW algorithm is adopted in this thesis for sequence comparison. DTW was originally applied to speech recognition [18] due to its capability of handling the problem of inconsistent speed. There exist similar problems in action sequences, such as fast or slow pace and sometimes acceleration in pace. All these problems can be well disposed with DTW. Our VDS algorithm enhances DTW with the combination of SVM for target classification, which will improve the accuracy of the recognition results.

Suppose there are two action sequences $x_1, \ldots, x_m$ and $y_1, \ldots, y_n$, where M and N represent the lengths of the two action sequences respectively, then the DTW distance $D(i, j)$ of the two action sequences can be calculated with the following:

$$D(i,j) = \min\{D(i,j-1), D(i-1,j), D(i-1,j-1)\} + d(x_i, y_i), \quad i = 1, \ldots, M,\ j = 1, \ldots, N. \tag{1}$$

The distance function $d(x_i, y_i)$ is a matching distance of two motion sequences that is obtained with dynamic rules:

$$d(x_i, x_j) = \frac{1}{n} \sum_{p_k \in x_i} \min_{q_t \in x_j} c(p_k, A(q_t)) + \frac{1}{m} \sum_{p_k \in x_i} \min_{q_t \in x_j} c(p_k, A(q_t)). \tag{2}$$

From (M, N), we can find the matching path by roll back. When rolling back to $(1, 1)$, we will get the shortest path. The initial value of $D(i, j)$ is 0 when i or j is less than 1.

Figure 1(a) shows the local path constraints of $D(i, j-1)$, $D(i-1, j)$, and $D(i-1, j-1)$. They are the essential constraints during the matching of two action sequences. Figure 1(b) is another local path constraint, corresponding to a new DTW value that should be recomputed in formula (1). The motion is generated in chronological order in motion recognition, and the shape is sequentially changed accordingly. Therefore, the path constraint [19] of Figure 1(a) can well describe the change of the motion sequence.

2.2. SVM Strategy. Next, we will use SVM to achieve action classification. Set the linear separable sample set $D = (x_i, y_i), i = 1, 2, \ldots, l, x \in R^d, y \in \{+1, -1\}$ to be the category label. For linearly inseparable samples, a relaxation term $\xi_i \geq 0$ is introduced. A general form of the linear discriminant function is $g(x) = w \cdot x + b$, and the classification equation is $(w \cdot x) + b = 0$, which transforms the optimized hyperplane problem into convex quadratic programming:

$$\begin{cases} \Phi(w, \xi) = \dfrac{1}{2} w^2 + C\left(\sum_{i=1}^{l} \xi_i\right), \\ \text{s.t.} \quad y_i[(w \cdot x_i) + b] - 1 + \xi_i \geq 0, \end{cases} \tag{3}$$

where C is the penalty factor. The constraint of formula (3) can be transformed into a maximization problem:

$$\Phi(w, \xi) = \frac{1}{2} w^2 + C\left(\sum_{i=1}^{l} \xi_i\right) - \sum_{i=1}^{l} a_i \{y_i[(w \cdot x_i) + b] - 1 + \xi_i\}, \tag{4}$$

where $a_i > 0$ is a Lagrangian coefficient. The optimal classification function is obtained by solving the Lagrangian function:

$$f(x) = \operatorname{sgn}\left\{\sum_{i=1}^{l} a_i^* y_i K(x_i, x) + b^*\right\}, \tag{5}$$

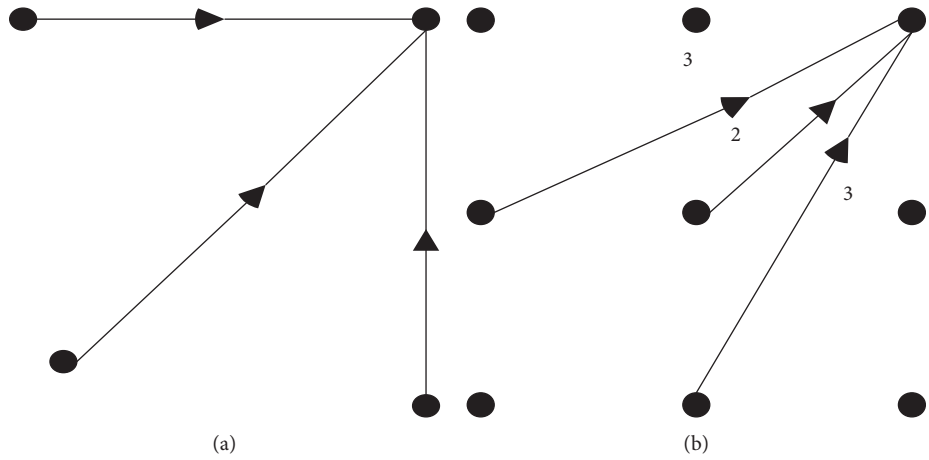

Figure 1: Different path constraints. (a) Path constraint *a*. (b) Path constraint *b*.

where sgn( ) is the symbol function; l is the number of training samples; $K(x_i, x)$ is the kernel function; x_i is the training sample; x is the sample to be decided, b^* is the threshold determined by the training sample; and a_i^* is determined by the quadratic programming, and the kernel function is $K(x, y) = \exp(-((\|x - y\|^2)/2\sigma^2))$.

Since SVM can only handle vectors with the same length, different sequences of eigenvectors cannot exist in the same vector space. Different length of motion sequence data will bring low resolution, and thus lead to less obvious separation effect. Our VDS model is capable of matching motion sequences automatically so that distances and similar velocity between motion sequences can reflect the similarity in symptoms, and thus achieve higher recognition accuracy of phlegm stagnation symptom accordingly. In VDS, the choice of kernel function will directly affect the accuracy and operation time. Considering the coincidence with DTW, we choose the radial basis kernel function. The inner product kernel function of RBF/VDS is obtained by combining the velocity characteristic parameters of sequential images:

$$K(x_i, x) = \exp\left\{\frac{-(\partial D + (1 - \partial)V)^2}{\sigma^2}\right\}, \quad (6)$$

where D is calculated by the DTW, that is, $D(i, j)$ in formula (1). The improvement of SVM kernel function will not affect the construction model and training of SVM, thus we can use SVM training method to make the classification of phlegm stagnation status [20].

3. Design of Phlegm Stagnation Learning Algorithm Based on Image Recognition

To judge whether the patient has phlegm stagnation symptom, this thesis proposes a Velocity Distance Support (VDS) algorithm. It processes the velocity of the moving target with the DTW algorithm and combines the classification of sequential images with the support vector machine (SVM) to identify the physical condition of the patient. The monitoring system sends the message back to the client in real time so that the caregiver can deal with problems promptly. The similarity distance between the feature vectors of input data and the prototype is calculated by DTW. It is a method based on nonparametric models. These methods can simply be implemented and can automatically match action sequences and calculate the distance between two sequences as well, while keeping a higher recognition rate than general methods based on parametric models. They can combine the similarity distance with velocity and then establish a laryngeal action identification model based on the SVM classifier. The diagnosis of phlegm stagnation can be carried out through parameters learning of the original training data set and classification of phlegm stagnation status.

3.1. Intelligent Video Surveillance System Structure. In a remote care system, the intelligent video monitoring system is introduced to help patients with phlegm accumulation. This intelligent video monitoring system can automatically record the video images of the scene monitored in real time through a camera. Then it will process and analyze these video frames to find the moving areas and extract moving targets from them [21], judge an abnormal phenomenon according to the relevant information of the moving target, and make an appropriate early warning for the abnormality. Thus, it can assist caregivers to deal with phlegm accumulation problems more effectively and make the care convenient. The process consists of video image input, moving target detection, feature extraction, classification training, warning module, etc. The overall process is shown in Figure 2.

3.2. Moving Target Detection in Video Images. With the rapid development of motion detection technology, more and more researches have been carried out for motion detection. There also exist great differences in the algorithms when targets have different shapes, detection environments, or camera properties changes. Most detection algorithms have some deficiencies and cannot provide satisfactory detection results. Motion detection algorithms mainly

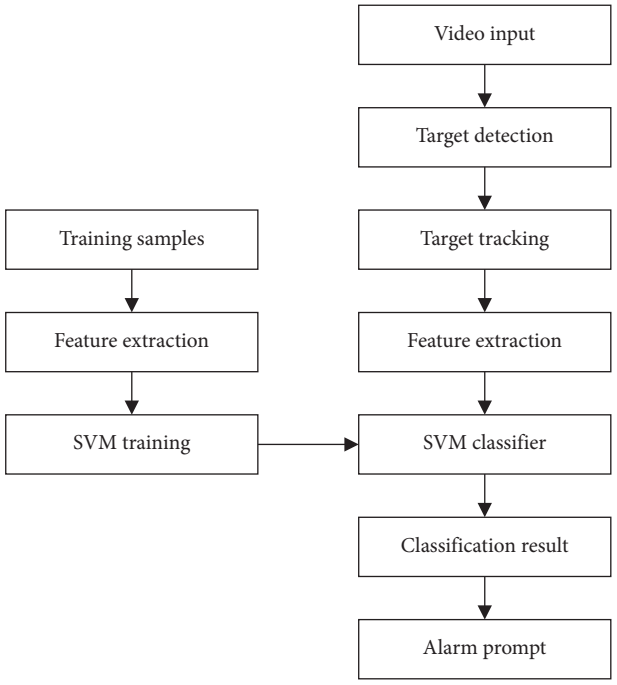

Figure 2: Process of intelligent video surveillance system.

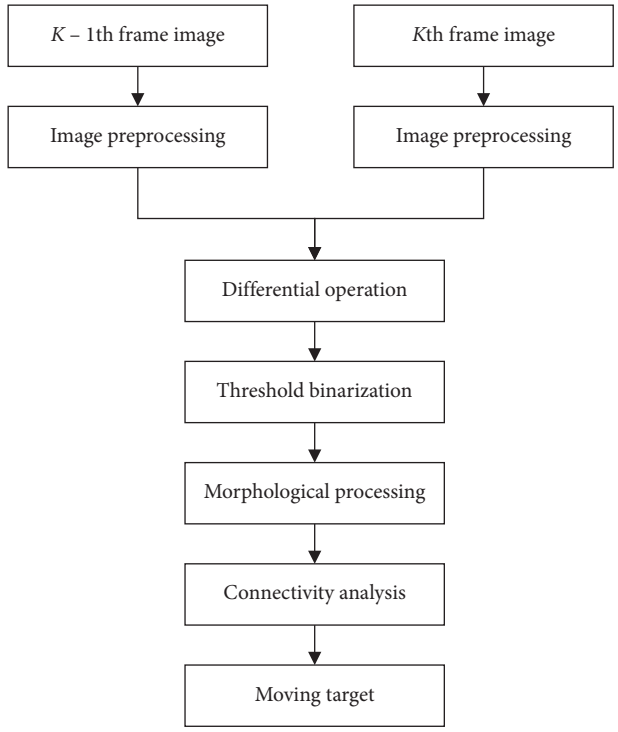

Figure 3: Process of interframe differencing.

include interframe differencing, background subtraction, and the optical flow method [8]. Due to the complexity and heavy computation cost, the optical flow method has poor real time performance; thus, it generally needs independent hardware support [10, 11]. To avoid these problems, the intelligent video monitoring system for older or terminal patients described in this paper will turn to a three-frame differencing.

Interframe differencing is a time-based differencing algorithm. It is a technique where the difference between two neighboring video frames is checked and a differencing image is obtained. Then, the moving target is picked out from the differencing image after smoothing, binarization, and other processing. For each pixel in a frame, two consecutive frames are differenced by the following formula:

$$D(x, y) = \left| f_k(x, y) - f_{k-1}(x, y) \right|,$$
$$R(x, y) = \begin{cases} 1, & D(x, y) \geq T, \\ 0, & D(x, y) < T, \end{cases} \quad (7)$$

$f_{k-1}(x, y)$ represents the gray value of the pixel of the $k-1$th frame, $f_k(x, y)$ represents that of the k th frame, $D(x, y)$ represents the differential result, $R(x, y)$ represents the binarization result, and T is the preset threshold. With too large T, there will be incomplete detection or leak detection; and on the contrary, there will be a lot of noise. The processing of interframe differencing is shown in Figure 3:

Generally, the detected moving target is regarded as the foreground image, and the other areas are background [12]. There is little difference between two consecutive frames in the value of background pixels or the difference only occurs in a very small area, but the pixels where the moving targets are located may change obviously. Therefore, a threshold filtering and morphological processing are carried out for the differential image. Finally a sufficiently large area with pixel changes is chosen as the moving target. This algorithm is simple and easy to implement, with adaptable and fast computational performance.

The results of interframe differencing are those areas with pixel changes in two consecutive frames. For areas with pixel changes in two consecutive frames where the moving targets are located, including the area where the moving targets were located in the previous frame and that in the current frame, the results are the sum of two areas with pixel changes. This means that the target displayed in the resulting image is larger than the actual one, which is called an image tail [13]. Besides, as many targets have little change in pixels by themselves, the areas with the moving targets in both frames also have little change in pixel values and are likely to be taken as foreground images. This appears as "holes" inside the detection results [14] and may weaken the detection effect of the interframe differencing largely.

To overcome the shortcomings of interframe differencing, a three-frame differencing was proposed. It extracts three consecutive frames ($k-1$, k, and $k+1$) and makes differencing computations on $k-1$, k frames and $k-1$, k frames, respectively. Then, an AND operation is performed on the differential images to remove the elongated portion of the moving target. Therefore, the moving target obtained by the three-frame differencing is more accurate than the interframe differencing, but there will still be some holes in the simultaneously detected moving target. The formula of three-frame differencing is described as follows:

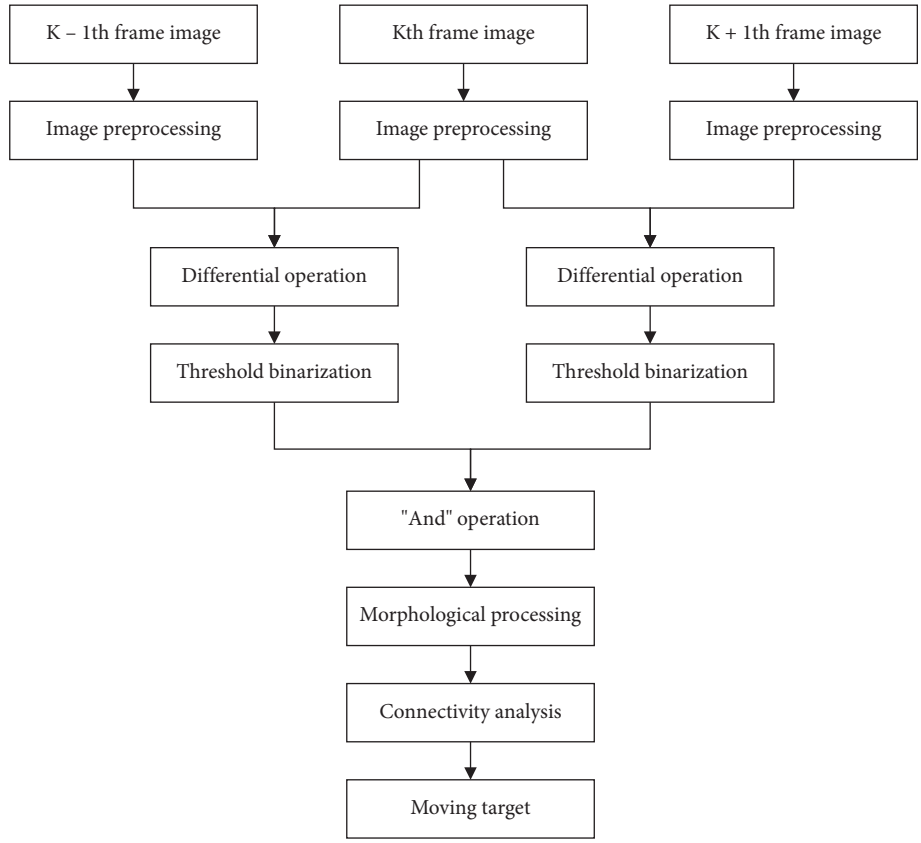

Figure 4: Process of three-frame differencing.

$$D_1(x, y) = \left| f_k(x, y) - f_{k-1}(x, y) \right|,$$
$$D_2(x, y) = \left| f_{k+1}(x, y) - f_k(x, y) \right|, \tag{8}$$

$$R_1(x, y) = \begin{cases} 1, & D_1(x, y) \geq T, \\ 0, & D_1(x, y) < T, \end{cases}$$
$$R_2(x, y) = \begin{cases} 1, & D_2(x, y) \geq T, \\ 0, & D_2(x, y) < T, \end{cases} \tag{9}$$

$$R(x, y) = R_1(x, y) \wedge R_2(x, y). \tag{10}$$

$R(x, y)$ denotes the resulting moving target, and $\wedge$ denotes an AND operation. Three-frame differencing is an improved version of interframe differencing. It solves the problem that the moving object is elongated and enlarged during the use of interframe differencing. When the target color is close to the background, there will be some omissions during detection, resulting in an incomplete moving target. The processing of three-frame differencing is shown in Figure 4.

3.3. Feature Parameters Extract from the Moving Target. Extracting feature parameters from the moving object means transforming abnormal and abstract behaviors into detailed digital features, and the velocity feature can also describe the behavioral features of the moving object. Velocity is a common physical quantity. In a short time, the velocity v can be calculated by the ratio of the displacement s of the moving object to the time interval t. It fulfills the relation $v = s/t$.

When velocity is used to describe the behavior of a moving target, it can be regarded as a point particle. In planar geometry, when a point particle moves from position a to position b through a certain period of time t_0, the coordinates of the positions a and b are recorded as $a\ (x_a, y_a)$ and $b\ (x_b, y_b)$, respectively.

Formula (11) denotes the distance that a point particle moves within the time period t_0.

$$d_0 = \sqrt{(x_2 - x_1)^2 + (y_2 - y_1)^2}. \tag{11}$$

After calculation of the distance d_0, the velocity v_0 of the point particle in the given time period t_0 can be calculated with $v_0 = d_0/t_0$.

Because the behaviors and actions of moving objects change with time, the features for extraction are also changing. When the object moves from one position to another, the coordinates of its mass center are also changing. Therefore, the displacement of an object over a period can be denoted by the changes in the coordinates of the mass center. Given the frame rate of a video object f_w, the moving object in the video has coordinates of mass center $f_1\ (x_1, y_1)$. After one frame of moving, the coordinates of the mass center change to $f_2\ (x_2, y_2)$. The displacement of the moving object that occurred during the above process can be calculated by (12).

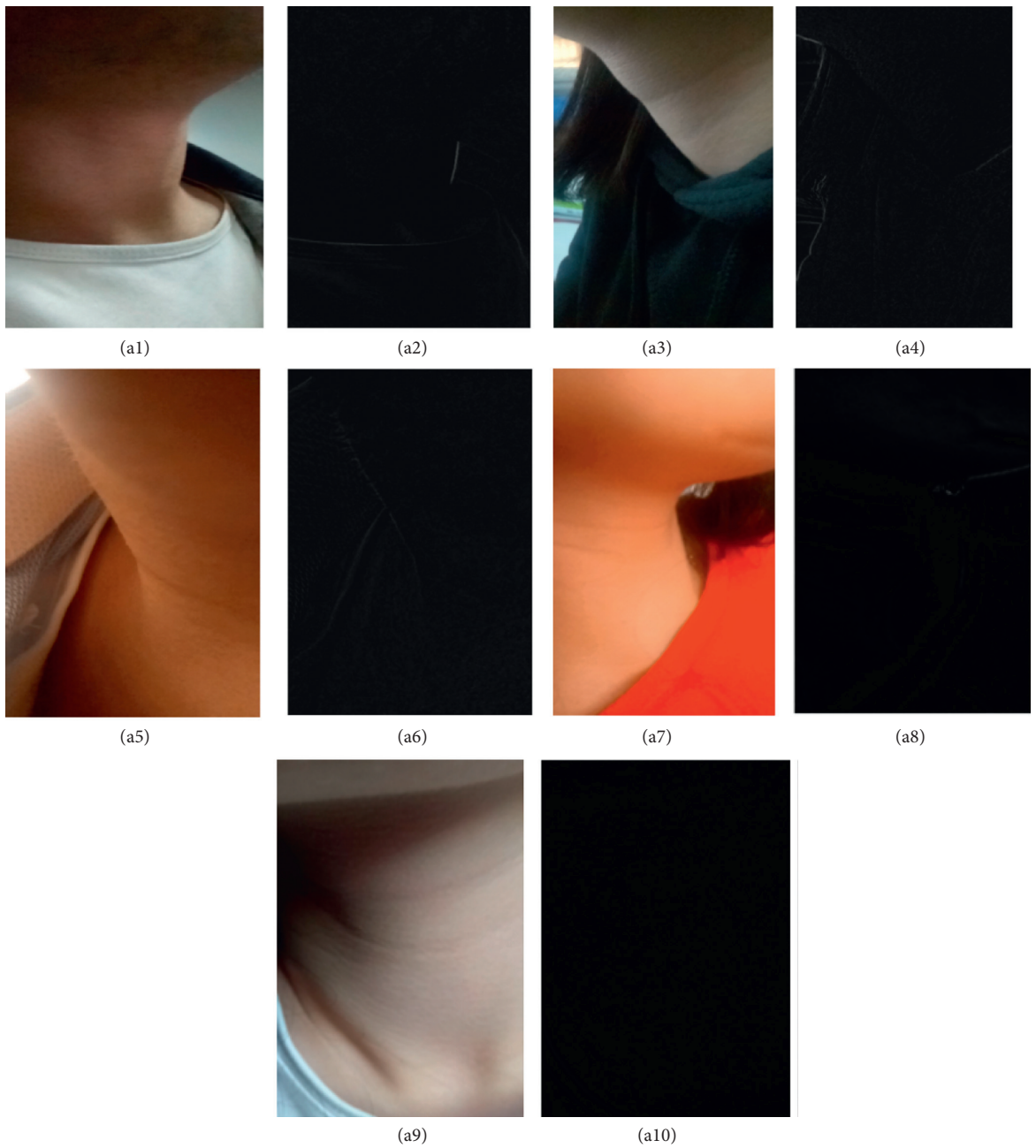

(a1) (a2) (a3) (a4)

(a5) (a6) (a7) (a8)

(a9) (a10)

(a)

Figure 5: Continued.

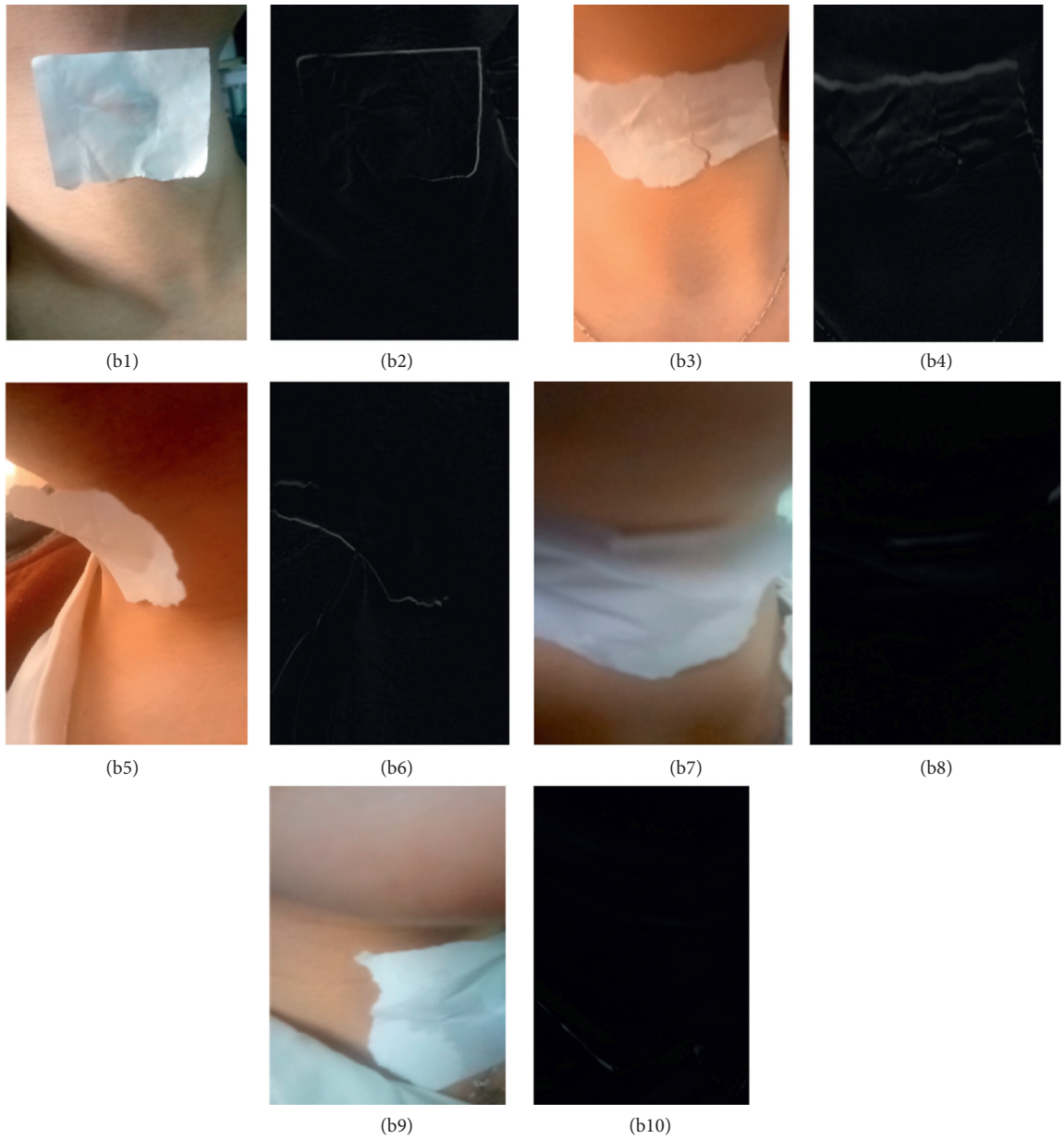

Figure 5: Effect of three-frame differencing for laryngeal video images. (a) Detection without a sticker. (b) Detection with a sticker.

$$l = \sqrt{(x_2 - x_1)^2 + (y_2 - y_1)^2}, \tag{12}$$

and the time it used is $t = 1/f_w$

According to the velocity formula of moving objects, it is easy to obtain the velocity of a moving object between adjacent frames. In this way, the velocity features of the moving target can be extracted with $v = l/t$.

3.4. Combining DTW Algorithm and SVM Algorithm for Sequence Image Classification. After target detection, the SVM model should be trained. The input of the SVM classifier is the extracted sample features, and the output is the resulting classification decision {1, 1}. Generally, the value −1 means action does not belong to the class of phlegm stagnation while value +1 means the action belongs to this class [22]. The training process of the SVM classifier is described as follows:

Step 1. Prepare a training set. Divide the training set into the same number of male and female sample sets, which should include a positive sample set and a negative sample set. The size of the training sample set directly affects the classification performance of the SVM classifier. The larger the training sample set is, the

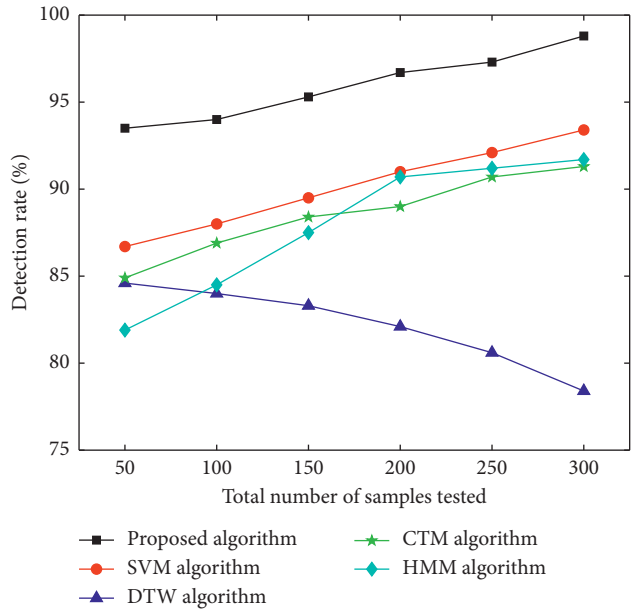

Figure 6: Detection rate of male phlegm samples.

better the classification performance will be, and the sample set should include all possible cases.

Step 2. Place the positive and negative samples in different folders and normalize the size of all training samples.

Step 3. Complete feature extraction of positive and negative samples and assign "+1" or "−1"olabels to all positive and negative samples, respectively.

Step 4. Input the positive and negative sample features and labels into the SVM for sample training and finally obtain the SVM target classifier.

Next is the target detection and recognition with VDS. First, carry out the feature extraction of targets to be detected. Work out the distance of two sequence images with DTW. Input velocity features into the trained SVM target classifier. Finally, the classifier will output class decisions. In this way, the target recognition process is accomplished.

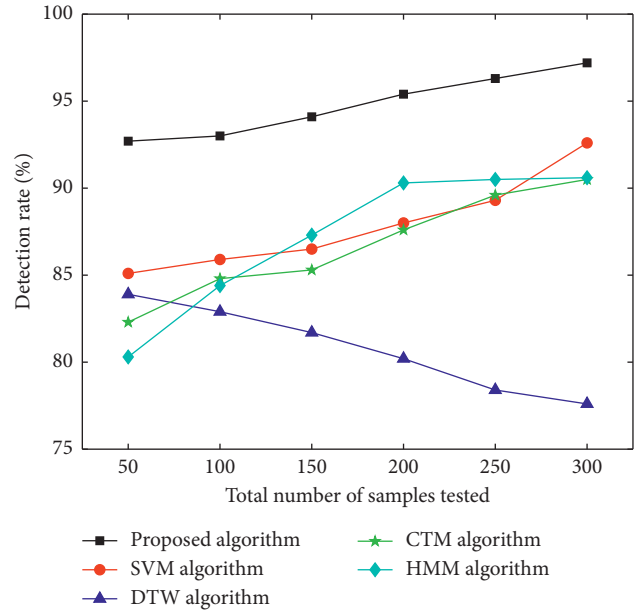

Figure 7: Detection rate of female phlegm samples.

4. Experiments and Result Discussion

The laryngeal video images were processed by three-frame differencing, and the effect was shown in Figure 5. Figure 5(a) is the test images without a sticker. Figure 5(b) is the detection image with a sticker. Figures 5a(a1)–5a(a10) are the originally collected video images without stickers and the results obtained by simulation. Figures 5b(b1)–5b(b10) are the originally collected video images with stickers and the simulation images. From these comparisons, we can see that images with stickers make the target clearer and easier to detect, which improves the accuracy in target feature detection and recognition. Therefore, this paper detected phlegm stagnation symptoms in patients with stickers in the throat to obtain better recognition accuracy. In practice, we can achieve the sticker effect by putting something on the patient's throat.

Samples used in the experiment were video images collected in those with the phlegm stagnation symptom from October 2017 to February 2018. On the MATLAB platform, the three-frame differencing method was implemented to extract moving objects from video images. The velocity of moving targets was extracted, and then the samples (i.e., the test set) were classified and recognized with the VDS algorithm. In this paper, we compared the VDS algorithm with DTW, SVM, CTM, and HMM algorithms in the target detection rate and average

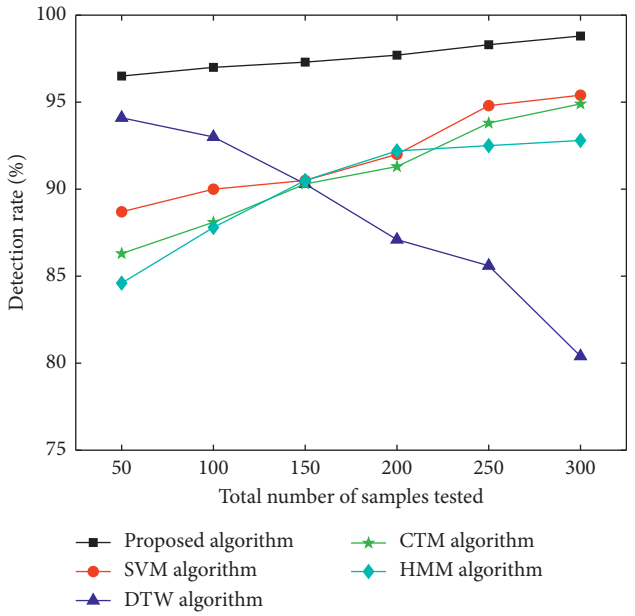

Figure 8: Detection rate of male nonphlegm sample.

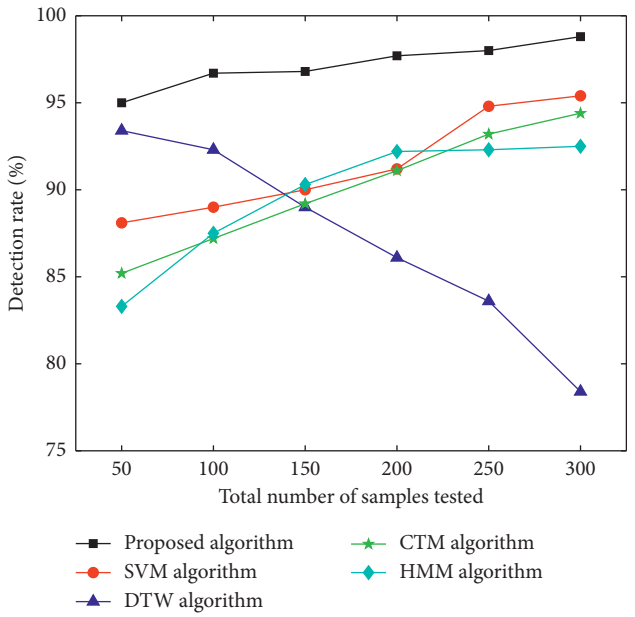

Figure 9: Detection rate of female nonphlegm samples.

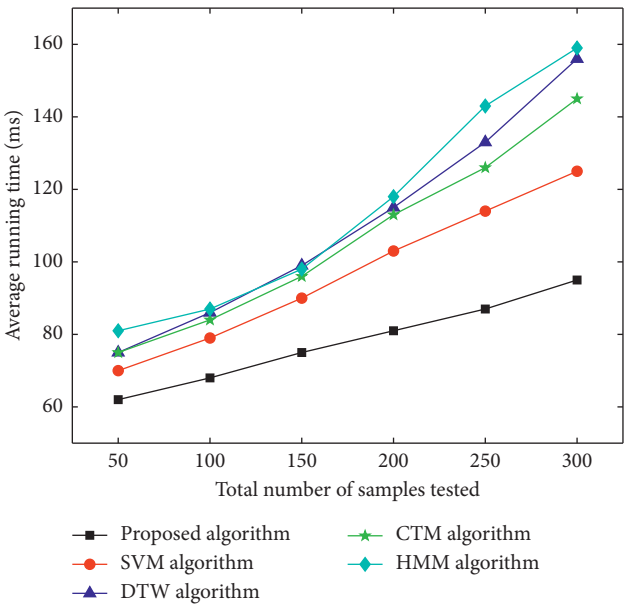

Figure 10: Average detection time on male samples.

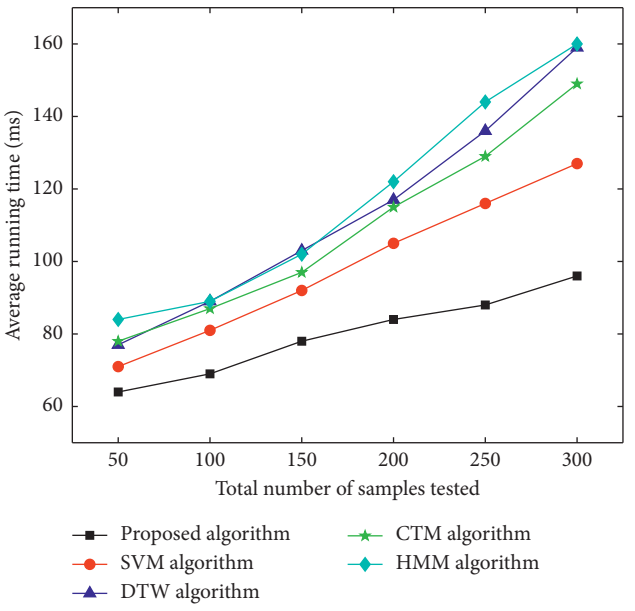

Figure 11: Average detection time on female samples.

running time under the same sample size and different sample sizes. The selected sample size was 50, 100, 150, 200, 250, and 300 male samples and the same number of female samples. The male samples are divided into two categories, namely, phlegm samples and nonphlegm samples. Phlegm samples and nonphlegm samples were tested at 25, 50, 75, 100, 125, and 150. Female samples were tested in the same situation as male samples. The detection rate and average running time of phlegm and nonphlegm samples in male and female samples were shown in Figures 6–11 and Tables 1–3. According to Tables 1–3, the detection rate of male samples, including both phlegm and nonphlegm, is higher than the female sample detection rate; the average running time of the experiment is lower than the average running time of the female sample. This is because the male throat features are more prominent and thus easier to detect and identify. According to Figures 6–11, the detection rate and average running time of the algorithm proposed in this paper were both significantly better than the other four algorithms, which means our method owns significant advantages. The feature of the SVM, CTM, and HMM classifier is that the

Table 1: Detection rate of phlegm samples (%).

	VDS (male)	VDS (female)	SVM (male)	SVM (female)	DTW (male)	DTW (female)	CTM (male)	CTM (female)	HMM (male)	HMM (female)
50	93.5	92.7	86.7	85.1	84.6	83.9	84.9	82.3	81.9	80.3
100	94	93	88	85.9	84	82.9	86.9	84.8	84.5	84.4
150	95.3	94.1	89.5	86.5	83.3	81.7	88.4	85.3	87.5	87.3
200	96.7	95.4	91	88	82.1	80.2	89.0	87.6	90.7	90.3
250	97.3	96.3	92.1	89.3	80.6	78.4	90.7	89.6	91.2	90.5
300	98.8	97.2	93.4	92.6	78.4	77.6	91.3	90.5	91.7	90.6

Table 2: Detection rate of nonphlegm samples (%).

	VDS (male)	VDS (female)	SVM (male)	SVM (female)	DTW (male)	DTW (female)	CTM (male)	CTM (female)	HMM (male)	HMM (female)
50	96.5	95	88.7	88.1	94.1	93.4	86.3	85.2	84.6	83.3
100	97	96.7	90	89	93	92.3	88.1	87.2	87.8	87.5
150	97.3	96.8	90.5	90	90.3	89	90.3	89.2	90.5	90.3
200	97.7	97.7	92	91.2	87.1	86.1	91.3	91.1	92.2	92.2
250	98.3	98	94.8	94.8	85.6	83.6	93.8	93.2	92.5	92.3
300	98.8	98.8	95.4	95.4	80.4	78.4	94.9	94.4	92.8	92.5

Table 3: Average detection time of samples (ms).

	VDS (male)	VDS (female)	SVM (male)	SVM (female)	DTW (male)	DTW (female	CTM (male)	CTM (female)	HMM (male)	HMM (female)
50	62	64	70	71	75	77	75	78	81	84
100	68	69	79	81	86	89	84	87	87	89
150	75	78	90	92	99	103	96	97	98	102
200	81	84	103	105	115	117	113	115	118	122
250	87	88	114	116	133	136	126	129	143	144
300	95	96	125	127	156	159	145	149	159	160

larger the sample set is, the better the classification performance it will have. So the trends of the VDS, SVM, CTM, and HMM algorithm curves were different from the DTW algorithm. The recognition time of DTW is proportional to the number of training samples, and the overall efficiency is very poor. Compared with the DTW model, the VDS, SVM, CTM, and HMM have very short training time and recognition time, which gives the VDS obvious efficiency advantages in the analysis of the monitoring results. Therefore, the combination of DTW and SVM algorithm can automatically match the action sequence, and the distance between the laryngeal action sequences and the similar rate can reflect the similarity of the symptoms, thus achieving a higher recognition rate of phlegm stagnation symptom. Experiments showed that the proposed method was applicable to the phlegm stagnation monitoring system. When the VDS algorithm recognized the phlegm stagnation symptom, the alarm device starts immediately. The caregiver can make timely sputum suction for patients. It can not only monitor the patient's physical condition in real time and thus promote the performance of the monitoring system but also brings more convenience to the caregiver. Free from real time manual monitoring, the caregiver is largely relaxed.

5. Conclusions

This paper proposed a VDS algorithm for phlegm stagnation symptom recognition in nonmedical sputum monitoring system. It combines speed characteristics, DTW, and SVM to identify laryngeal actions and classify phlegm stagnation status. The experiments showed that our method can adapt to the laryngeal movement of different lengths and speeds. It is applicable to the phlegm stagnation symptom identification and monitoring system. When the VDS algorithm recognizes the phlegm stagnation status, an alarm device is activated immediately. The nursing staff can solve the problem of phlegm stagnation easily by using the suction method, which can monitor the patient's condition in real time, improve the monitoring system, and bring great convenience to the nursing staff as well. With no need of manual operation all the time, our method will greatly reduce the pressure of nursing staff.

Data Availability

The image data used to support the findings of this study are available from the corresponding author upon request.

Conflicts of Interest

The authors declare that they have no conflicts of interest.

References

[1] Y. Shi, Y. Wang, M. Cai, B. Zhang, and J. Zhu, "An aviation oxygen supply system based on a mechanical ventilation model," *Chinese Journal of Aeronautics*, vol. 31, no. 1, pp. 197–204, 2018.

[2] Y. Shi, B. Zhang, M. Cai, and W. Xu, "Coupling effect of double lungs on a VCV ventilator with automatic secretion clearance function," *IEEE/ACM Transactions on Computational Biology and Bioinformatics*, vol. 16, no. 4, pp. 1280–1287, 2019.

[3] B. Daicoff, L. MRJr Jr., T. Mullet, and H. Yarandi, "Physiologic response to two endotracheal suctioning techniques in newborn lambs with and without acute pulmonary hypertension," *American Journal of Critical Care*, vol. 4, no. 6, pp. 453–459, 1995.

[4] M. Kou, Q. Wang, and T. Tan, "Google map research on google map algorithm and application," *Computer Technology and Development*, vol. 22, no. 4, pp. 204–206, 2012.

[5] Y. Yin and H. Mo, "The identification method of cough signals using mel-frequency cepstrum coefficient," *Information Technology*, vol. 1, no. 10, pp. 85–91, 2012.

[6] S. H. Shin, T. Hashimoto, and S. Hatano, "Automatic detection system for cough sounds as a symptom of abnormal health condition," *IEEE Transactions on Information Technology in Biomedicine: A Publication of the IEEE Engineering in Medicine and Biology Society*, vol. 13, no. 13, pp. 486–493, 2009.

[7] T. Drugman, J. Urbain, N. Bauwens et al., "Objective study of Sensor relevance for automatic cough detection," *IEEE Journal of Biomedical and Health Informatics*, vol. 17, no. 3, pp. 699–707, 2013.

[8] X. TAN and Y. WU, "Research and application of moving target detecting method based on OpenCV," *Video Application & Project*, vol. 34, no. 1, pp. 184–193, 2010.

[9] T. Ling, L. Chong, X. Jingming, and C. Jun, "Application of self-organizing feature map neural network based on K-means clustering in network intrusion detection," *Computers, Materials & Continua*, vol. 61, no. 1, pp. 275–288, 2019.

[10] Y. Ye, Y. Guan, and J. Li, "Foreground target detection based on Gaussian mixture model and code book algorithm," *Computer Engineering*, vol. 3, no. 5, pp. 1–4, 2012.

[11] X. Song and J. Chen, "A robust moving objects detection based on improved Gaussian mixture model," in *Proceedings of International Conference on Artificial Intelligence and Computational Intelligence*, IEEE Press, Sanya, China, October 2010.

[12] F. Yu, "Research on intelligent video surveillance and retrieval system,"Wuhan University of Technology, Master's thesis, 2013, pp. 5–1, Wuhan University of Technology, Wuhan, China.

[13] D. Wang, R. He, J. Han, M. Fattouche, and F. M. Ghannouchi, "Sensor network based oilwell health monitoring and intelligent control," *IEEE Sensors Journal*, vol. 12, no. 5, pp. 1326–1339, 2012.

[14] X. Sun and S.-A. Zhu, "Intelligent monitoring Security alarm system," *Electronic Technology*, vol. 39, no. 2, pp. 28–32, 2012.

[15] F. Meng, Y. Wang, Y. Shi, and H. Zhao, "A kind of integrated serial algorithms for noise reduction and characteristics expanding in respiratory sound," *International Journal of Biological Sciences*, vol. 15, no. 9, pp. 1921–1932, 2019.

[16] J. Niu, Y. Shi, M. Cai et al., "Detection of sputum by interpreting the time-frequency distribution of respiratory sound signal using image processing techniques," *Bioinformatics*, vol. 34, no. 5, pp. 820–827, 2017.

[17] S. Ren, M. Cai, Y. Shi, W. Xu, and X. D. Zhang, "Influence of bronchial diameter change on the airflow dynamics based on a pressure-controlled ventilation system," *International Journal for Numerical Methods in Biomedical Engineering*, vol. 34, no. 3, p. e2929, 2018.

[18] L. Rabiner, *Fundamentals of Speech Recognition*, Prentice-Hall, Boston, MA, USA, 1993.

[19] D. Sankoff and J. B. Kruskal, *The Theory and Practice of Sequence Comparison*, Addison-Wesley, Boston, MA, USA, 1983.

[20] Z. Zhao, X. Wang, and T. Wang, "A novel measurement data classification algorithm based on SVM for tracking closely spaced targets," *IEEE Transactions on Instrumentation and Measurement*, vol. 68, no. 4, pp. 1089–1100, 2019.

[21] Y. Zhang, D. Zhu, Bi Hui et al., "Scattering key-frames extraction for comprehensive video SAR summarization: a spatiotemporal background subtraction perspective," *IEEE Transactions on Instrumentation and Measurement*, 2019.

[22] W. Xie, P. Gaydecki, and A.-L. Caress, "An inhaler tracking system based on acoustic analysis: hardware and Software," *IEEE Transactions on Instrumentation and Measurement*, vol. 68, no. 11, pp. 4472–4480, 2019.

Hindawi
Journal of Healthcare Engineering
Volume 2020, Article ID 6968713, 11 pages
https://doi.org/10.1155/2020/6968713

Research Article

EEG-Controlled Wall-Crawling Cleaning Robot Using SSVEP-Based Brain-Computer Interface

Lei Shao,[1] Longyu Zhang,[1] Abdelkader Nasreddine Belkacem,[2] Yiming Zhang,[1] Xiaoqi Chen,[1] Ji Li,[1] and Hongli Liu[1]

[1]*Key Laboratory for Control Theory & Applications in Complicated Systems, Tianjin University of Technology, Tianjin 300384, China*
[2]*Department of Computer and Network Engineering, College of Information Technology, United Arab Emirates University, Al Ain, P.O. Box 15551, UAE*

Correspondence should be addressed to Abdelkader Nasreddine Belkacem; belkacem@uaeu.ac.ae

Received 13 August 2019; Revised 29 October 2019; Accepted 29 November 2019; Published 11 January 2020

Guest Editor: Ludovico Minati

The assistive, adaptive, and rehabilitative applications of EEG-based robot control and navigation are undergoing a major transformation in dimension as well as scope. Under the background of artificial intelligence, medical and nonmedical robots have rapidly developed and have gradually been applied to enhance the quality of people's lives. We focus on connecting the brain with a mobile home robot by translating brain signals to computer commands to build a brain-computer interface that may offer the promise of greatly enhancing the quality of life of disabled and able-bodied people by considerably improving their autonomy, mobility, and abilities. Several types of robots have been controlled using BCI systems to complete real-time simple and/or complicated tasks with high performances. In this paper, a new EEG-based intelligent teleoperation system was designed for a mobile wall-crawling cleaning robot. This robot uses crawler type instead of the traditional wheel type to be used for window or floor cleaning. For EEG-based system controlling the robot position to climb the wall and complete the tasks of cleaning, we extracted steady state visually evoked potential (SSVEP) from the collected electroencephalography (EEG) signal. The visual stimulation interface in the proposed SSVEP-based BCI was composed of four flicker pieces with different frequencies (e.g., 6 Hz, 7.5 Hz, 8.57 Hz, and 10 Hz). Seven subjects were able to smoothly control the movement directions of the cleaning robot by looking at the corresponding flicker using their brain activity. To solve the multiclass problem, thereby achieving the purpose of cleaning the wall within a short period, the canonical correlation analysis (CCA) classification algorithm had been used. Offline and online experiments were held to analyze/classify EEG signals and use them as real-time commands. The proposed system was efficient in the classification and control phases with an obtained accuracy of 89.92% and had an efficient response speed and timing with a bit rate of 22.23 bits/min. These results suggested that the proposed EEG-based clean robot system is promising for smart home control in terms of completing the tasks of cleaning the walls with efficiency, safety, and robustness.

1. Introduction

The idea of interfacing brains with machines/robots has long captured the human imagination. Brain-computer interface (BCI) technology intend to build an interface between the brain and any electrical/electronic device (e.g., a wheelchair, smart home appliances, and robotic devices) using electroencephalogram (EEG) which is a noninvasive technique for measuring electrical potentials from electrodes placed on the scalp produced by brain activity. Nowadays, the EEG technique has been used to establish portable synchronous and asynchronous controls for BCI applications. Noninvasive EEG-based BCIs are the most promising interface for space of applications for people with severe motor disabilities because of their noninvasiveness, low cost, practicality, portability, and being easy to use. For some disabled patients with physical disability or paralysis while the brain function is still normal, although they have a normal large brain consciousness and thought, they cannot communicate with the external environment through the severely

damaged muscle and nervous system and complete the daily work independently. This has caused serious physical and mental trauma, and their lives are very painful, which will affect their recovery process to some extent. How to restore or enhance their control and communication capabilities to the outside world has been the goal that has been pursued for many years in the field of medical rehabilitation. Therefore, BCIs can be used for helping patients with severe brain disorders or muscle damages to regain their ability to communicate directly with the outside environment through the brain electrophysiology response [1–3]. BCI can also be beneficial for the elderly as advanced assistive and rehabilitative technologies and useful for young able-bodied for controlling video games for entertainment [4, 5] or controlling a robotic arm for several purposes [6–9]. However, most of the traditional brain-computer interface equipment is expensive, bulky, and tedious, which makes it difficult to popularize and apply brain-computer interface technology in real life. The portable brain-computer interface has become one of the hotspots in the field of the brain-computer interface because of its advantages of easy to carry, easy to use, safe, and reliable.

BCI technology is mainly divided into two types of brain activity measurement, invasive BCI, and noninvasive BCI, depending on the way of putting the electrodes to record the electrical brain activity [10–14]. Among them, the invasive BCI might lead to an immune reaction, which causes serious harm to the user, and it is hardly accepted by disabled people because of the invasiveness of the technique which requires a dedicated surgery, and its cost with equipment is very expensive and not covered by many governments yet. Although the noninvasive brain-computer interface is less accurate than the invasive BCI, it is still relatively cheaper compared with all other techniques and everyone can easily accept it. There are several paradigms to control machine or computer using our brain signal characteristics and the most popular ones are motor imagery [15, 16], P300 wave [17, 18], steady state visual evoked potentials (SSVEP) [19–21] for building practical brain-computer interface systems. So far, the SSVEP method was applied widely because of the high signal-to-noise ratio and robustness [22]. SSVEP induction means that when the human brain receives the stimulation of a fixed frequency scintillation block, an uninterrupted response related to the stimulation frequency will be generated in the visual cortex of the human brain. This SSVEP brain response is a very useful natural involuntary phenomenon which has been tested by researchers many times. The earliest SSVEP-BCI system, designed by Regan , in 1979, allowed subjects to select a flashing button on the computer screen by simply looking at the computer screen [23], basically achieving the desired design goals. Then, Mullerputz and Guneysu and Akin applied the SSVEP-BCI system to the physical control of neural limb and humanoid robot, respectively, and achieved good control results [24]. In this paper, we chose SSVEP because it does not need any training phase for subjects and has very high accuracy compared with P300 or motor imagery using single trial electroencephalography (EEG) signal. The commonly used signal processing and classification methods of SSVEP include fast Fourier transform (FFT), wavelet transform, canonical correlation analysis (CCA), linear discriminant analysis (LDA), and support vector machine (SVM). In this paper, CCA was used for developing our signal processing algorithm. Compared with other SSVEP signal classification algorithms [10–14, 25], CCA classification algorithm is fast, efficient, simple, and easy to use.

In some previous researches, the SSVEP paradigm was successfully used in writing tasks [26]. In the paper [27], we can see that the authors proposed a hybrid brain-computer interface system that combines P300 and SSVEP modalities. This combined system has improved the accuracy of EEG-based wheelchair control. In addition, SSVEP has been also used in the mental spelling system [28, 29]. In the paper [30], the authors used three flash speeds to control the small robot car. Lee et al. only use OZ as the reference electrode to collect and process EEG signals. In the paper [31], Lu and Bi have proposed a longitudinal control system for brain-controlled vehicles based on EEG signals. However, it is still unknown whether it can be used in the industry.

In this paper, a new type of intelligent crawler robot is designed for cleaning the walls, which is considered as one of the smart home appliances. Compared with the wheeled robot [32], the crawler robot has the advantages of long life and high carrying capacity. The intelligent crawling robot for the walls used in this experiment adds an adsorption device using negative vacuum pressure, which effectively solves the problem of sliding of the cleaning robot on a wall with a certain inclination angle. The BCI based on SSVEP can usually provide a high information transmission rate, the verification process of the system is relatively simple, and no training of the subjects is required. However, because the SSVEP of some subjects is very weak and vulnerable to the interference of other noise signals, how to accurately identify SSVEP from a short time window is still a challenging problem in BCI research based on SSVEP. This is also the subject that we will continue to study in the future. In this study, the SSVEP paradigm was designed to control the crawler robot for cleaning the dust on the walls. We used the high accuracy SSVEP paradigm to cooperate with our cleaning robot to complete the designed experiment. To our best knowledge, this is the first report, which used brain machine interface for crawling cleaning robot control to help persons with disabilities to improve their quality of life.

This paper is arranged as follows: in the Materials and Methods section, the experimental paradigm and analysis method of brain signal and the motion model of the intelligent crawling robot were introduced. At the same time, the offline experiment and online experiment are completed, and the data analysis is carried out. In the Results section, the offline and online experiments were summarized and discussed separately, and the accuracy and ITR of the experiment were obtained. Our experiments validate our views and achieve the desired results. In the Discussion part, we mainly talk about the limitations of the system and put forward the future changes. Finally, conclusion and prospects of future work are given in Section 5.

2. Materials and Methods

2.1. Participants and Experimental Paradigm. Seven healthy volunteers (4 males and 3 females, 23–27 years of age) were invited to join the experiment for performing some robot control tasks using their brain activity. None of the subjects have prior experience on brain-computer interfaces. Clear written informed consent was obtained from all the participants, who were informed in detail about the purpose and possible consequences of the experiment. The experimental protocol was carried out in accordance with the latest version of the Declaration of Helsinki.

The experiments were carried out in a quiet and comfortable environment to reduce the noise effect on our EEG recording. Subjects sat on a chair which is 60 cm away from the screen which contains the stimulation interface. In order to ensure the accuracy of the experiment, participants were required to avoid gnashing during the experiment. Because the SSVEP paradigm was easy to cause fatigue, the subjects can take a rest after one session. The flow of the experiment is shown in Figure 1. The experimental process is mainly divided into three parts. Firstly, the EEG acquisition device should be worn correctly for the subject and the subject's position should be adjusted. Secondly, the collected data are processed and classified by a signal processing computer. Finally, the processed instructions are sent to the lower computer, that is, the intelligent crawling robot.

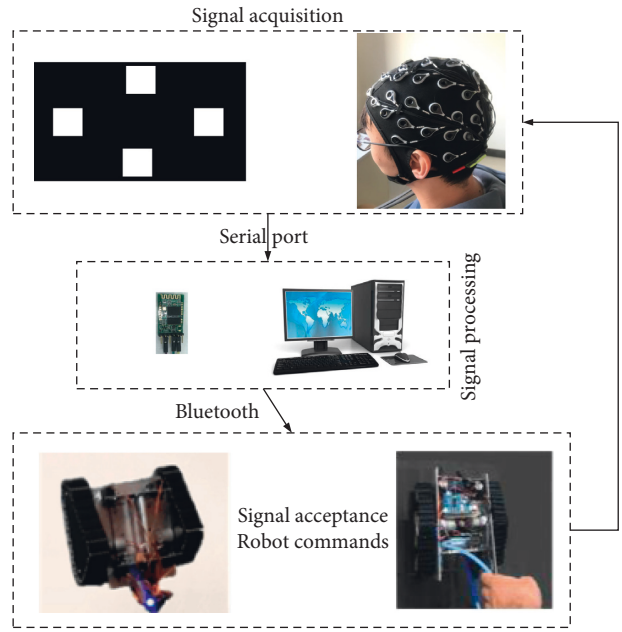

Figure 1: Experimental flowchart for our proposed SSVEP EEG-based BCI for robot control system.

2.2. Experimental Materials. As shown in Figure 1, the hardware system in this experiment mainly includes five parts: EEG signal acquisition system (Brain Products, Germany), computer for displaying visual stimulation interface, computer for signal processing, Bluetooth module for transmitting signals wirelessly, and intelligent crawling robot for cleaning dust on the walls.

We have avoided in this study to use EMOTIVE EPOC equipment which is relatively cheap consumer-grade EEG signal acquisition device because its measurement signal quality is not good enough for getting high classification accuracy using SSVEP modality. On the contrary, Brain Products can effectively collect the EEG signals induced by SSVEP, record real-time characteristic signals, and have good effects. EEG equipment (Brain Products) has the advantages of lightweight, flexible usage, and excellent and stable signals. Therefore, this EEG equipment was used to collect brain signals in our experiment. The EEG signal acquisition device used in our experiment is shown in Figure 2.

The EEG signal acquisition device selected in the experiment consists of 64 electrodes. 32 black circles represent effective electrodes and white circles are invalid electrodes. All 32 channel electrodes which include 30 EEG signals acquisition channels, 1 reference channel, and 1 ground channel were used to record brain signal. The position of each channel was shown by black circles. The sampling rate was 500 Hz. During the experiment, the impedance of each channel was always below 10 k ohms to ensure the quality of EEG signals. Because the SSVEP signal is generated by the visual cortex of the brain, the EEG signals of O1, O2, P7, and P8 channels near the visual cortex are collected in the experiment, which will not affect the acquisition of SSVEP signal, but also greatly reduce the amount of data processed by EEG.

The stimulation interface of the experimental paradigm was designed by using MATLAB psychology toolbox. This interface contains four blocks which flash at frequencies 6 Hz, 7.5 Hz, 8.57 Hz, and 10 Hz, respectively, four blocks were shown in the top, bottom, left, and right part of the screen, and the refresh rate of the screen was set in 60 Hz. The driving chip of the intelligent component used in the experiment is the L298P double H-bridge DC motor driving chip, which integrates most of the functions, making the chip more suitable for robot development. We designed a new crawler robot and also upgraded the adsorption capabilities of this robot. The traditional suction cup has a small adsorption capacity and is unstable, so the adsorption device we use uses a vacuum pump to generate a negative pressure to avoid the disadvantages of the conventional suction cup. Most of the photovoltaic robots on the market are roller brushes. The roller brushes are not only easy to absorb dust, but also occupy a relatively large area of the robot. Therefore, the crawling cleaning robot we use uses a three-legged brush head. After a series of experiments, the most suitable for the cleaning of the walls is to use a motor with a speed of 200 rpm to control our three-legged brush head. The robot relies on the suction cup to be adsorbed on the walls, and the walls can be stably and selectively cleaned, thereby reducing the trouble of cleaning the entire walls.

2.2.1. Offline Experiment. The whole experiment was divided into offline and online subexperiments. Offline experiment was held to confirm the experiment set up and

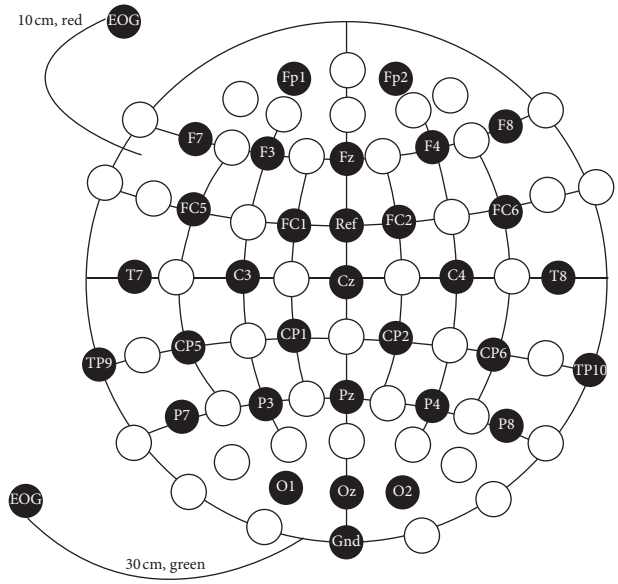

Figure 2: EEG electrodes placement used in our experiment using Brain Products equipment.

adjust the parameter for each subject. The offline experiment steps are as follows: start our stimulation interface, which starts with an exclamation mark to remind the subjects to start the experiment. After that the four different frequency blocks on the top, bottom, left, and right of the screen start to flicker. During the offline experiment, the subjects listened to the arrangement to look at each of the four different frequencies blocks. The subjects were assigned to look at each of the four scintillation blocks for five times, and the duration of each time was between 20 and 25 seconds. Twenty datasets were collected for each subject.

2.2.2. Online Experiment. The experimental process of the subjects is shown in Figure 3. First, start our cleaning robot and turn on the cleaning device. Before the online experiment, we must ensure that the subject is in a comfortable position and that the EEG signal collection cap is correctly worn. Secondly, ensure that the cleaning robot is connected to our upper computer normally. In addition, the speed of the cleaning robot is set. After that, we started our online experiment. In the online experiment, the subjects confirm the position of the cleaning robot and the dirty place on the wall. Then, the subjects make the decision, which directs the clean robot to move and look at the responding flash block on the screen. At the same time, the EEG data were recorded from the participants; then it was analyzed at the host computer. The algorithm could recognize which block the subject looked at and transform the control command of the clean robot. Then, the command, which was recognized, was sent to the clean robot by the Bluetooth module. According to the command, the clean robot will move and make the walls cleaner.

To evaluate the experiment performance more easily, we set up several groups of online experiments. First, the clean robot was put on the wall, and the dirty place was not so far away from the original place of the clean robot. Therefore, the subjects can control the clean robot to reach the dirty place within 30 steps with optimized route, as shown in Figure 4.

This figure shows the path of a subject during an online experiment. For each session, the subject was limited to perform 30 steps. If the subject cannot control the clean robot to reach the destination, this experiment will finish and the task and system performance will be evaluated.

2.3. Signal Acquisition and Processing. The flowchart of signal acquisition and processing is shown in Figure 5. During our experiment, we used BrainVision Recorder software to record the EEG signals of the subjects. When using BrainVision Recorder software, we ensure that the impedance of the subjects' electrodes is below 10 k ohms. P7, P8, O1, and O2 channels, which cover the vision areas of the brain, were mainly analyzed.

Wavelet transform was employed as band-pass filter, removing DC Component of Signal. For SSVEP paradigm, canonical correlation analysis is a multivariate statistical analysis method that reflects the overall correlation between two groups of indicators by using the correlation between pairs of comprehensive variables; it has a good recognition effect in multichannel EEG signals. Compared with other SSVEP signal classification algorithms, CCA classification algorithm is fast, efficient, simple, and easy to use. In the paper [33], the CCA classification algorithm is compared with the power spectral density analysis (PSDA). The test results show that the classification accuracy of CCA classification algorithm is higher than that of PSDA. In the paper [34], the CCA classification algorithm is compared with the minimum energy combination (MEC), and the anti-interference ability of the CCA classification algorithm is found to be stronger. These results fully demonstrate the reliability of the CCA classification algorithm. Therefore, CCA is applied to the brain-computer interface system based on

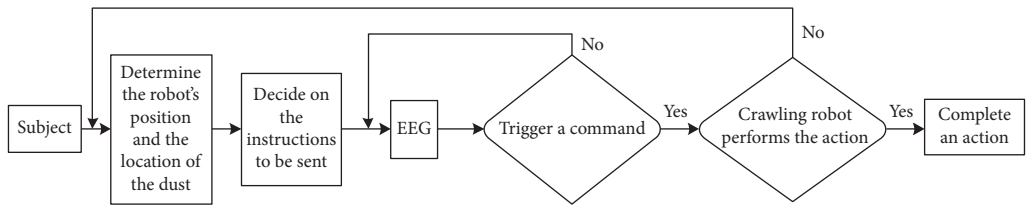

Figure 3: Flowchart of the subject performing a brain control task.

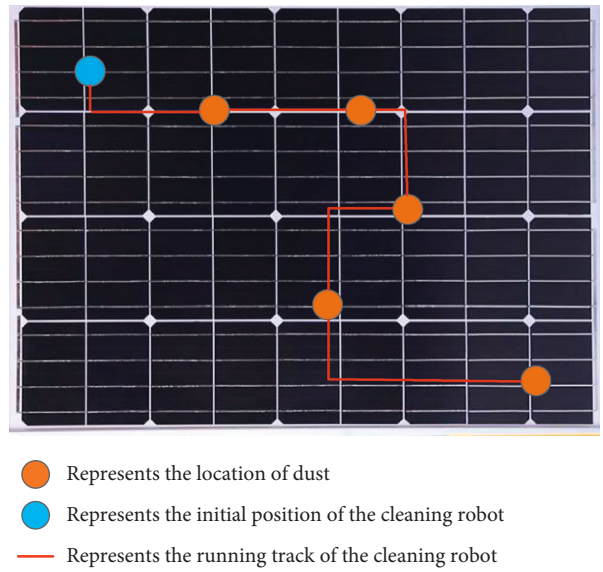

Figure 4: The online experimental paradigm with respect to the path of a representative subject.

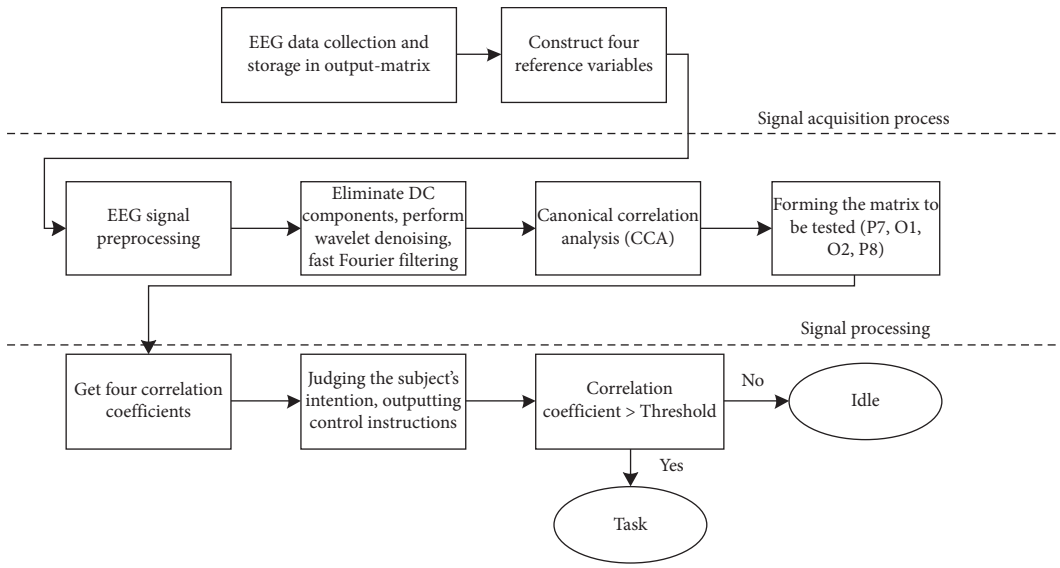

Figure 5: Signal analysis and processing steps of the proposed algorithm for decoding SSVEP from the EEG signal.

SSVEP. After preprocessing, CCA was used to analyze the brain signal.

One set of EEG signals is denoted as $x(t)$, and the second set of signals $y(t)$ is composed of signals with the same number of stimulation frequencies. We decompose a series of periodic signals into a series of Fourier functions. For a specific frequency f, there is the following equation

$$Y(f) = \begin{bmatrix} \sin 2\pi fn \\ \cos 2\pi fn \\ \sin 4\pi fn \\ \cos 4\pi fn \\ \cdots \\ \sin 2N_h \pi fn \\ \cos 2N_h \pi fn \end{bmatrix}, \quad n = \frac{1}{f_s}, \frac{2}{f_s}, \ldots, \frac{N}{f_s}, \tag{1}$$

where N is the number of sampling points. f_s is the sampling frequency, and N_h is the number of harmonics.

The feature extraction method of CCA is shown in Figure 6. Suppose that there are two groups of sample signals $X = (x_1, \ldots, x_n)$, $Y = (y_1, \ldots, y_m)$, and the linear combination of $x = X^T W_x$, $y = Y^T W_y$. Canonical correlation analysis method calculated the correlation $\rho(x, y)$ between x and y under the condition that the coefficients W_x and W_y is maximum. The equation was shown as follows:

$$\max_{W_x, W_y} \rho(x, y) = \frac{E[x^T y]}{\sqrt{E[x^T x]E[y^T y]}} = \frac{E\left[W_x^T X Y^T W_y\right]}{\sqrt{E\left[W_x^T X X^T W_x\right]E\left[W_y^T Y Y^T W_y\right]}}. \tag{2}$$

The correlation coefficient between the brain signal and four classes was computed. Therefore, the control command was set as the class with the maximum correlation coefficient.

In this study, information transmission rate (ITR) was calculated to evaluate the transmission performance of brain machine system. ITR (bit/min) can be calculated by the following formula:

$$\mathrm{ITR} = \frac{60}{t}\left[\log_2 N + \mathrm{Acc}\log_2 \mathrm{Acc} + (1 - \mathrm{Acc})\log_2 \mathrm{Acc}\frac{1 - \mathrm{Acc}}{N - 1}\right], \tag{3}$$

where t represents the sampling time, Acc represents the correct rate, and N represents the number of classifications.

2.4. Motion Model Analysis of Intelligent Crawling Robot. The intelligent crawling robot we use communicates with the upper computer through the Bluetooth module. The speed of the cleaning robot can be set according to needs using Bluetooth serial port assistant. Among them, the running speed of the cleaning robot affects its turning angle. The turning motion model is as follows:

(i) We set a time parameter t; when $t = 0$, the robot is in the original position, assuming that the position of the cleaning robot coincides with the coordinate system $\{X, O, Y\}$, and the coordinates of the robot are $\{X_{R0}, O_{R0}, Y_{R0}\}$, as shown in the blue position in Figure 7.

(ii) After that, the robot performs a turning action. Where the time is t, the robot reaches a new position with coordinates of $\{X_{Rt}, O_{Rt}, Y_{Rt}\}$, as shown in the red position in Figure 7.

The whole turning process of the robot takes the origin as the center. For the turning motion of the robot, for any time t, we have the following:

$$\begin{cases} x(t) = \frac{1}{2}\int_0^t [v_L(t) + v_R(t)]\cos[\theta(t)]\mathrm{d}t = 0, \\ y(t) = \frac{1}{2}\int_0^t [v_L(t) + v_R(t)]\sin[\theta(t)]\mathrm{d}t = 0, \end{cases} \tag{4}$$

where v_L is the speed of the left wheel of the crawling robot, v_R is the speed of the right wheel of the crawling robot, and θ represents the rotation angle of the crawling robot. We assume that $v_L = -v_R$; at this time, the crawling robot makes a rotation movement with the origin as the center, and the rotation angle is as follows:

$$\theta(t) = \frac{1}{D}\int_0^t [v_R(t) - v_L(t)]\mathrm{d}t = \frac{2v_R}{D}t, \tag{5}$$

where D is the distance between the two crawler wheels of the crawling robot.

3. Results

3.1. Offline Experiment and Result Analysis. For offline use, experiment data was saved in header file ".vhdr," and EEGLAB toolbox was used to process the data. In order to achieve a good effect in our online experiment, we need to process the offline experiment data of different subjects and adjust the parameters. The CCA threshold divides the state of subjects into idle state and task state. By comparing the CCA correlation coefficient of the subject in the idle state with the CCA correlation coefficient in the task state, we can determine the threshold of each subject. We adjusted the subject threshold based on the analysis of the subjects' offline data, which were shown in Table 1.

3.2. Online Experiment and Result Analysis. In order to make our experimental data more accurate, when the subject completes the cleaning task within 30 steps, the time is

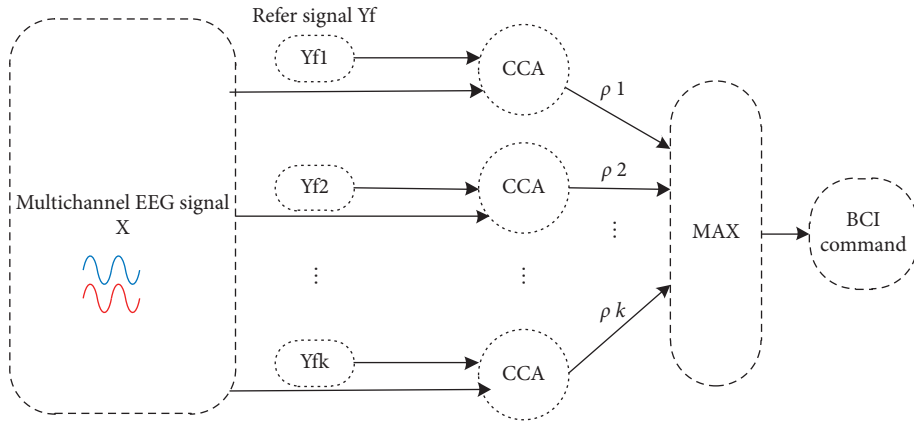

Figure 6: Feature extraction phase of CCA.

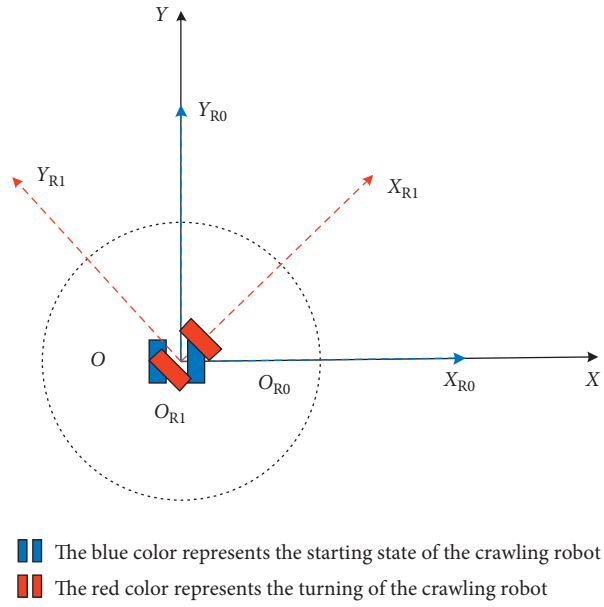

Figure 7: Moving model of the crawler robot turning.

stopped when the task is completed, but the subject continues to perform the task until the end of the 30 steps. When the subject does not complete the task within 30 steps, the time is counted based on the time when 30 steps are completed. Each subject has to perform six sets of tasks.

After the experiment, we performed some statistical analysis methods to evaluate the subjects' completion of the tasks. Four people were able to complete all the tasks with high accuracy and precision. The statistic results are shown in Table 1. The experimental data showed that the average accuracy of the subjects was 89.92 (with standard deviation of ±3.81%), and the ITR reached 22.23 ± 1.19 bits/min. The experimental situation of the subjects is shown in Table 2. In order to further verify the reliability of our experimental results and make the data statistically significant, we performed the variance calculation, and the variance calculation results are shown in Table 3. Accuracy in Table 3 is the average of the ratio of the total number of correct commands to the total number of commands in six experiments per person.

We noticed that our online experiments seem to have good output results compared to the existing BCIs in terms of task, accuracy, and ITR. We have listed the graphs for intuitive statistics and comparisons, as shown in Figure 8. These results show that our experiments validate our views and achieve the desired results.

4. Discussion

In this paper, EEG-controlled wall-crawling cleaning robot using SSVEP brain-computer interface is proposed, and the CCA algorithm is used for signal analysis. In this engineering study, the experiment results showed that our

Table 1: Coefficients for different SSVEP states.

SSVEP state	Mean ± SD
6 Hz	0.40 ± 0.12
7.5 Hz	0.44 ± 0.09
8.57 Hz	0.50 ± 0.10
10 Hz	0.51 ± 0.05
Idle	0.16 ± 0.04

Table 2: Experimental statistics.

Subject	Number of completed tasks	The average time
S1	6	6′25″
S2	6	6′56″
S3	6	6′17″
S4	6	5′59″
S5	4	6′00″
S6	5	6′56″
S7	4	7′00″

Table 3: Data statistics of subjects.

Subject	Accuracy (%)	ITR (bits/min)	Variance
S1	91.11	22.52	9.88
S2	89.45	22.26	12.65
S3	91.11	22.52	6.16
S4	91.11	22.52	9.88
S5	91.67	22.61	13.89
S6	88.89	22.17	13.57
S7	86.11	21.04	5.25
Average	89.92 ± 3.81	22.23 ± 1.19	10.18 ± 4.93

proposed brain-computer interface system is very promising and could control the proposed designed intelligent clean robot successfully to complete the cleaning tasks of a wall. The offline experiment provided the threshold for the next experiments. In addition, the test range of different experimenters can be determined by the same offline experiment. The online experiment was used to adjust the threshold to improve the classification accuracy of the experiment. After analyzing and calculating the data, we got the following results: the average accuracy of online experiment was 89.92%, and the ITR reached 22.23 bits/min. This shows that our experiments validate our research hypothesis and achieve the desired target. However, there are still some issues and limitations in the proposed BCI system.

The main innovation of this paper is to design a new type of cleaning robot that can enhance the abilities of the elderly users and help handicapped patients to control home appliances that might be available in their usual environment to increase their personal autonomy to be able to perform daily activities. Practicing EEG-based control in daily life might be a good option for enhancing brain abilities too. However, eye movements are also another option instead of using brain activity.

Electrooculography (EOG) is a technique for measuring the corneo-retinal standing potential that exists between the front and the back of the human eye. This technique has been widely used in developing human machine interfaces and it can be easily combined with brain activity. However, the signal of eye movements/blinking is relatively not weak. Therefore, it is difficult to remove this electrical interference due to the synchronization with EEG signal. If we use the eye movements directly to control the cleaning robot, we need to add eye gaze/tracking equipment, which needs to be well calibrated. In the process of eye movements' acquisition, the structure of the human eye leads to fatigue. In addition, the users are unable to look at the same target point for a long time. This long gaze concentration leads to the eye movements, the false eye jump, and the unconsciousness blinking [35]. These erroneous and unconscious EEG signals will bring difficulties to feature extraction and classification, resulting in a low recognition rate [36, 37].

In this paper, SSVEP is mainly used to overcome the shortcomings of using only eye movement instrument. Moreover, the combination of EEG and EOG (eye movement) as an innovative research for building hybrid BCIs is the direction of our future consideration.

After Hotelling put forward the typical classical algorithm in 1936, it has received great attention in various research fields. Some Japanese researchers adopted the canonical correlation analysis (CCA) method to extract two layers of reference signals from the actual SSVEP signal training concentration. Combining the obtained reference signals with CCA, an effective spatial filter for frequency recognition is derived, which greatly improves the recognition accuracy and information transmission rate of SSVEP [34]. Twelve categories of SSVEP signals were generated by modulating waveforms and were analyzed by CCA algorithm with an average accuracy of 92.31% [38]. Obviously, the application of CCA in EEG signal processing has been quite common, especially the frequency recognition of SSVEP signal which has high accuracy. In this paper, the traditional classical analysis algorithm is used. CCA algorithm is used to analyze SSVEP, the correlation coefficients between brain signal and four kinds of brain signal are extracted and calculated, and the transmission rate and the accuracy of online experiment are calculated. Although the CCA algorithm used in this paper has great advantages in SSVEP, compared with SVM method [25], it still needs to be improved. Because the human brain has complex neural mechanisms, it may not be a simple linear transformation in the transmission of electrical signals in the brain. In addition to the time and frequency characteristics that we usually consider, EEG also contains other important data characteristics, such as the variability between experiments and the specificity between subjects [12, 39]. Therefore, improving feature extraction and classification algorithm will be the focus of our future research to improve the robustness and accuracy of the system and reduce errors.

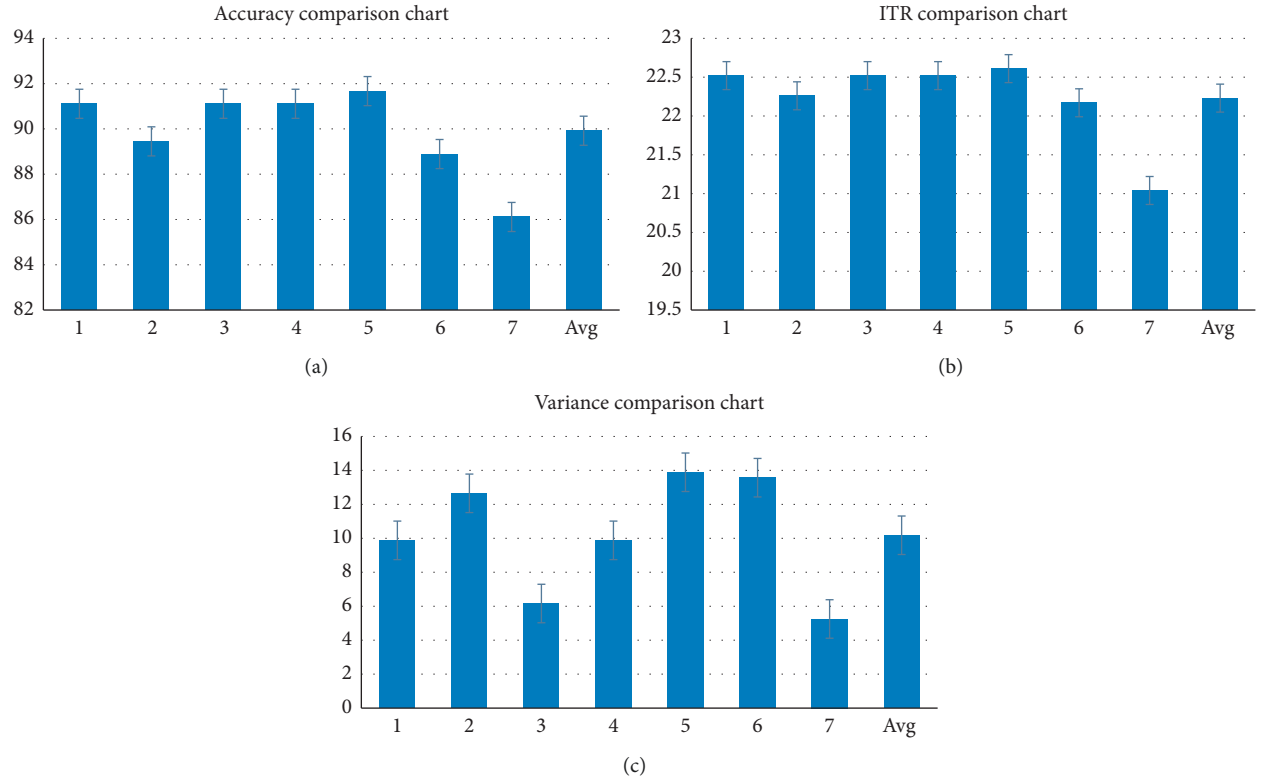

Figure 8: Experimental results of our proposed BCI system for evaluating the classification accuracies, ITR, and variance value among subjects. (a) The classification accuracy for each subject. (b) Information transfer rate for each subject. (c) Variance value for each subject.

5. Conclusion

In this paper, we proposed a new experimental paradigm for EEG-based clean robot control, which extended the usage of brain-computer interface. Compared with other paradigms like motor imager and P300, SSVEP is better for real-time application because SSVEP-based paradigm is not a subject-specific BCI, which requires individual data calibration regularly and system training, and it has achieved higher accuracy across subjects. For different subjects, the corresponding conditions are also different. During the experiment, we have selected the appropriate EEG acquisition cap according to different subjects. In addition, the fatigue issue was clearly observed in some subjects. Therefore, we eliminated the inaccurate experimental data caused. Although the conditions of different subjects are different, we also verified our system through our experiments.

Noninvasive brain-computer interface technology has built a bridge between human brain and smart robots, which has important research significance. In the near future, daily life BCI applications will be involved in fields that are more new. With the development of science and technology, brain-computer interface technology will not only bring hope to people with disabilities, but will also be more integrated into the life of ordinary people, bringing more convenience and use to our life. Through this experiment, we hope that in the future, we can recruit more subjects to verify the proposed system and make complex system in different conditions such as controlling a swarm of cleaning robots by one operator brain only.

Data Availability

The datasets generated and analyzed during the current study are not publicly available due to Tianjin University of Technology policy but are available from the first author upon reasonable request.

Conflicts of Interest

The authors declare that there are no conflicts of interests regarding the publication of this paper.

Acknowledgments

Part of this study was funded by the United Arab Emirates University (start-up grant G00003270 “31T130”).

References

[1] D. M. Taylor, S. I. H. Tillery, and A. B. Schwartz, “Direct cortical control of 3D neuroprosthetic devices,” *Science*, vol. 296, no. 5574, pp. 1829–1832, 2002.

[2] H. Wang and A. Bezerianos, “Brain-controlled wheelchair controlled by sustained and brief motor imagery BCIs,” *Electronics Letters*, vol. 53, no. 17, pp. 1178–1180, 2017.

[3] B. Rebsamen, C. Cuntai Guan, H. Zhang et al., “A brain controlled wheelchair to navigate in familiar environments,”

IEEE Transactions on Neural Systems and Rehabilitation Engineering, vol. 18, no. 6, pp. 590–598, 2010.

[4] A. N. Belkacem, S. Saetia, K. Zintus-art et al., "Real-time control of a video game using eye movements and two temporal EEG sensors," *Computational Intelligence and Neuroscience*, vol. 2015, Article ID 653639, 10 pages, 2015.

[5] K. Sumi, K. Yabuki, T. J. Tiam-Lee et al., "A cooperative game using the P300 EEG-based brain-computer interface," *Assistive and Rehabilitation Engineering*, 2019.

[6] A. N. Belkacem, S. Nishio, T. Suzuki, H. Ishiguro, and M. Hirata, "Neuromagnetic decoding of simultaneous bilateral hand movements for multidimensional brain–machine interfaces," *IEEE Transactions on Neural Systems and Rehabilitation Engineering*, vol. 26, no. 6, pp. 1301–1310, 2018.

[7] Q. Gao, L. Dou, A. N. Belkacem, and C. Chen, "Noninvasive electroencephalogram based control of a robotic arm for writing task using hybrid BCI system," *BioMed Research International*, vol. 2017, Article ID 8316485, 8 pages, 2017.

[8] W. He, Y. Zhao, H. Tang, C. Sun, and W. Fu, "A wireless BCI and BMI system for wearable robots," *IEEE Transactions on Systems, Man, and Cybernetics: Systems*, vol. 46, no. 7, pp. 936–946, 2016.

[9] V. Gilja, P. Nuyujukian, C. A. Chestek et al., "A high-performance neural prosthesis enabled by control algorithm design," *Nature Neuroscience*, vol. 15, no. 12, pp. 1752–1757, 2012.

[10] I. Seanez-Gonzalez, C. Pierella, A. Farshchiansadegh et al., "Static versus dynamic decoding algorithms in a non-invasive body–machine interface," *IEEE Transactions on Neural Systems and Rehabilitation Engineering*, vol. 25, no. 7, pp. 893–905, 2017.

[11] K. Watanabe, H. Tanaka, K. Takahashi, Y. Niimura, K. Watanabe, and Y. Kurihara, "NIRS-based language learning BCI system," *IEEE Sensors Journal*, vol. 16, no. 8, pp. 2726–2734, 2016.

[12] C. Chen, J. Zhang, A. N. Belkacem et al., "G-causality brain connectivity differences of finger movements between motor execution and motor imagery," *Journal of Healthcare Engineering*, vol. 2019, Article ID 5068283, 12 pages, 2019.

[13] A. N. Belkacem, H. Ishiguro, S. Nishio, M. Hirata, and T. Suzuki, "Real-time MEG-based brain-geminoid control using single-trial SVM classification," in *Proceedings of the 2018 3rd International Conference on Advanced Robotics and Mechatronics (ICARM)*, pp. 679–684, Singapore, July 2018.

[14] A. N. Belkacem, S. Nishio, T. Suzuki, H. Ishiguro, and M. Hirata, "Neuromagnetic geminoid control by BCI based on four bilateral hand movements," in *Proceedings of the 2018 IEEE International Conference on Systems, Man, and Cybernetics (SMC)*, pp. 524–527, Miyazaki, Japan, October 2018.

[15] L. He, D. Hu, M. Wan, Y. Wen, K. M. von Deneen, and M. Zhou, "Common bayesian Network for classification of EEG-based multiclass motor imagery BCI," *IEEE Transactions on Systems, Man, and Cybernetics: Systems*, vol. 46, no. 6, pp. 843–854, 2016.

[16] V. Mishuhina and X. Jiang, "Feature weighting and regularization of common spatial patterns in EEG-based motor imagery BCI," *IEEE Signal Processing Letters*, vol. 25, no. 6, pp. 783–787, 2018.

[17] B. O. Mainsah, K. D. Morton, L. M. Collins, E. W. Sellers, and C. S. Throckmorton, "Moving away from error-related potentials to achieve spelling correction in P300 spellers," *IEEE Transactions on Neural Systems and Rehabilitation Engineering*, vol. 23, no. 5, pp. 737–743, 2015.

[18] V. Martinez-Cagigal, J. Gomez-Pilar, D. Alvarez, and R. Hornero, "An asynchronous P300-based brain–computer interface web browser for severely disabled people," *IEEE Transactions on Neural Systems and Rehabilitation Engineering*, vol. 25, no. 8, pp. 1332–1342, 2017.

[19] Y. Wang, R. Wang, X. Gao, B. Hong, and S. Gao, "A practical VEP-based brain–computer interface," *IEEE Transactions on Neural Systems and Rehabilitation Engineering*, vol. 14, no. 2, pp. 234–240, 2006.

[20] P.-L. Lee, C.-L. Yeh, J. Y.-S. Cheng, C.-Y. Yang, and G.-Y. Lan, "An SSVEP-based BCI using high duty-cycle visual flicker," *IEEE Transactions on Biomedical Engineering*, vol. 58, no. 12, pp. 3350–3359, 2011.

[21] R. Z. T. Camilleri, O. Falzon, and K. P. Camiller, "To train or not to train? A survey on training of feature extraction methods for SSVEP-based BCIs," *Journal of Neural Engineering*, vol. 15, no. 5, p. 1741, 2018.

[22] K.-K. Shyu, Y.-J. Chiu, P.-L. Lee, J.-M. Liang, and S.-H. Peng, "Adaptive SSVEP-based BCI system with frequency and pulse duty-cycle stimuli tuning design," *IEEE Transactions on Neural Systems and Rehabilitation Engineering*, vol. 21, no. 5, pp. 697–703, 2013.

[23] D. Regan, "Electrical responses evoked from the human brain," *Scientific American*, vol. 241, no. 6, pp. 134–146, 1979.

[24] A. Guneysu and H. L. Akin, "An SSVEP based BCI to control a humanoid robot by using portable EEG device," in *Proceedings of the 2013 35th Annual International Conference of the IEEE Engineering in Medicine and Biology Society*, pp. 6905–6908, IEEE, Osaka, Japan, July 2013.

[25] C. Chen, X. Li, A. N. Belkacem et al., "The mixed kernel function SVM-based point cloud classification," *International Journal of Precision Engineering and Manufacturing*, vol. 20, no. 5, pp. 737–747, 2019.

[26] H. Nezamfar, S. S. M. Salehi, M. Moghadamfalahi, and D. Erdogmus, "FlashType™: a context-aware c-VEP-based BCI typing interface using EEG signals," *IEEE Journal of Selected Topics in Signal Processing*, vol. 10, no. 5, pp. 932–941, 2016.

[27] Y. Li, J. Pan, F. Wang, and Z. Yu, "A hybrid BCI system combining P300 and SSVEP and its application to wheelchair control," *IEEE Transactions on Biomedical Engineering*, vol. 60, no. 11, pp. 3156–3166, 2013.

[28] E. Yin, Z. Zhou, J. Jiang, Y. Yang, and D. Hu, "A dynamically optimized SSVEP brain–computer interface (BCI) speller," *IEEE Transactions on Biomedical Engineering*, vol. 62, no. 6, pp. 1447–1456, 2015.

[29] A. Abdullah, J. S. Norton, and T. Bretl, "An SSVEP-based brain–computer interface for text spelling with adaptive queries that maximize information gain rates," *IEEE Transactions on Neural Systems and Rehabilitation Engineering*, vol. 23, no. 5, pp. 857–866, 2015.

[30] P.-L. Lee, H.-C. Chang, T.-Y. Hsieh, H.-T. Deng, and C.-W. Sun, "A brain-wave-actuated small robot car using ensemble empirical mode decomposition-based approach," *IIEEE Transactions on Systems, Man, and Cybernetics-Part A: Systems and Humans*, vol. 42, no. 5, pp. 1053–1064, 2012.

[31] Y. Lu and L. Bi, "EEG signals-based longitudinal control system for a brain-ControlledVehicle," *IEEE Transactions on Neural Systems and Rehabilitation Engineering*, vol. 27, no. 2, pp. 323–332, 2019.

[32] Z. Lin, C. Zhang, W. Wu, and X. Gao, "Frequency recognition based on canonical correlation analysis for SSVEP-based BCIs," *IEEE Transactions on Biomedical Engineering*, vol. 53, no. 12, pp. 2610–2614, 2006.

[33] W. Nan, C. M. Wong, B. Wang et al., "A comparison of minimum energy combination and canonical correlation

analysis for SSVEP detection," in *Proceedings of the 2011 5th International IEEE/EMBS Conference on Neural Engineering*, pp. 469–472, Cancun, Mexico, April 2011.

[34] M. Nakanishi, Y. Wang, Y.-T. Wang, Y. Mitsukura, and T.-P. Jung, "Enhancing unsupervised canonical correlation analysis-based frequency detection of SSVEPs by incorporating background EEG," in *Proceedings of the 2014 36th Annual International Conference of the IEEE Engineering in Medicine and Biology Society*, pp. 3037–3040, IEEE, Chicago, IL, USA, August 2014.

[35] P. P. Banik, M. K. Azam, C. Mondal, and M. A. Rahman, "Single channel electrooculography based Human-Computer Interface for physically disabled person," in *Proceedings of the International Conference on Electrical Engineering & Information Communication Technology*, Dhaka, Bangladesh, May 2015.

[36] P. Lukas, N. Iveta, and C. Martin, "Make life easier based on detection of eyes movements, laboratory measurement," *IFAC PapersOnLine*, vol. 48, no. 4, pp. 268–271, 2015.

[37] N. Sarkar, B. O'Hanlon, A. Rohani et al., "A resonant eye-tracking microsystem for velocity estimation of saccades and foveated rendering," in *Proceedings of the IEEE International Conference on Micro Electro Mechanical Systems*, Las Vegas, NV, USA, January 2017.

[38] Y. Tanji, M. Nakanishi, K. Suefusa, and T. Tanaka, "Waveform-based multi-stimulus coding for brain-computer interfaces based on steady-state visual evoked potentials," in *Proceedings of the 2018 IEEE International Conference on Acoustics, Speech and Signal Processing (ICASSP)*, pp. 821–825, IEEE, Calgary, Canada, April 2018.

[39] E. Dong, C. Li, L. Li et al., "Classification of multi-class motor imagery with a novel hierarchical SVM algorithm for brain computer interfaces," *Medical & Biological Engineering & Computing*, vol. 55, no. 10, pp. 1809–1818, 2017.

Hindawi
Journal of Healthcare Engineering
Volume 2019, Article ID 1672940, 9 pages
https://doi.org/10.1155/2019/1672940

Research Article

Design and Quantitative Analysis of Cancer Detection System Based on Fluorescence Immune Analysis

Lei Shao,[1] Longyu Zhang ,[1] Shilin Li,[2] and Pengyuan Zhang[3]

[1]*Tianjin Key Laboratory for Control Theory & Applications in Complicated Systems, Tianjin University of Technology, Tianjin 300384, China*
[2]*Tianjin Xinuo Biomedicine Co., Ltd., Tianjin, China*
[3]*Tianjin Yirui Biotechnology Co., Ltd., Tianjin, China*

Correspondence should be addressed to Longyu Zhang; 546081030@qq.com

Received 21 June 2019; Revised 4 November 2019; Accepted 20 November 2019; Published 24 December 2019

Guest Editor: Duk Shin

Human blood is an important medical detection index. With the development in clinical medical detection instruments and detection technology, the requirements for detection accuracy and efficiency have been gradually improved. Fluorescent immunochromatography is a new detection technique. It has the characteristics of high efficiency, convenience, no pollution, and wide detection range. Human blood can be detected quickly using fluorescent immunochromatography. At present, it has received great attention from the field of clinical testing. In this paper, a set of fluorescent immunochromatographic analyzer has been designed. It is mainly based on the principle of fluorescence immunochromatography. A new method of signal analysis and system design for fluorescent immunochromatography analyzer is proposed. By using the improved threshold function denoising algorithm, the quantitative detection of fluorescent immunochromatographic strip is realized. The concentration of pathogenic factors (cancer cells) in human serum can be measured conveniently and accurately. The system integrates many peripheral modules, including fluorescence signal acquisition, fluorescence signal processing, quantitative curve fitting, and test results. In this paper, the quantitative detection experiments of the system are carried out in three aspects: linearity, repeatability, and sensitivity. The experimental results show that the linear correlation coefficient is up to 0.9976, and the limit of detection is up to 0.05 ng/ml. The requirements of the system are satisfied. The system performance is good, and the quantitative result is accurate. Therefore, the establishment of a fluorescence analysis system is of great significance.

1. Introduction

With the improvement in medical standards and technology, testing instruments are constantly improving. It is developing in the direction of simple operation, accurate results, and higher detection efficiency. At present, immunology is the conventional method for clinically testing blood and body fluids, which is used for quantitative or qualitative analysis [1, 2]. Quantitative immunoassay is an immunological method for quantitative detection of various physiological and pathological indexes in samples based on the principle of antigen-antibody reaction or supplemented by various marker-tracer techniques and special detection equipment. It has the characteristics of high sensitivity and high specificity. Antigens and antibodies are specific and sensitive, so fluorescent immunochromatography has been widely used in the detection of trace substances in clinical specimens [3, 4]. The most common methods are the radioimmunoassays, the enzyme-labeled immunoassay, the chemiluminescence immunoassay, and the colloidal gold immunoassay. These analytical techniques have played an important role in biology, medicine, and other fields since they came out one after another in the middle of the 20th century. In recent years, with the automation of analytical methods and the commercialization of matching reagents, quantitative immunoassay technology has been more and more widely used in clinical laboratories and has become an important means of disease diagnosis and efficacy evaluation. In general, the detection of blood in vivo by medical workers is the colloidal gold immunoassay, and its marker is

colloidal gold, which is combined with the labeled antibody protein by physical adsorption, and then precipitates and produces color [5]. The most obvious characteristics of this method are convenient operation, low cost, and high stability, so it is very suitable for hospital and family use. Colloidal gold immunochromatography has the following advantages: observe the results directly with the naked eye without any instrument and equipment, rapid detection, good stability, and it has no toxicity to the operator and no pollution to the environment. However, these characteristics are mainly reflected in the qualitative detection of solid-phase immunity, which cannot meet the clinical needs of accurate and quantitative analysis. It uses human eyes to identify, especially in the case of weak positive, which is easy to lead to missed detection, so the colloidal gold immunoassay is more suitable for semiquantitative and manual qualitative detection, but it is difficult to meet the requirements of quantitative detection. At the same time, the external noise will cause error to the detection results of the colloidal gold immune method, and its markers are only gold markers, and other markers cannot be used.

In recent years, with the development in fluorescence labeling technology, the combination of fluorescence labeling technology, immunochromatographic reaction, and photoelectron analysis technology, a detection technology called fluorescence immunochromatography is widely used in the field of medical detection [6]. It is mainly used in the diagnosis of bacteria, viruses, and serum antibodies. According to the characteristics of color and photoluminescence, the researchers combined it as a fluorescent marker with the substance to be tested, successfully applied it for the detection of immunochromatographic strip, and realized the detection of sample concentration. Compared with the colloidal gold immunochromatographic method, the fluorescence immunochromatographic analyzer has the advantages of convenient testing and simple operation and overcomes the two major defects of low sensitivity and unstable detection results. The fluorescence immunochromatographic detection method has the characteristics of strong specificity, high sensitivity, and good repeatability. At present, it has become a future development trend in the fields of biomedicine and other related fields.

Therefore, a set of fluorescent immunochromatography analyzer based on fluorescence immunochromatography is designed to improve the sensitivity of traditional methods. According to the principle of fluorescence immunoassay, the appropriate fluorescein was selected, and the best wavelength was selected according to its characteristic spectral characteristics to select the excitation light source. Based on the basic principle and system requirements of fluorescent immunochromatography, the design scheme of the system is determined. At the same time, because of the noisy characteristics of fluorescence signals, the wavelet transform method is introduced into the quantitative detection of fluorescent immunochromatography analyzer. Due to the deficiency in traditional wavelet threshold denoising, this paper proposes an improved threshold function method and verifies its feasibility. After a large number of repeated experiments, the test results show that the design system can basically achieve the desired results and can achieve patient management information and more accurate measurement of solution concentration. If cancer patients can seek medical treatment in time, the design instrument can be used to predict the pathological changes, so as to meet the needs of hospitals and patients.

2. Fluorescence Processing

2.1. Principle of Immune Chromatography. Immunochromatography is also called immunoaffinity chromatography. The specific antigen-antibody binding reaction has high affinity and specificity. Antigen or antibody can be coupled to column packing by using immunochromatography to prepare an affinity chromatography column. The specific immune components that are simple with antigens or antibodies can be quickly and efficiently isolated and purified from complex mixed samples by the chromatography column. It is the most selective and effective method for isolation and purification of specific antibodies [6, 7]. The immunochromatographic reaction was carried out on the nitrocellulose membrane of the reagent strip. The main immunochromatographic strip has the characteristics of strong maneuverability, high accuracy, and no pollution, which is mainly composed of sample pad, binding pad, nitrocellulose membrane, and water absorption filter paper [8]. Immunochromatographic reaction is on the cellulose membrane and the control zone. The realization of chromatography requires a mobile phase and a stationary phase [9, 10]. The mobile phase is a substance that flows transversely in the reagent strip, and the stationary phase is a nitrocellulose membrane on the reagent strip, which mainly exists in the test zone and the control zone. When the mixture flows through the stationary phase with the mobile phase, its different substances are separated by affinity chromatography [11]. *T*-line (test line) has specific immune response, and *C*-line (control line) has specific immune response, as can be seen in Figure 1.

In this paper, double-antibody sandwich method was used to detect the concentration of samples. It is carried out on the basis of the indirect method of fluorescent immune reaction. The fluorescein used in the immunochromatographic strip is a europium antibody chelate. It forms a europium-resistant compound by adding an enhancer containing β-diketone ligand. A schematic diagram of the principle of immune response by double-antibody sandwich method is showed in Figure 2.

The specific processes are as follows: a specific antibody containing the marker is dropped on the binding pad, and a specific antibody is added at a location of the nitrocellulose membrane. After the sample liquid of the sample to be tested is added to the sample pad, through the action of the capillary tube, the sample solution and the marker are uniformly diffused at the binding pad. The sample solution reacts with the europium chelate to form the complex of the europium antibody chelate. The complex containing the europium antibody chelate then flows forward. When the complex moves to the detection band, because the detection

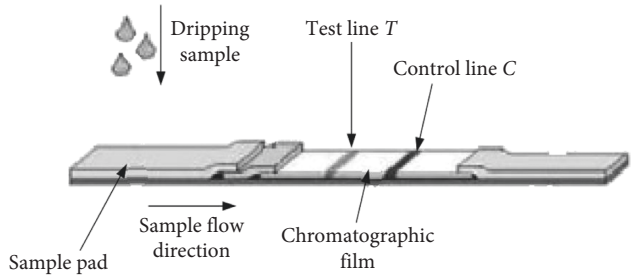

Figure 1: Schematic diagram of immunochromatography.

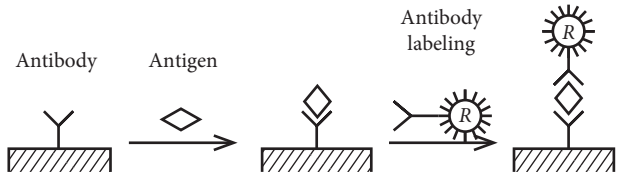

Figure 2: Immune schematic diagram of the double-antibody sandwich method.

band contains a specific antibody, it has a specific immune reaction with the europium antibody chelate-containing antigen and finally forms the immune complex of antigen-antibody-europium antibody complex. At the same time, the labeled antibody was also captured on the test line and stayed in the test line, while the redundant markers continued to flow forward and were adsorbed to the control band by the protein antibody on the membrane, and the complex specific binding occurred on the control line, and at the same time, the labeled antibody was also captured on the control line. According to the difference of marker types, the signal is detected by color or instrument, so as to achieve the purpose of qualitative or quantitative detection.

2.2. Traditional Wavelet Denoising Function. In the process of quantitative detection by using a fluorescence immunochromatography analyzer, the collected fluorescence signal will be affected by external or internal noise, which will lead to inaccurate quantitative detection results. External noise is caused by external environment and human factors. Internal noise includes thermal noise, particle noise, low-frequency noise, and so on. Common filtering algorithms include sliding average filter and wavelet analysis [12]. Wavelet analysis is a new branch of mathematics, which is based on the development of Fourier transform [13–15]. The main characteristics of wavelet analysis are that the time is subdivided at high frequency, and the frequency is subdivided at low frequency, which satisfies the analysis of the time-frequency signal according to different conditions. Therefore, wavelet analysis is a new localization analysis in time and frequency domains, but it is more beneficial to deal with nonstationary signals than Fourier transform. This method not only preserves the ability of local analysis of Fourier transform but also adapts to the window and shape of wavelet according to the characteristics of different signals [16]. There are three kinds of common wavelet analysis: wavelet transform modulus maxima method, spatial correlation filtering denoising, and wavelet threshold denoising. The principle of the wavelet threshold denoising method is simple. The wavelet decomposition coefficients of the original and noise signals are different and processed. And the calculation is relatively small, and the noise can be eliminated almost completely. In this paper, according to the characteristics of white noise in the collected fluorescent signal, the wavelet threshold denoising method is selected to improve the accuracy of the fluorescent signal.

After wavelet decomposition, the energy of the signal is mainly concentrated in some large wavelet coefficients, and most of the noise is the wavelet coefficient with small amplitude [17–19]. Assuming that the original signal is a (t), the contaminated noise signal is $b\,(t)$ and the noise signal is $n\,(t)$, and then the noise-containing basic model may be expressed as represented in the following equation:

$$b(t) = a(t) + n(t). \tag{1}$$

Formula (1) is subjected to wavelet transform to obtain the following equation:

$$b_{j,k} = a_{j,k} + n_{j,k}. \tag{2}$$

As shown in formula (2), $b_{j,k}$ represents the wavelet coefficients containing the signal $b\ (t)$, and $a_{j,k}$ and $n_{j,k}$ represent the wavelet coefficients of the original signal $a\ (t)$ and the noise signal $n\ (t)$, respectively.

The amplitude of the wavelet coefficient of the original signal is larger than that of the noise signal, and most of them are distributed in the low-frequency wavelet coefficient. Therefore, a suitable threshold T is selected, and the wavelet coefficient threshold is processed to obtain the wavelet coefficient $\widehat{b}_{j,k}$ after threshold quantification at different scales, and $\widehat{b}_{j,k}$ is reconstructed to obtain the denoised signal $\widehat{a}(t)$. The specific process is shown in Figure 3.

2.3. Threshold Selection and Threshold Function Selection. Multiresolution thoughts are the basis of wavelet transform. The combination of the wavelet transform and the threshold method can effectively remove the noise in the signal [20]. The threshold selection of wavelet denoising will affect the effect of denoising. If the threshold of selection is too large, the useful signal may be eliminated as a signal in the process of denoising, resulting in signal distortion. If the selected threshold is too small, the noise cannot be completely

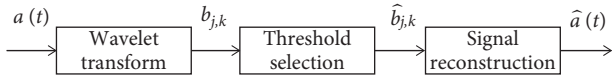

Figure 3: Basic principle block diagram of wavelet threshold denoising.

eliminated, which will affect the experimental results. The commonly used threshold selection is as follows: VisuShrink, Rigrsure, Sqtwolog, Heursure, and Minimax. In this paper, the global unified VisuShrink threshold is selected for denoising. VisuShrink can be seen as a universal threshold selector. It provides near-optimal error properties. It also ensures that estimates are as stable as true basic functions. It uses a threshold value T_1, which is proportional to the standard deviation of the noise. It is defined as follows:

$$T_1 = \sigma_n \sqrt{2 \ln N}. \tag{3}$$

In formula (3), σ_n is the estimate of noise deviation present in the signal and N represents the signal size or number of samples.

Wavelet threshold denoising is to decompose the signal into L-layer discrete binary wavelet as wavelet coefficients. Each layer has a fixed threshold. Processing of high-frequency coefficients is decomposed by wavelet using different threshold functions in the wavelet threshold denoising algorithm. It is also important to select a suitable threshold function. In general, there are two kinds of wavelet threshold functions: hard threshold function and soft threshold function.

If the setting T_1 is the threshold, the hard threshold function may be expressed as follows:

$$S = \begin{cases} X, & |X| > T_1, \\ 0, & |X| \le T_1. \end{cases} \tag{4}$$

The hard threshold function decomposes the noisy signal wavelet and obtains the high frequency coefficient, which preserves the wavelet coefficient whose absolute value is greater than the threshold value. When the wavelet coefficient is less than the threshold, the wavelet coefficient is set to zero. Hard threshold can protect local characteristics. Therefore, the wavelet coefficients of the whole wavelet domain will have a certain influence on the accuracy of the denoising result in the whole wavelet domain due to the discontinuity in the reconstructed signal.

If T_1 is set as the threshold, then the soft threshold function can be represented as shown in the following equation:

$$S = \begin{cases} \mathrm{SIGN}(X)(|X| - T_1), & |X| > T_1, \\ 0, & |X| \le T_1. \end{cases} \tag{5}$$

The soft threshold function sets the wavelet coefficient greater than its threshold value as the difference between the wavelet coefficient and the threshold value. And the wavelet coefficients less than the threshold are set to zero. The result of the process may be relatively smooth, and there will be a blurry at some of the contours or edge locations.

2.4. The Improved Threshold Function. The wavelet coefficients after denoising by the hard threshold method are discontinuity although they can better retain the effective part of the original signal. However, the reconstructed signal after denoising will get the unsmooth signal curve, which will lead to the concussion of the reconstructed signal. The problem that the denoising effect of hard threshold function is not obvious can be solved by using soft threshold function denoising, but the soft threshold function generates a fixed difference in the processing process, resulting in reduced signal accuracy after the reconstruction and also distortion of the reconstructed signal amplitude. In the practical application, it is necessary to carry out the derivation operation on the soft threshold function, but the derivative of the soft threshold function is not continuous and has certain limitations.

In order to take into account the advantages of these two thresholds and eliminate their disadvantages, this paper proposes a new function to solve the soft and hard threshold functions based on the shortcomings of the above threshold functions, as shown in the following equation:

$$\hat{a}_{j,k} = \begin{cases} \mathrm{sign}\left(a_{j,k}\right)\left(\left|a_{j,k}\right| - \dfrac{T_j}{1 + \log_2^{\left(1+\left|a_{j,k}\right|-T_j\right)}}\right), & \left|a_{j,k}\right| \ge T_j, \\ 0, & \left|a_{j,k}\right| < T_j, \end{cases} \tag{6}$$

where $a_{j,k}$ is the original wavelet coefficient, $\hat{a}_{j,k}$ is the wavelet coefficient after threshold processing, and T_j is the threshold. Through mathematical analysis, the continuity, progressiveness, and deviation of threshold function in formula (4) are verified, and the feasibility of threshold function is proved.

As $|a_{j,k}|$ increases, the improved threshold function eventually approaches $a_{j,k}$. The deviation between the reconstructed wavelet coefficient and the actual wavelet coefficient is also gradually reduced. The corresponding denominator also increases. It leads $\hat{a}_{j,k}$ to $a_{j,k}$. Thus, the defects of soft and hard thresholds are overcome, and the problem of deviation in $\hat{a}_{j,k}$ and $a_{j,k}$ is solved. Because the wavelet coefficient of noise decreases with the increase in the decomposition scale, the threshold in different decomposition layers should decrease with the increase in the decomposition scale. At the same time, in order to solve the common threshold defect, an improved threshold selection method is proposed in this paper. The threshold selected in this article is as shown in the following equation:

$$T_{nj} = \sigma_j \frac{\sqrt{2 \ln N_j}}{\ln (e + j)}, \tag{7}$$

where σ_j is the standard deviation of layer j noise signal, N_j is the length of signal, and T_{nj} is the threshold of layer j.

The new threshold function is more effective than the traditional threshold function to eliminate the oscillation of the reconstructed signal, and the noise reduction effect is better. The details are presented in Figure 4, where (a) is the

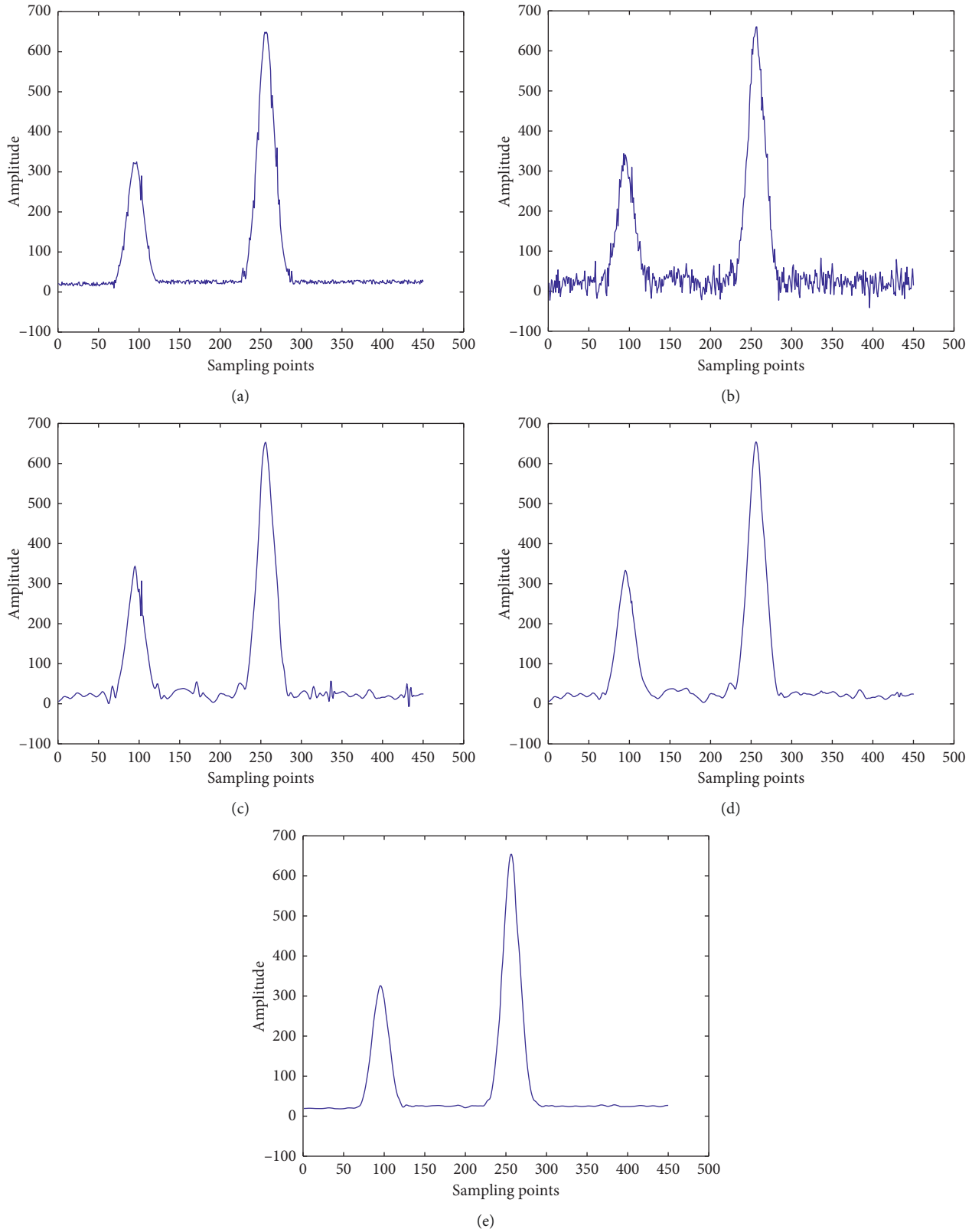

Figure 4: Different kinds of threshold function denoising images: (a) original signal; (b) noisy signal; (c) signal after hard threshold function denoising; (d) signal after soft threshold function denoising; (e) signal of a new threshold function denoising.

original signal, (b) is the noisy signal, (c) is the signal after hard threshold function denoising, (d) is the signal after soft threshold function denoising, and (e) is the signal of a new threshold function denoising.

Signal evaluation standard is the criterion to judge the effect of signal processing [21]. The commonly used indexes to evaluate the quality of the signal are signal-to-noise ratio (SNR) and root mean squared error (RMSE). SNR is defined as follows: the ratio between the energy of the original signal and the noise, where $x(n)$ is for the original signal, $y(n)$ is for the noise signal, and N is the signal length. The formula is shown as follows:

$$\mathrm{SNR} = 10 * \lg\left(\frac{\sum_{n=1}^{N} x(n)^2}{\sum_{n=1}^{N} [x(n) - y(n)]^2}\right). \tag{8}$$

RMSE is used to judge the error between the original signal and the noise signal. The formula is shown as follows:

$$\mathrm{RMSE} = \sqrt{\frac{\sum_{n=1}^{N} [x(n) - y(n)]^2}{N}}. \tag{9}$$

According to the definition, the smaller the mean square error is, the better the denoising effect is. As shown in Table 1, it compares the SNR and RMSE of the three denoising methods.

In comparison of the denoising index, the improved threshold function denoising method is used to make the fluorescent signal have a higher signal-to-noise ratio (SNR). Root mean square error is low. The effect is better.

Table 1: Evaluated parameters for test signals.

Signal	RMSE	SNR
The hard threshold function	11.8552	20.6510
The soft threshold function	10.3338	21.8439
The improved threshold function	7.1187	25.0811

3. System Design

3.1. System Selection and Structure. There are two options for the system. The first option is based on the rapid development of digital image processing technology and the use of a CCD camera to take a photograph of a test strip throughout the detection area [22, 23]. A digital image processing algorithm is used to analyze and calculate the gray value of the analyte concentration and the wavelength band of the detection area and the control area. The second option can eliminate the defect of capturing the image data during the mechanical transmission process and shorten the time. The second option is adding a mechanical scan structure to a legacy optical module. The light is excited by the optical module, and the optical path is concentrated on the test strip. The fluorescence is excited on the test strip and focused on the photodetector. The optical module uses the preamplifier circuit to complete the photocurrent acquisition, and the optical module can complete the fluorescence signal acquisition on the test rod. The mechanical transmission can drive the optical module or place the test rod platform in the direction, which can form a straight line in these two ways. It can complete the entire detection area of the fluorescence collection. The fluorescence curve of the entire detection area is scanned, and then the fluorescence curve is processed to infer the contents of the analyte. This scheme is mature and of low cost, the light module is very small, and this is a common product scheme [24] in the market. The fluorescent immunochromatography analyzer designed in this paper is mainly used in hospitals, families, and other places. Therefore, the system is mainly considered in person from low power consumption, strong anti-interference ability of signal acquisition, and so on. Compared with the above two solutions, we choose the second solution from the perspective of current technological maturity.

The hardware system is mainly composed of optical system and control system. The main contents of the work are as follows: the driving scanning reagent strip of the motor amplifies the adopted signal and converts the optical signal into electrical signal under the action of fluorescence immunochromatography reaction and realizes the signal acquisition. The software system is mainly composed of touch screen and PC. It can complete the analysis of the signal and carry out data storage and query. The system framework of the fluorescence immunochromatographic analyzer is shown in Figure 5.

The specific work flow of the detection system of fluorescent immunochromatography analyzer designed in this paper is as follows. First, the excitation light generated by the internal timer of the single-chip microcomputer passes through the filter, and the whole reagent strip is scanned under the motion of the drive driven step motor. Silicon photodiode receives the optical signal and converts optical signals into electrical signals. Then, the data are transmitted to the single-chip computer through the A/D sampling. Finally, the obtained data are sent to the single-chip microcomputer through the serial port, and the collected signals are processed by the single-chip microcomputer. After calculating the concentration value, the detection results are displayed and outputted to the user.

3.2. Selection of Light Source. In the fluorescent immunochromatographic reaction, different markers should be selected to correspond to different light sources [25, 26]. In the traditional optical system, the optional types of light sources are xenon lamp, laser, and LED lamp. The advantages of xenon lamp light source emit a wide range of spectra which is from infrared to ultraviolet. The emission intensity of the xenon lamp is very high. The disadvantage of the xenon lamp light source is that the light effect is low, it needs to be under high voltage, and the requirement of power supply is very high. The laser light source has the advantages of a small output pulse width, high signal-to-noise ratio, and high

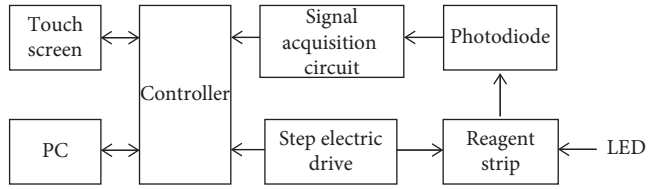

Figure 5: Structure of a fluorescence immunoassay system.

sensitivity. But it has short service life, small number of pulses per second, and large volume, which is not conducive to the portability of the instrument. Although the LED light source is poor in monochromaticity and brightness, it has the advantages of small volume, output power, stable beam wavelength, and long lifetime. Combined with the needs of this system, LED light source is more suitable as the excitation light source of fluorescent immunochromatography analyzer.

The function of the filter is to filter out the interference of radiation from other spectral segments of the system. In the receiving optical path, the bandpass filter needs to be selected. And the peak of the transmission peak is 610 nm. Therefore, a filter having a center wavelength of 610 nm, a peak transmittance of $T_s > 90\%$, and a cut-off depth T_p of less than 0.1% is selected.

4. Quantitative Detection Experiments and Results

4.1. Linearity Test. The sample solution of *Cryptococcus* pods-like polysaccharide with the concentration of 100 ng/ml was divided into several parts. The solution was diluted to 0.05 ng/ml, 0.1 ng/ml, 1 ng/ml, 10 ng/ml, and 100 ng/m with evaporated feed water. The values of the control line and the test line are measured, respectively, and the characteristic values are obtained, as shown in Table 2.

The fluorescence intensity of the control band and the detection band on the test strip reflects the degree of reaction of the antigen and the antibody. The characteristic value in Table 2 is the ratio of the fluorescence intensity of the control band to the detection band, which indicates the number of fluorescent immune complexes.

The linear correlation coefficient of the fluorescent immunoanalyzer used in this paper is $R^2 = 0.9976$, as shown in Figure 6. It is shown that the detection system improved by this instrument has the best linear characteristics and can truly reflect the concentration of the object to be measured.

4.2. Repeatability Test. The repeatability of the detection results is an important index to test the performance of the fluorescent immunochromatography analyzer. According to the three concentration ranges of low, medium, and high, the experiment was prepared into three concentrations of 1 ng/ml, 10 ng/ml, and 100 ng/ml. In the same location, the same operator uses the same device to repeat the operation 3 times. The experimental data are shown in Table 3.

The coefficient of variation (CV) can be obtained by using the following equation:

Table 2: Linearity test.

Sample concentration	The value of T	The value of C	Characteristic value
100 ng/ml	13392	20244	0.661529362
10 ng/ml	2747	26454	0.103840627
1 ng/ml	442	35354	0.012502122
0.1 ng/ml	193	36069	0.005350855
0.05 ng/ml	318	39575	0.008035376
0	292	26233	0.011131018

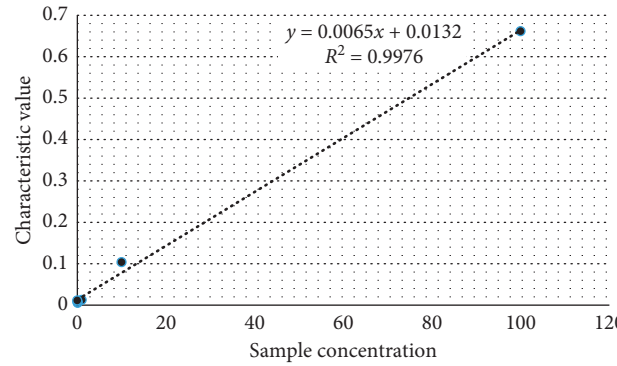

Figure 6: Fitting curve of the linearity test.

$$\mathrm{CV} = \frac{\overline{X}}{\sigma} * 100\%, \tag{10}$$

where σ is the standard deviation of the sample and $\bar{X}$ is the average value of the sample.

After statistics, the instrument was used to test the sample solution with a concentration of 1 ng/ml, 10 ng/ml, and 100 ng/ml using an improved algorithm. The measurement results show that the repeatability of the instrument at high concentration can be better. In medium and low concentrations, the repeatability of low concentrations is relatively poor. But overall, it shows that the detection system has good repeatability and meets the requirements of the system.

4.3. Minimum Test. Take the same batch of the reagent strip. The sample concentration was 100 ng/ml, and the release concentration was 100 ng/ml, 10 ng/ml, 1 ng/ml, 0.1 ng/ml, and 0.05 ng/ml. The solution was dripped on 5 strips and blank strips, respectively, to test it as a detection limit. The specific test data are given in Table 4.

As shown in the table, when the sample concentration is 0.05 ng/ml, the characteristic values are close to those of the

Table 3: Linearity test.

Sample concentration	The value of T	The value of C	Characteristic value	Average value ($\bar{X}$)	Standard deviation (σ)	Coefficient of variation (CV)
100 ng/ml	13392	20244	0.661529362	0.698657612	0.032308661	0.046243913
	14896	20678	0.720379174			
	18430	25810	0.7140643			
10 ng/ml	2747	26454	0.103840627	0.115863316	0.015736094	0.135816017
	3928	29385	0.133673638			
	3131	28444	0.110075684			
1 ng/ml	442	35354	0.012502122	0.016030887	0.003334025	0.207975068
	595	36143	0.016462386			
	613	32047	0.019128155			

Table 4: Minimum test.

Sample concentration	100 ng/ml	10 ng/ml	1 ng/ml	0.1 ng/ml	0.05 ng/ml	0
Characteristic value	0.6987	0.1159	0.0160	0.0090	0.0085	0.0080

blank test paper. Therefore, the limit of *Cryptococcus* capsule polysaccharide solution can be measured by this system.

5. Discussion and Conclusion

The system of fluorescent immunochromatography analyzer mainly adopts optical measurement and control module. The invention can realize the quantitative detection of the fluorescent material on the reagent strip under the detection of the concentration of the fluorescent substance solution. The measurement results are reliable and accurate. Through the experiment, we get the following data: the linear correlation coefficient is up to 0.9976, and the limit of detection is up to 0.05 ng/ml. These data prove that the system has the advantages of convenient operation, low power consumption, good stability, and high precision.

The fluorescent immunochromatography analyzer designed in this paper has basically completed the core function. However, due to limited time and lack of time to carry out and explore in depth, there is still a need for improvement in many areas:

(1) In the process of sample detection, it will bring noise to the outside and inner boundaries of the system. The next step is to improve the optical system and build more sophisticated optical system modules to stop the noise. At the same time, an amplification circuit with adjustable gain is selected in the control system. The range of fluorescence signals can be controlled within a certain range. And the detection accuracy can be improved.

(2) The degree of automation of the system needs to be improved. In this paper, the signal denoising and eigenvalue solution are based on Matlab software. The next plan can be completed in the upper computer system instead of using Matlab to complete the data processing.

(3) The fluorescence immunochromatographic analyzer is still being developed and tested. It is not officially in use. A lot of data are needed before formal investment. And we need a lot of samples.

At present, most of the fluorescence signal curves measured by the fluorescence immunochromatographic analyzer are of great noise. They fit most of the curves in the way they deal with noise, and this will bring errors to the system analysis for quantitative analysis. And most of them only stay in theoretical research, and the experimental results are less. Therefore, in this paper, in view of the problems existing in the development, the in-depth study is carried out, and a large number of existing problems are analyzed and solved. At present, there are also many medical enterprises into the research and development of fluorescent immunochromatography analyzer. Although the performance of the instrument has been improved, the cost and maintenance costs are too high, despite the fact that a number of enterprises and research institutes have been well-studied. As a result, the level of technology is to be improved, and further improvements in product innovation and technology upgrading are needed.

Data Availability

The datasets generated and analyzed during the current study are not publicly available due to Tianjin University of Technology policy but are available from the corresponding author on reasonable request.

Conflicts of Interest

The authors declare that there are no conflicts of interest regarding the publication of this paper.

Authors' Contributions

Lei Shao designed the research, supervised the project, and revised the article. Longyu Zhang performed the research, analyzed data, and drafted the article. Shilin Li and

Pengyuan Zhang provided a large number of data research basis for this experiment.

Acknowledgments

This work was a Major Science and Technology Project for High-End Medical Devices (16ZXQXSY00020), which is about the Research and Development of *Aspergillus*, Cryptococci, and *Candida albicans* triple nucleic acid detection kit and supporting Q-PCR instrument.

References

[1] F. Di Nardo, L. Anfossi, C. Giovannoli et al., "A fluorescent immunochromatographic strip test using quantum dots for fumonisins detection," *Talanta*, vol. 150, pp. 463–468, 2016.

[2] D. Pyo and J. Yoo, "New trends in fluorescence immunochromatography," *Journal of Immunoassay and Immunochemistry*, vol. 33, no. 2, pp. 203–222, 2012.

[3] H. Guan and M. J. Shi, "Research progress in immunoassay technology," *Asia-Pacific Traditional Medicine*, vol. 3, no. 10, pp. 33–36, 2007.

[4] Y. L. Zhao and G. P. Zhang, "Development of a lateral flow collloidal immunoassay strip for the rapid detection of enrofloxaein lresidues," *Journal of Agricultural and Food Chemistry*, vol. 50, no. 4, pp. 511–515, 2005.

[5] J. Singh, S. Sharma, and S. Nara, "Evaluation of gold nanoparticle based lateral flow assays for diagnosis of enterobacteriaceae members in food and water," *Food Chemistry*, vol. 170, pp. 470–483, 2014.

[6] L. T. Goodnough and C. C. Hill, "Use of point-of-care testing for plasma therapy," *Transfusion*, vol. 52, no. 5, pp. 56S–64S, 2012.

[7] C. G. Lad and A. O. Gkubb, "Lmmuno-capillary migration with enzyme-labeled antibodies: rapid quantification of C-reactive protein in human plasma," *Anal Biochemistry*, vol. 116, no. 2, pp. 335–340, 1981.

[8] X. Liu, M. Du, Y. Li, and Y. Gao, "Design of fluorescence immune-chromatographic quantitative detection system," *Journal of Electronic Measurement and Instrument*, vol. 27, no. 9, pp. 859–866, 2013.

[9] J. Yao, G. Xing, J. Han et al., "Novel fluoroimmunoassays for detecting ochratoxin A using CdTe quantum dots," *Journal of Biophotonics*, vol. 10, no. 5, pp. 657–663, 2017.

[10] C. Gui, K. Wang, C. Li, X. Dai, and D. Cui, "A CCD-based reader combined with CdS quantum dot-labeled lateral flow strips for ultrasensitive quantitative detection of CagA," *Nanoscale Research Letters*, vol. 9, no. 1, pp. 1–8, 2014.

[11] J. Zhao, R. Mo, L. M. Tian et al., "Oriented antibody immobilization and immunoassay based on boronic acid-containing polymer brush," *Chinese Journal of Polymer Science*, vol. 36, no. 4, pp. 472–478, 2018.

[12] M. Srivastava, E. R. Georgieva, and J. H. Freed, "A new wavelet denoising method for experimental time-domain signals: pulsed dipolar electron spin resonance," *The Journal of Physical Chemistry A*, vol. 121, no. 12, pp. 2452–2465, 2017.

[13] O. Oluropo, K. L. Jae, and W. R. Gethin, "Wavelet de-noising of GNSS based bridge health monitoring data," *Journal of Applied Geodesy*, vol. 10, pp. 273–282, 2014.

[14] E. Dong, C. Li, L. Li, S. Du, A. N. Belkacem, and C. Chen, "Classification of multi-class motor imagery with a novel hierarchical SVM algorithm for brain-computer interfaces," *Medical & Biological Engineering & Computing*, vol. 55, no. 10, pp. 1809–1818, 2017.

[15] C. Chen, J. Zhang, A. N. Belkacem et al., "G-causality brain connectivity differences of finger movements between motor execution and motor imagery," *Journal of Healthcare Engineering*, vol. 2019, Article ID 5068283, no. 3, p. 12, 2019.

[16] X. H. Wang and Y. C. Niu, "Optimizing signal de-noising algorithm for AcousticEmission leakage of wavelet," *Cybernetics and Information*, vol. 10, pp. 116–125, 2016.

[17] W. Jiao, L. Zhenchun, and W. Deying, "A method for wavelet threshold denoising of seismic data based on CEEMD," *Geophysical Prospecting for Petroleum*, vol. 53, no. 2, pp. 164–172, 2014.

[18] R. V. Maheswari, B. Vigneshwaran, and L. Kalaivani, "Genetic algorithm based automated threshold estimation in translation invariant wavelet transform for denoising PD signal," *COMPEL—The International Journal for Computation and Mathematics in Electrical and Electronic Engineering*, vol. 34, no. 4, pp. 1252–1269, 2015.

[19] Q. Gao, L. Dou, A. N. Belkacem, and C. Chen, "Noninvasive electroencephalogram based control of a robotic arm for writing task using hybrid BCI system," *BioMed Research International*, vol. 2017, Article ID 8316485, p. 8, 2017.

[20] N. Akshay, N. A. V. Jonnabhotla, N. Sadam et al., "ECG Noise Removal and QRS Complex Detection Using UWT," in *Proceedings of the International Conference on Electronics and Information Engineering*, Kyoto, Japan, August 2010.

[21] H. Li, X. Tuo, R. Shi et al., "A de-noising algorithm to improve SNR of segmented gamma scanner for spectrum analysis," *Nuclear Instruments and Methods in Physics Research Section A: Accelerators, Spectrometers, Detectors and Associated Equipment*, vol. 818, pp. 68–75, 2016.

[22] Y. M. Gao and T. Z. Yi, "Fluorescent immune-chromatographic strip quantitative detection based on two-dimensional otsu method and region growth algorithm," *Chines Journal of Sensors and Actuators*, vol. 50, no. 9, pp. 1357–1359, 2016.

[23] L. H. Huang and K. Guo, "Development of a high performance reader for colloidal gold lateral flow strip," *Chinese Lasers*, vol. 40, no. 7, pp. 107–115, 2013.

[24] X. Zhang and D. Li, "A CCD-based reader combined quantum dots-labeled lateral flow strips for ultrasensitive quantitative detection of antibody," *Journal of Biomedical Nanotechnology*, vol. 8, no. 3, pp. 372–379, 2012.

[25] R. Bingqiang, L. Huang, and H. Huang, "Time-resolved fluorometer based on immunochromatography," *Chinese Journal of Scientific Instrumen*, vol. 30, no. 6, pp. 1330–1335, 2009.

[26] S. H. Wang, W. Shan, and L. L. Song, "Principle and application of AD620 instrumentation amplifier," *Microprocessors*, vol. 29, no. 4, pp. 38–40, 2008.

Hindawi
Journal of Healthcare Engineering
Volume 2019, Article ID 5397814, 17 pages
https://doi.org/10.1155/2019/5397814

Research Article

A Multichannel Convolutional Neural Network Architecture for the Detection of the State of Mind Using Physiological Signals from Wearable Devices

Sabyasachi Chakraborty,[1] **Satyabrata Aich**,[2] **Moon-il Joo**,[2] **Mangal Sain**,[4] **and Hee-Cheol Kim**[1,2,3]

[1]*Department of Computer Engineering, Inje University, Gimhae, Republic of Korea*
[2]*Institute of Digital Anti-Aging Healthcare, Inje University, Gimhae, Republic of Korea*
[3]*u-HARC, Inje University, Gimhae, Republic of Korea*
[4]*Division of Computer Engineering, Dongseo University, Busan, Republic of Korea*

Correspondence should be addressed to Hee-Cheol Kim; heeki@inje.ac.kr

Received 18 June 2019; Revised 12 August 2019; Accepted 27 August 2019; Published 3 October 2019

Guest Editor: Duk Shin

Detection of the state of mind has increasingly grown into a much favored study in recent years. After the advent of smart wearables in the market, each individual now expects to be delivered with state-of-the-art reports about his body. The most dominant wearables in the market often focus on general metrics such as the number of steps, distance walked, heart rate, oximetry, sleep quality, and sleep stage. But, for accurately identifying the well-being of an individual, another important metric needs to be analyzed, which is the state of mind. The state of mind is a metric of an individual that boils down to the activity of all other related metrics. But, the detection of the state of mind has formed a huge challenge for the researchers as a single biosignal cannot propose a particular decision threshold for detection. Therefore, in this work, multiple biosignals from different parts of the body are used to determine the state of mind of an individual. The biosignals, blood volume pulse (BVP), and accelerometer are intercepted from a wrist-worn wearable, and electrocardiography (ECG), electromyography (EMG), and respiration are intercepted from a chest-worn pod. For the classification of the biosignals to the multiple state-of-mind categories, a multichannel convolutional neural network architecture was developed. The overall model performed pretty well and pursued some encouraging results by demonstrating an average recall and precision of 97.238% and 97.652% across all the classes, respectively.

1. Introduction

Biosignals or physiological signals are those signals that can provide the details about the physiological states and their associated dynamics in the body of a human being [1]. The biosignals can be further analyzed to detect the physiological state based on the time series analysis of the signal [2]. Till date, many researchers have highlighted the relationship between biosignals and its associations in several contexts such as emotional behavior, social behavior, and expressive behavior [3, 4]. Emotional feeling or emotional judgment, which is also a subsection of the state of mind, mostly gets enhanced due to the physiological responses and can be detected by analyzing explicit patterns of the biosignals [5, 6]. The emotional changes are found to be related with the biosignals such as the skin conductance and heart rate, and this relationship helps to interpret the states of emotion such as stress and the other states of mind [7, 8]. Therefore, the detection of the proper state of the mind for maintaining a balance with health is necessary.

In the past, the acquisition process of the biosignals was a very cumbersome process that primarily included a clinical environment with a huge number of sensors and moreover, the process was quite expensive altogether. But, after the

advent of wearable technologies or smart wearables, which has grown into much popularity, it is now quite easier to fetch the data and analyze it [9]. Wearable devices also help to quantify the parameters in space and time that help to monitor the desired state depending on the application and the purpose.

In the proposed study, different physiological signals of the subjects are coupled together to detect each state of the mind more accurately and precisely. The complete study was performed by engineering state-of-the-art features and followed by applying a multichannel convolutional neural network for the prediction of the states of the mind. The major novelty of the work can be put forward in multiple ways. First, the data that have been used in the study have been fetched from multiple subjects over a long period of time [10]. Second, the data have been fetched by using two different devices, namely, a wrist-worn wearable and a chest-worn wearable device. The usage of two different devices allows us to fetch much more localized information from the data. Third, the engineering of the features has been performed using a peak detection technique, which allows us to understand cumulative information about the data for a particular cycle. And finally, for the learning task, a multichannel convolutional neural network was developed. The network allows different biosignals to pass through different channels for optimum feature learning and, at the end, provides the prediction probabilities by concatenating the feature maps of all the channels.

The rest of the paper is structured as follows: The second section provides the details about the related work that has been performed in a particular segment of stress detection, wearable technology, machine learning, and deep learning. The third section presents a deep understanding of the data preprocessing and feature engineering. The fourth section discusses the development of the deep learning model and discusses the training procedure. The fifth section provides the results that were achieved in the work followed by the sixth section, which discusses the complete inflow of data to the prediction and also explains the societal impact of the work. Lastly, the paper is concluded in the seventh section.

2. Related Work

In the past, many researchers have highlighted the importance of biosignals for detecting different positive or negative emotions and different mental states depending on the situations. In [10], a data set was introduced for the wearable and stress detection known as WESAD, which holds the very basic need for the work. The data set was obtained from 15 subjects who had undergone an experimental process of answering a set of question that analyzed the affective state of mind of a subject. The biological signal data from the subjects were extracted using two wearable devices, that is, a wrist-worn wearable device and a chest-worn pod. The complete experimental procedure managed to obtain the data for 5 different activities namely, baseline condition, amusement condition, stress condition, meditation, and recovery. The study also performed a machine-learning classification task and a comparative analysis between the multiple algorithms that have been considered. Furthermore, the complete classification task was divided into two categories namely, a three-class classification based on the baseline, stress, and amusement class, and a two-class classification based on stress and nonstress, respectively.

But, in a perceptive case, it can be widely assumed that the decision thresholds for identifying a particular state of mind may not be the same across all the times for a particular individual. Therefore, a normalization factor was devised in [11] to reduce the stress variability, which was primarily maintained to check the tradeoff between the physiological data and the biosignals of the individual. In the study, the author collected the data from around 10 subjects but in a different way, that is, the data were captured for 5 days using three devices namely, wristband, smart necklace, and a chest band. The manner in which the particular work is different from the work performed by others in stress detection is that the data extraction process is not performed in a controlled way or in a laboratory environment rather was extracted for the complete time of 24 hours and that too for 5 days. Therefore, it was suggested in the work that there are many physiological thresholds that differ from individual to individual and must be considered for determining stress in a person. Also, the author demonstrated the usage of few regression models to predict the amount of stress in a person, which also presented some astounding results.

Moreover, the type of activities that are pursued by the people also has a different perspective towards maintaining the decision threshold. While pursuing some strenuous activities such as driving, the amount of mental stress threshold for a particular person increases drastically from the normal state to the mobile state. Therefore, to answer this particular subjective scenario, a stress detection model was developed in [12] for drivers in the real world. In the study, a real-world driving task across 24 drivers for around 50 minutes each was performed. However, the complete study was based on the amount of stress undertaken by the driver on the route driven rather than the natural stress elements. Also, in [13], a novel method for the detection of psychological arousal while driving a car using smart wearable sensors was proposed. The work performed the data extraction process on 11 participants who underwent a driving simulation while wearing a wrist wearable device that propelled out the physiological signals such as heart rate, skin conductance, and skin temperature. These physiological signals were further trained on a convolutional neural network that outperformed other baseline neural network models and denoising autoencoder models.

Now, as discussed previously, a wide range of stress detection or stress classification has been performed for the driving activity but the relevance of the sensors used for deriving a particular outcome is one of the concerns. Therefore, [14] performed a study for the selection of features and also the sensors for the detection of stress in drivers. For the model development, supervised machine-learning classifiers were used for two different calibrations namely, the driver at rest versus driving and driving on the highway versus driving in the city. From the work, it was obtained that for differentiating between rest and driving,

heart rate, EDA (electrodermal activity), and respiration came out to be the best sensors. And, for distinguishing between low stress and high stress, heart rate and respiration turned out to be the most relevant ones. However, the study also demonstrated an interesting method for plotting the interindividuality between the subjects by normalizing each feature using the standard deviation of all the features across all the patients.

The development of a generic model for the state of mind detection of different individuals seemed to be quite important as each individual has a wide range of different grant roots or thresholds for a specific condition. Therefore, for solving this particular scenario, a study was performed by [15] on the stress detection using the heart rate variability. The method produced a normalized approach to account for the interindividual physiological difference using a baseline methodology. In another scenario, a classification model was devised by [16] for the detection of presurgery stress in patients, as surgery is a strenuous situation and the adverse effects of stress on patients undergoing surgery are irrefutable. The study leveraged the electrodermal activity of the patients that were extracted using a wrist wearable. The data were fetched from 41 patients who underwent different surgeries. The model developed in the work was based on adaptive partitioning of the data for stress detection where the interindividual variability of the electrodermal activity of a person was based on the sweat gland density and skin thickness.

For the stress detection of individual using electroencephalography (EEG), [17] published a DEAP data for emotion analysis using EEG and physiological signals. The data were generated while the subject viewed a 40-minute clip of a video. And after the data fetch was completed, a learning process was initiated, which resulted in classifying the EEG signals into different emotional classes. Reference [18] proposed and demonstrated a method for determining the stress level for the patients suffering from dementia. The study collected data from a single wearable sensor attached to the subjects' body to classify the stress level in 6 classes. The study was performed on 36 subjects, of which 30 were normal people and 6 were patients suffering from dementia. The study was further validated with the observational data of the behavioral patterns that were extracted by the clinical staff and were matched with the threshold-based sensor data.

Furthermore, in the study regarding emotional stress detection using EEG signals, [19] leveraged deep learning algorithms to analyze the fluctuations of electrical activity in the brain. The data used in the study were captured from the test subjects using a NeuroSky device, while the test subjects were listening to the music. Furthermore, into the learning process, a backpropagation deep neural network was implemented for stress detection, which resulted in the accuracy of 80%.

As primarily, the studies performed for the detection of stress predominantly used the wearable devices and noninvasive sensors for the extraction of signals, therefore [20] developed a system for determining stress detection using the bioradar respiratory signals. The work implemented two unique approaches, one for the acquisition of signals and other for the engineering of the features. For the data acquisition process, a noninvasive and a noncontact method were devised, and for the engineering of the features, recurrence quantification analysis was performed. For the learning process, a multilayer perceptron was designed to perform a binary classification over steady and stress class, respectively.

The above-highlighted work further motivated us to explore the proposed study by developing a multichannel deep learning architecture with regard to stress detection by leveraging multiple biosignals and also to perform a check upon the interindividuality of the subjects during the learning process.

3. Data Preprocessing and Feature Extraction

For the implementation of the multichannel convolutional neural network, multiple prerequisite steps are to be followed. As the data are in the raw format, generalizing the data based on the international system of units remains one of the most primary concerns. Moreover, as the data have been derived from the biosensors, it contains a multitude of abstracted information, which in turn can be difficult for the deep learning algorithms to identify [21]. Therefore, feature engineering on the raw data is to be performed to find the optimum features for the deep learning algorithms to work upon.

3.1. Data Set. The data set used in the work was fetched from the UCI machine learning repository that was posted by [10]. The data used in the work were taken from 15 subjects who wore the RespiBAN Professional on the chest and Empatica E4 on the wrist. The RespiBAN was utilized to fetch ECG, EMG, EDA, temperature, accelerometer, and respiration data, whereas Empatica E4 was used to fetch the BVP, EDA, temperature, and accelerometer data. The 15 participants who participated in the data acquisition process were the graduate students of the research facility. The participants chosen for the study were of the mean age of 27.5 ± 2.4 years and out of the 15 participants, 12 were male and 3 were female. For choosing the right candidates, an exclusion principle was introduced where people with pregnancy, chain-smoking, psychological disorders, and cardiovascular disorders were not entertained. For the data acquisition process, the participants were asked to avoid caffeine and tobacco for one hour before the beginning of the procedure. For baseline conditions, the participants were asked to sit or stand near a table and a random magazine was provided to them for reading. For amusement condition, the participants were asked to watch a set of 11 funny video clips where each video clip had a neutral interval of 5 seconds. For determining the stress condition, the participants were exposed to a Trier social stress test (TSST) where the participants were asked to deliver a five-minute speech in front of a panel of three members on personal traits focusing on strength and weaknesses. The participants were provided with a 3-minute interval for the preparation of the speech and were not allowed to refer to their notes while delivering

the speech. Post delivering the speech, the participants were asked to count from 2023 to 0 and whenever the participants made a mistake, they were asked to start over. For calibrating the meditation condition, the participants were subjected to a breathing exercise in closed eyes and a comfortable sitting position. And lastly, for the recovery condition, all the sensors were again synchronized using a double-tap gesture and were removed from the participant's body.

3.2. Data Conversion and Preprocessing. The data generated from both the wearable devices were in raw format. Therefore, the primary task that had to be performed for getting ahead in the process was to perform the conversion and generalization of the data into the SI units.

3.2.1. Electrocardiography (ECG) Data from the Chest. The ECG data provided by [10] was extracted from the subject by using RespiBAN that was attached to the subjects' chest during the complete experimental procedure. The raw data of the ECG were transformed to its SI unit that is millivolt (mV) using the following formula:

$$\left(\frac{\text{signal}}{\text{Chan\_Bit}} - 0.5\right) * V_{\text{CC}}\ \text{mV}, \tag{1}$$

where the signal is the value at a particular epoch, Chan_Bit refers to the output size, which is equal to 216, and V_{CC} refers to the voltage input, which is equal to 3 mV.

3.2.2. Electromyography (EMG) Data from the Chest. The EMG data were extracted from the subject at the sampling rate of 700 Hz from the chest using the RespiBAN device. The raw data of the EMG were converted to its SI unit that is microvolts (μV) using the following formula:

$$\left(\frac{\text{signal}}{\text{Chan\_Bit}} - 0.5\right) * V_{\text{CC}}\ \mu V, \tag{2}$$

where the signal is the value at a particular epoch, Chan_Bit refers to the output size which is equal to 216 and V_{CC} refers to the voltage input which is equal to 3 μV.

3.2.3. Respiration Data from the Chest. The respiration data were extracted from the subject's chest using the RespiBAN device at 700 Hz of sampling frequency during the experimental procedure. The raw data was converted to a form of displacement percentage using the piezoelectric sensors. The formula for the conversion is as follows:

$$\left(\frac{\text{signal}}{\text{Chan\_Bit}} - 0.5\right) * 100\%, \tag{3}$$

where the signal is the value at a particular epoch, and Chan_Bit refers to the output size, which is equal to 216.

3.2.4. Triaxial Accelerometer from the Wrist. The triaxial accelerometer data were captured from the wrist using Empatica E4, which sampled the data to 32 Hz, and the data provided were in the units of 1/64 g. Therefore, the following formula ensures the conversion of the raw data from the triaxial accelerometer to its SI units that is m/s^2:

$$\frac{\text{signal} * 2 * 9.8}{128}\ \text{m/s}^2. \tag{4}$$

3.2.5. Blood Volume Pulse (BVP) from the Wrist. The BVP data are also known as the photoplethysmograph (PPG) data that were extracted from the subjects' wrist using the Empatica E4 at a sampling rate of 64 Hz. The PPG basically narrows down the change in the volume of blood that is being caused by the pressure pulse by illuminating the skin with a light-emitting diode and detecting the amount of light transmitted and reflected back using a photodiode.

3.2.6. Temperature Data from the Wrist. The temperature data from the wrist were pursued using the Empatica E4 device that performed the data generation at a sampling frequency of 4 Hz. The data generated from the subject were in the unit of degree Celsius.

Post conversion and generalization of the raw data to their SI units, the next step that was undertaken was data preprocessing. The data that have been fetched in the study comes from different regions of the subject's body, and multiple devices have been used for the extraction of the data. Moreover, we can observe that there is a lot of variance in terms of the sampling rate of different signals. Therefore, for generalizing the frequencies of all the signals, we tend to convert all the low-sampled signals to 700 Hz initially. Therefore, the triaxial accelerometer data, blood volume pulse, and temperature data have been upsampled to 700 Hz. Now, as the signals have been upsampled to 700 Hz, therefore the data for 15 subjects captured for 100 minutes turned out to be huge in size. So, the signals were further downsampled to 10 Hz by aggregating every 70 samples together using statistical techniques. Also, on the other hand, the labels were downsampled to 10 Hz by taking the mode of the labels for every 70 samples. Finally, after performing all the aggregations and changes in the sampling frequency, the total number of samples of the whole data set for 15 subjects turned out to be 573,480. The distribution of the state of the mind categories has been depicted in Table 1, from which we can find out that the data set is extremely unbalanced in nature.

3.3. Feature Engineering. The features that have been engineered from the raw biosignals data are primarily varied in three different forms. The first form is the one-to-one variance or continuous feature variable. In this type of feature, each and every sample of the data set gets an individual value and is continuous in nature. The second form is the subject-wise variance where all the samples of a particular subject are provided with the same value for a particular feature. The third form of feature is based on

Table 1: State of the mind category distribution.

State of the mind class	Number of samples
Baseline	274,790
Amusement	117150
Stressed	65450
Meditation	37090
Recovery	79000

minute-based variance, where all the samples of a particular minute are provided with the same value. Therefore, using such methods usually provides the features with an optimum variance, which can lead to a better model in terms of generalizability and better classification performance.

The features derived from the ECG, EMG, respiration, and BVP are peak-based features, and the features derived from the accelerometer are purely statistical in nature. The peak-based features for the 1-dimensional biosignals are determined by calculating the local maxima of the cycle of the signal by leveraging the information of the threshold and the definite distance that is needed to be maintained between consecutive peaks.

3.3.1. Electrocardiography (ECG) Features. The features for electrocardiography are basically in the form of minute-based variance where each minute of particular feature gets a different value. Moreover, the features defined in the purpose of ECG are peak-based features as it is a primary notion in terms of biosignals that the peaks of the signal carry a summative value to an entire cycle.

Figure 1 shows the ECG signal of the second subject for the first 30 seconds, which corresponds to 300 samples as the sampling frequency of the signal was aggregated to 10 Hz. Also, in the figure, we can see the local maximas that have been identified, which further helps to obtain multiple features for the work.

In Table 2, we can observe four features have been mentioned that persuasively points out the patterns in the ECG signal of an individual. Moreover, the features described in the work provides a varied understanding of the subject's nominal peak ranges in the ECG signal, which in turn can be used to determine the state of the subject at a particular instant of time.

3.3.2. Electromyography (EMG) Features. The electromyography signals are well known to measure and record the electrical coefficient of skeletal muscles that tend to define the activation level and figures out the medical abnormalities in a subject. The features calculated for the EMG signal are minute-wise varied to offer an optimum variance across each feature.

Figure 2 portrays the EMG signals of subject 2 for the first 30 seconds of the experimental procedure. The red markings shown in the image are the local maxima, which primarily depict the impulsiveness of the electrical coefficient of the skeletal muscles of the subject. Moreover, the peaks or the local maxima tend to identify the pattern in the EMG signals, which can further identify the medical abnormalities in the subject too.

The features demonstrated in Table 3 points out the initial patterns of the EMG signals of a subject, also considering the features based on the peaks of the signals rules in summative information of the signal.

3.3.3. Respiration Features. The respiration data have been extracted from the chest, which shows the tone and rhythm of the breath and also places the ratio between multiple breath cycles. Also, the respiration data have always been helpful in terms of determining the state of mind and in determining the level of arousal or rate of bio-intensity of a particular subject. The features derived from the respiration data are minute-based such as ECG and EMG. Figure 3 shows the respiration data for the first 10 seconds during the experimental analysis on subject 2.

Moreover, Table 4 points out the features that depict the patterns across the respiration of the subject. Seeking out the patterns allows for performing some primary anomaly detection on the behavior of the subject across a particular time interval. Therefore, in this work, we considered the usage of respiration signals as a feature to analyze the state of mind of an individual.

3.3.4. Blood Volume Pulse Features. The BVP signal is specifically derived from the photoplethysmogram that illuminates the skin to determine the changes in the light absorption. From the peaks of BVP, we can determine the heart rate of an individual as every time the heart pumps blood, there is a slight change in the volumetric quantity of blood in arteries, which can be detected using a BVP Signal. In Figure 4, we can see the BVP data that have been plotted for subject 2 for 20 seconds and the peak has been determined.

The features for BVP signal are also varied on the terms of a minute where each minute gets a different value. Table 5 shows the features that have been used in terms of generating impactful patterns from the BVP data. The trends and the pattern of a particular subject can be readily obtained from the features as it intends to capture the essential details of the signal.

3.3.5. Accelerometer Features. The accelerometer signals are quite reliable in terms of analyzing the level of stress in an individual by seeking out the patterns in the movement [22]. The features are varied with respect to the subjects where all the samples of a particular subject are utilized for the computation of the feature and each subject gets a unique value. The features engineered from the accelerometer signal are being depicted in Table 6 where it can be observed that except correlation-based features, all other features are standalone features. Only the correlation-based are based on the interaction of two axes. Moreover, the features that have been mentioned in Table 6 have been calculated for all the three axes of the accelerometer.

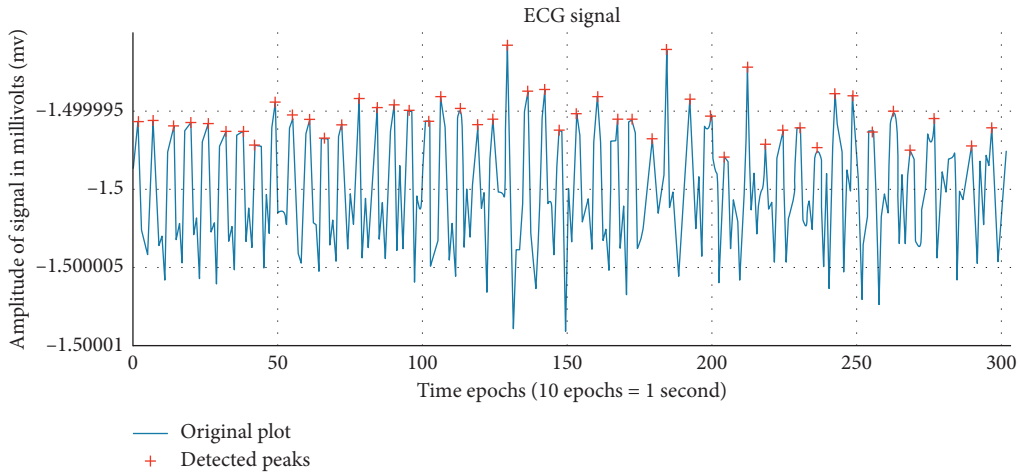

Figure 1: ECG signal for 30 seconds of subject 2.

Table 2: Electrocardiography (ECG) features.

Feature name	Description
ECG_Peaks	This gives out the number of local maxima in a minute
ECG_Average_Amplitude	This feature gives out the average amplitude of the local maximas in a minute
ECG_Differ_Mean	This feature pursues the average difference between consecutive local maxima in a minute
ECG_Resting	This feature shows out the resting motion of a subject, which means the number of local maxima within 10 samples that is 1 second

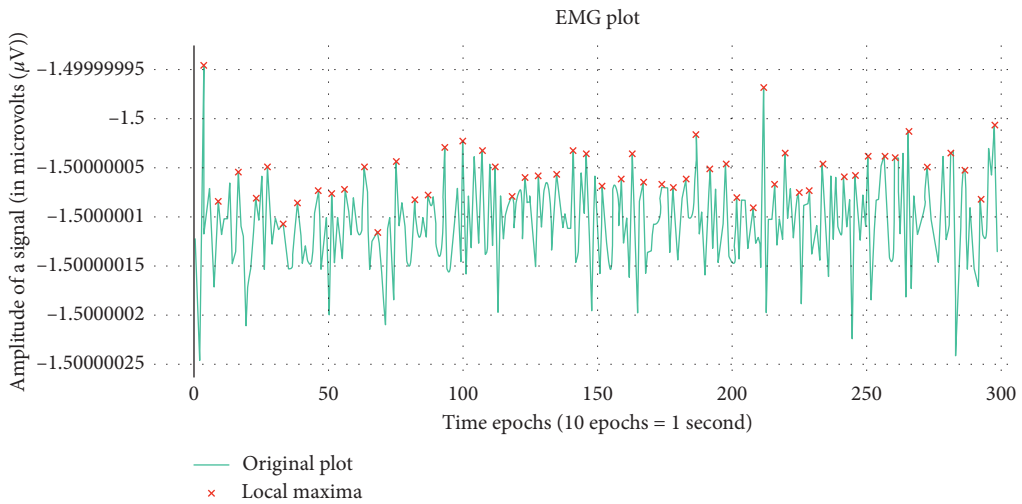

Figure 2: EMG signal for 30 seconds of subject 2.

4. Deep Learning

4.1. Multichannel Convolutional Neural Network Architecture. In recent years, it has been observed how supervised learning techniques have evolved to create some most innovative architectures for solving a particular problem. More evidently, the rise in popularity can be observed for the deep learning algorithms too, which has undergone a major paradigm shift in terms of structure, optimizer functions, and the architecture [23]. Moreover, in the field of health care, the usage of deep learning algorithms has created a reform in terms of image analysis, aneurysm detection in images, biosignals, and a lot more.

In this work, biosignals from chest and wrist wearables have been used for the detection of the state of the mind

Table 3: Electromyography (EMG) features.

Feature name	Description
EMG_Peaks	This gives out the number of local maxima in a minute
EMG_Average_Amplitude	This feature gives out the average amplitude of the local maximas in a minute
EMG_Differ_Mean	This feature pursues the average difference between consecutive local maxima in a minute

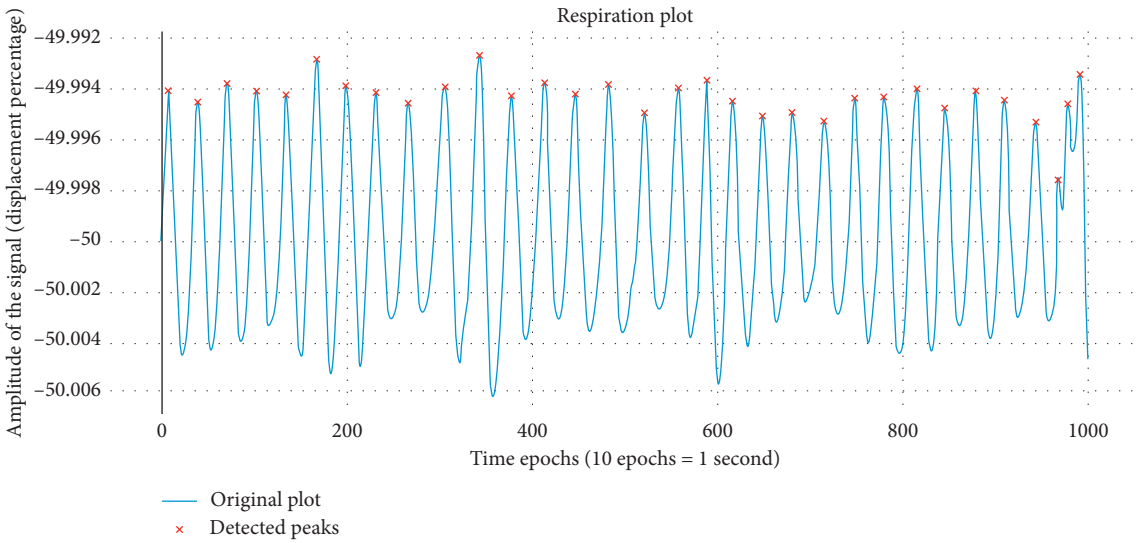

Figure 3: Respiration signal for 100 seconds of subject 2.

Table 4: Respiration features.

Feature name	Description
RESP_Peaks	Number of breath cycles in a minute
RESP_Average_Amplitude	This feature gives out the average amplitude of the local maximas in a minute
RESP_Differ_Mean	This feature pursues the average difference between consecutive local maxima in a minute

while undergoing a stress interview. The major significance of this work stands with identifying the stress segment of an individual. For the identification and the predictions of the state of mind, a multichannel convolutional neural network has been used for guaranteeing the optimum generalizability and for identifying complex patterns in the biosignals.

The model architecture for the multichannel convolutional neural network has been depicted in Figure 5. The architecture shows 5 different input channels for ECG, EMG, respiration, BVP, and accelerometer, respectively. The reason for going forward in separating the channels for different biosignals lies with the fact that the initial feature learning using convolutional neural network for a particular biosignal is being kept discrete with respect to other biosignals for preventing the initial information mixing between individuals [24, 25]. Therefore, the features corresponding to each biosignal such as ECG (4 features), EMG (3 features), respiration (3 features), BVP (3 features), and an accelerometer (15 features) have been coupled respectively and passed along the respective channels.

The most distinctive aspect of convolutional neural networks is the convolution layer, which is used for traversing along the matrix of the data to create a penultimate feature matrix of spatially oriented features using an adaptive kernel or a filter. The adaptive filters for the convolution layers in the multiple channels are to be adjusted on the basis of the input shape of the data matrix. Therefore, the following equation has been used to choose the optimum shape for the filter.

$$f(x, 1) = \left[\text{round}\left(\frac{x}{2}\right) + x\%2\right], \tag{5}$$

where $(x, 1)$ represents the shape of the filter. The equation takes the input size or the number of features used for training as an input, which is denoted by x. The term x further undergoes a summation of a round function over x

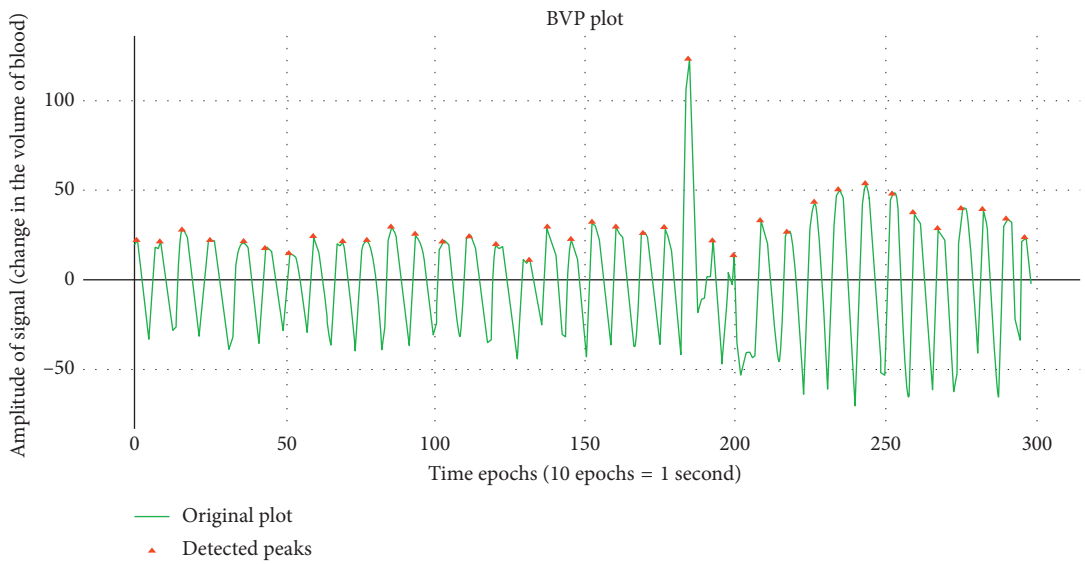

Figure 4: Blood volume pulse for 30 seconds of subject 2.

Table 5: Blood volume pulse features.

Feature name	Description
BVP_Peaks	This gives out the number of local maxima in a minute
BVP_Average_Amplitude	This feature gives out the average amplitude of the local maximas in a minute
BVP_Differ_Mean	This feature pursues the average difference between consecutive local maxima in a minute

Table 6: Accelerometer signal features.

Feature	Equation	Description
Mean	$\overline{x} = (1/n)\sum_{i=0^n}(x_i)$	The mean of the signal for each subject
Standard deviation	$\sigma = \sqrt{1/N\sum_{i=1^N}(x_i - \overline{x})^2}$	The standard deviation of the signal is calculated for each value
Correlation	$\mathrm{Corr} = (1/(N-1))\sum_{n=1^N}((x_i - \overline{x})(y_i - \overline{y}))/(\mathrm{std}(x) * \mathrm{std}(y))$	The correlation coefficient between the two accelerometer signals
Kurtosis	$\mathrm{Kurt}(x) = (E[(x - \overline{x})^4]/\mathrm{std}(x)^2) - 3$	Kurtosis shows the peakedness of a signal
Crest factor	$\mathrm{Crest}(x) = ((\max(x(n)))/(\sqrt{(1/(N-1))\sum_{n=1^N} a(n)^2}))$	It shows the signal impulsiveness with the maximum accelerometer value

and a modulo function over x, which further provides us the shape of the adaptive filter or the kernel. As in the work we are dealing with $1 - D$ convolutions, the shape of the kernel is always in the form of $(x, 1)$.

The feature maps from the first convolution layer are further passed to the second layer of convolution without using any subsampling layer in between. By considering the huge spatial volume of the data that is being trained on the CNN architecture, it can be duly argued that using subsampling layer, such as pooling in between consecutive CNN layers, can make the solution less computationally expensive. But, the usage of subsampling layers for the data whose numerical significance is more important than the spatial arrangement possesses information loss [26]. Therefore, in this architecture, the usage of pooling or subsampling layers has been avoided.

The generated feature matrix by the 2nd convolution layer is then subjected to a fattening layer. The flattening layer first converts the feature matrix from a 2-dimensional matrix to a 1-dimensional array because the subsequent stages of the network contain dense layers. And, for passing a set of data to the dense layer, it is required that the data must be in 1-dimensional format.

After the data are subjected to a flattening layer, they is then subjected to a dropout layer. The dropout layer that has been used in the architecture is basically used for performing regularization and it also assists the model in preventing overfitting. The dropout layer allows the model to fetch for

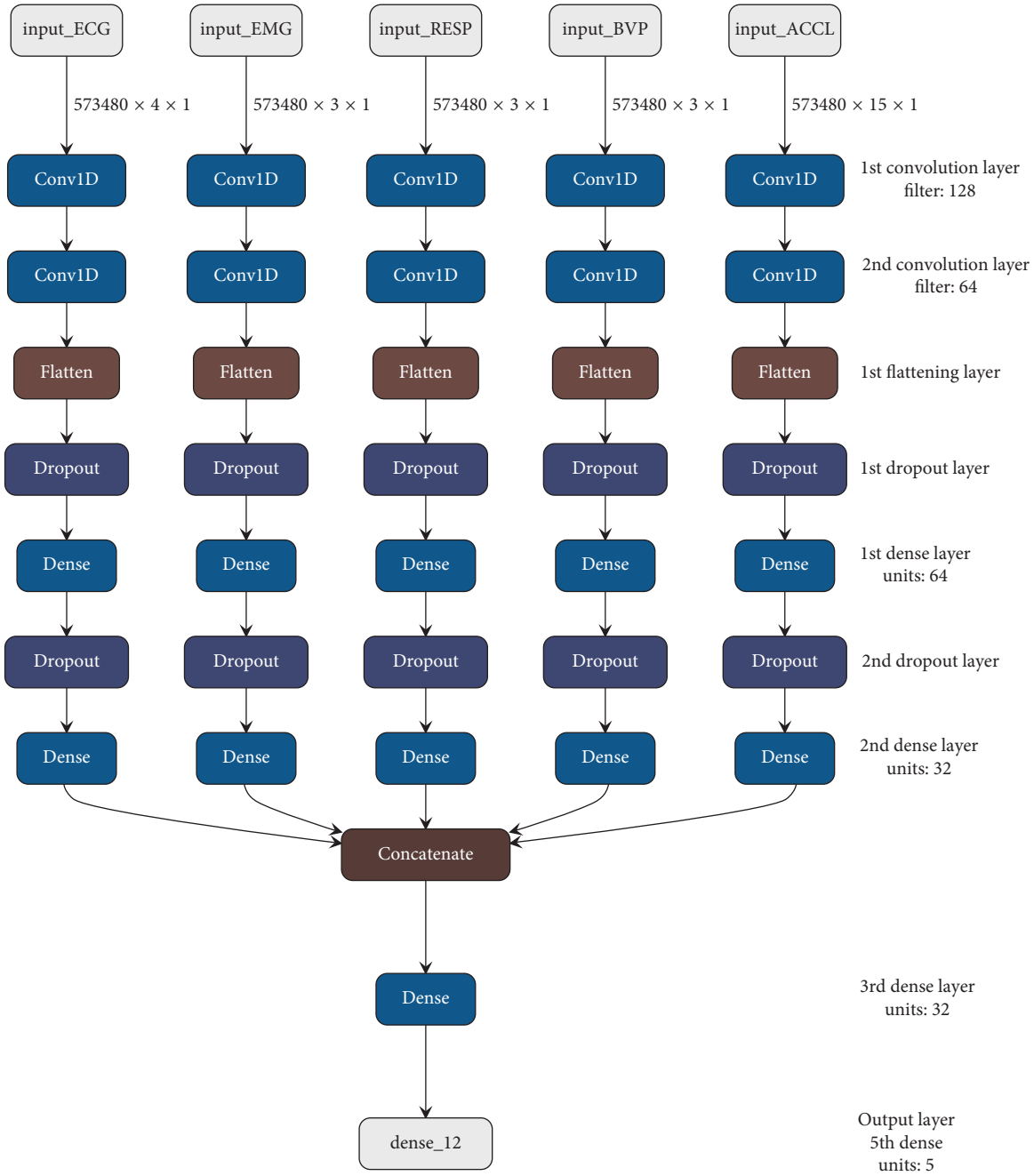

Figure 5: Multichannel CNN architecture.

more complex and robust feature relationships by dropping a set of neurons from the visible and the hidden layers to perform more randomized feature learning.

The 6th layer in the architecture is a dense layer, which is the fully connected layer with 64 units. The dense layer allows the model to perform a linear operation on the feature matrix that has been generated by the convolution layer. Moreover, as the convolution layers work locally for the spatial set of defined filters that traverses along with the data matrix, the dense layer acts as a global layer where all the nodes of the layer participate and are connected to all the other nodes in the following layers. Therefore, the usage of dense layers in this work allows the model to establish a global relationship between the features and also accounts for the abstraction of more complex patterns in the data.

The 9^{th} layer in the network is the concatenation layer that allows us to combine the feature matrices from all the channels. The reason behind the concatenation of the feature matrices lies in accordance with our problem statement, which is to detect the state of the mind based upon multiple signals. Therefore, for obtaining the decision threshold based upon all the biosignals, the concatenation of the feature matrices from all the channels is required.

The subsequent layer after the concatenation layer is fully connected layer with 32 units. This fully connected layer is used for fetching out the composite relationships between the concatenated feature matrices from the multiple channels. This layer majorly plots the complex features, complex relationships, and the patterns among the combined feature matrices that support the generation of the decision threshold. The last layer or the output layer that is depicted in Table 7 as well as in Figure 5 consists of 5 units for the 5 classes that are to be predicted namely, baseline condition, amusement condition, stress condition, meditation, and recovery condition. The final dense layer yields the prediction probability of each sample for the 5 classes.

4.2. Training Procedure and Cross Validation. The model training in the work used two varied procedures namely Type I and Type II. The type I procedure predominantly was utilized for tuning the hyperparameters and choosing the most viable optimizers for increasing the model performance. Moreover, the type I model was also used to check an initial performance of the model for randomized sequence. For creating the model based on type I procedure, the complete data set was split as 70% of the data were allotted to the training set, 20% were allotted to the validation set and lastly, 10% were allotted to the testing set. The samples that were placed on different sets of data were chosen randomly to remove any correlation in terms of subjects. Table 8, therefore, points out the number of samples and input features in all the channels for training, validation, and testing in a more constructive way for the type I procedure.

On the other hand, another procedure for training the model was also undertaken by using a cross-validated approach using the data of individual subjects as the testing set. This particular approach was named as Type II procedure. More particularly, for creating the type II model, a 15-fold cross-validation was performed on the data of 15 subjects, where the data of a particular subject were always kept aside for creating the test set. The remaining data of 14 subjects were further allocated to the training and the validation set based on a randomized split with a ratio of 80 : 20. This particular model was developed only for the sake of understanding the capability of the model to generalize across different subjects. Table 9 demonstrates the number of samples that were used in the training, validation, and testing for each fold by keeping a particular subject's data in the testing set only.

4.3. Model Hyperparameters, Loss, and Optimization Functions. The development of a model architecture is one of the prime components of the system that is being developed in the work. But, more advertently, the component that works for the state-of-the-art model architectures is the control over the training process and to optimize the model's performance and outcomes. Therefore, the components such as the model hyperparameters, loss functions, and the optimizer functions are discussed in the following sections.

4.3.1. Model Hyperparameters. The control of the training process is generally held by the hyperparameters that are used for the tuning of the model. As of the current scenario, the optimization of the models by minimizing the testing error is considered to be one of the toughest challenges. But in an intermittent way, the tuning of the elements that reside outside of the model actually influences the complete performance of the model and can be considered as the most challenging part in solving the problem. The primary reason behind the difficulty lies with the fact that the chosen hyperparameters must be model-specific and not training set-specific because hyperparameters that are tuned on the basis of the training set often develop poor model generalizability. Therefore, choosing the right set of hyperparameters is important to maintain the overall tradeoff between model generalizability and optimum objective score.

So, for the choice of right set hyperparameters, Bayesian Sequential Model-Based Optimization (SMBO) is used. Bayesian SMBO is a type of hyperparameter optimization that minimizes a particular objective function by developing a surrogate model (probability function) based on the previous evaluation results of the objective function. The basic objective function of the Bayesian SMBO is given by

$$P(\text{score} \mid \text{hyperparamters}) = \frac{P(\text{hyperparamters} \mid \text{score}) P(\text{score})}{P(\text{hyperparamters})}. \tag{6}$$

The surrogate model is considered to be less expensive to be optimized than the main objective function [27]. Therefore, the next set of values that are to be evaluated are selected by using the expected improvement criterion [28]. The expected improvement criterion is defined by:

$$\text{EI}(x) = E\left(\max\left(f(x) - f^*, 0\right)\right), \tag{7}$$

where x belongs to the set of hyperparameter values and considered to be an improvement in the value of the objective function $f(x)$, and f^* is the maximum value of the objective that has been observed.

The set of hyperparameters that were obtained by running Bayesian SMBO on the model are

$$\begin{aligned} \text{learning rate:}\ & 0.00125, \\ \text{beta\_1:}\ & 0.9765841, \\ \text{beta\_2:}\ & 0.8541287, \\ \text{decay:}\ & 0.000235. \end{aligned} \tag{8}$$

4.3.2. Model Loss Function. The loss function is a very integral part of the deep learning and the machine learning models. The loss functions are basically used to measure the variability between the predicted output ($\hat{y}$) and the actual value (y). The loss functions are nonnegative values that increase the generalizing capability of the model by decreasing the value of the loss function [29]. The basic structure of the loss functions is

Table 7: Multichannel CNN architecture.

Layer	Layer type	Filters	Size	No. of parameters	Output dimension	Activation
1	Input	—	—	—	ECG: (4, 1) EMG: (3, 1) RESP: (3, 1) BVP: (3, 1) ACCL: (15, 1)	—
2	Conv1D (1st layer)	128	ECG: (2, 1) EMG: (2, 1) RESP: (2, 1) BVP: (2, 1) ACCL: (8, 1)	ECG: 384 EMG: 384 RESP: 384 BVP: 384 ACCL: 1152	ECG: (3, 128) EMG: (2, 128) RESP: (2, 128) BVP: (2, 128) ACCL: (8, 128)	ReLU
3	Conv1D (2nd layer)	64	ECG: (2, 1) EMG: (2, 1) RESP: (2, 1) BVP: (2, 1) ACCL: (8, 1)	ECG: 16448 EMG: 16448 RESP: 16448 BVP: 16448 ACCL: 65600	ECG: (2, 64) EMG: (1, 64) RESP: (1, 64) BVP: (1, 64) ACCL: (1, 64)	ReLU
4	Flatten		—	—	ECG: 128 EMG: 64 RESP: 64 BVP: 64 ACCL: 64	—
5	Dropout	—	—	—	—	
6	Dense (1st layer)	64	—	ECG: 8256 EMG: 4160 RESP: 4160 BVP: 4160 ACCL: 4160	ECG: 64 EMG: 64 RESP: 64 BVP: 64 ACCL: 64	ReLU
7	Dropout	—	—	—	—	—
8	Dense (2nd layer)	32		ECG: 2080 EMG: 2080 RESP: 2080 BVP: 2080 ACCL: 2080	ECG: 32 EMG: 32 RESP: 32 BVP: 32 ACCL: 32	ReLU
9	Concatenate	—		0	160	
10	Dense (3rd layer)	32	160	5152	32	ReLU
11	Dense (output)	5	32	165	5	SoftMax

Table 8: Training, validation, and testing divisions for all the channels and number of features for Type I.

Channel	Training samples	Testing samples	Validation set	No. of features
ECG channel	616,413	176,118	88,059	4
EMG channel	616,413	176,118	88,059	3
Respiration channel	616,413	176,118	88,059	3
BVP channel	616,413	176,118	88,059	3
Accelerometer channel	616,413	176,118	88,059	15

$$L(\theta) = \frac{1}{n}\sum_{i=1}^{n} L\left(y^{(i)}, f\left(x^{(i)}, \theta\right)\right), \tag{9}$$

where θ represents the parameters of the model, x represents the feature matrix of the model, and y represent the actual labels of the model.

The loss function used in the work is the categorical cross-entropy loss, which is also known as the SoftMax loss. In the categorical cross-entropy loss function, each prediction is compared to the actual class value and a score is calculated. The score is further used to penalize the probability of the prediction based on the difference from the actual value. The penalty that is offered to the predicted value is purely logarithmic in nature where a small score is allotted to tiny differences and the huge score is allotted to larger differences [30]. The equation for the categorical cross-entropy loss is given by

$$L(y, \hat{y}) = -\frac{1}{n}\sum_{i=1}^{n}\sum_{j=1}^{c}\left(y_{i,j}\log\left(\hat{y}_{i,j}\right)\right), \tag{10}$$

Table 9: Number of samples for each fold of training.

The subject in the test set	Training set	Validation set	Testing set
Subject 1	656,872	164,218	59,500
Subject 2	654,184	163,546	62,860
Subject 3	654,264	163,566	62,760
Subject 4	655,896	163,974	60,720
Subject 5	649,320	162,330	68,940
Subject 6	663,744	165,936	50,910
Subject 7	661,960	165,490	53,140
Subject 8	664,144	166,036	50,410
Subject 9	661,728	165,432	53,430
Subject 10	663,824	165,956	50,810
Subject 11	650,536	162,634	67,420
Subject 12	658,360	164,590	57,640
Subject 13	654,512	163,628	62,450
Subject 14	653,984	163,496	63,110
Subject 15	659,280	164,820	56,490

Table 10: Comparative analysis of the model performance based on the optimizer algorithms for subject 1 in the testing set.

Metric	Adam	RMSprop	SGD
Accuracy	97.62	90.45	92.51
Recall "baseline"	0.9861	0.8945	0.9063
Precision "baseline"	0.9703	0.9106	0.9542
F1 score "baseline"	0.9716	0.9033	0.9311
Recall "amusement"	0.9891	0.9322	0.9256
Precision "amusement"	0.9956	0.9158	0.9428
F1 score "amusement"	0.991	0.9288	0.9299
Recall "stress"	0.9832	0.9647	0.9568
Precision "stress"	0.9784	0.94	0.9487
F1 score "stress"	0.9693	0.9561	0.9509
Recall "meditation"	0.9583	0.9428	0.9467
Precision "meditation"	0.9752	0.9022	0.9788
F1 score "meditation"	0.9680	0.9312	0.9635
Recall "recovery"	0.9456	0.9365	0.9387
Precision "recovery"	0.9711	0.9174	0.9579
F1 score "recovery"	0.9620	0.9258	0.9466

where the double sum has been performed on the ith data samples ranging from 1 to N and the classes that range from 1 to C. The term $y_{i,j}$ in the equation corresponds to the actual one hot encoded label at i^{th} index of j^{th} category. And the term $\hat{y}_{i,j}$ corresponds to the prediction of the model for the samples as i^{th} index [30].

4.3.3. Model Optimizer Functions. The optimizer functions are the ones that play an integral part in the optimization of the internal parameters of a model. The internal parameters of the type of model that is being dealt with in the work are the weights and biases. Now, in the previous segment, we have discussed the loss function of the model that needs to be minimized over the training iterations. But the loss function is more of a mathematical way of determining what is the error rate between the predictions and the actual labels. Therefore, optimizer functions are used to incorporate the loss function with the models' internal parameters such as weight and biases for updating the same based on the response generated from the loss functions.

In this work, multiple optimizer algorithms were used and a comparative analysis was performed with regard to which optimizer function relates to the best minimization of the categorical cross-entropy loss and ties best with the hypothesis of the problem. The comparative analysis can be seen in Table 10 between the multiple optimizer functions and the best optimizer for the problem statement was found to be Adam optimizer.

5. Results

The multichannel convolutional neural network model developed in the work aimed to provide very sound and effective results on the basis of the classification of the different state of minds for a particular subject. Also, the model developed in the work provided with the results by prompting an average recall and precision of 97.238% and 97.652%, respectively, for all the classes. The model also showcased a constant tendency of precision and recall in the random data folds of training and testing.

Moreover, with prior accordance to the hypothesis that was developed in the initial phase stated the rules that the precision and recall of all the class must be above the same threshold providing a fixed classification rate in all classes. As in the previous work [10] we have seen that the hypothesis tends to prioritize more on the third class, which is the stress, but in this work, we tend to predict the samples of all the five classes precisely.

In Figure 6, we can see the confusion matrix that has been derived on the basis of the classification results of the test data set. Therefore, we can see from the confusion matrix that it has full accordance with the hypothesis with regard to the correct true positives and true negatives of each class. But in Figure 6, it can be observed that the baseline class has a greater number of mispredictions than other classes and also other classes have got a lot of the samples that have been mispredicted to the baseline class. The primary reason behind such an incident is that the features of the data sample belonging to the baseline class have a strong correlation with features of the data samples belonging to other classes. But, such a scenario can be avoided by lowering the prediction threshold from 0.2 of all the classes except the baseline class, which in turn will reduce the mispredictions in the baseline class. However, dampening of the prediction threshold of the classes may lead to an invariant scenario of less generalizability of the model. Therefore, to maintain a tradeoff between the correct predictions and the mispredictions, the situation is been kept as it is.

The metrics used for evaluating the potential of the model are precision, recall, and the F1 score of all the classes. In the current scope of this work, the recall of each class provides us the information, with regard to the number of data samples that the model has correctly predicted to be of a particular class. The precision on the other hand of a particular class determines the confidence of prediction to belong to a particular class. And lastly, the F1 score suggests the weighted average of both precision and recall and

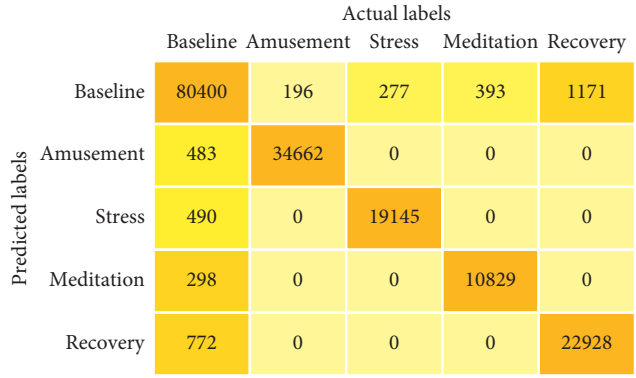

Figure 6: Confusion matrix of the multichannel CNN model.

therefore takes a leap over all the wrongly predicted samples of a particular class.

Figure 7 shows the training and validation convergence of the model. The model iteration that has been shown in the figure is the final model that is trained with the hyperparameters mentioned in Section 4.3.1 and the optimizer algorithm Adam.

Table 10 puts forward the classification report of the model with respect to different optimizer algorithms that were used to optimize the internal parameters of the model. From the table, it can be seen that all the three optimization algorithms namely, Adam, RMSprop, and SGD provided us with decent results. But, for the creation of the final binary serialized object of the model, Adam was selected. The reason for choosing Adam in this scenario lies behind a few reasons:

(i) The overall performance of the Adam Optimized model is better than the other two.

(ii) The model optimization is very much time-efficient.

(iii) The model optimization is computationally efficient.

(iv) As the type of data, we are dealing within the work, there is no prospect for an upper bound or lower bound of a particular type of biosignal. Therefore, for reproducibility of the model in the future, it may happen that the gradients might change for a particular type of subject. So, having an algorithm to optimize the model which is not varied by the rescaling of the gradient will turn out to be useful [31].

Table 11 plots the comparative analysis between the performance of the multichannel convolutional neural network and conventional single-channel convolutional neural network. Both the networks have been trained with the same optimizer function that is Adam but for the single-channel convolutional neural network, a different set of hyperparameters were used, which were derived by using the same Bayesian SMBO. From Table 11, it can be evidently observed that the single-channel also performed respectively well. But, the performance of the multichannel convolutional neural outperformed that of the single-channel convolutional network. Moreover, in the "meditation class" of the single-channel convolutional neural network, it can be observed that the recall is pretty low than other classes. The lower value of the recall for the meditation class is because there are comparatively a smaller number of samples in the meditation class than other classes. Therefore, it was found that the multichannel convolutional neural network overcomes the hurdle regarding such imbalanced classification where there is an identifiable disparity in the number of samples across the classes.

Table 12 depicted below further shows the model performance of the multichannel convolutional neural network model, which was trained using the cross-validated approach or type II model. The type II model seemed to provide decent results. But, we can see that there is quite a difference between the performance level depicted in Table 11 by the Type I model where the training, validation, and testing sets were randomized samples and in Table 12 by the Type II model where the sample of a particular subject is only on the testing set. The primary reason behind this deviation in the model performance is that every subject has altogether different kind of thresholds when it comes to biosignal-based predictions.

6. Discussion

In the present world, as the life of people have changed in a varied way where they are much suited to the new customized lifestyle and the disorientation of the biological clock, it has been very necessary and of paramount importance that the state of mind and health must be maintained properly. But, people these days have turned out to be more reluctant to spend their time with the therapists or the doctors for pursuing a proper check on their health. Therefore, with the emergence of smart healthcare, the process could be very much maintained and measured using the wearable devices that have grown into much affluence in society. We know that the smart wearables that have presently arrived in the sector support multiple biosignals of the user such as movement, heart rate variability, pulse pressure, vascular respiration, perfusion index, etc. Therefore, these biosignals, if properly monitored for a particular subject, will be able to identify

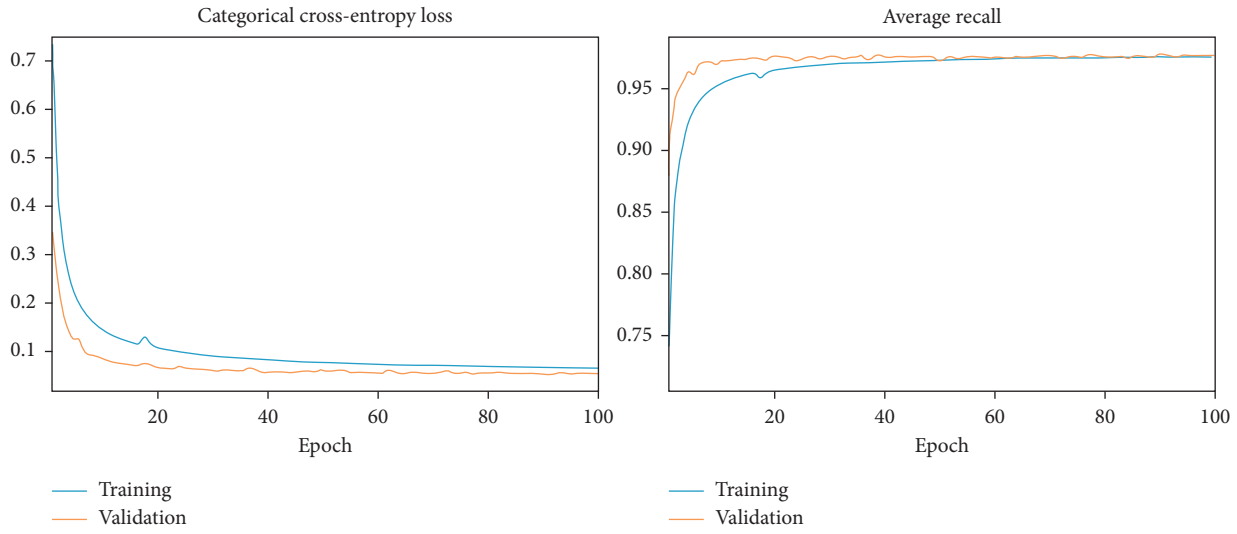

Figure 7: Model training process using Adam optimizer for 100 epochs.

Table 11: Comparative analysis of the model performance for multichannel CNN and single-channel CNN for subject 1 in the testing set.

Metric	Multi channel CNN	Single channel CNN
Accuracy	97.62	87.53
Recall "baseline"	0.9861	0.9524
Precision "baseline"	0.9703	0.9347
F1 score "baseline"	0.9716	0.9435
Recall "amusement"	0.9891	0.9311
Precision "amusement"	0.9956	0.9006
F1 score "amusement"	0.991	0.9132
Recall "stress"	0.9832	0.8991
Precision "stress"	0.9784	0.9157
F1 score "stress"	0.9693	0.9036
Recall "meditation"	0.9583	0.7658
Precision "meditation"	0.9752	0.8631
F1 score "meditation"	0.9680	0.8122
Recall "recovery"	0.9456	0.9136
Precision "recovery"	0.9711	0.9217
F1 score "recovery"	0.9620	0.9178

the health conditions as well as will be able to detect the primary anomalies in the health.

The data that have been used in the work have been properly curated from the wearable device worn by the subject during the experimental process for detecting the certain state of mind that can be very much useful to understand the mental conditions of the subject. In the data amalgamation process, five key classes were noted namely, recovery, baseline, stress, amusement, and meditation. And for the classification purpose, multiple biosignals were utilized such as accelerometer, electrocardiography, electromyography, blood volume pulse, and body temperature. The signals were further analyzed to perform optimum feature engineering where the summative information of complete signals is extracted using the maxima and the minima of the signal at a particular instance of time.

For the classification purpose, a multichannel convolutional neural network architecture was developed in the work. The primary concern for the development of a multichannel architecture is that as we have different biosignals from different parts of the body, we tried to avoid the initial intermixing of the features of different biosignals. But later on, at the penultimate region, the feature matrixes conceived by different channels are concatenated for pursuing an integrated decision threshold for the detection of the state of the mind from all the biosignals. But at a certain point, a question can be raised that "Why deep learning has been used for solving the particular problem?" The answer to the question lies in the fact that as the biosignals are of an abstract nature and there are multiple complex interactions and patterns in the data, manually engineering the right features would be very difficult. Therefore, in this work, deep learning is performed as the method has the ability to produce extremely complex feature representations and also allows model reproducibility, which will allow us to perform incremental learning if a certain new set of data arrives.

Table 12: Comparative analysis of the model performance for multichannel CNN for Type-II model.

Metrics	Subject 1	Subject 2	Subject 3	Subject 4	Subject 5	Subject 6	Subject 7	Subject 8	Subject 9	Subject 10	Subject 11	Subject 12	Subject 13	Subject 14	Subject 15
Accuracy	75.34	78.66	74.56	0.7644	75.84	76.54	77.8	79.89	78.26	76.20	76.79	77.72	77.66	78.08	76.14
Recall “baseline”	0.724	0.79	0.741	0.748	0.739	0.873	0.793	0.874	0.814	0.813	0.791	0.831	0.884	0.83	0.719
Precision “baseline”	0.752	0.795	0.771	0.715	0.769	0.718	0.798	0.715	0.79	0.727	0.742	0.809	0.8	0.775	0.713
F1 score “baseline”	0.738	0.792	0.756	0.731	0.754	0.788	0.795	0.787	0.802	0.768	0.766	0.82	0.84	0.802	0.716
Recall “amusement”	0.723	0.75	0.718	0.676	0.669	0.694	0.678	0.705	0.709	0.694	0.676	0.686	0.714	0.682	0.728
Precision “amusement”	0.727	0.813	0.818	0.841	0.81	0.835	0.714	0.769	0.752	0.742	0.777	0.816	0.844	0.79	0.736
F1 score “amusement”	0.725	0.78	0.765	0.75	0.733	0.758	0.696	0.736	0.73	0.717	0.723	0.745	0.774	0.732	0.732
Recall “stress”	0.719	0.734	0.786	0.74	0.804	0.718	0.744	0.744	0.806	0.734	0.767	0.749	0.746	0.747	0.801
Precision “stress”	0.785	0.796	0.769	0.788	0.843	0.781	0.836	0.778	0.813	0.785	0.815	0.844	0.805	0.76	0.838
F1 score “stress”	0.751	0.764	0.777	0.763	0.823	0.748	0.787	0.761	0.809	0.759	0.79	0.794	0.774	0.753	0.819
Recall “meditation”	0.734	0.798	0.775	0.873	0.779	0.756	0.835	0.849	0.759	0.788	0.757	0.819	0.766	0.791	0.773
Precision “meditation”	0.846	0.808	0.822	0.811	0.843	0.822	0.851	0.776	0.778	0.841	0.785	0.834	0.862	0.871	0.887
F1 score “meditation”	0.786	0.803	0.798	0.841	0.81	0.788	0.843	0.811	0.768	0.814	0.771	0.826	0.811	0.829	0.826
Recall “recovery”	0.867	0.861	0.723	0.785	0.801	0.786	0.84	0.819	0.825	0.781	0.849	0.801	0.773	0.854	0.786
Precision “recovery”	0.814	0.841	0.803	0.795	0.837	0.782	0.808	0.836	0.81	0.798	0.795	0.814	0.789	0.785	0.824
F1 score “recovery”	0.84	0.851	0.761	0.79	0.819	0.784	0.824	0.827	0.817	0.789	0.821	0.807	0.781	0.818	0.805

7. Conclusion

In the proposed study, a multichannel convolutional neural network architecture was developed for the detection of state of the mind by leveraging biosignals from the wearable devices. The different types of biosignals used in the work are electrocardiography, electromyography, respiration, blood volume pulse, and accelerometer. The model developed performed pretty well by prompting an average recall and precision of 97.238% and 97.652%, respectively, across all the classes. In the work, a comparative analysis was performed for choosing the right optimizer by keeping in mind the performance of the optimizer with respect to the cost of computation, time efficiency, and model reproducibility. Finally, it was found that the model optimized with Adam optimizer performed the best with respect to the other optimizer functions.

To conclude, the outcome of the study is very motivating. However, in the area of classification of the state of the mind and the analysis of the biosignals, there is still a huge scope for further research. Therefore, it is very much recommended to investigate multiple ways of solving the particular type of problem and to understand the complete capability of multichannel deep learning architectures, which will further impact the society in a novel and a positive way.

Data Availability

The data used to support the experiments and the findings of the study have been duly included in Section 3.1.

Conflicts of Interest

The authors of the paper declare that there are no conflicts of interest regarding the publication of the paper.

Acknowledgments

This research was funded by the Basic Science Research Program through the National Research Foundation of Korea (NRF), supported by the Ministry of Science, ICT & Future Planning (NRF-2017R1D1A3B04032905).

References

[1] A. Cohen, "Biomedical signals," in *Electrical Engineering Handbook, The Biomedical Engineering Handbook*, CRC Press, Boca Raton, FL USA, 2nd edition, 1999.

[2] A. Schmidt, "Biosignals in human-computer interaction," *Interactions*, vol. 23, no. 1, pp. 76–79, 2015.

[3] F. Liu, D. Ford, C. Parnin, and L. Dabbish, "Selfies as social movements," *Proceedings of the ACM on Human-Computer Interaction*, vol. 1, pp. 1–21, 2017.

[4] N. Howell, L. Devendorf, R. K. Tian et al., "Biosignals as social cues," in *Proceedings of the 2016 ACM Conference on Designing Interactive Systems-DIS 16*, Brisbane, Australia, June 2016.

[5] A. F. Ax, "The physiological differentiation between fear and anger in humans," *Psychosomatic Medicine*, vol. 15, no. 5, pp. 433–442, 1953.

[6] R. W. Levenson, "The autonomic nervous system and emotion," *Emotion Review*, vol. 6, no. 2, pp. 100–112, 2014.

[7] S. D. Kreibig, "Autonomic nervous system activity in emotion: a review," *Biological Psychology*, vol. 84, no. 3, pp. 394–421, 2010.

[8] R. W. Levenson and A. M. Ruef, "Physiological aspects of emotional knowledge and rapport," in *Empathic Accuracy*, W. J. Ickes, Ed., pp. 44–72, New York Guilford Press, New York, NY, USA, 1997.

[9] S. Aich, P. Pradhan, J. Park, N. Sethi, V. Vathsa, and H.-C. Kim, "A validation study of freezing of gait (FoG) detection and machine-learning-based FoG prediction using estimated gait characteristics with a wearable accelerometer," *Sensors*, vol. 18, no. 10, p. 3287, 2018.

[10] P. Schmidt, A. Reiss, R. Duerichen, C. Marberger, and K. V. Laerhoven, "Introducing WESAD, a multimodal dataset for wearable stress and affect detection," in *Proceedings of the 2018 on International Conference on Multimodal Interaction-ICMI 18*, Boulder, CO, USA, February 2018.

[11] B. Lamichhane, U. Großekathöfer, G. Schiavone, and P. Casale, "Towards stress detection in real-life scenarios using wearable sensors: normalization factor to reduce variability in stress physiology," in *Lecture Notes of the Institute for Computer Sciences, Social Informatics and Telecommunications Engineering*, pp. 259–270, Springer, Cham, Switzerland, 2016.

[12] J. A. Healey and R. W. Picard, "Detecting stress during real-world driving tasks using physiological sensors," *IEEE Transactions on Intelligent Transportation Systems*, vol. 6, no. 2, pp. 156–166, 2005.

[13] A. Saeed, S. Trajanovski, M. V. Keulen, and J. V. Erp, "Deep physiological arousal detection in a driving simulator using wearable sensors," in *Proceedings of the 2017 IEEE International Conference on Data Mining Workshops (ICDMW)*, New Orleans, LA, USA, November 2017.

[14] S. Ollander, C. Godin, S. Charbonnier, and A. Campagne, "Feature and sensor selection for detection of driver stress," in *Proceedings of the PhyCS*, pp. 115–122, Lisbon, Portugal, July 2016.

[15] G. Tanev, D. B. Saadi, K. Hoppe, and H. B. D. Sorensen, "Classification of acute stress using linear and non-linear heart rate variability analysis derived from sternal ECG," in *Proceedings of the 2014 36th Annual International Conference of the IEEE Engineering in Medicine and Biology Society*, Chicago, IL, USA, August 2014.

[16] A. S. Anusha, P. Sukumaran, V. Sarveswaran et al., "Electrodermal activity based pre-surgery stress detection using a wrist wearable," *IEEE Journal of Biomedical and Health Informatics*, 2019.

[17] S. Koelstra, C. Muhl, M. Soleymani et al., "DEAP: a database for emotion analysis; using physiological signals," *IEEE Transactions on Affective Computing*, vol. 3, no. 1, pp. 18–31, 2012.

[18] B. Kikhia, T. Stavropoulos, S. Andreadis et al., "Utilizing a wristband sensor to measure the stress level for people with dementia," *Sensors*, vol. 16, no. 12, p. 1989, 2016.

[19] C.-Y. Liao, R.-C. Chen, and S.-K. Tai, "Emotion stress detection using EEG signal and deep learning technologies," in *Proceedings of the 2018 IEEE International Conference on Applied System Invention (ICASI)*, Tokyo, Japan, April 2018.

[20] J. R. M. Fernández and L. Anishchenko, "Mental stress detection using bioradar respiratory signals," *Biomedical Signal Processing and Control*, vol. 43, pp. 244–249, 2018.

[21] Y. Jiang, N. Bosch, R. S. Baker et al., "Expert feature-engineering vs. Deep neural networks: which is better for sensor-free affect detection?," in *Lecture Notes in Computer Science*, pp. 198–211, Springer, Cham, Switzerland, 2018.

[22] T. B. Tang, L. W. Yeo, and D. J. Lau, "Activity awareness can improve continuous stress detection in galvanic skin response," in *Proceedings of the IEEE Sensors 2014*, pp. 1980–1983, Valencia, Spain, November 2014.

[23] R. Miikkulainen, J. Liang, E. Meyerson et al., "Evolving deep neural networks," in *Artificial Intelligence in the Age of Neural Networks and Brain Computing*, pp. 293–312, Academic Press, Cambridge, MA, USA, 2019.

[24] H. Cecotti and A. Graser, "Convolutional neural networks for P300 detection with application to brain-computer interfaces," *IEEE Transactions on Pattern Analysis and Machine Intelligence*, vol. 33, no. 3, pp. 433–445, 2011.

[25] S. Opałka, B. Stasiak, D. Szajerman, and A. Wojciechowski, "Multi-channel convolutional neural networks architecture feeding for effective EEG mental tasks classification," *Sensors*, vol. 18, no. 10, p. 3451, 2018.

[26] D. Yu, H. Wang, P. Chen, and Z. Wei, "Mixed pooling for convolutional neural networks," in *Proceedings of the 9th International Conference, RSKT*, Shanghai, China, October 2014.

[27] P. I. Frazier, "A tutorial on Bayesian optimization," 2018, https://arxiv.org/abs/1807.02811.

[28] M. A. Osborne, "Bayesian Gaussian processes for sequential prediction, optimisation and quadrature," Doctoral Dissertation, Oxford University, Oxford, UK, 2010.

[29] K. Janocha and W. M. Czarnecki, "On loss functions for deep neural networks in classification," 2017, http://arxiv.org/abs/1702.05659.

[30] Z. Zhang and M. Sabuncu, "Generalized cross entropy loss for training deep neural networks with noisy labels," in *Advances in Neural Information Processing Systems*, pp. 8792–8802, 2018.

[31] D. P. Kingma and J. Ba, "Adam: a method for stochastic optimization," 2014, http://arxiv.org/abs/1412.6980.